Theoretical investigation of the atomic spectra of neutral and trivalent lanthanides : Application to ultracold gases and doped solids

Gohar Hovhannesyan

THÈSE DE DOCTORAT DE L'ÉTABLISSEMENT UNIVERSITÉ BOURGOGNE FRANCHE-COMTÉ PRÉPARÉE AU LABORATOIRE INTERDISCIPLINAIRE CARNOT DE BOURGOGNE

École doctorale n°553
École Doctorale Carnot-Pasteur

Doctorat de Physique

Par

Mme HOVHANNESYAN Gohar

Theoretical investigation of the atomic spectra of neutral and trivalent lanthanides: Application to ultracold gases and doped solids

Thèse présentée et soutenue à Dijon, France, le 14 décembre 2023

Composition du Jury :

M. Olivier DULIEU	Laboratoire Aimé Cotton, Université Paris-Saclay	Rapporteur
Mme Lydia TCHANG-BRILLET	LERMA, Observatoire de Paris-PSL and Université de Sorbonne	Rapporteure
M. Jean-François CLEMENT	IEMN, Université de Lille	Examinateur
M. Gérard COLAS DES FRANCS	Laboratoire ICB, Université de Bourgogne	Président
M. Vincent BOUDON	Laboratoire ICB, Université de Bourgogne	Directeur de thèse
M. Maxence LEPERS	Laboratoire ICB, Université de Bourgogne	Codirecteur de thèse

Contents

Summary

Laser cooling and trapping of lanthanides has opened the possibility to carry out new experiments with ultracold dipolar gases, which can be used, for example, for quantum simulation of solid state physics. To identify new suitable candidates for laser-cooling, it is crucial to have a precise spectroscopic knowledge of the atom under consideration. First general direction of the thesis is the modeling of the energy levels of neutral lanthanides, firstly for neutral erbium (Er), an element belonging to the right part of the lanthanide row, which is particularly attractive because of a narrow-inner shell transition, connecting the erbium ground state to a long-lived excited state and secondly for neutral neodymium (Nd), an element belonging to the left part of series, which has not yet been considered for laser-cooling. Using the semi-empirical method implemented in the Cowan suite of codes, we have improved the levels of odd parity configurations of Er by incorporating more configuration interaction parameters than in previous calculations. We have calculated quantities such us Lande g factors, excited state lifetime, and polarizabilities, which were then compared with experimental results done by a group in Innsbruck, Austria. During the collaborative work few magic wavelength conditions were proposed. Then, for Nd, we were able to interpret more than 200 experimental levels of the NIST database belonging to both parities. For Nd, after doing precise spectroscopic calculations, we have proposed new laser-cooling transitions. The logical continuation and perspective of the work for the future will be the calculation of the Einstein coefficients, which are necessary to characterize the efficiency of laser cooling and trapping of atoms.

Most of the lanthanides usually exist as trivalent cations. Because of the presence of unpaired electrons lanthanides exhibit strong electromagnetic and light properties. In their trivalent form, lanthanides are widely used for industrial purposes, in lasers, and as (co-) dopants in doped-fiber optical amplifiers; for example, in Er-doped fiber amplifiers. Second general direction of the thesis is devoted to trivalent lanthanides, especially to discussion when they are doped in a host material. All the transitions that ware interesting for these applications are activated by the crystal field. Judd-Ofelt theory has been used for decades to describe these transitions, but there are some restrictions arising from the way it is derived. This is especially the case for Eu^{3+}. In the thesis we have done spectroscopic calculations, using the same methodology as for neutral lanthanides, for three elements: Eu^{3+}, Nd^{3+} and Er^{3+}. We have proposed an extension of Judd-Ofelt theory in which we include precise spectroscopic calculations of the considered ion and account for wavelength dependence of the refractive index. The results of the extension are satisfactory, we are able to give a physical insight

into all the transitions within the ground electronic configuration, including the ones that were forbidden before by the standard version of the theory, and also to reproduce quantitatively experimental absorption oscillator strengths. The code used to make the calculations is available on GitLab. As a prospect, we plan to treat transitions with polarized light or between individual ion-crystal sublevels. This will be possible in our model, because the only fitted parameters are the crystal-field ones. This can open the possibility to model the spectroscopic properties of Ln^{3+}-doped nanometer-scale host materials.

Résumé

Le refroidissement laser et le piégeage des lanthanides ont ouvert la possibilité de réaliser de nouvelles expériences avec des gaz dipolaires ultra-froids, qui peuvent être utilisés, par exemple, pour la simulation quantique de la physique du solide. Pour identifier de nouveaux candidats au refroidissement laser, il est crucial de disposer d'une connaissance spectroscopique précise de l'atome considéré. La première grande orientation de ma thèse est la modélisation du spectre des lanthanides neutres, d'une part de l'erbium (Er), un élément de la partie droite de la rangée des lanthanides, particulièrement attractif en raison d'une transition très fine, reliant l'état fondamental et un état excité métastable, et d'autre part du néodyme (Nd), un élément de la partie gauche de la rangée, qui n'a pas encore été explorée pour le refroidissement laser. En utilisant la méthode semi-empirique implémentée dans les codes de Cowan, nous avons amélioré la description des niveaux de configurations impaires de Er. Nous avons aussi calculé des quantités telles que le facteur de Landé, la durée de vie et la polarisabilité de l'état excité cité plus haut, pour les comparer aux résultats expérimentaux obtenus par un groupe d'Innsbruck en Autriche. Ensuite, pour Nd, nous avons pu interpréter plus de 200 niveaux expérimentaux de la base de données du NIST appartenant aux deux parités, puis nous avons proposé de nouvelles transitions de refroidissement laser. La suite logique de ces travaux est le calcul des coefficients d'Einstein, nécessaires pour caractériser l'efficacité du refroidissement laser et du piégeage des atomes.

La plupart des lanthanides existent généralement sous forme de cations trivalents. En raison de la présence d'électrons non appariés, les lanthanides présentent d'intéressantes propriétés électromagnétiques et lumineuses. Sous leur forme trivalente, ils sont largement utilisés à des fins industrielles, dans les lasers et comme (co-)dopants dans les amplificateurs optiques à fibres, par exemple dopée à l'erbium. La deuxième grande orientation de ma thèse est consacrée aux lanthanides trivalents, utilisés comme dopants dans un matériau hôte. Toutes les transitions intéressantes pour ces applications sont induites par le champ cristallin. La théorie de Judd-Ofelt est utilisée depuis des décennies pour décrire ces transitions, mais il existe certaines restrictions liées à la manière dont elle est formulée, en particulier pour l'europium (Eu^{3+}). Dans cette thèse, nous avons effectué des calculs spectroscopiques, en utilisant la même méthodologie que pour les lanthanides neutres, pour trois éléments : Eu^{3+}, Nd^{3+} et Er^{3+}. Nous avons proposé une extension de la théorie de Judd-Ofelt dans laquelle nous incluons une description précise du spectre de l'ion dopant, et nous tenons compte de la variation de l'indice de réfraction du matériau hôte avec la longueur d'onde. Les résultats de notre modèle sont satisfaisants, car il nous donne un aperçu physique de toutes les

transitions observées, y compris celles qui sont interdites par la version standard de la théorie. Par ailleurs, notre modèle reproduit quantitativement les forces d'oscillateurs d'absorption expérimentales. Le code utilisé pour effectuer les calculs est disponible sur GitLab. Comme perspective, nous prévoyons de traiter les transitions en lumière polarisée ou entre des sous-niveaux individuels des ions. Cela sera possible dans notre modèle, car les seuls paramètres ajustés sont ceux du champ cristallin. Cela ouvre la possibilité de modéliser les propriétés spectroscopiques de matériaux hôtes à l'échelle nanométrique.

Acknowledgments

Throughout my life I had quite a few examples on how important is the human connection. This belief reached its peak during my PhD. I am forever grateful for people who has been with me during this challenging time and I will use the opportunity in my manuscript to write a few words of appreciation to each one of them. All the people in my life know how emotional I am, but here I will try to keep it professional.

First I would like to thank the jury members, for giving me part of their precious time, for agreeing to read this manuscript.

My most profound appreciation goes to my primary supervisor Maxence Lepers. I am thankful to the fate, or universe for having the gentlest, most considerate supervisor anyone can ask for. I have worked with Maxence Lepers for almost 4 years during my masters internship and my PhD. Your constant support, your kindness and your attentiveness to detail made this work possible. I hope the future holds many other projects and opportunities for us to work together, because these four years were extraordinary and I hope to have the honor of working with you again. Your human qualities are prime examples how a "great supervisor" should be. Your professional abilities will always be a motivation for my career. Your vast wisdom and wealth of experience have inspired and will inspire me throughout my life. Thank you for all the comments, feedback, all the discussions we had: they all are and will be helpful for me.

I would like to thank Vincent Boudon for his time, effort, for all the guidance, support, and instruction he provided me throughout my doctoral studies. Thank you for the thoughtful comments and recommendations on the thesis and not only. I have enjoyed greatly being in your team and working with you.

My warmest regards goes to my friends (the gang: the perfect family that I have created). You are one of the best parts of my life, and nothing could have been possible without you. Thank you for your unconditional support, for coffee breaks, for fun games, for very smart physics jokes and for all the time we spent together. This endeavor would not have been possible without my friends who live in Armenia. Thank you for being in my life and for your strong moral support. Thank you my best friend Astghik here in France and Feya and Yeva in Armenia, for being there for me in all the situations, especially for the ones, where even I could not be there for myself. I am lucky I know you and I will cherish you forever. Thank you for all the emotional support, Astghik, you have no idea how much you helped me. Many thanks to Lily, Vahan and Emily for supporting me during my PhD and colouring many of my days in bright colours. I am thankful to my family for all the support and encouragement I got despite the distance separating us. Kilometers are powerless in front of the love

and confidence you have for me. Thank you for believing in me.

Enfin, je voudrais remercier mon adorable copain, Nathan, qui est entré dans ma vie au cours des derniers (les plus difficiles) mois de mon doctorat comme un cadeau bien conçu de l'univers et me donne tout l'amour et le soutien émotionnel dont je pourrais rêver. Chéri, tu es (ma) personne merveilleuse et je suis bénie de t'avoir rencontré. La vie est meilleure avec toi. Merci, je t'aime.

Many thanks to all the people I met during these exciting years, lab members, administrative workers, secretaries, technical support providers, all of you have a small contribution in my life and thesis.

Thank you. I love you all.

- But what if I fall?
- Oh, darling, what if you fly?

Source unknown

Introduction

Spectroscopy as a broad field of experimental and theoretical research has provided much to our knowledge with regard to the physical nature of life and various things, not only of our own Earth but of the Sun, of planets, of interstellar space and of distant stars too. Although the Romans were already familiar with the ability of a prism to generate a rainbow of colors [1], it is very appropriate to say that Isaac Newton is the traditional founder of spectroscopy, but it is only fair to acknowledge that he was not the first scientist to study and report on solar spectrum. The works of Athanasius Kircher (1646), Jan Marek Marci (1648), Robert Boyle (1664), and Francesco Maria Grimaldi (1665), predate Newton's optics experiments (1666–1672). Sir Isaac Newton's experiments discovered that the white light could be split up into component colors when passing through a prism, and that these components can be recombined to generate a white light. It was for him to show that the colors did not originate in the crystal, the prism is not imparting or creating the colors, but that the colors were the necessary ingredients that make up the sunlight. The band of colors falling on a screen Newton called a *spectrum*. If Newton had used a narrow slit as a secondary source of light and examined the spectrum, he would have very probably discovered the dark absorption lines on the Sun's spectrum, as did Joseph von Fraunhofer almost 100 years later. He made a significant experimental leap forward by replacing a prism with a diffraction grating as the source of wavelength dispersion. Fraunhofer built off the theories of light interference developed by Thomas Young, François Arago and Augustin-Jean Fresnel. He performed his own experiments to demonstrate the effect of passing light through a single rectangular slit, then two slits, and so forth, eventually developing a means of closely spacing thousands of slits to form a diffraction grating. Fraunhofer made and published systematic observations of the solar spectrum, and the dark bands he observed and specified the wavelengths of are still known as Fraunhofer lines [2].

It was around this time when lanthanides were first discovered. In 1787, in a small Swedish town called Ytterby was identified the first mineral that contained a lanthanide. This unusual black mineral was later separated into different elements, and in 1800s would be called gadolinite, after the chemist Johan Gadolin, who found the first compound. The name Ytterby has been vastly used after this; ytterbium (Yb), yttrium (Y), terbium (Tb), and erbium (Er) have been named after this little town. The privilege to be the first lanthanide to be obtained as an element, was cerium's (Ce). In 1839 lanthanum was discovered by Carl Gustav Mosander and got its name because it was "lying hidden" or "escaping notice" in a cerium mineral.

The systematic acknowledgment of spectra of chemical elements began only in the 1860s by Robert Bunsen and Gustav Kirchhoff. By making spectro-chemical analysis in laboratory and astrophysical science, they established the linkage between chemical elements and their unique spectral patterns. In the process, they instituted the technique of analytical spectroscopy. These works led to the demonstration that spectroscopy could be used for trace chemical analysis and they have discovered several chemical elements, which were previously unknown. One of the example of this is the discovery of gadolinium (Gd) by Jean Charles de Marignac, who detected its oxide by using spectroscopy. It is named after the mineral gadolinite. The link between the nature of absorption and emission was established exactly at this period. Later, the husband-and-wife team of William and Margaret Huggins used spectroscopy to determine that the stars were composed of the exactly same elements as found on Earth. This became a good step forward for lanthanide chemistry.

In 1923, George Charles de Hevesy and Dirk Coster discovered hafnium (Hf) at the University of Copenhagen and named it after the city's New Latin name: Hafnia. Using an x-ray spectra of the elements, Moseley proved that there are 14 elements between Lanthanum and Hafnium. The fifth element was named Holmium (Ho) after the city Stockholm, thulium was named after the old name Thule (Tm) and samarium (Sm) was named after the mineral samarskite from which it was isolated. The pure neodymium (Nd) was isolated in 1925 and got its name from the Greek words *neos*: new, and *didymos*: twin. Praseodymium's (Pr) name was derived similarly, from Ancient Greek *prasinos*: leek-green, and means green twin, since it appears with different shades of yellow-green when incorporated into glasses. All these elements were classified as "rare earth" elements, because they were obtained in rare minerals. In 1925 Victor Goldschmidt introduced the term lanthanides, which was a natural choice since the lanthanum is the first element of the series. Although the word comes from the Greek word *lanthanein*: "to lie hidden", it does not reflect the idea of the natural abundance of these elements, but rather refers to the fact that they like to "hide" behind each other in minerals. Dysprosium (Dy) was similarly named, using the Greek *dysprositos* for "hard to get at". Europium (Eu) was named after the continent, since it was separated from the mineral samaria in magnesium-samarium nitrate by the French chemist Eugène-Anatole Demarcay. Promethium (Pm) was the last to be discovered in 1947 at Oak Ridge National Laboratory. Czech chemist Bohuslav Brauner was surprised with the differences in properties between neodymium and samarium, since these were larger and more abnormal than between any two consecutive lanthanides; as a conclusion, the idea of another element existing between these two was suggested. The newly found element got its name from the Greek Titan Prometheus, who stole fire from Zeus and passed it to people. The element's name is a reference to the courage and pain needed to synthesize it. So, with the exception of Promethium, all the rare earths were discovered in the span of a little more than a century. Although lanthanides are very difficult to separate from each other, in the 19th century, the scientists, working on such minerals, found that the characteristics of the light emitted by hot atoms of a particular element were distinctive to the elements. For example, the street lamps that give strong yellow light contain sodium.

If we do a scientific jump to early 20th century we will be encountering the inter-

pretation of spectral series of hydrogen by Lyman and the creation of the basics of quantum theory by Plank [3] and Einstein [4], which was later developed by Pauli, Heisenberg, Schrödinger, and Dirac. This is also the time span where Bohr formulated his quantum mechanical model of atom and published a theory about hydrogen-like atoms, which could explain the observed wavelengths of spectral lines due to electrons transitioning from different energy states [5]. After some advances in quantum mechanics, such as understanding of the spin and exclusion principle that allowed conceiving how electron shells of atoms are filled with the increasing atomic number, a special attention was drawn to the branch of spectroscopy that deals with radiation related with atoms that are missing several electrons. These are called multiply ionized atoms, or multiply charged ions, or highly charged ions. It turns out that these ions are quite ever-present in nature and are caught to be responsible for diverse phenomena from the luminescence of the Sun to the existence of the Earth's ionosphere. Atoms in their ionic state may have a different color from neutral atoms. The lowest excited electron shells of such ions can decay into stable ground states; this produces photons in ultraviolet, extreme-ultraviolet and soft X-ray spectral regions.

After this analytical and exploratory period, lanthanide unique optical properties were taken advantage of in optical glasses, filters, and lasers. In the mid-1970s, E. Soini and I. Hemmila proposed lanthanide luminescent probes for time-resolved immunoassays [6] and this has been the starting point of the present numerous bio-applications based on optical properties of lanthanides. The natural occurrences for different ionization states varies from one element to another. In low ionisation stages the lanthanides appear in astrophysics: neutron stars, chemically peculiar stars, kilo novaes. Recent studies show that kilo novae photospheric spectra exhibit absorption features of La^{3+} and Ce^{3+} in the NIR region [7].

Most of the lanthanides usually exist as trivalent cations. Because of the presence of unpaired electrons lanthanides exhibit strong electromagnetic and light properties. In their trivalent form, lanthanides are widely used for industrial purposes [8]. Trivalent lanthanide (globally referred as Ln^{3+}) compounds and doped inorganic materials are used as catalysts, magnetic, optical and laser materials, in rechargeable hybrid batteries, organic electronics, wind- and solar-energy conversion, economical lighting, bio-analyses, imaging, etc. Most lanthanides are widely used in lasers, and as (co-) dopants in doped-fiber optical amplifiers; for example, in Er-doped fiber amplifiers, which are used as repeaters in the terrestrial and submarine fiber-optic transmission links that carry internet traffic. These elements deflect ultraviolet and infrared radiation and are commonly used in the production of sunglass lenses. In addition, Ln^{3+} doped crystal analyses are still in the object of fundamental studies. The electronic configuration for trivalent lanthanides is [Xe] $4f^w$, where [Xe] is the ground configuration of xenon, only composed of closed subshells, w is varying from 0 (La) to 15 (Lu) ($w = 6$ for Eu^{3+} for example). The first excited configuration is $4f^{w-1}5d$.

The applications mentioned before imply transitions between levels of the ground configuration, which are forbidden in the free-ion case. They become allowed in solids due to the coupling with levels of higher configuration, especially $4f^{w-1}5d$, created by the crystal field around the Ln^{3+} ion. Therefore, these applications require the knowledge of the ground and first excited configurations energy levels, and the intensities of

transitions between levels of the ground configuration.

Moreover, in spectroscopy, electromagnetic fields are used to probe the structure of internal states. Extensions of the same techniques developed for spectroscopy allow one to control the internal degrees of freedom coherently. Laser cooling and trapping techniques allow one to do the same with the external degrees of freedom of the atom. Ultracold gases are ensembles of atoms held at a temperature near absolute zero. Experiments with ultracold atoms study a variety of phenomena, including quantum phase transitions, Bose–Einstein condensation (BEC), bosonic superfluidity, quantum magnetism, many-body spin dynamics, etc. Samples of ultracold atoms are typically prepared through the interaction of a dilute gas with a laser field. Evidence for radiation pressure, was demonstrated independently by Lebedev, and Nichols and Hull in 1901. In 1933, Otto Frisch demonstrated the deflection of individual sodium particles by light generated from a sodium lamp. Owing to their unique quantum properties, ultracold atoms have a wide variety of applications. They have been proposed as a platform for quantum computation and quantum simulation [9], accompanied by very active experimental research to achieve these goals.

In the field of ultracold atomic and molecular matter, quantum gases composed of particles with a strong intrinsic permanent dipole moment, called dipolar gases, have attracted great interest in the last few years because they can be controlled by external electric or magnetic fields. Through long-range and anisotropic interactions between particles, dipolar gases enable the production and study of highly correlated quantum matter, which is critical for quantum information or for modeling many-body or condensed matter physics [9–11].

Open-shell atoms have a permanent magnetic dipole moment that is determined by their total angular momentum. In the context of ultracold matter, important achievements were also the first Bose-Einstein condensates of highly magnetic atoms obtained with chromium [12]. Later, much attention began to be attracted to the lanthanides. These atoms open up new possibilities for interactions, not only because of their large ground state magnetic dipole moments, enabling long-range and anisotropic interactions, but also because of the large number of optical transitions with widely varying properties that provide controllability that can help exploit these interactions. These distinctive properties are primarily due to a unique electronic structure: the so-called submerged f-shell configuration. All lanthanides have a completely filled 6s shell and an inner 4f shell filled to some extent. Moreover, among the lanthanide atoms with the largest atomic numbers, many share a common set of properties and often have similar transitions at the same wavelengths, which helps the theoreticians in various analysis and can be, for some cases, considered interchangeably in certain experiments [13, 14]. These characteristic properties enable enhanced control over ultracold atoms and their interactions. So far, laser cooling has been demonstrated in erbium [15, 16], dysprosium [17, 18], holmium [19], thulium [20, 21] and europium [22], as well as in erbium–dysprosium mixtures [23].

These achievements stimulated both theoretical and experimental studies, in particular aiming to identify new suitable species for laser cooling. In this respect, among the Ln elements of the left half of the lanthanides series in the periodic table, neodymium (Nd) and praseodymium (Pr) represent the most suitable energy spectrum for the for-

mation of a dipolar gas. Nd represents the great advantage of having bosonic and fermionic stable isotopes, which makes Nd a very attractive candidate for such experiments.

In order to find possible laser-cooling transitions, it is essential to carefully model the spectrum - energies and transition dipole moments (TDMs). Particular attention should be paid to accurately describing configuration-interaction (CI) mixing, to which TDMs are very sensitive, especially those that lead to weak transitions, which play an important role in this design. The main technical difficulty comes from the least-square fitting of energy levels, because we need to determine to which experimental counterparts each computed energy level should converge.

Evidently, the success of projects aimed at laser cooling of neutral lanthanides, as well as the analysis of crystals doped with Ln^{3+}, requires a thorough study of the spectroscopic data of the corresponding elements and/or their ions. This is the leading principle of this research work.

The thesis has three parts: Theoretical Background, Trivalent Lanthanides and Neutral Lanthanides, and each part has two chapters. In chapter one, which is named "Elements of atomic-structure theory", I recall some theory which can be necessary for the reader to understand the essence of the work and to go further into the research. The chapter starts with a summary of spectra for atoms and ions and prompts on angular momentum. The chapter also includes the description of one-electron atom, then we go one step further to describe a two-electron atom and, finally, the idea is generalized to reach to N-electron atom system. The chapter is concluded by recalling some properties of transitions.

Chapter two is dedicated to a description of transition intensities in solids when they are doped with lanthanides. It covers a broad chronicle on lanthanides as a series of elements and an explanation to why are those elements so attractive for science. We carry on the chapter description with general theoretical remarks on ions in solids, and their uniqueness as a physical system. The last section of the chapter is devoted to the Judd-Ofelt theory, which was derived in the 1960s and is used to characterize the intensities of lanthanide and actinide transitions in solids and solutions. The section includes explanation of the theory as well as the challenges that arise for some trivalent lanthanides, for example Eu^{3+}, Pr^{3+}, Sm^{3+}, Tb^{3+}, etc.

No scientific work is complete without a well thought methodology of calculations designed carefully and specifically for the research topic. I cover this narration in first section of chapter three. It includes description for the software, program and the calculation approach we adopted for the sake of precision in this research work. In chapter three I also describe free-ion calculations on three trivalent lanthanides, which was done with the calculation technique described in the previous chapter. It includes three sections; each designed for the description of individual calculations performed on those three elements that were considered in the work: Nd^{3+}, Er^{3+} and Eu^{3+}.

Chapter four shows and summarizes the attempts done in order to overcome the challenges that arise in Judd-Ofelt theory and making the later more inclusive for lanthanides. It has two sections that cover the evolution of the extension theory, by describing the steps we have taken for our objective. Each of those steps are followed with a benchmarking calculations on three lanthanides that were described in chapter

three.

Since ultracold atomic physics is one of the most prolific and fastest growing research areas in modern physics, I have carried out spectroscopic calculations on neutral Erbium and Neodymium, which are described in chapters five and six, respectively. In chapter five I describe the observation and coherent excitation of atoms on the narrow inner-shell orbital transition at 1299 nm, connecting the erbium ground state to the excited state done by the experimental group in Innsbruck as well as the theoretical work done by us to improve the spectroscopic data of erbium and support the experiment. In chapter six, I present a detailed modeling of the energy levels of neutral neodymium, which will help to identify possibly laser-cooling transitions.

The thesis is then summarized with conclusion marks and possible points for future improvements.

Part I

Theoretical Background

Chapter 1

Elements of atomic-structure theory

Spectroscopic studies of the light emitted or absorbed by atoms and ions date from the early nineteenth century. From these studies, it gradually became clear that the particular wavelengths of light associated with atoms of a given element are characteristic of that element, and that spectral information must therefore provide clues to the internal structure of the atom. During the last quarter of the nineteenth century, important regularities were discovered among the wavelengths of hydrogen and other comparatively simple spectra [24].

The spectrum emitted by atom or ion provides reliable signature to analyze the composition of alloys or other mixtures of atoms; indeed, several elements (among them helium, rubidium, cesium, gallium, indium, and thallium) were discovered spectroscopically. A good example of this is the Fraunhofer lines, which were originally observed as dark features (absorption lines) in the optical spectrum of the Sun.

Understanding the lines emitted by the atoms was the initial motivation to derive the quantum theory. The fact that the light is radiated by an atom at only certain discrete wavelengths is associated with the fact that the atom can exist only in stationary states having certain discrete values of internal energy E. The various possible energies of the atom are called energy levels. The lowest possible energy is called the ground level and each quantum state of the atom having this energy (there may be more than one such state) is called a ground state. All other levels are called excited levels and the corresponding quantum states are called excited states. The fundamental problem in the theory of atomic structure is the calculation of the wavefunction for each quantum state of interest. But before moving to a calculation part wee need to understand the theory that lies behind all this physics. This chapter is dedicated to the theoretical background for all the applications mentioned in the introduction. It also includes the theory necessary to understand the calculations and the results that will be presented later in the thesis.

The outline of the chapter is as follows, in section 1.2 we will remind some angular momentum theory and then we will go from the simplest atoms to most complex cases: one-electron atom (1.4), two-electron atom (1.5) and finally, N-electron atom (1.6). In this chapter we also briefly introduce the creation of coupled functions, followed by

a discussion about possible coupling schemes. We recall state notations that will be used throughout this research and some properties and examples of 3n-j symbols. The chapter is concluded with transition properties.

1.1 Characteristics of spectra of atoms and ions

Each atom or ion emits a line spectrum which is characteristic of that atom or ion. The spectrum emitted by neutral atoms of a given element is called the first spectrum of that element, and is denoted by the Roman numeral I, the spectrum emitted by a singly ionized atoms is called the second spectrum and is denoted by the Roman numeral II, etc. Obviously the number of different possible line spectra of an element is equal to its atomic number Z, consequently there exist spectra H I, He I, He II, Li I, Li II, etc. By extension Roman numerals are used to refer also to the ion that produced the spectrum: C I is the neutral carbon, C II is the singly ionized atom C^+, C IV is C^{3+}, etc. The wavelengths of spectrum lines are most commonly given in Angstroms (1Å $= 10^{-8}$ cm $= 10^{-10}$ m), but sometimes in microns or micrometers. Most commonly, however, spectrum lines are described simply in terms of the wavenumber σ, or the number of wavelengths (in vacuum) per unit of length (usually per centimeter: cm^{-1}): $\sigma = \frac{E}{hc}$, where h is the Planck constant and c is the speed of light in vacuum. E/hc is called the pseudo-energy unit and is used almost exclusively. The energies of the various levels of an atom are most commonly specified in terms of the excitation energy above the ground state. A frequently used unit, especially for levels corresponding to excitation of inner-shell electrons, is the electron-volt. The equivalences between the energy and pseudo-energy units are: 1 eV = 8065.479 cm^{-1}.

The possible energy levels of an atom are conveniently depicted by means of a diagram in which each level is represented by a short horizontal line placed at the appropriate point along a vertical energy scale. Each level is usually placed in one of several different columns, according to certain properties of the quantum state(s) that correspond to that level. An example of an energy diagram is figure 1.1, which will be discussed in section 3.4 for Eu^{3+}.

If an atom exists in an excited state of energy E_2 it may spontaneously decay to some other state of lower energy E_1 the energy difference appearing as a photon of energy $E_2 - E_1$. This photon corresponds to emitted radiation of frequency ν, vacuum wavelength λ, and wavenumber σ given by: $E_2 - E_1 = h\nu = \frac{hc}{\lambda} = hc\sigma$, or if the energy levels are given in the pseudo-energy units $\frac{E}{hc}$: $\frac{E_2}{hc} - \frac{E_1}{hc} = \frac{1}{\lambda} = \sigma$. On the other hand, if the atom exists in the state 1 and lies in a radiation field that includes radiation of wavenumber σ, it may be excited to the state 2 by absorption of one photon of energy E_2 - E_1. The Ritz combination principle states that any two energy levels of the atom can combine in the above manner to give rise to a spectrum line. The visual representation of absorption and emission is shown in figure 1.2.

The presence of an external electric or magnetic field may result in either a slight decrease or a slight increase in the energy of an atom. In an energy-level diagram, each possible level is in general split into several possible sublevels. The magnitude of the effect depends how strong the external field is. Each spectrum line is then split into

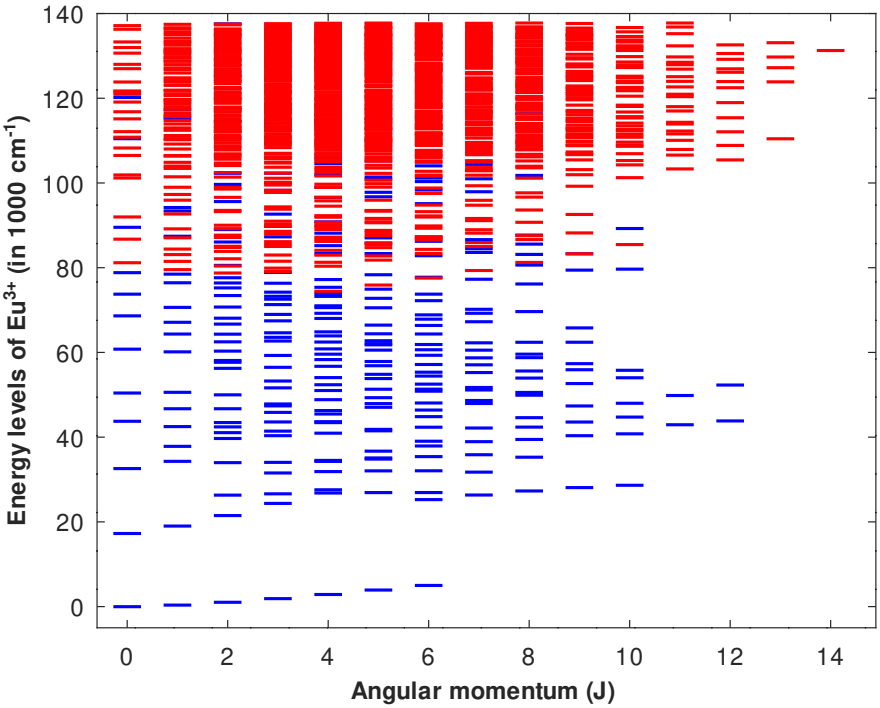

Figure 1.1: Energy diagram of the $4f^6$ (blue) and $4f^5 5d$ (red) configurations of Eu^{3+} as functions of the electronic angular momentum J. All energy values are in cm^{-1} and the graph is limited to 140000 cm^{-1}.

several parts. This effect is called Stark effect if the external field is electric and Zeeman effect if the field is magnetic. In addition to the splittings produced by external fields, each level may be split into a number of sublevels as a result of hyperfine-structure splitting (caused primarily by magnetic interactions of the electrons with the nuclear magnetic moment).

The classical problem of experimental spectroscopy is to deduce the possible energy levels of an atom or ion from the observed wavenumbers of its spectrum lines. In comparatively simple atoms, there is in principle no real problem in making purely empirical spectrum analysis. In practice, there can be serious difficulties in carrying the procedure beyond the determination of some of the lower-lying levels, especially in the more complex atoms. Energy levels and spectra are very useful for direct practical reasons, knowledge of the level structure of an atom is one of the final goals in which scientists are interested. Energy levels and line strengths provide the main clues to a fundamental understanding of the electronic structure of the atom. These clues, however, can be interpreted meaningfully only in terms of a theoretical model. There were many attempts to find a suitable model for adequately describe atomic structure. The state of the art was well summarized in 1935 by Condon and Shortley [25]. Then a very powerful mathematical technique, the algebra of irreducible tensor operators, was developed by Racah [26].

The theory of atomic structure can be used to predict the numbers and types of energy levels for any given atom. It can be used in a semi-empirical parameterized

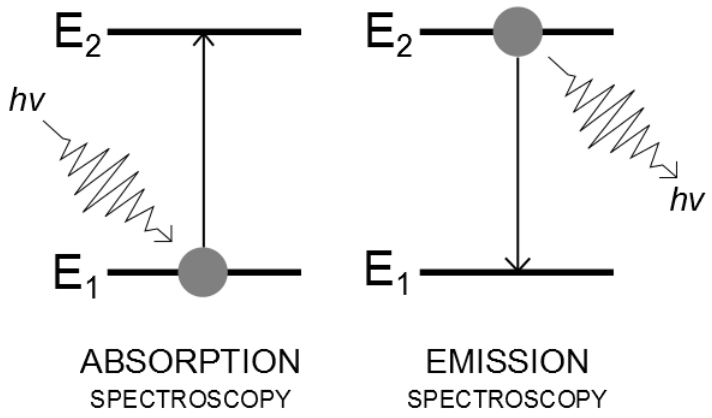

Figure 1.2: A simple diagram for absorption and spontaneous emission.

form, in which the values of certain theoretical parameters are determined by least-squares fitting of empirically determined energy levels. The theory can also be used in a completely *ab initio* fashion by computing theoretical values for above mentioned parameters. The accuracy of computed results is limited, especially for very complex neutral atoms, but the predicted energy level structures can still provide a very helpful guide for getting a start to an empirical spectrum analysis. In the *ab initio* form of the theory (and to a certain extent in the semi-empirical form also), one obtains not only level energies but also the wavefunctions of the corresponding quantum states. From these wavefunctions one can compute any desired properties of the atom, for example the strengths of spectrum lines.

The fundamental problem in the theory of atomic structure is the calculation of the wavefunction for each considered quantum state. For practical purposes, it is convenient to be able to describe each wavefunction briefly in terms of characteristic properties of the function; these properties then serve also to provide an informative and useful designation for the corresponding energy level. The properties in question consist primarily of certain symmetry properties of the wavefunction. When discussing atoms or molecules in crystals, the use of group theory is essential, but for free atoms, which show a spherical symmetry the pertinent full rotation group is closely related to the angular momentum properties of the atom. This gives us permission to work directly in terms of the quantum mechanical theory of angular momentum.

1.2 Reminder on angular momentum

In physics, angular momentum is the rotational analog of linear momentum. It is an important physical quantity. The angular momentum is especially useful in the problems with central forces and central potentials, because it is a constant of motion, i.e. it is conserved. Conservation of angular momentum is also why hurricanes form spirals and neutron stars have high rotational rates. The angular momentum is a

constant of motion also for the isolated composed systems. There are two special types of angular momentum: the spin angular momentum is the angular momentum around the object's centre of mass, and the orbital angular momentum is the angular momentum around a chosen center of rotation. The Earth has an orbital angular momentum by the nature of its rotation around Sun, and a spin angular momentum by the nature of its daily rotation around the polar axis. The total angular momentum is the sum of the spin and orbital angular momentum.

In quantum mechanics, angular momentum (like other quantities) is expressed by an operator, and its one-dimensional projections have quantized eigenvalues. Angular momentum is subject to Heisenberg's uncertainty principle, which implies that at any given time only one projection (also called a component) can be measured with a certain accuracy, while the other two then remain undefined.

An example of isolated composed system is an atom in the absence of external field. In classical mechanics, the orbital angular momentum $\vec{L}$ (about some given reference point) of a particle moving with linear momentum $\vec{p}$ at a position $\vec{r}$ with respect to that point is defined as $\vec{L} = \vec{r} \times \vec{p}$, or for example for the z component it is $L_z = xp_y - yp_x$. Other components are obtained by circular permutation. The corresponding quantum-mechanical operators, obtained as usual by replacing p_x with $-i\hbar\frac{\partial}{\partial x}$, etc., are given by $L_z = -i\hbar(x\frac{\partial}{\partial y} - y\frac{\partial}{\partial x})$.

The commutation relation for a general angular-momentum operator $\vec{J}$ is $[J_i, J_j] = \epsilon_{ijk} i\hbar J_k$, where ϵ_{ijk} is the Levi-Civita symbol and is 1 if (i, j, k) is an even permutation of (x, y, z), -1 if it is an odd permutation, and 0 if any index is repeated. They are applicable to electron spin $\vec{S}$ as well as to orbital angular momentum $\vec{L}$. It is possible to find functions that are not only eigenfunctions of one component of $\vec{J}$ (usually J_z) but also are eigenfunctions of $\vec{J}^2 = \vec{J} \cdot \vec{J} = J_x^2 + J_y^2 + J_z^2$, which is possible, because $\vec{J}^2$ and J_z commute. They also commute with the Hamiltonian of isolated system or with the Hamiltonian with central field potential. The possible eigenvalues of $\vec{J}^2$ is found to be $j(j+1)\hbar^2$ where $j = 0, 1/2, 1, 3/2, 2, ...$ For any given value of j, the possible eigenvalues of J_z are $m_j\hbar$, where $m_j = -j, -j+1, -j+2, ..., j-1, j$. The eigenstates of $\vec{J}^2$ and J_z are $|jm_j\rangle$. The quantum numbers m_l and m_s are used in the cases of orbital and spin momenta.

An electron is known from both empirical evidence and the relativistic Dirac theory to possess an intrinsic angular momentum corresponding to the value $j = 1/2$. For electron spin, the general symbols $\vec{J}$, j, and m_j are customarily replaced by $\vec{S}$, $s(= 1/2)$, and m_s. For a single electron, the only possible eigenvalue of $\vec{S}^2$ is $s(s+1)\hbar^2 = \frac{3}{4}\hbar^2$ and the possible eigenvalues of S_z are $m_s\hbar$, where $m_s = -\frac{1}{2}$ or $\frac{1}{2}$. Electrons are also known to carry orbital angular momentum, which is a property of electron's rotational motion and is related to the shape of the orbital of the electron. In the theory it is marked as ℓ and can have integer values.

1.3 Coupled angular-momentum states and Wigner 3n-j symbols

The physical reason for our interest in angular-momentum coupled states is that there usually exists some sort of interaction between the two subsystems to which the angular momenta J_1, and J_2 have a reference. For example, in the case of two electrons, that will be discussed in section 1.5, in an atom moving with orbital angular momenta l_1, and l_2, there exists the Coulomb repulsion of either electron by the other; in the case of a single electron, there exists a magnetic interaction between the magnetic dipole associated with the spin angular momentum s and that associated with the orbital angular momentum l. As a consequence, each subsystem exerts a force on the other, causing a rotation, so that neither J_1 nor J_2 are constant of motion, on the other hand if there is no external force acting on the combined system of $J_1 J_2$ then the total momentum J remains constant. With the presence of an external force the z-components of J_1 and J_2 are not constant and m_1 and m_2 are not physically significant or "good" quantum numbers, but the sum $J_{1z} + J_{2z}$ remains constant and so the good quantum numbers are $m_1 + m_2$. The coupled wavefunction discussed below, reflects this situation: each corresponds to definite values of the quantum numbers j and m, in agreement with the fact that the magnitude and orientation of J are constant in time, but consists of a mixture of uncoupled functions for all possible pairs of values m_1, m_2 such that $m_1 + m_2$ is equal to m.

Namely, we consider two angular momenta $\vec{J}_1$ and $\vec{J}_2$ characterized by their individual quantum numbers j_1, m_1, j_2 and m_2. The corresponding states $|j_1 m_1 j_2 m_2\rangle$, which are eigenvectors of J_1^2, J_{1z} ...., are said to be uncoupled. If we define the total angular momentum $\vec{J}$, it is possible to define the eigenvectors $|j_1 j_2 j m\rangle$ of J_1^2, J_2^2, J^2 and J_z, which are said to be coupled. The relation between the coupled and uncoupled states is:

$$\big|j_1 j_2 j m\big\rangle = \sum_{m_1=-j_1}^{j_1} \sum_{m_2=-j_2}^{j_2} C^{jm}_{j_1 j_2 m_1 m_2} \big|j_1 m_1 j_2 m_2\big\rangle, \tag{1.1}$$

but summation can only include the terms for which $m_1 + m_2 = m$, which implies that each coefficient C must contain $\delta_{m_2, m-m_1}$ factor and so the equation simplifies to:

$$\big|j_1 j_2 j m\big\rangle = \sum_{m_1} C^{jm}_{j_1 j_2 m_1 m-m_1} \big|j_1 m_1 j_2 m - m_1\big\rangle, \tag{1.2}$$

where the coefficients are called vector-addition or Clebsch-Gordon coefficients [27], which will be used in the discussion of this research very often.

1.3.1 Coupling of two angular momenta, Clebsch-Gordan coefficients and 3-j symbols

The Clebsch-Gordan coefficients can be very simply expressed as:

$$C^{j_3 m_3}_{j_1 m_1 j_2 m_2} = (-1)^{j_1 - j_2 + m_3} [j_3]^{1/2} \begin{pmatrix} j_1 & j_2 & j_3 \\ m_1 & m_2 & -m_3 \end{pmatrix}. \tag{1.3}$$

where $[j] \equiv 2j+1$ and the expression in parenthesis is called a Wigner 3j symbol. Those symbols, or their close relatives, called the Clebsch-Gordon and Racah coefficients, are very important for quantitative calculations of atomic structure and spectra.

The 3j symbol represents the probability amplitude that three angular momenta j_1, j_2 and j_3 are coupled to give zero angular momentum:

$$\begin{pmatrix} j_1 & j_2 & j_3 \\ m_1 & m_2 & m_3 \end{pmatrix} = (-1)^{j_1-j_2+j_3} \sum_{j'm'} C^{j'm'}_{j_1 m_1 j_2 m_2} C^{00}_{j'm' j_3 m_3}. \tag{1.4}$$

The 3j function is defined (i.e., is non-zero) only for values of j_i and m_i which are either integral or half-integral, such that $j_1+j_2+j_3$ and $m_1+m_2+m_3$ must be integral and that $j_1 - j_2 + m_3$ is integral so that the 3j symbol is real. Also, the three j_i must satisfy the three inequalities:

$$\begin{aligned} j_1 + j_2 &\geq j_3, \\ j_2 + j_3 &\geq j_1, \\ j_3 + j_1 &\geq j_2, \end{aligned} \tag{1.5}$$

these inequalities together with the integral-sum restriction are referred to as the triangle relations.

The 3j symbols satisfy the symmetry properties:

$$\begin{pmatrix} j_2 & j_1 & j_3 \\ m_2 & m_1 & m_3 \end{pmatrix} = \begin{pmatrix} j_1 & j_3 & j_2 \\ m_1 & m_3 & m_2 \end{pmatrix} = (-1)^{j_1+j_2+j_3} \begin{pmatrix} j_1 & j_2 & j_3 \\ m_1 & m_2 & m_3 \end{pmatrix}. \tag{1.6}$$

From these two relations it follows that

$$\begin{pmatrix} j_i & j_k & j_n \\ m_i & m_k & m_n \end{pmatrix} = \epsilon \begin{pmatrix} j_1 & j_2 & j_3 \\ m_1 & m_2 & m_3 \end{pmatrix}, \tag{1.7}$$

where ϵ is -1 or $(-1)^{j_1+j_2+j_3}$ according as (ikn) is an even or odd permutation of (123).

It can be also seen that:

$$\begin{pmatrix} j_1 & j_2 & j_3 \\ -m_1 & -m_2 & -m_3 \end{pmatrix} = (-1)^{j_1+j_2+j_3} \begin{pmatrix} j_1 & j_2 & j_3 \\ m_1 & m_2 & m_3 \end{pmatrix}. \tag{1.8}$$

These symmetry properties make it possible to greatly shorten calculations.

As stated before $[j] \equiv 2j + 1$, and the following abbreviated notation will be used in the calculations very often as well $[j_1, j_2, \cdots] \equiv (2j_1 + 1)(2j_2 + 1)\cdots$. Various notations have been introduced for different quantities that are related to 3j symbols, for convenience of cross-reference we present here as a reminder the relation between Clebsch-Gordon coefficients and the 3j symbols:

$$(j_1 j_2 m_1 m_2 | j_1 j_2 j_3 m_3) = (-1)^{j_1-j_2+m_3} [j_3]^{1/2} \begin{pmatrix} j_1 & j_2 & j_3 \\ m_1 & m_2 & -m_3 \end{pmatrix}. \tag{1.9}$$

1.3.2 Coupling of three angular momenta and 6-j symbols

When we have two angular momenta to couple, the problem is rather simple, since we have only two different ways: either the second one can be coupled to onto the first one or the first one can be coupled onto the second one. Things are getting slightly more difficult when we have more than two angular momenta to couple. In this case the coupling can be done on a number of different ways. Let's discuss the case when we have three different momenta j_1, j_2 and j_3, we can first couple j_2 and j_1, to get j_{12}, and then we can couple j_3 to j_{12} getting the total momentum J. Using (1.1) and (1.3), the coupled wavefunction in this case will be:

$$\begin{aligned}\big|[(j_1j_2)j_{12},j_3]jm\rangle \;=\; & \sum_{m_{12}m_3}(-1)^{j_{12}-j_3+m}[j]^{1/2}\begin{pmatrix} j_{12} & j_3 & J \\ m_{12} & m_3 & -m\end{pmatrix} \\ & \times\sum_{m_1m_2}(-1)^{j_1-j_2+m_{12}}[j_{12}]^{1/2}\begin{pmatrix} j_1 & j_2 & j_{12} \\ m_1 & m_2 & -m_{12}\end{pmatrix}\big|j_1m_1\rangle\big|j_2m_2\rangle\big|j_3m_3\rangle. \quad (1.10)\end{aligned}$$

Another possibility for three angular momentum coupling is to couple j_3 to j_2 to get j_{23}, and then couple j_{23} to j_1 to get the total J. For this case we will have:

$$\begin{aligned}\big|[j_1,(j_2j_3)j_{23}]jm\rangle \;=\; & \sum_{m_1m_{23}}(-1)^{j_1-j_{23}+m}[j]^{1/2}\begin{pmatrix} j_1 & j_{23} & j \\ m_1 & m_{23} & -m\end{pmatrix} \\ & \times\sum_{m_2'm_3'}(-1)^{j_2-j_3+m_{23}}[j_{23}]^{1/2}\begin{pmatrix} j_2 & j_3 & j_{23} \\ m_2' & m_3' & -m_{23}\end{pmatrix}\big|j_1m_1\rangle\big|j_2m_2'\rangle\big|j_3m_3'\rangle. \quad (1.11)\end{aligned}$$

To go from one basis to another, there exists a basis transformation whose matrix elements are given by:

$$\begin{aligned}\langle j_1j_2(j_{12})j_3jm|j_1,j_2j_3(j_{23})j'm'\rangle \;=\; & \\ & \delta_{jj'}\delta_{mm'}(-1)^{j_1+j_2+j_3+j}[j_{12}j_{23}]^{1/2}\begin{Bmatrix} j_1 & j_2 & j_{12} \\ j_3 & j & j_{23}\end{Bmatrix} \quad (1.12)\end{aligned}$$

The 6j symbol is a function of six arguments that may be defined as $\begin{Bmatrix} j_1 & j_2 & j_{12} \\ j_3 & j & j_{23}\end{Bmatrix}$. In atomic-structure theory, the 6j symbol usually arises as a five-fold summation over a product of four 3j symbols. They are related to the coefficients of transformation between different coupling schemes of three angular momenta discussed in the previous section. If we have angular momenta j_1, j_2 and j_3 they can be coupled in three different ways:

- $\vec{j_1}+\vec{j_2}=\vec{j_{12}}, \qquad \vec{j_{12}}+\vec{j_3}=\vec{j}$

- $\vec{j_2} + \vec{j_3} = \vec{j_{23}}, \qquad \vec{j_1} + \vec{j_{23}} = \vec{j}$
- $\vec{j_1} + \vec{j_3} = \vec{j_{13}}, \qquad \vec{j_{23}} + \vec{j_2} = \vec{j}.$

By definition the value of the 6j symbol is unchanged if any two columns are interchanged, or if any two numbers in the bottom row are interchanged with the corresponding two numbers in the top row.

1.3.3 Coupling of four angular momenta and 9-j symbols

Similarly, the 9j symbol is defined as: $\begin{Bmatrix} j_1 & j_2 & j_{12} \\ j_3 & j_4 & j_{34} \\ j_{13} & j_{24} & j \end{Bmatrix}$, where all nine arguments are obviously angular-momentum quantum numbers, and hence non-negative integers or half-integers. They are associated with the coefficients of transformation which connects different coupling schemes of four angular momenta. Let's consider four angular momenta j_1, j_2, j_3 and j_4, for which there exists different coupling schemes. for the sake of simplicity we will consider the following two schemes:

- $\vec{j_1} + \vec{j_2} = \vec{j_{12}}, \qquad \vec{j_3} + \vec{j_4} = \vec{j_{34}}, \qquad \vec{j_{12}} + \vec{j_{34}} = \vec{j},$
- $\vec{j_1} + \vec{j_3} = \vec{j_{13}}, \qquad \vec{j_2} + \vec{j_4} = \vec{j_{24}}, \qquad \vec{j_{13}} + \vec{j_{24}} = \vec{j}.$

The Wigner 9j symbols can be introduces a basis transformation between these two coupling schemes:

$$\langle j_1 j_2 (j_{12}) j_3 j_4 (j_{34}) jm | j_1 j_3 (j_{13}) j_2 j_4 (j_{24}) j' m' \rangle = \delta_{jj'} \delta_{mm'} [j_{12} j_{13} j_{24} j_{34}]^{1/2} \begin{Bmatrix} j_1 & j_2 & j_{12} \\ j_3 & j_4 & j_{34} \\ j_{13} & j_{24} & j \end{Bmatrix}. \quad (1.13)$$

The 9-j symbol is zero unless the arguments in each row and in each column satisfy the triangle relations. The value of the 9j symbol is unchanged upon reflection about either diagonal; upon permutation of the rows or of the columns, the value of the 9j symbol is unchanged or is multiplied by $(-1)^S$, where S is the sum of all nine arguments, according as the permutation is even or odd respectively.

Higher-order 3n-j symbols can be also defined: there are two essentially different 12-j symbols, five different 15-j symbols, and eighteen different 18-j symbols, for example. But we will mainly use 3j and 6j symbols throughout this work. Also higher-order symbols can always be expressed using 3j, 6j or 9j symbols.

1.4 One-electron atom

The prototype system for the quantum description of atoms is the so-called one-electron atom, consisting of a single electron, with charge $-q_e$, and an atomic nucleus, with charge $+Zq_e$. Examples are the hydrogen atom, the helium atom, when one of its

electrons is removed, the lithium atom with two electrons removed, etc. There are two features of the one-electron atom that gives simplifications for various analysis. First, because the nucleus is so much heavier than the electron, it is possible to use a very good approximation and treat the nucleus as fixed in space, with the electron moving around it. Second, because there are no other electrons present, the potential energy is $V(r) = -\frac{Zq_e^2}{4\pi\varepsilon_0 r}$, due to the Coulomb attraction of the electron and the nucleus, which depends only on the distance, r, of the electron from the nucleus. In the potential energy formula q_e is the elementary charge, ε_0 is the vacuum permitivity, Z is the atomic number and r is the distance between the electron and nucleus.

The Schrödinger equation for the single electron of mass m_e and charge $-q_e$ moving in the electrostatic field of the (stationary) nucleus of charge Zq_e, whose mass is supposed infinite, with a potential energy $V(r)$, is:

$$H\psi = -\frac{\hbar^2}{2m_e}\nabla^2\psi + V(r)\psi = E\psi. \tag{1.14}$$

Here we have a referential system whose origin is taken at the nucleus and $\vec{r}$ is expressed in spherical coordinates, $\vec{r} = (r, \theta, \phi)$. By expressing the Laplacian operator in spherical coordinates, we have the following for H:

$$\begin{aligned} H &= -\frac{\hbar^2}{2m_e}\left[\frac{1}{r}\frac{\partial^2}{\partial r^2}r + \frac{1}{r^2\sin\theta}\left(\frac{\partial}{\partial\theta}\sin\theta\frac{\partial}{\partial\theta}\right) + \frac{1}{r^2\sin^2\theta}\frac{\partial^2}{\partial\phi^2}\right] + V(r) \\ &= -\frac{\hbar^2}{2m_e}\frac{1}{r}\frac{\partial^2}{\partial r^2}r + \frac{\vec{L}^2}{2m_e r^2} + V(r), \end{aligned} \tag{1.15}$$

where $\hbar$ is reduced Planck's constant, and $\vec{L}^2$ is the orbital angular momentum of the electron introduced in section 1.2.

Because $V(r)$ is not dependent on θ and ϕ and spin, the wavefunctions can be factorized in radial, angular and spin parts. For bound energies, $E < 0$, the total wavefunction of this eigenvalue equation is of the form

$$\psi_{nlm_lm_s}(r, \theta, \phi, s_z) = \frac{1}{r}P_{nl}(r)Y_{lm_l}(\theta, \psi)\sigma_{m_s}(s_z), \tag{1.16}$$

where the functions $Y_{lm_l} = \langle\theta, \phi|\ell m_\ell\rangle$ are the spherical harmonics, i.e. the eigenfunctions of the orbital angular momentum operators $\vec{L}$ and L_z in position space and $\sigma_{m_s}(s_z)$ is the one-electron spin eigenfunction. Radial function P_{nl} must be everywhere finite, P_{nl} must satisfy the boundary conditions $P_{nl}(0) = 0$ and $P_{nl}(\infty) = 0$. Moreover, if ψ is to be normalized, then P_{nl} must be normalized: $\int_0^\infty P_{nl}^*(r)P_{nl}(r)dr = 1$. The precise form of P_{nl} can be found in [24]. $n = 1, 2, 3, ...$ is the new quantum number, which is called the principal quantum number. Orbital angular-momentum states corresponding to $l = 0, 1, 2$, and 3 are called s, p, d, and f states, respectively. For values of $l \geq 3$, successive letters of the alphabet following f are used. The notations $nl = 1s, 2s, 3p$, etc., are used to characterize the orbitals.

When $E < 0$, the equation (1.14) accepts discrete values of energy, corresponding to bound levels of atoms: $E_n = -\frac{Z^2}{n^2}$ Ry, where Ry$= \frac{me^4}{2\hbar^2} = 13.6058$ eV is the Rydberg constant.

Relativistic corrections When the atomic number Z increases, the mean speed of the electron becomes fraction of the speed of light and because of that the relativistic effects come into play. The electron starts to move very fast, especially if it is very close to the nucleus. To treat this we need the Dirac equation, but doing Taylor expansion of that equation, we retrieve the Schrödinger equation, but with additional corrections in the Hamiltonian, which are the relativistic corrections. The complete Hamiltonian becomes:

$$H = -\nabla^2 + V - \frac{\alpha^2}{4}\left(\frac{dV}{dr}\right)\frac{\partial}{\partial r} + \frac{\alpha^2}{2}\frac{1}{r}\left(\frac{dV}{dr}\right)(l\cdot s), \tag{1.17}$$

where all distances are measured in Bohr units a_0, all energies are measured in Rydberg units and $\alpha = \frac{e^2}{4\pi\varepsilon_0\hbar c} = \frac{1}{137.036}$ is the fine-structure constant.

To solve the Schrödinger equation with this Hamiltonian, we first have to define a new angular-momentum operator $\vec{j} = \vec{l} + \vec{s}$. The operators $\vec{l}$ and $\vec{s}$ commute with each other because they act on entirely different sets of coordinates. We seek a solution of the Schrödinger equation (1.14) with Hamiltonian (1.17) having the following form:

$$\psi_{nljm_j}(r,\theta,\phi,s_z) = \frac{1}{r}P_{nlj}(r)\,F_{lsjm_j}(\theta,\phi,s_z), \tag{1.18}$$

where $F_{lsjm_j}(\theta,\phi,s_z) = \sum_{m_l,m_s} C^{j,m_j}_{l,s,m_l,m_s} Y_{lm_l}(\theta,\phi)\sigma_{m_s}(s_z)$ is not only an eigenfunction of the four operators l^2, s^2, j^2 and j_z, but also an eigenfunction of $\vec{l}\cdot\vec{s} = \frac{1}{2}(\vec{j}^2 - \vec{l}^2 - \vec{s}^2)$, but not of l_z and s_z. The coefficients C are called vector-addition or Clebsch-Gordan coefficients.

The corresponding energies are:

$$E_{nlj} = -\frac{Z^2}{n^2} + E_m + E_D + E_{so}, \tag{1.19}$$

where E_m is called the mass-velocity correction term, because it arises from the relativistic variation of mass with velocity and has the following final expression:

$$E_m = -\frac{\alpha^2 Z^4}{4n^4}\left[\frac{4n}{l+1/2} - 3\right]\mathrm{Ry}. \tag{1.20}$$

The third term of equation (1.19) is the Darwin correction term, which arises from relativistically-induced electric moment of the electron, or from the relativistic non-localizability of the electron. E_D has the final expression of:

$$E_D = \delta_{l0}\frac{\alpha^2 Z^4}{n^3}Ry. \tag{1.21}$$

The most important part in equation (1.19) is the spin-orbit correction

$$E_{so} = (1-\delta_{l0})\,\frac{\alpha^2 Z^4}{n^3 l(l+1)(2l+1)}\left[j(j+1) - l(l+1) - s(s+1)\right]\,Ry, \tag{1.22}$$

because it induces splitting in the levels. A good example of this is the "yellow doublet of Na". The $3p$ level is split into states with total angular momentum $j = 3/2$ and $j = 1/2$ due to the presence of the spin-orbit interaction. The mass velocity E_m and Darwin E_D corrections are responsible for a global shift only.

1.5 Two electron atom

This section is dedicated to the atom of two electrons. All the expressions below can be used, for example, for a helium atom (Z=2). The Hamiltonian operator for the atom of two electrons, including relativistic corrections, is:

$$H = -\nabla_1^2 - \nabla_2^2 - \frac{2Z}{r_1} - \frac{2Z}{r_2} + \frac{2}{r_{12}} + \zeta_1(r_1)\,(\vec{l_1}\cdot\vec{s_1}) + \zeta_2(r_2)\,(\vec{l_2}\cdot\vec{s_2}), \qquad (1.23)$$

where $r_{12} = |\vec{r_2} - \vec{r_1}|$ is the distance between first and second electron. The proportionality factor ζ_i in the Hamiltonian (1.23) is called the spin-orbit integral and is measured in Rydbergs (with l and s in units of $\hbar$) and is given by the expression $\zeta(r_i) = \frac{\alpha^2}{2}\frac{1}{r_i}\left(\frac{dV}{dr_i}\right)$. The first two terms in the Hamiltonian are the kinetic energies of electron 1 and electron 2, third and forth terms are interaction between the electrons and the nuclei, fifth term is Coulombic repulsion between two electrons and, finally, the last term is spin-orbit interaction term. Energies are in Rydberg and distances are in Bohr units.

For the first step we consider that the spin-orbit interaction is 0. Here, for the case of the atom of two electrons, we can not use the wavefunction of hydrogen atom because of the electron-electron interaction term: $V_{12} = \frac{2}{r_{12}}$. We will use the following technique. We will consider that the first electron is submitted to the mean field (which has central symmetry) of the second electron and vice versa. This is the principle of Hartree-Fock (HF) approximation. With this consideration the two electrons look independent from each other, because we do not have the dependence on the instantaneous position of the other electron. Therefore, the wavefunction can be written as a product of wavefunctions of independent electrons: $\psi_{n_1 l_1 m_{l_1} m_{s_1}} \times \psi_{n_2 l_2 m_{l_2} m_{s_2}}$, but the underlying $P_{n_i l_i}$ is not the same as for the case of hydrogen.

Now we can introduce in the compact form, dropping the m quantum numbers, the product $n_1 l_1\, n_2 l_2$, which is called an *electron configuration*, or simply a *configuration*. If $n_1 l_1 = n_2 l_2$ we have equivalent electrons and the configuration can be written $(n_1 l_2)^2$. Helium only has 2 electrons and therefore it has a ground configuration of $1s^2$.

Now we want to go little bit further in the description, by taking into account the correlation between the electrons. As we have mentioned before, for an isolated system the total angular momentum is conserved. The total orbital angular momentum for the system of two electrons is $\vec{L} = \vec{l_1} + \vec{l_2}$, the total spin angular momentum is $\vec{S} = \vec{s_1} + \vec{s_2}$ and the total angular momentum of the atom is $\vec{J} = \vec{L} + \vec{S}$. Now we have new, so called, coupled basis function

$$|n_1 l_1 n_2 l_2 LSJM\rangle = \sum_{M_L M_S} C^{JM}_{LM_L SM_S} \sum_{m_{l_1} m_{l_2}} C^{LM_L}_{l_1 m_{l_1} l_2 m_{l_2}} \times \sum_{m_{s_1} m_{s_2}} C^{SM_s}_{s m_{s_1} s m_{s_2}} |n_1 l_1 m_{l_1} m_{s_1}\rangle |n_2 l_2 m_{l_2} m_{s_2}\rangle, \quad (1.24)$$

where the coefficients C are Clebsch-Gordan (CG) coefficients as in the equation (1.18). The Pauli exclusion principle states that:

No two electrons can occupy the same spin-orbital state. This means that the wave function of electrons must be antisymmetric with respect to permutations of two electrons. So $|n_1 l_1 n_2 l_2 LSJM\rangle_A = N[|n_1 l_1 n_2 l_2 LSJM\rangle - (-1)^{L+S+l_1+l_2+s_1+s_2}|n_2 l_2 n_1 l_1 LSJM\rangle]$, where $N = \frac{1}{\sqrt{2(1+\delta_{m_1 m_2}\delta_{l_1 l_2})}}$ is a normalisation factor and the phase factor is coming from the permutation of quantum numbers of two electrons in Clebsch-Gordon coefficients. Here we have another restriction, which states that $L + S$ must be even for equivalent electrons (see in more detail in appendix A). This is the reason why $1s^2$ has only $^1S_0$ and not $^3S_1$ in the case of Helium.

Now we consider non-zero spin-orbit interaction in (1.23). This spin-orbit matrix element can couple different values of $L' = L, L \pm 1$ and $S' = S, S \pm 1$. As long as spin-orbit interaction is smaller than the Coulombic interaction the eigenvectors of the Hamiltonian have one value of L and one value of S. This is the case of LS or Russell-Saunders coupling [24]. Otherwise, the eigenvectors of Hamiltonian are sums of basis functions with different L and S. So, when the spin-orbit interaction becomes greater than the Coulombic interaction, it is better to define functions with $\vec{j_i} = \vec{l_i} + \vec{s_i}$ and $\vec{J} = \vec{j_1} + \vec{j_2}$. This is called jj coupling scheme.

1.6 N-electron atom

The more general and inclusive case is the case of an atom containing N electrons. Theoretical treatment of such a system requires first of all knowledge of a suitable Hamiltonian operator. An appropriate operator may be obtained by generalizing the two-electron operator (1.23):

$$H = -\sum_i \nabla_i^2 - \sum_i \frac{2Z}{r_i} + \sum_{i>j}\sum \frac{2}{r_{ij}} + \sum_i \zeta_i(r_i)(\vec{l_i} \cdot \vec{s_i}). \tag{1.25}$$

Here $r_i = |r_i|$ is the distance of the i^{th} electron from the nucleus, $r_{ij} = |r_i - r_j|$ is the distance between the i^{th} and j^{th} electrons and the summation is over all pairs of electrons.

Our task is to solve the Schrodinger equation:

$$H\Psi^k = E^k\Psi^k \tag{1.26}$$

to obtain the wavefunction Ψ^k and the energy E^k of the atom for every stationary quantum state k of interest. However, the wavefunction is a function of 4N variables (three space and one spin coordinate for each electron), and the quantum mechanical problem is extremely complex.

The usual approximation is to assume some form of wavefunction that contains several adjustable parameters, and to vary the values of these parameters to obtain the best possible function, as judged by some appropriate criteria. If the inter-electronic distances r_{ij} are included explicitly in the wavefunction in order to properly take into account the correlations among positions of the various electrons owing to their mutual Coulomb repulsions, the problem becomes already complex even for N = 3 or

4. Even accurate perturbation calculations of correlation energies (using simpler zero-order wavefunctions) are extremely lengthy for N greater than 6. For spectroscopic purposes, we are interested in tens, hundreds, or even thousands of different levels of each atom and ion. It is obvious that we must approach the problem by making very drastic approximations.

The first approximation method that we can use is developed by Slater and later expended by Cordon and Shortley, it is commonly known as Slater-Cordon theory. The basis idea is to expand the unknown Ψ^k wavefunction in terms of set of known basis functions,

$$\Psi^k = \sum_b y_b^k \Psi_b, \tag{1.27}$$

where Ψ_b are basis functions and are assumed to be members of a complete set of orthonormal functions:

$$\langle \Psi_b | \Psi_{b'} \rangle = \delta_{bb'}. \tag{1.28}$$

In general this set has an infinite number of members, and so in principle represents an infinite series. In practice, it is necessary to truncate the series to a finite number of terms.

The N electrons in the atom interact with each other through their mutual Coulomb repulsions, and in order to obtain reasonably accurate results the resulting correlation between the positions of the various electrons must be reflected in our basis functions. We begin with the central-field and mean-field approximations of the atom: we make the approximation that any given electron i moves independently of the others in the electrostatic field of the nucleus and the other $N-1$ electrons. This field is assumed to be time-averaged over the motion of the $N-1$ electrons, and therefore to be spherically symmetric. The assumption of spherical symmetry and the mean-field approximation with the Hamiltonian, which includes the relativistic correction, is a well known method called the HFR (Hartree-Fock and relativistic) approximation. This method is used to approximate the wavefunction and the energy of a quantum multi-electron system in a stationary state. This approximation assumes that the exact N-body wavefunction of the system can be approximated by a product of single-electron wavefunctions. In other words the Hartree-Fock approximation breaks down a multi-electron wave function into a set of one-electron wave functions.

In the central-field model the wavefunction can be described by a one-electron wavefunction that is identical in form with equation (1.16) and reads:

$$\psi_i(r_i) = \frac{1}{r} P_{n_i l_i}(r_i) Y_{l_i m_{l_i}}(\theta_i, \phi_i) \sigma_{m_{s_i}}(s_{i_z}), \tag{1.29}$$

where (r_i, θ_i, ϕ_i) is the position of electron i with respect to the nucleus and also the spin orientation s. The angular momentum of electron i is a constant of motion, so the above written function is an eigenfunction of the one-electron angular-momentum operators l_i^2, l_{z_i}, s_i^2 and s_{z_i} with eigenvalues $l_i(l_i+1)$, m_{l_i}, $s_i(s_i+1) = 3/4$ and m_{s_i}, respectively, but in comparison with equation (1.16) there is a difference in radial wavefunction P_{nl}, because the potential energy is no longer a simple Coulomb function. The quantitative

calculations of wavefunctions and energy levels involves two stages: first it is necessary to determine the detailed shape of the function P_{nl} that form the radial part of the one electron spin-orbitals (1.16). Then it is required to calculate the energy matrix elements $H_{bb'} = \langle b|H|b'\rangle$ using the basis functions Ψ_b, which means that before finding a method to specify the form of P_{nl}, we need to construct a basis function for the entire atom. The first idea is to take as a basis function the simple product of spin-orbitals in a form:

$$\Psi = \psi_1(r_1)\psi_2(r_2)\psi_3(r_3)...\psi_N(r_N), \tag{1.30}$$

where each subscript i is an abbreviation for $n_i l_i m_{l_i} m_{s_i}$, but the problem with this product wavefunction is that it does not include the fermionic character of electrons, which requires that when two electrons are interchanged the total wave function must change sign. After following the same reasoning and discussions done for two-electron atom discussed in section 1.5 antisymmetrized function can be written in the form of a determinant:

$$\Psi = \frac{1}{N!^{1/2}} \begin{vmatrix} \psi_1(r_1) & \psi_1(r_2) & \psi_1(r_3) \\ \psi_2(r_1) & \psi_2(r_2) & \psi_2(r_3) \\ \psi_3(r_1) & \psi_3(r_2) & \psi_3(r_3) \\ . & . & . \\ . & . & . \\ . & . & . \end{vmatrix} \tag{1.31}$$

and is therefore referred to as a determinantal function or a Slater determinant. It can be written in the following form:

$$\Psi = (N!)^{-1/2} \sum_P (-1)^p \psi_1(r_1)\psi_2(r_2)\psi_3(r_3)...\psi_N(r_N), \tag{1.32}$$

which is antisymmetric upon interchange of any two electron coordinates. The summation is over all N! possible permutations $P = 123...N$ of the normal coordinates, and p is the parity of the permutation P (p = 0 if P is obtained from the normal ordering by an even number of interchanges, and p = 1 if an odd number of interchanges is involved).

In such a basis function there are q different radial functions $P_{n_j l_j}(r)$ one for each subshell of equivalent electrons $n_j l_j^{w_j}$. The radial matrix elements and hence the eigenvalues depend on these values. $P_{n_j l_j}(r)$ functions should be determined by the criteria that they minimize the calculated energy of atom according to the variational principle, while respecting the orthonormalization conditions. It is convenient to be able to describe the energy of a configuration in terms of an appropriate form of an average value. The simple form reads as:

$$E_{av} = \frac{\sum_b \langle b|H|b\rangle}{N_{bas}}, \tag{1.33}$$

where b are all the basis functions belonging to the configuration in question and N_{bas} is the number of these functions. In the case of uncoupled basis functions are considered, the E_{av} is build by averaging over all possible sets of values of the one-electron magnetic quantum numbers $m_{l_i} m_{s_i}$. Such an average is equivalent to performing a spherically

symmetrized average over the angular distribution of the electrons in the atom, which is consistent with the central-field model we have adopted. Therefore the determination of the $P_{n_j l_j}$ by minimizing E_{av} is consistent with the fact that the form of the spin-orbitals (1.16) was determined in the first place on the basis of the central field model of the atom. Minimization of E_{av} with respect to variations in the form of $P_{n_j l_j}$ leads to a set of coupled differential equations known as the spherically averaged Hartree-Fock (HF) equations. Then, with the help of radial wavefunctions P_{nl}, that can be determined by the solution of the HF equations, the determinantal functions (1.32) are known. These function can be used as basis functions for evaluation of the matrix elements of Hamiltonian and therefore to calculate the energy levels.

The Hamiltonian operator that should be used has the form of (1.25), the first three terms of which are one-electron operators that have the form of $\sum_{i=1}^{N} f_i = \sum_i f(r_i)$ and are symmetric in the spatial and spin coordinated r_i of all N electrons. The last term of the Hamiltonian is a two-electron operator that is symmetric in all N(N-1)/2 pairs of coordinates and has the form $\sum_{i=2}^{N}\sum_{j=1}^{i-1} g_{ij} = \sum\sum_{i>j} g(r_i, r_j)$. These symmetry conditions are coming from the indistinguishability of electrons. Simplification of matrix elements for determinantal functions is a complicated procedure. Here we will not recall all the steps. The expression for (1.33) becomes:

$$\begin{aligned} E_{av} = &\sum_i \langle i|\nabla^2|i\rangle_{av} + \sum_i \langle i| - 2Z/r_i|i\rangle_{av} \\ &+ \sum\sum_{i>j} [\langle ij|2/r_{ij}|ij\rangle_{av} - \langle ij|2/r_{ij}|ji\rangle_{av}], \end{aligned} \tag{1.34}$$

that can be written in the equivalent form of

$$E_{av} = \sum_i E_k^i + \sum_i E_n^i + \sum\sum_{i>j} E^{ij}. \tag{1.35}$$

The kinetic energy E_k^i has the following form:

$$E_k^i = \langle i|\nabla^2|i\rangle = \int_0^\infty P^*_{n_i l_i}(r)\Big[-\frac{d^2}{dr^2} + \frac{l_i(l_i+1)}{r^2}\Big] P_{n_i l_i}(r) dr. \tag{1.36}$$

Electron-nuclear energy E_n^i can be written as:

$$E_n^i = \langle i| - 2Z/r|i\rangle = \int_0^\infty (-2Z/r)|P_i(r)|^2 dr. \tag{1.37}$$

The electron-electron Coulomb interaction can be written in the following form:

$$\frac{2}{r_{ij}} = \sum_{k=0}^{\infty} \frac{2r_<^k}{r_>^{k+1}} \sum_{q=-k}^{k} (-1)^q C^{(k)}_{-q}(\theta_i, \phi_i) C^{(k)}_q(\theta_j, \phi_j), \tag{1.38}$$

and involve two contributions: direct and exchange, where $r_<$ and $r_>$ are respectively the lesser and greater of the distances r_i and r_j of the electrons from the nucleus. The $C_q^{(k)}(\theta_j, \phi_j)$ are Racah spherical harmonics related to the usual ones by $C_q^{(k)}(\theta_j, \phi_j) =$

$\sqrt{4\pi/(2k+1)}\times Y_{kq}(\theta_j,\phi_j)$. The direct terms the electron-electron Coulomb interaction represent the positive energy of mutual electrostatic repulsion for an uncorrected spatial distribution of the electrons; the exchange terms represent the decrease in this energy that results when one includes the positional correlation of parallel-spin electrons. Evaluation of the matrix elements of the electron-electron interaction is a somewhat lengthy process. We recall here only the results:

$$\begin{aligned}\langle ij|\frac{2}{r_{12}}|tu\rangle \;&=\; \delta_{m_{s_i}m_{s_t}}\delta_{m_{s_j}m_{s_u}}\sum_{k=0}^{\infty}R^k(ij,tu)\\ &\times\sum_{q=-k}^{k}\delta_{q,m_{l_t}-m_{l_i}}\delta_{q,m_{l_j}-m_{l_u}}(-1)^q c^k(l_i,m_{l_i},l_t,m_{l_t})c^k(l_j,m_{l_j},l_u,m_{l_u}),\end{aligned}\quad(1.39)$$

where

$$\begin{aligned}R^k(ij,tu)\;&=\;\int_0^\infty\int_0^\infty\frac{2r_<^k}{r_>^{k+1}}P_i^*(r_1)P_j^*(r_2)P_t(r_1)P_u(r_2)dr_1dr_2\\ &=\;\int_0^\infty\left\{\frac{2}{r_2^{k+1}}\int_0^{r_2}r_1^kP_i^*P_tdr_1\;+\;r_2^k\int_{r_2}^\infty\frac{2}{r_1^{k+1}}P_i^*P_tdr_1\right\}P_j^*P_udr_2,\end{aligned}\quad(1.40)$$

where

$$\begin{aligned}c^k(l_i,m_{l_i},l_t,m_{l_t})&=\langle l_im_{l_i}|C_q^{(k)}|l_tm_{l_t}\rangle=\sqrt{\frac{2l_t+1}{2l_i+1}}C^{l_im_{l_i}}_{l_tm_{l_t}kq}C^{l_i0}_{l_t0k0}\\ &=(-1)^{m_{l_i}}\sqrt{(2l_i+1)(2l_t+1)}\begin{pmatrix}l_i & k & l_t\\ -m_{l_i} & q & m_{l_t}\end{pmatrix}\begin{pmatrix}l_i & k & l_t\\ -0 & 0 & 0\end{pmatrix}.\end{aligned}\quad(1.41)$$

Abbreviations ij and tu refer only to the corresponding quantum numbers nl (not m_lm_s) pertinent to the radial factors P_{nl} of the spin-orbitals. In the equation (1.39), the c^k are angular coefficients, that are contained in particular in Clebsch-Gordan coefficients. They impose $m_{l_i}=m_{l_t}+q$, $|l_i-l_t|\le k\le l_i+l_t$ and l_i+l_t+k is even and, similarly, for j and u. We can also express the matrix element of $\frac{2}{r_{12}}$ in the coupled basis, see eq. (1.24), which imposes $L'=L$, $S'=S$, $J'=J$ and $M'=M$. If $i=t$ and $j=u$, we have a specific case, direct contribution:

$$F^k(ij)\;=\;R^k(ij,ij)\;=\;\int_0^\infty\int_0^\infty\frac{2r_<^k}{r_>^{k+1}}\,|P_i(r_1)|^2\,|P_j(r_2)|^2dr_1dr_2.\quad(1.42)$$

If $i=u$ and $t=j$, we have an exchange contribution:

$$G^k(ij)\;=\;R^k(ij,ji)\;=\;\int_0^\infty\int_0^\infty\frac{2r_<^k}{r_>^{k+1}}\,P_i^*(r_1)P_j^*(r_2)P_j(r_1)P_i(r_2)dr_1dr_2.\quad(1.43)$$

Here, the radial integrals F^k and G^k (or more generally, R^k) are frequently referred to as Slater integrals. The triangle relation imposes that the only k values for radial integrals

$F^k(ij)$ are $k = 0, 2, 4, ..., \min(2l_i, 2l_j)$ and $k = |l_i - l_j|, |l_i - l_j| + 2, |l_i - l_j| + 4, ..., l_i + l_j$ for $G^k(ij)$.

After solving the problem of averaging overall all permissible values of the four quantum numbers, we find for non-equivalent electrons:

$$\begin{aligned} E^{ij} &= \langle ij|2/r_{12}|ij\rangle_{av} - \langle ij|2/r_{12}|ji\rangle_{av} \\ &= F^0(ij) - \frac{1}{2}\sum_k \begin{pmatrix} l_i & k & l_j \\ 0 & 0 & 0 \end{pmatrix}^2 G^k(ij). \end{aligned} \tag{1.44}$$

For equivalent electrons we obtain:

$$E^{ii} = F^0(ii) - \frac{2l_i + 1}{4l_i + 1}\sum_{k>0} \begin{pmatrix} l_i & k & l_i \\ 0 & 0 & 0 \end{pmatrix}^2 F^k(ii). \tag{1.45}$$

If we had used product functions rather than antisymmetrized (determinantal) functions, we would have obtained only the direct matrix elements and would have found for either equivalent or non-equivalent electrons the same results:

$$E^{ij} = \langle ij|2/r_{12}|ij\rangle_{av} = F^0(ij). \tag{1.46}$$

As discussed earlier, the $P_{n_i l_i} \equiv P_i$ should be chosen so as to minimize the center-of-gravity for the configuration $(n_1\, l_1)^{w_1}\, (n_2\, l_2)^{w_2}\, ...\, (n_q\, l_q)^{w_q}$, where $\sum_{j=1}^{q} w_q$ = N, and q is the number of subshells and w is the number of electrons. When dealing with the P_i it will be more convenient to replace summations over the N spin-orbitals by summations over the q subshells, with a weighting factor w_i for the i^{th} subshell. For any small variations of $\delta P_i(r)$ the $P_i(r)$ should be such that the resulting δE_{av} will be zero, while the orthonormalization conditions

$$\int_0^\infty P^*_{n_i l_i}(r_i) P_{n_i l_i}(r_i) dr_i = \delta_{n_i n_j} \tag{1.47}$$

and boundary conditions $P_i(r) = 0$ at r = 0 and ∞ are satisfied. This is the basis of the variational method: choosing a "trial wavefunction" depending on one or many parameters and then finding the values of these parameters for which the energy has the lowest possible value.

The expression of E_{av} may be written in the form:

$$\begin{aligned} E_{av} &= \sum_{j=1}^{N} \big\{ E_k^j + E_n^j + \frac{1}{2}\sum_{t\neq j}^{N} E^{jt} \big\} \\ &= \sum_{j=1}^{q} w_j \big\{ E_k^j + E_n^j + \frac{1}{2}(w_j - 1)E^{jj} + \frac{1}{2}\sum_{t\neq j}^{q} w_t E^{jt} \big\}, \end{aligned} \tag{1.48}$$

from which we can determine the variation of E_{av} caused only by a variation of P_i:

$$\delta_i E_{av} = w_j \big\{ \delta_i E_k^j + \delta_i E_n^j + \frac{1}{2}(w_i - 1)\delta_i E^{ii} + \frac{1}{2}\sum_{t\neq i} w_t \delta_i E^{it} + \frac{1}{2}\sum_{j\neq i} w_j \delta_i E^{ji} \big\}, \tag{1.49}$$

where the last two elements are the same since $E^{ij} = E^{ji}$. Then with the aid of equations (1.36), (1.37), (1.44) and (1.45) we can get one equation for each value of i, meaning one for each subshell $n_i l_i$. This set of equations is called Hartree-Fock equations. Without going into detail, we obtain:

$$\Big[-\frac{d^2}{dr^2}+\frac{l_i(l_i+1)}{r^2}-\frac{2Z}{r}+\sum_{j=1}^{q}(w_j-\delta_{ij})\int_0^\infty\frac{2}{r_>}P_j^2(r_2)dr_2-(w_i-1)A_i(r)\Big]P_i(r)$$
$$=\varepsilon_i P_i(r)+\sum_{j(\neq i)=1}^{q}w_j[\delta_{l_i l_j}\varepsilon_{ij}+B_{ij}(r)]P_j(r), \tag{1.50}$$

where

$$A_i(r)=\frac{2l_i+1}{4l_i+1}\sum_{k>0}\begin{pmatrix}l_i & k & l_i\\ 0 & 0 & 0\end{pmatrix}^2\int_0^\infty\frac{2r_<^k}{r_>^{k+1}}P_i^2(r_2)dr_2 \tag{1.51}$$

and

$$B_{ij}(r)=\frac{1}{2}\sum_{k}\begin{pmatrix}l_i & k & l_j\\ 0 & 0 & 0\end{pmatrix}^2\int_0^\infty\frac{2r_<^k}{r_>^{k+1}}P_j(r_2)P_i(r_2)dr_2, \tag{1.52}$$

where $r_<$ and $r_>$ represent the lesser and the greater of r and r_2 and the terms involving Lagrangian multipliers ε_{ij} are arising from the orthogonality requirements. The solution of these HF equations are the required radial wavefunctions.

In equation (1.50) the first two terms come from the variation of E_k^i, the third term comes from E_n^i, the next term arises from the direct portion of the electron-electron interactions E^{ij} and the terms involving A_i and B_{ij} come from the exchange portions of E^{ij}. The next steps to take are the following: assuming a set of trial wavefunctions, for each i computing A_i, B_{ij} and ε_{ij}, then solving the HF equation for new wavefunctions. These steps are repeated until the assumed and calculated wavefunctions are identical.

In order to simply summarize the calculation results, we will use the example of Eu^{3+}. When we take a configuration to calculate we have the parameter E_{av}, then we have for each open non-s subshell the spin-orbit parameter ζ_i, where i=(4f,5d), as well as for each subshell with two or more electrons and two or more vacancies the parameters F_k(ii) (for example: F_2(4f4f), F_4(4f4f), F_6(4f4f)). We need for couples of open subshells the parameters F_k and G_k(ij): F_2(4f5d), F_4(4f5d), G_1(4f5d), G_3(4f5d), G_5(4f5d) and for each couple of configurations differing at most by two electrons the CI parameters, for example R^2(4f5d,4f6s) and R^3(4f5d,6s4f) for Eu^{3+} (for configurations $4f^5$ 5d ans $4f^5$ 6s, if we were to consider CI mixing). Sometimes, a set of so called "effective parameters" are introduced that help with the precision of the calculations. These parameters will be described in section 3.1. For each parity and for each angular momenta value J, the fully coupled states are built, then the matrix elements of Hamiltonian are expressed using above mentioned Slater parameters.

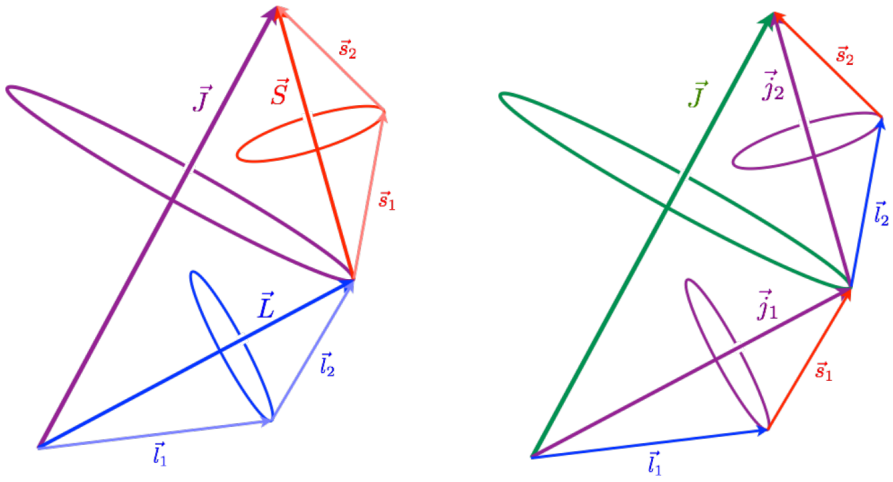

Figure 1.3: The figure on the left is the visual representation of LS coupling scheme, in which case, the interaction between the electrons is stronger than the spin-orbit interaction in each of them. The one on the right demonstrates the jj coupling scheme, in which case, the individual coupling between the electrons, via the spin-orbit interaction, is stronger than the electrostatic interaction between them.

1.7 Coupling schemes

In an atom containing N electrons with N $>$ 1, there are more than 2 elementary angular momenta. There are N orbital angular momenta l_i, and N spin momenta s and the total angular momentum of the atom is $\vec{J} = \sum_{i=1}^{\mathrm{N}} (\vec{l}_i + \vec{s}_i)$. The order in which the momenta are coupled together can be chosen in many different ways; any specific choice is known as a coupling scheme. The individual wavefunctions will correspond most closely to the various physical states of the atom if the coupling scheme used corresponds to the coupling of successive momenta in the order of decreasing strength of the various interactions. Usually, the strongest interactions among the electrons of an atom are their mutual Coulomb repulsions. These repulsions affect only the orbital angular momenta and not the spins. It is thus most appropriate to first couple together all the orbital angular momenta to give eigenfunctions of L^2 and L_z, where $\vec{L} = \sum_i \vec{l}_i$, is the total angular momentum of the atom and similarly to couple together all the spins to give eigenfunctions of S^2 and S_z, where $\vec{S} = \sum_i \vec{s}_i$ is the total spin angular momentum. $\vec{L}$ and $\vec{S}$ are then coupled together to give eigenfunctions of J^2 and J_z, where $\vec{J} = \vec{L} + \vec{S}$. This scheme is known as the LS or Russell-Saunders coupling scheme.

State notations

In order to manipulate better and make the discussions of orbital and spin angular momentum of electrons and atoms universal customary notations are employed. Orbital angular-momentum states corresponding to $l = 0$, 1, 2, 3 are called s, p, d and f states

respectively. This set of labels had its origin in the early work of experimental atomic spectroscopy. The letter s stood for *sharp*, p for *principal*, d for *diffuse* and f for *fundamental* in characterizing spectral lines of the alkali and alkaline-earth elements. From the letter f onwards the naming of the orbitals is alphabetical $l = 4, 5, 6 \rightarrow g, h, i, ...$ For orbital-angular momentum states of the atom as a whole analogous capital-letter notation is used. For LS-coupled functions, in which the all-electron total quantum numbers for orbital L, spin S and total J angular momenta are good quantum numbers, Russell and Saunders introduced a shorthand notation, also called a *term symbol*, which is used universally and can be written as:

$$^{2S+1}L_J, \tag{1.53}$$

where the value of $2S + 1$ is called the multiplicity of the term or simply a spin multiplicity, which is the number of possible values of the spin magnetic quantum number.

In the special case of a one-electron atom discussed in section 1.4, S is equal to $s = 1/2$ and L is necessarily equal to l, the possible values of notation (1.53) are:

$$^2S_{1/2},\ ^2P_{1/2},\ ^2P_{3/2},\ ^2D_{3/2},\ ^2D_{5/2},\ .... \tag{1.54}$$

In atomic spectroscopy, **term** is specified by L and S together, L, S and J specify a **level** and, finally, a **state** is described by L, S, J and M. In descriptions of electronic states of an atom the electronic configuration is also used along with the term symbol.

The list of N pairs of quantum numbers $n_i\, l_i$, that defines a set of coupled or uncoupled functions is called an *electron configuration*, or simply a *configuration*. In general there may be more than one spin-orbital with a given value of $n_i\, l_i$ and so the list is written by the following notation $(n_1\, l_1)^{w_1}\, (n_2\, l_2)^{w_2} \ldots (n_q\, l_q)^{w_q}$, where $\sum_{j=1}^{q} w_q$ = N. w_j is called an *occupation number*. The maximum number of electrons that can exist in a given subshell is $4l + 2$. A subshell occupied by the maximum number of electrons is called a *filled* or *closed* subshell. For each open subshell, there is one L_q and S_q.

When there are two or more allowed terms of l^w with the same values of LS, the additional quantity is required to distinguish the terms from each other. The "seniority number" α is a quantity introduced by Racah to serve this purpose, for example $^5D1$, $^5D2$, $^5D3$ terms of the $4f^6$ configuration of Eu^{3+}. Term symbols can be used in neutral and charged atoms, to their ground and excited states. They are most often used to describe the totality for all electrons, but sometimes can be used to discuss electrons in a given subshell, or even a set of subshells.

In LS-coupling conditions the electrostatic interactions between electrons are much stronger than the interaction between the spin of an electron and its own orbital motion. With increasing Z, the spin-orbit interactions become increasingly more important. When these interactions become much stronger than the Coulomb terms, the coupling conditions approach pure jj coupling. In the jj-coupling scheme, basis functions are formed by first coupling the spin of each electron to its own orbital angular momentum and then coupling together the various resultants j_i to obtain the total angular momentum $\vec{J} = \sum_i \vec{j_i}$: For example the jj coupling scheme for two electron atom may be described by the condensed notation

$$[(l_1, s_1)\, j_1,\ (l_2, s_2)\, j_2]JM, \tag{1.55}$$

and the usual jj-coupling notation for energy levels which is analogous to the Russell-Saunders notation, is $(j_1, j_2)_J$.

In jj coupling, the Pauli principle takes the form that no two electrons may have the same set of one-electron quantum numbers $n_i l_i j_i m_i$. The jj-coupled basis states are used extensively in nuclear physics. However, for atomic-electron subshells l^w, the coupling conditions are usually closer to the LS than to the jj scheme, and the latter is rarely considered except in a very few high Z cases. At the same time, the coupling between different subshells may lie close to pure jj conditions. The visual representation of these two coupling scheme is shown on Figure 1.3. There are of course many other coupling schemes.

Pair coupling

The coupling conditions under which the energy levels tend to appear in pairs, is called pair coupling. These conditions occur for excited configurations in which the energy depends only slightly on the spin s of the excited electron; the level pairs correspond to the two possible values of J that are obtained when s is added to the resultant, K, of all other angular momentum. Pair-coupling conditions occur mainly when the excited electron has large angular momentum (f or g electron) because such an electron tends not to penetrate the core and thus experiences only a small spin-dependent (exchange) Coulomb interaction, and its spin-orbit interaction is likewise small. The more common limiting type of pair coupling, jK coupling, occurs when the strongest interaction is the spin-orbit interaction of the more tightly bound electron, and the next strongest interaction is the spin-independent (direct) portion of the Coulomb interaction between the two electrons.

The corresponding angular-momentum coupling scheme is

$$\{[(l_1, s_1)\, j_1,\ l_2]K, s_2\}\, JM. \tag{1.56}$$

The other form of pair coupling is called LK (or Ls) coupling. In two-electron configurations, it corresponds to the case in which the direct Coulomb interaction is greater than the spin-orbit interaction of either electron, and the spin-orbit interaction of the inner electron is next most important. The coupling scheme is

$$\{[(l_1, l_2)\, L, s_1]K, s_2\}\, JM. \tag{1.57}$$

There are many coupling schemes, but the ones mentioned above are the most common coupling schemes.

Parity

In addition to the classification of wavefunctions by means of their angular-momentum properties, they can be further described in terms of the important concept of parity, with respect to the inversion of all electronic coordinates around the nuclei:

$$P = (-1)^{\sum l_i}, \tag{1.58}$$

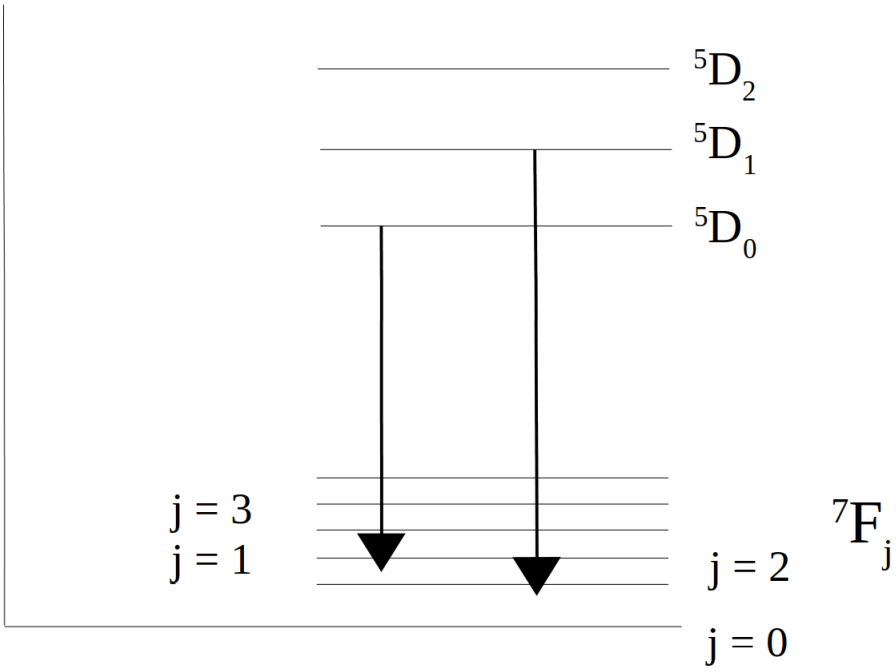

Figure 1.4: Schematic representation of some levels of the two lowest manifolds ^{7}F and ^{5}D of Eu^{3+}.

where the sum is over all N values of i. A wavefunction is said to have even or odd parity according to the value of P is +1 or -1, respectively. When odd parity levels are discussed, an superscript "o" is added in term designation, for example the level $4f^5(^6H^o)\,5d(^7K_4^o)$ in the case of the first excited configuration of Eu^{3+}.

1.8 Radiative transition probabilities

In atomic physics and chemistry, an atomic electron transition (also called an electronic (de-)excitation, atomic transition) is a change of an electron from one energy level to another within an atom. Sometimes it is called a quantum jump. It was first theorized by Niehls Bohr in 1913, after that, James Franck and Gustav Ludwig Hertz proved experimentally that atoms have quantized energy states.

Electronic transitions cause the emission or absorption of electromagnetic radiation in the form of quantized units called photons. The larger the energy separation of the states between which the electron jumps, the shorter the wavelength of the photon that is emitted.

An atom in an excited state 2 of energy E_2 can in general make a spontaneous radiative transition to a state 1, that has a lower energy E_1. This process happens with an emission of a photon of energy:

$$h\nu_2 = E_2 - E_1. \tag{1.59}$$

The probability per unit time that an atom in state 2 will make such a transition to state 1 is denoted by a_{21}. For an isolated, field-free atom in a state with total angular

momentum j_1, there are $g_1 = 2J_1 + 1$ degenerate states of energy E_1, that correspond to the $2J_1 + 1$ possible values of the magnetic quantum number M_1. The Einstein spontaneous emission transition probability rate is defined to be the total probability per unit time of an atom in a specific state 2 making a transition to any of the g_1, states of the energy level 1:

$$A_{21} = \sum_{M_1} a_{21}. \tag{1.60}$$

The Einstein coefficient $A_{21}(\mathrm{s}^{-1})$ for spontaneous emission is related to oscillator strength f_{12} with the following expression:

$$A_{21} = \frac{2\pi\nu^2 e^2}{\varepsilon_0 m_e c^3}\frac{g_1}{g_2} f_{12}, \tag{1.61}$$

where e is the electron charge, m_e is the electron mass.

An important quantity for describing spectral lines is weighted transition probability and is defined as:

$$g_2 A_2 = g_2 \sum_{M_1} a_{21}. \tag{1.62}$$

States are also defined by a quantity called lifetime: $\tau_2 = \left(\sum_1 A_{21}\right)^{-1}$, which is the natural lifetime of the atom in any one of the states of the level 2. Some emission transitions are simply presented in figure 1.4.

In contrary, when an atom, ion, or molecule moves from a lower-energy state to a higher-energy state it absorbs photons with energies equal to the difference in energy between the two states. The process is described by the Einstein coefficient B_{12} $(\mathrm{m}^3 J^{-1} s^{-2})$:

$$B_{12} = \frac{e^2}{4\varepsilon_0 m_e h\nu} f_{12}, \tag{1.63}$$

where f_{12} is the oscillator strength.

Every element has a unique set of absorption and emission lines. The pattern of lines is known as a spectral signature. The absorption and emission spectra of each element are inverses of each other: The wavelengths of a particular element's absorption lines are the same as the wavelengths of its emission lines. The Einstein transition probabilities are physical properties of the atom depending only on the states 1 and 2, and are independent of whether or not a state of thermodynamic equilibrium actually exists.

The calculation of the coefficient gA involves making multipole expansions to find the contribution to gA from the interaction between the electromagnetic field and each electric and magnetic multipole moment of the atom. The various contributions are denoted $E1$ (also called ED), $E2$, $E3$, for the electric dipole, quadrupole, octupole, etc. moments and $M1$, $M2$, $M3$, for the corresponding magnetic moments. The ED Einstein coefficient for the spontaneous emission from level 2 to 1 is:

$$A_{\mathrm{ED}} = \frac{e^2 a_0^2 (E_2 - E_1)^3}{3\pi\varepsilon_0 \hbar^4 c^3 (2J_2 + 1)} \mathcal{S}_{\mathrm{ED}}, \tag{1.64}$$

where $\mathcal{S}_{\mathrm{ED}}$ is called transition line strength and is the square of the reduced ED matrix element, $\mathcal{S}_{\mathrm{ED}} = |\langle\Psi_1\|P^{(1)}\|\Psi_2\rangle|^2$, where $P^{(1)}$ is the electric dipole moment. The line strength has the following relation with oscillator strength:

$$\mathcal{S}_{\mathrm{ED}} = \frac{3\hbar^2(2J_1+1)}{2m_e a_0^2(E_2-E_1)} f_{12,\mathrm{ED}}, \tag{1.65}$$

where 1 (2) denotes the lower (upper) levels of energy E_1 (E_2) and total angular momentum J_1 (J_2), $\hbar$ is the reduced Planck constant, m_e the electron mass, $a_0 = 4\pi\varepsilon_0\hbar^2/m_e e^2$ the Bohr radius, ε_0 the vacuum permitivity and e the electron charge. In Eq. (1.65), the ED line strength is in atomic units (units of $e^2a_0^2$). Because the oscillator strength for stimulated emission is defined as $f_{21} = -\frac{2J_1+1}{2J_2+1} f_{12}$, the so-called weighted oscillator strength

$$g f_{\mathrm{ED}} = (2J_1+1) f_{12,\mathrm{ED}} = -(2J_2+1) f_{21,\mathrm{ED}} \tag{1.66}$$

does not depend on the nature of the transition.

	S	L	J (No $0 \leftrightarrow 0$)	Parity
Electric Dipole	ΔS = 0	ΔL = 0, $\pm$ 1	ΔJ = 0, $\pm$ 1	opposite
Magnetic Dipole	ΔS = 0	ΔL = 0	ΔJ = 0, $\pm$ 1	same
Electric Quadrupole	ΔS = 0	ΔL = 0, $\pm$1, $\pm$2	ΔJ = 0, $\pm$ 1, $\pm$2	same

Table 1.1: Selection rules for E1, M1 and E2 transitions.

The MD Einstein coefficients A_{MD}, can be calculated by:

$$A_{\mathrm{MD}} = \frac{e^2a_0^2(E_2-E_1)^3}{3\pi\varepsilon_0\hbar^4c^3(2J_2+1)} \mathcal{S}_{\mathrm{MD}}, \tag{1.67}$$

where the MD line strength is written in units of $e^2a_0^2$ [24]

$$\mathcal{S}_{\mathrm{MD}} = \frac{\alpha^2}{4} \left|\langle\Psi_1\|\,\mathbf{L} + g_s\mathbf{S}\,\|\Psi_2\rangle\right|^2 \tag{1.68}$$

with α the fine-structure constant and g_s the electronic-spin g-factor. Because the orbital $\mathbf{L}$ and spin $\mathbf{S}$ angular momenta are even-parity tensors of rank one, MD transitions can occur in free space or in solids, between levels of the same configuration and with $\Delta J \leq 1$ except $(J_1, J_2) = (0, 0)$. Unlike the magnetic-dipole (MD) and electric-quadrupole (E2) transitions [28], the ED ones are activated by the presence of the host material, which relaxes the free-space selection rules. The E1 selection rules are the following: $\Delta S = 0$, $\Delta L = 0, \pm 1$ and $\Delta L = 0, \pm 1$. The rest of the selection rules for E1, M1 and E2 transitions are shown in table 1.1. Some of these selection rules are convicted to change when the ions are hosted in an environment (see chapter 2).

Chapter 2

Lanthanides in gas and in solid phases

Even before the advent of lasers, the rare earths presented a puzzle in trying to understand their spectral properties in the context of the quantum theory that blossomed in 1920's and 1930's. It was called a puzzle because it was well known that rare earths exhibited sharp spectral lines, which would be expected if the transitions occurred between levels inside the 4f electronic shell. Such transitions were known to be forbidden by the free-ion or Laporte selection rules (see section 1.8), which says that states with even parity can be connected by electric dipole (E1, or ED) transitions only with states of odd parity, and odd states only with even ones. Another way of saying this is that the algebraic sum of the angular momenta of the electrons in the initial and final state must change by an odd integer. For transitions within the 4f shell, ED transitions are forbidden, but allowed d for magnetic dipole (M1) or electric quadrupole (E2) radiation. The terms forbidden and allowed are not strictly accurate. The term forbidden means a transition may occur in principle, but with low probability. The first possibility would be indicative of broad spectral lines in contrast to the sharp lines that were observed. Magnetic dipole radiation could account for some transitions, but not all transitions, and represents a special case. Quadruple radiation could account for more transitions, but was too weak to account for the observed intensities. Only ED radiation was a reasonable solution, but it is forbidden by the Laporte selection rule. The solution considered a distortion of the electronic motion by crystalline fields in solids, so that the selection rules for free atoms no longer applied.

In this chapter I give a general description on lanthanides in the first section, covering discussion on their various properties that will be interesting in our further discussions. Then the next section is devoted to describing the ions in solids: why are they interesting as a system, what special properties they have, etc. Then, I go on with the description of well known Judd-Ofelt theory, which is used to describe the transitions of ions when they are hosted in a solid or a glass.

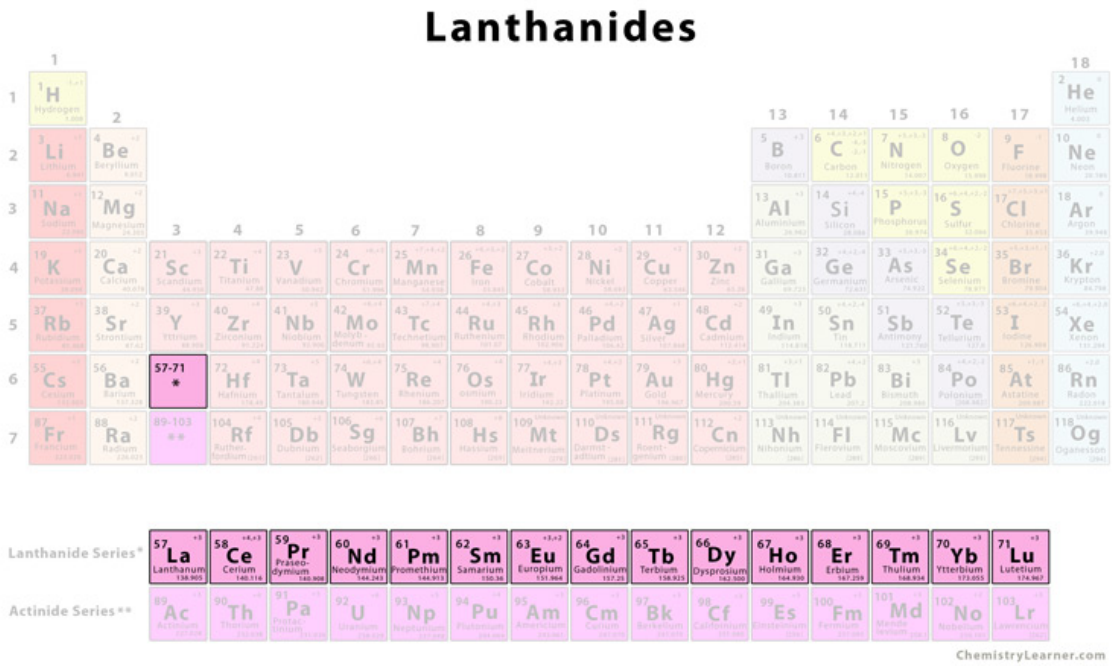

Figure 2.1: The lanthanide row highlighted from the periodic table of the (chemical) elements.

2.1 Lanthanides in free space

The lanthanide series of chemical elements comprises the 15 metallic chemical elements with atomic numbers 57–71, from lanthanum through lutetium (see figure 2.1). The informal chemical symbol Ln is used in general discussions of lanthanide chemistry to refer to any lanthanide. All lanthanide elements form trivalent cations, Ln^{3+}. They are called lanthanides because the elements in the series are chemically similar to lanthanum. These elements, along with the chemically similar elements scandium and yttrium, are often collectively known as the rare earth elements. Most of these elements were discovered over a period of time stretching from the late 18th century to the early 20th century. In the universe, the rare earths are approximately 10^6 times less abundant than the more common element silicon. In spite of their scarcity and difficulty in obtaining, the rare earths are highly valued for their unique properties, especially as optically active elements in their ionized state for lasers [29]. All lanthanides except one (lutetium) are f-block elements, corresponding to the filling of the 4f electron shell, while lutetium is a d-block element and so also a transition metal. The electronic configurations of the free atoms are nearly all [Xe] $4f^{0-14}5d^{0-1}6s^2$, where 4f orbital is gradually filled as the atomic number increases. The exceptions are cerium (Ce), gadolinium (Gd) and lutetium (Lu). The lanthanum (La) has 5d orbital singly occupied but after La further filling of 5d orbital is discontinued. In comparison with the trivalent lanthanides, the lowest configurations of neutral lanthanides are very close in energy, namely $4f^w\ 6s^2$, $4f^w\ 5d\ 6s$, $4f^{w-1}\ 5d\ 6s^2$ and $4f^{w-1}\ 5d^2\ 6s$, where $w = 4$ for Nd and $w = 12$

for Er.

The first two ionization stages of the lanthanides involve simply the removal of the two $6s$ electrons. The third ionization then removes a $4f$ electron. The lanthanides usually exist as trivalent cations, in which case their electronic configuration, for example, is [Xe] $4f^w$, where Xe is a chemical element, with atomic number 54, called xenon. w is varying from 0 (La^{3+}) to 14 (Lu^{3+}) and $w = 6$ for Eu^{3+}. The parity is $(-1)^{3w} = (-1)^w$. The first excited configuration is the promotion of $4f$ towards $5d$ orbital: $4f^{w-1}5d$, which has an opposite parity. The levels can be quite high-several 10000 cm^{-1}. The gap between the configuration decreases when ionized stage decreases. There are many levels for $4f^w$ and even more for $4f^{w-1}5d$. Because of the large number of quantum states that may belong to an $4f^w$ sub-shell, the number of levels of a configuration involving additional partially filled sub-shells may be enormous. The spectra of rare-earth atoms are very complex and one spectrum may contain tens or hundreds of thousands of observable lines.

The $4f$ electrons of rare-earth atoms lie rather close together. Consequently, their mutual Coulomb repulsions are quite large and the values of the Slater integrals $F^k(4f, 4f)$ are also large: 50000 to 100000 cm^{-1}. Because of the gradual contraction of the 4f orbital with increasing Z, the parameter values F^k and ζ increase with Z, so that the level spacings tend to increase also. The spin-orbit parameters ζ increase much faster with Z than do the Coulomb parameters F^k.

Configurations that involve partially filled sub-shells in addition to the $4f$ sub-shell have of course more complicated level structures. Although all lanthanide spectra are exceptionally complex, those in the right half of the series tend to be somewhat simpler than those in the left half, in that the former spectra tend to show contrasting strong and weak lines whereas lines of the latter tend to be more uniform in intensity. The reasons for this are associated with the gradual contraction of the $4f$ orbital with increasing Z, so that the $4f^w$ sub-shell becomes more and more deeply buried within the atom and therefore interacts less and less strongly with the outer valence electrons.

2.2 Lanthanide ions in solids

An ion in a solid can be understood as an impurity embedded in the solid host material, usually in small quantities. These impurities replace host ions and form optically active centers that exhibit luminescence when excited by an appropriate excitation source. When speaking of solids, in general, we mean glass or crystal. Glasses are amorphous over a long range, but may contain a local order. On the other hand the crystals have definite long-range order in a lattice structure. The host material and their properties play a fundamental and important role while describing the nature of observed spectra of the impurity ions. These impurities or dopant ions are usually transition metal or lanthanide series ions characterized by unfilled shells in the interior of the ion. The atomic structure for both are shown in figure 2.2.

All lanthanide ions are characterized by a [Xe] core, an unfilled 4f shell, and some outer shells that screen the 4f shell from outside perturbing influences. This screening effect protects the optically active electrons to some extent from the influence of the

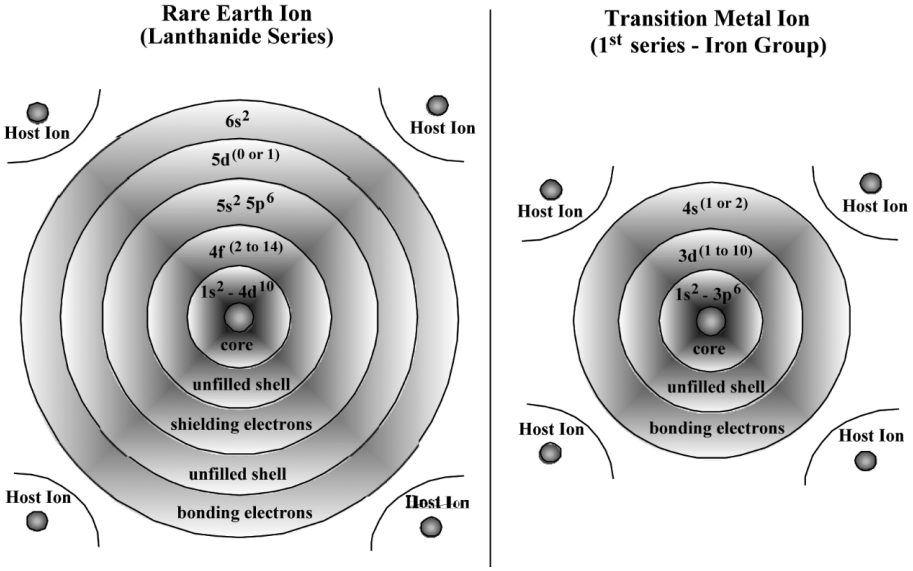

Figure 2.2: Atomic structure of lanthanide and transition metal ions. Representations are not on scale and are shown simply to give an overall visual insight on their structure [29].

crystal field, giving the lanthanides their characteristic sharp and well defined spectral features. In other words they are very similar to free ion spectra. This particular property will give us permission to use good approximation in our further descriptions. The crystal field plays an important role in influencing the features of optical spectra. It also plays an obvious role in the Stark effect regarding the splitting of energy levels of ions in solids. It is the influence it has on the ionic states regarding selection rules that makes such transitions possible, as will be discussed. The ligand, or crystalline field is totally external to the optically active dopant ion and has the symmetry determined by the chemical composition of the host. In an ionic crystal, the optically active dopant ions feel the influence of electrons, belonging to crystal host ions, as a repulsion, and of the nuclei, belonging to the crystal host, as an attraction. The accumulation of these influences can be considered as a net electric field, known as the crystalline field. This crystal field is small in comparison to spin-orbit interactions. The interaction with the environment is smaller than the free ion energies [29]. Contrary to the lanthanides, for which the 4f shell is weakly affected by surrounding host ions, for transition metal ions 3d shell is strongly affected by host ions. Lanthanides are characterised with narrow spectral lines and large cross sections, while transition metal ions mainly have broad spectral lines and small cross sections.

The applications that were listed in the first chapter imply transitions between levels of the ground configuration, which are forbidden in the free-ion case, but become allowed because of the crystal field. Since the quantum numbers for crystal doped ions are the same as for the free ion, the spectrum of Ln^{3+} -doped crystals can be understood as a free ion spectrum, but perturbed by the crystal field. For this purposes we need to study the energy spectrum, transition probabilities and radial matrix elements for

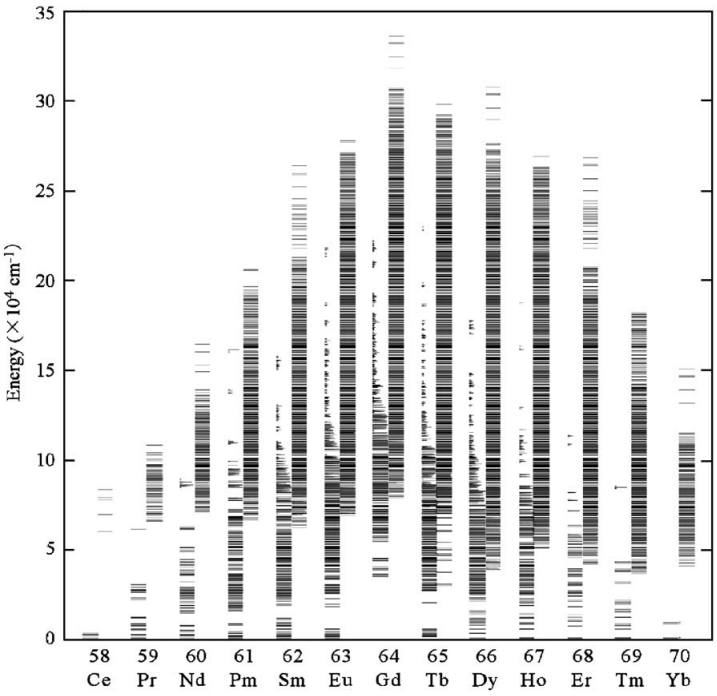

Figure 2.3: Energy level diagram for $4f^w$ (left columns) and $4f^{w-1}5d$ (right columns) configurations of the trivalent lanthanides calculated in $LiYF_3$ crystal [30]

Ln^{3+}. These matrix elements are integrals of the electric-multipole operators between the upper and lower wave functions of the transition, where the integration takes place over the volume of the atom. The radial matrix elements can be used in the Judd-Ofelt theory, which describes the intensities of lanthanide transitions between levels of the ground configuration in solids and solutions and will be discussed in the next section. Figure 2.3 shows energy level diagram for the trivalent lanthanides in $LiYF_3$ calculated by K. Ogasawara and coworkers [30]. In figure 2.3, the energy levels of $4f^w$ and $4f^{w-1}5d$ configurations are shown in the left and right columns, respectively. The lengths of the lines denote the contribution of each configuration.

2.3 Judd-Ofelt theory

The Judd-Ofelt (JO) theory is based on the static, free-ion and single configuration approximations. In the static model, the central ion is affected by the surrounding host ions via a static electric field, referred to as the ligand or crystal field. In the free-ion model, the host environment produces the static crystal field, and is treated as a perturbation on the free-ion Hamiltonian [31,32]. In the single configuration model, the interaction of electrons between configurations is neglected. Simply stated, the Judd-Ofelt theory describes the intensities of lanthanide and actinide transitions in solids and solutions. During the transition the atom can be considered an electric dipole oscillating at some frequency, in what case the amplitude is proportional to the value of this matrix element. It is the interaction of this dipole moment with the electric field

of the electromagnetic wave that induces the transition. On the other hand quantum mechanically, the situation is more complicated because the parity between the upper and lower electronic states must be considered. In quantum mechanics, electric dipole transitions between electronic states of the same parity are forbidden. This results from the fact that the expectation value of the position operator $\mathbf{r}$, is odd under inversion, and vanishes for definite parity. In free ions this implies that ED transitions within the $4f$ shell of lanthanide ions are forbidden. However, electric dipole transitions can be forced if opposite parity states from higher lying configurations outside the $4f$ shell are mixed into the upper state, which become possible when the ions are placed in a noncentrosymmetric perturbing field such as the crystal field. The odd-order parts of the crystal field, which can be expanded in a series of spherical harmonics, perturb the system and produce mixed parity states making electric dipole transitions allowed. This is the starting point of standard Judd-Ofelt calculations.

The essence of the Judd-Ofelt theory is to characterize this admixture using time-independent quantum perturbation theory. It allows to calculate the transition intensity by calculating the matrix elements of the ED operator between the initial and final levels. Using angular-momentum theory, JO theory helps deriving selection rules for the transitions.

We assume that the nucleus of Ln^{3+} is located at the center of the referential frame and the coordinates of the electron j are $r_j = (r_j, \theta_j, \phi_j)$. The perturbation created by the host material (crystal or glass environment) is considered to be an electrostatic potential that creates the crystal-field (CF) potential energy, which has the following form:

$$V_{\mathrm{CF}} = -q_e \sum_{j=1}^{N} \Phi(\mathbf{r}_j), \tag{2.1}$$

where $-q_e$ is the electronic charge and N the number of electrons in the dopant. Assuming that Φ is created by point charges distributed in the ligand atoms, $\mathrm{V_{CF}}$ can be written using the multipolar expansion:

$$V_{\mathrm{CF}} = -q_e \sum_{j=1}^{N} r_j \sum_{k=0}^{+\infty} \sum_{q=-k}^{+k} A_{kq} C_q^{(k)}(\theta_j, \phi_j) = \sum_{k=0}^{+\infty} \sum_{q=-k}^{+k} A_{kq} P_q^{(k)}, \tag{2.2}$$

where A_{kq} are structural parameters characterizing the local electrostatic potential at the ion position,

$$P_q^{(k)} = -q_e \sum_{j=1}^{N} r_j C_q^{(k)}(\theta_j, \phi_j) \tag{2.3}$$

are the ionic multipole moments of rank k and component q.

The unperturbed or zeroth-order states $|\Psi_i^0\rangle$ are the free-ion ones. In the ground configuration they are $|4f^w\, LSJM\rangle$ and $|4f^{w-1}5d\, LSJM\rangle$ for the first excited one, where LS coupling scheme is assumed for simplicity, and L and S characterize the orbital and spin angular momenta, J and M the total (electronic) angular momentum and its z-projection. The general form for both configurations is $|n\ell^{w-1}n'\ell'\, LSJM\rangle$, with $n'\ell' = n\ell = 4f$ or $n'\ell' = 5d$.

Perturbation theory requires the calculation of the matrix elements of the perturbation operator in the unperturbed basis,

$$\left\langle \Psi_1^0 \right| V_{\mathrm{CF}} \left| \Psi_2^0 \right\rangle = \sum_{kq} A_{kq} \left\langle \Psi_1^0 \right| P_q^{(k)} \left| \Psi_2^0 \right\rangle , \tag{2.4}$$

where $|\Psi_1^0\rangle$ and $|\Psi_2^0\rangle$ have angular momentum M_1 and M_2, respectively. Because the multipole moments are irreducible tensors, their matrix elements can be calculated using the Wigner-Eckart (WE) theorem

$$\begin{aligned} \left\langle \Psi_1^0 \right| P_q^{(k)} \left| \Psi_2^0 \right\rangle &= \frac{C^{J_1 M_1}_{J_2 M_2 k q}}{\sqrt{2J_1+1}} \left\langle \Psi_1^0 \| P^{(k)} \| \Psi_2^0 \right\rangle \\ &= (-1)^{J_1 - M_1} \begin{pmatrix} J_1 & k & J_2 \\ -M_1 & q & M_2 \end{pmatrix} \left\langle \Psi_1^0 \| P^{(k)} \| \Psi_2^0 \right\rangle , \end{aligned} \tag{2.5}$$

where $C^{J_1 M_1}_{J_2 M_2 k q}$ is a Clebsh-Gordan (CG) coefficient, (:::) a Wigner 3-j symbol (see section 1.3), and $\langle \Psi_1^0 \| P^{(k)} \| \Psi_2^0 \rangle$ is called the reduced matrix element and is independent from M_1, M_2 and q. The WE theorem imposes some selection rules: $|J_2 - J_1| \leq k \leq J_1 + J_2$ and $M_1 = M_2 + q$. The complete expression of the reduced matrix element is quite involved and depends on the levels configuration, but we can simplify it as follows:

$$\left\langle \Psi_1^0 \| P^{(k)} \| \Psi_2^0 \right\rangle \propto \delta_{S_1 S_2} \begin{pmatrix} \ell_1' & k & \ell_2' \\ 0 & 0 & 0 \end{pmatrix} \left\langle n_1' \ell_1' \right| r^k \left| n_2' \ell_2' \right\rangle , \tag{2.6}$$

which gives the following information:

1. The Kronecker symbol imposes $S_1 = S_2$: since the electric multipole moments only depend on the positions of the electrons, the electronic spin is spectator.

2. The 3-j symbol is non-zero provided that $\ell_1' + k + \ell_2'$ is even and that $|\ell_1' - \ell_2'| \leq k \leq \ell_1' + \ell_2'$.

3. $\left\langle n_1' \ell_1' \right| r^k \left| n_2' \ell_2' \right\rangle = \int_0^{+\infty} dr P_{n_1' \ell_1'}(r)\, r^k\, P_{n_2' \ell_2'}(r)$ is a radial integral involving the wave function $P_{n\ell}(r)$, solution of the one-electron radial Schrödinger equation.

The free states are $(2J+1)$-time degenerate and their energies are M-independent. In this case, the first-order corrections on energies will be obtained by diagonalizing the perturbation operator in each subspace of degeneracy, that is to say, for the ground configuration. The corresponding eigenvalues and eigenvectors describe the Stark sublevels. Some of them can still be degenerate, depending on the symmetry of the host site. In the reduced matrix element (eq. (2.6)), because in our case $\ell_1' = \ell_2' = 3$, the 3-j symbol imposes $k = 0$, 2, 4, 6. The Stark sublevels depend on the even-order crystal-field parameters A_{2q}, A_{4q} and A_{6q} and $k = 0$ gives a shift which is identical for all the states.

At present we want to calculate the ED transition amplitude between the levels $|\Psi_1^1\rangle$ and $|\Psi_2^1\rangle$ of the ground configuration, perturbed by the CF potential. The derivation in standard version of Judd-Ofelt theory starts with a first-order correction on

eigenvectors:

$$|\Psi_i^1\rangle = \sum_{t\neq i} |\Psi_t^0\rangle \frac{\langle\Psi_t^0|V_{CF}|\Psi_i^0\rangle}{E_i^0 - E_t^0}, \tag{2.7}$$

where the E_i^0 and E_t^0 are the unperturbed energies and i = ground configuration and t = excited configuration. In order to characterize the photon absorption or emission we need to calculate the matrix element $D_{12} = P_p^{(1)}$ up to the first order

$$\begin{aligned} D_{12} = \langle\Psi_i^1|P_p^{(1)}|\Psi_2^0\rangle + \langle\Psi_i^0|P_p^{(1)}|\Psi_2^1\rangle = \sum_{t_1\neq 1} \frac{\langle\Psi_1^0|V_{CF}|\Psi_{t_1}^0\rangle}{E_1^0 - E_{t_1}^0}\langle\Psi_{t_1}^0|P_p^{(1)}|\Psi_2^0\rangle \\ + \sum_{t_2\neq i_2} \langle\Psi_1^0|P_p^1|\Psi_{t_2}^0\rangle \frac{\langle\Psi_{t_2}^0|V_{CF}|\Psi_2^0\rangle}{E_2^0 - E_{t_2}^0}, \end{aligned} \tag{2.8}$$

where p stands for the light polarization ($p = 0$ for π and $p = \pm$ for $\sigma^{\pm}$). In what follows we consider $|\Psi_{1,2}^0\rangle$ belong to the ground configuration $4f^n$. If we apply the selection rules described after equation (2.6), we will obtain $\ell_{t_1} + \ell_1 + 1$ even and since $\ell_1 = 3$ it necessarily means that $2 \leq \ell_{t_1} \leq 4$, meaning that $|\ell_{t_1}\rangle$ belongs to an excited configuration. The denominator of equation (2.8) indicates the configuration with the lowest energy mainly contributes to the ED moment, which is $4f^{w-1}$ 5d in the case of Ln^{3+}. When we apply the selection rules on $\langle\Psi_1^0|V_{CF}|\Psi_{t_1}^0\rangle$, we find $k = 1, 3, 5$. We can reach the same reasoning with $|\Psi_{t_2}^0\rangle$. Therefore, the ED transitions inside $4f^w$ are due to small couplings with $4f^{w-1}$ 5d configuration and this coupling is happening under the effect of the odd-rank terms $k = 1, 3, 5$ of the crystal-field potential. After expending the product equation (2.8) as a sum of tensor operators and keeping in mind that $|\Psi_{t_1}^{(0)}\rangle = |n\ell^{w-1}n'\ell'L'S'J'M'\rangle$, we get:

$$\begin{aligned} &\langle\Psi_1^0|P_q^{(k)}|{\Psi_{t1}}^0\rangle\langle{\Psi_{t1}}^0|P_p^{(1)}|\Psi_2^0\rangle \\ &= \frac{C^{J_1M_1}_{J'm'kq}C^{J'M'}_{J_2M_21p}}{\sqrt{(2J_1+1)(2J'+1)}}\langle\Psi_1^0||P^{(k)}||{\Psi_{t1}}^0\rangle\langle{\Psi_{t1}}^0||P^{(1)}||\Psi_2^0\rangle \\ &= \sum_{\lambda=k-1}^{k+1}\sum_{\mu=-\lambda}^{+\lambda}(-1)^{J_1+J_2-\lambda}\sqrt{\frac{2\lambda+1}{2J_1+1}}C^{\lambda\mu}_{kq1p}C^{J_1M_1}_{J_2M_2\lambda\mu}\begin{Bmatrix} k & 1 & \lambda \\ J_2 & J_1 & J' \end{Bmatrix}\langle\Psi_1^0||P^{(k)}||{\Psi_{t1}}^0\rangle\langle{\Psi_{t1}}^0||P^{(1)}||\Psi_2^0\rangle, \end{aligned} \tag{2.9}$$

which appears as a sum of irreducible tensors of rank λ and component μ coupling directly Ψ_1^0 and Ψ_2^0, to which we can apply the Wigner-Eckart theorem. We recall here that equation (2.9) contains the reduced matrix elements between levels of the ground configuration $|\Psi_1\rangle = |4f^w\alpha LSJM\rangle$ and of the first excited one $|\Psi_{t1}\rangle = |n\ell^{w-1}n'\ell'L'S'J'M'\rangle$. We get the following selection rules:

$$|J_2 - J_1| \leq \lambda \leq J_1 + J_2. \tag{2.10}$$

Generally speaking the $P_q^{(k)}$ is a sum of one-electron operators, so we can write:

$$\langle\Psi_t^0||P^{(k)}||\Psi_i^0\rangle = \langle n'\ell'||P^{(k)}||n\ell\rangle \times \langle\Psi_t^0||\sum_i u^k(i)||\Psi_i^0\rangle, \tag{2.11}$$

where $u^k(i)$ is the one-particle (i) unit tensor operator of rank k and we can define $U^{(k)} = \sum_i u^k(i)$, where sum runs over open-shell electrons. In equation (2.9) we expend the product of multipole moments $\langle \Psi_1^0 | P_q^{(k)} | \Psi_{t1}{}^0 \rangle \langle \Psi_{t1}{}^0 | P_p^{(1)} | \Psi_2^0 \rangle$, as a sum of irreducible tensor operators. We rewrite it as:

$$\begin{aligned}
&\langle \Psi_1^0 | P_q^{(k)} | \Psi_{t1}{}^0 \rangle \langle \Psi_1^0 | P_p^{(1)} | \Psi_2^0 \rangle \\
&= \sum_{\lambda=k-1}^{k+1} \sum_{\mu=-\lambda}^{+\lambda} (-1)^{J_1+J_2-\lambda} \sqrt{\frac{2\lambda+1}{2J_1+1}} C^{\lambda\mu}_{kq1p} C^{J_1 M_1}_{J_2 M_2 \lambda\mu} \left\{ \begin{array}{ccc} k & 1 & \lambda \\ J_2 & J_1 & J' \end{array} \right\} \\
&\times \langle n\ell \big\| P^{(k)} \big\| n'\ell' \rangle \langle n'\ell' \big\| P^{(1)} \big\| n\ell \rangle \langle \Psi_1^0 \big\| U^{(k)} \big\| \Psi_{t1}{}^0 \rangle \langle \Psi_{t1}{}^0 \big\| U^{(1)} \big\| \Psi_2^0 \rangle \\
&= \langle n\ell \big\| P^{(k)} \big\| n'\ell' \rangle \langle n'\ell' \big\| P^{(1)} \big\| n\ell \rangle \sum_{\lambda\mu} \frac{C^{\lambda\mu}_{kq1p} C^{J_1 M_1}_{J_2 M_2 \lambda\mu}}{\sqrt{2J_1+1}} \langle \Psi_1^0 \big\| W^{(\lambda)} \big\| \Psi_2^0 \rangle,
\end{aligned} \tag{2.12}$$

where

$$\langle \Psi_1^0 \big\| W^{(\lambda)} \big\| \Psi_2^0 \rangle = (-1)^{J_1+J_2-\lambda} \sqrt{2\lambda+1} \left\{ \begin{array}{ccc} k & 1 & \lambda \\ J_2 & J_1 & J' \end{array} \right\} \langle \Psi_1^0 \big\| U^{(k)} \big\| \Psi_{t1}{}^0 \rangle \langle \Psi_1^0 \big\| U^{(1)} \big\| \Psi_2^0 \rangle \tag{2.13}$$

is a reduced matrix element of a tensor operator of rank λ as well and connects the levels of the ground configuration. It can be transformed as:

$$\begin{aligned}
\langle \Psi_1^0 \big\| W^{(\lambda)} \big\| \Psi_2^0 \rangle &= \langle nl^w \alpha_1 L_1 S_1 J_1 \big\| W^{(\lambda)} \big\| nl^w \alpha_2 L_2 S_2 J_2 \rangle \\
&= \sigma_{S_1 S_2} (-1)^{L_1+S_2+J_2+\lambda} \sqrt{(2J_1+1)(2J_2+1)} \\
&\times \left\{ \begin{array}{ccc} L_2 & S_2 & J_2 \\ J_1 & \lambda & L_1 \end{array} \right\} \langle nl^w \alpha_1 L_1 \big\| W^{(\lambda)} \big\| nl^w \alpha_2 L_2 \rangle \\
&= \sigma_{S_1 S_2} (-1)^{l+S_2+J_2} \sqrt{(2J_1+1)(2J_2+1)(2L_1+1)(2L_2+1)} \\
&\times \langle n\ell \| \, W^{(\lambda)} \, \| n\ell \rangle \, (nl^{w-1} \overline{\alpha} \overline{LS} | nl^w \alpha_1 L_1 S_1)(nl^{w-1} \overline{\alpha} \overline{LS} | nl^w \alpha_2 L_2 S_2),
\end{aligned} \tag{2.14}$$

where $(\overline{\alpha}\overline{LS})$ are the terms of $n\ell^{w-1}$, and

$$\begin{aligned}
\langle n\ell \| \, W^{(\lambda)} \, \| n\ell \rangle &= (-1)^\lambda w \sqrt{2\lambda+1} \left\{ \begin{array}{ccc} k & 1 & \lambda \\ \ell & \ell & \ell' \end{array} \right\} \langle n\ell \| \, u^{(k)}(i=w) \, \| n'\ell' \rangle \, \langle n'\ell' \| \, u^{(1)}(i=w) \, \| n\ell \rangle \\
&= (-1)^\lambda w \sqrt{2\lambda+1} \left\{ \begin{array}{ccc} k & 1 & \lambda \\ \ell & \ell & \ell' \end{array} \right\}.
\end{aligned} \tag{2.15}$$

The operators $U^{(\lambda)}$ that will be introduced in the JO line strengths are such that

$$\langle \Psi_1^0 \big\| W^{(\lambda)} \big\| \Psi_2^0 \rangle = (-1)^\lambda \sqrt{2\lambda+1} \left\{ \begin{array}{ccc} k & 1 & \lambda \\ \ell & \ell & \ell' \end{array} \right\} \langle \Psi_1^0 \big\| \, U^{(\lambda)} \, \big\| \Psi_2^0 \rangle \, . \tag{2.16}$$

The $\langle \Psi_1^0 \big\| U^{(\lambda)} \big\| \Psi_2^0 \rangle$ are actually the reduced matrix elements that would appear in the calculation of a rank-λ electric-multipole matrix element $\langle \Psi_1^0 \| P^{(\lambda)} \| \Psi_2^0 \rangle$ between levels

of the ground configuration, namely $\langle \Psi_1^0 \| P^{(\lambda)} \| \Psi_2^0 \rangle = \langle n\ell \| P^{(\lambda)} \| n\ell \rangle \times \langle \Psi_1^0 \| U^{(\lambda)} \| \Psi_2^0 \rangle$. The quantities $\langle \Psi_1^0 \big\| W^{(\lambda)} \big\| \Psi_2^0 \rangle$ are invariant under permutation of k, which is the rank of crystal-field, and 1, which is the rank of electric dipole.

Since the excited configuration levels are very high in energy, we can make the assumption that all the transitions in equation (2.8) have approximately the same energy and we can demonstrate that the two terms in equation (2.8) are equal for $\lambda = k \pm 1$ and they cancel out for $\lambda = k$. The final (strong) assumption of the Judd-Ofelt theory is to solely conserve the term $\lambda = k + 1$, supposed to be dominant. Therefore, to $k = 1, 2, 3$ correspond $\lambda = 2, 4, 6$ (the term $\lambda = 0$ is not included). This selection rule explains the fact that the standard Judd-Ofelt theory can not account for transitions $J_1 = 0 \leftrightarrow J_2 = 0$, $J_1 = 0 \leftrightarrow J_2 = 1$ and $J_1 = 1 \leftrightarrow J_2 = 0$, for example the case of transitions $^7\mathrm{F}_0 \leftrightarrow {}^5\mathrm{D}_{J_{odd}}$, $^7\mathrm{F}_{J_{odd}} \leftrightarrow {}^5\mathrm{D}_0$ and $^7\mathrm{F}_0 \leftrightarrow {}^5\mathrm{D}_0$ of Eu^{3+}. After the assumptions above, the ED expression is the following:

$$D_{12} = \frac{2}{\Delta E} \sum_{kq} A_{kq} \sum_{\lambda\mu} \delta_{\lambda,k+1} (-1)^{\lambda} \times \sqrt{\frac{2\lambda+1}{2J_1+1}} C^{\lambda\mu}_{kq1p} C^{J_1 M_1}_{J_2 M_2 \lambda\mu} \times \begin{Bmatrix} k & 1 & \lambda \\ l & l & l' \end{Bmatrix} \langle \Psi_1^0 \big\| U^{(\lambda)} \big\| \Psi_2^0 \rangle \langle n\ell \big\| P^{(k)} \big\| n'\ell' \rangle \langle n'\ell' \big\| P^{(1)} \big\| n\ell \rangle, \tag{2.17}$$

where

$$\langle n\ell \big\| P^{(k)} \big\| n'\ell' \rangle = (-1)^{\ell} [\ell\ell']^{1/2} \begin{pmatrix} \ell & k & \ell \\ 0 & 0 & 0 \end{pmatrix} \times \langle n\ell | r^k | n'\ell' \rangle. \tag{2.18}$$

A similar development can be carried out for the term $\langle \Psi_1^0 | P_q^{(1)} | \Psi_{t1}{}^0 \rangle \langle \Psi_1^0 | P_p^{(k)} | \Psi_2^0 \rangle$. The result is the same, except that the pairs of indices (1,p) and (k,q) in the CG are interchanged. This results in a factor of $(-1)^{1+k-\lambda}$.

The utility of the Judd-Ofelt theory is that it provides a theoretical expression for the line strength. From equation (2.17) we can calculate the ED line strength $S_{ED} = \sum_{pM_1M_2} [D_{12}]^2$, on which depend the absorption oscillator strength and the Einstein coefficients:

$$\mathcal{S}_{\mathrm{ED}} = \sum_{\lambda=2,4,6} \Omega_\lambda \left| \left\langle \Psi_i^0 \right\| U^{(\lambda)} \left\| \Psi_2^0 \right\rangle \right|^2, \tag{2.19}$$

with

$$\Omega_\lambda = \frac{4}{\Delta E^2} \sum_{kq} \delta_{\lambda,k+1} \frac{|A_{kq}|^2}{2k+1} (2\lambda+1) \left[\begin{Bmatrix} 1 & k & \lambda \\ \ell & \ell & \ell' \end{Bmatrix} (2\ell+1)(2\ell'+1) \right]^2 \times \left[\begin{pmatrix} \ell & 1 & \ell' \\ 0 & 0 & 0 \end{pmatrix} \begin{pmatrix} \ell' & k & \ell \\ 0 & 0 & 0 \end{pmatrix} \langle n\ell | r | n'\ell' \rangle \langle n'\ell' | r^k | n\ell \rangle \right]^2 \tag{2.20}$$

and $\langle \Psi_1^0 \| U^{(\lambda)} \| \Psi_2^0 \rangle$ is the reduced matrix element of the so-called unit tensor operator of rank λ, that were discussed earlier. They are only functions of angular-momentum quantum numbers J_1, J_2, J', ..., and can therefore be calculated exactly. By contrast, the Judd-Ofelt parameters Ω_λ depend on the atomic and crystal-field properties, which are difficult to evaluate from first principles. The parameter Ω_2 indicates the covalent

nature of ion-ligand bonds and the asymmetric nature of Nd^{3+} ion local environment. On the other hand, the Ω_4 and Ω_6 parameters are related to the rigidity of the host matrix. These parameters are treated as adjustable parameters in the linear least-square fitting of experimental and theoretical line strengths.

Due to the spin-orbit interaction in the $4f$ subshell, the unperturbed states are linear combination of LS states, and can be written as:

$$\left|\Psi_i^0\right\rangle = \sum_{\alpha_i L_i S_i} c_{\alpha_i L_i S_i} \left|n\ell^w\, \alpha_i L_i S_i J_i M_i\right\rangle , \tag{2.21}$$

where L_i, S_i and J_i are the quantum numbers associated with the orbital, spin and total electronic angular momentum respectively, while M_i is associated with the z-projection of the latter. The index α_i is sometimes necessary to distinguish manifolds with the same L_i and S_i (for example $^5D1$, $^5D2$ and $^5D3$ in Eu^{3+}). The $c_{\alpha_i L_i S_i}$ coefficients are the eigenvector components of the ionic Hamiltonian. For Ln^{3+} ion in the lowest configuration, there is most often one dominant LS component (with $|c_{\alpha_i L_i S_i}|^2 > 0.7$) and smaller ones.

In the case of Eu^{3+}, for example, the levels of the ^7F manifold are slightly coupled to the ^5D, and vice versa. Therefore, the pair coupling (2.21) allows to describe the spin-changing transitions between quintuplet and septuplet levels. However, the standard JO theory does not account for the influence of the spin mixing in the excited configuration $4f^5 5d$.

Despite its remarkable efficiency, this standard JO theory cannot reproduce some of the observed transitions, because of its strong selection rules. It is especially the case for europium (Eu^{3+}) [33, 34], well known to challenge the standard JO theory [29]. Many extensions of the original model have been proposed to overcome this drawback [35], including *e.g.* J-mixing [36–38], the Wybourne-Downer mechanism [39, 40], velocity-gauge expression of the electric-dipole (ED) operator [41], relativistic or configuration-interaction (CI) effects [30, 42–45], purely *ab initio* intensity calculations [46]. In this respect, Smentek and coworkers were able to reproduce experimental absorption oscillator strengths with a very high accuracy, with up to 17 adjustable parameters [47]. But in spite of all these improvements, even the most recent experimental studies use the standard version of the JO theory [48,49]. This restrictions caused by the standard JO theory and many (not fully successful) attempts of extending it, make the desire and the need for an extension of JO theory very natural.

As stated before in the standard JO theory, the line strength characterizing a given transition is a linear combinations of three parameters Ω_λ (with $\lambda = 2$, 4 and 6), which are functions of both the properties of the Ln^{3+} ion and the crystal-field parameters [29, 50]. Since the Ω_λ-parameters are adjusted by least-square fitting, those two types of contributions cannot be separated. However, the properties of the impurity can be investigated by means of free-ion spectroscopy. As discussed in sections 2.1 and 2.2, lanthanides have special structure, due to a very submerged subshell, f electrons are shielded from the environment, and therefore they weakly interact with the environment. When discussing different types of interactions within the ion, it is evident that the ion-crystal interaction (having a magnitude of ~ 100 cm^{-1}) is small compared to the Columbic interaction (having a magnitude of ~ 10000 cm^{-1}). As

a consequence, the spectrum of Ln^{3+}-doped crystals can be understood as a free-ion spectrum but perturbed by the crystal field. This being the case, the necessity of a very accurate free-ion spectrum and properties is inevitable. In this respect we have to do free-ion spectroscopic calculations for the elements for which we plan to discuss the JO theory and its possible extension.

The next chapter is dedicated to the description of the methodology used for free-ion calculations.

Part II

Trivalent Lanthanides

Chapter 3

Free-ion calculation on trivalent lanthanides

Investigations on the spectroscopic properties of triply ionized lanthanides have been always attractive to scientists. All the applications described in previous chapters require precise free-ion calculations of energies for the elements that are planned to be discussed. This chapter is devoted to discussion of results for free-ion calculations on three lanthanide ions: Eu^{3+}, Nd^{3+} and Er^{3+}. The calculations are done using the methodology and the software, Robert Cowan's atomic structure suite of code, that will be reported in section 3.1.

Among all the lanthanides, Eu^{3+} is well known ion to challenge the standard JO theory, described in chapter 2, so the choice of this ion is only natural. Moreover, a collaborative work was performed with an experimental group at ICB, where they were working with Eu^{3+} in nanorods and needed assistance in discussion of transitions [51]. Along with Eu^{3+}, we have done the calculations also Nd^{3+} and Er^{3+}, since the excited configuration levels for these elements are known in detail and those are elements with many applications, for example, lasers. Our fitting calculations require experimental energies. For Nd^{3+}, Er^{3+} and the ground configuration of Eu^{3+} we find them in the NIST ASD database [52], however no experimental level has been reported for the $4f^5 5d$ configuration. Among the lanthanide series the $4f^w$ configurations (with $2 \leq w \leq 12$) and the $4f^{w-1}5d$ ones (with $3 \leq w \leq 13$) possess the same energy parameters. This fact allows us to perform a least-square fitting calculation of some $4f^{w-1}5d$ configurations for which experimental levels are known, namely for Nd^{3+} ($w = 3$) and Er^{3+} ($w = 11$) [53–55]. Then, relying on the regularities of the scaling factors f_X that are seen for lanthanide series, we do the calculations for the excited configuration of Eu^{3+} as well, using the calculated parameters of trivalent neodymium and erbium.

In order to respect the chronology and the sense of the calculation we first describe the free-ion calculations done for Nd^{3+} (section 3.2) and Er^{3+} (section 3.3) and only after we discuss the calculation on Eu^{3+} (section 3.4).

3.1 Methodology of calculations

The calculation with simple configurations involving only one or two open subshells are relatively easy, provided that the coupling conditions lie close to some pure-coupling scheme, so that the Hamiltonian matrix is nearly diagonal in appropriate representation. The task of calculating energy levels is particularly easy in the near-LS case. However, very often, routine calculations of energy levels and spectra are practical only with elaborate computer programs. It is obvious that for configurations containing two or more open subshells, the matrices can become very large.

The suite of computer codes based on the famous book of Robert Cowan "The Theory of Atomic structure and Spectra" published in 1981, continue to be highly influential and convenient for such calculations [24]. It calculates atomic structure and spectra via the superposition-of-configuration method. Robert Cowan's codes are based on *ab initio* calculation and least-square fitting. The latest version of Cowan's code package is presently distributed by Cormac McGuinness at the University of Dublin, Ireland [56]. Another version of the codes are developed by Alexander Kramida. He introduced a drastic modification to the least squares fitting procedure [57]. The Kramida version includes also visual modifications of the output files.

Generally speaking, the codes use non-relativistic Hartree–Fock method, while the relativistic effects are accounted for as perturbations. The radial wavefunctions are calculated using a hydrogenic single-configuration approximation. More complex and maybe more accurate *ab initio* methods are present in the literature, but these codes give better accuracy only for limited number of spectra. The situation is far more complex in the case of lanthanides and actinides and so the *ab initio* calculations alone can not handle the cases where configuration interactions are large and numerous. It is inevitable to have strong CIs between closely-lying levels of the same parity and the same J value. In the suite of Cowan codes this problem is overcome by introducing least squares fitting of all levels. The package includes four subprograms written in FORTRAN. The names of these programs are made of Cowan's initials: "RC", followed by a code letter. The codes run in sequence, since each subprogram produces output files which are simultaneously input files for the next subprogram of the chain.

The calculations start with the code called ***RCN***, which calculates the single-configuration or one-electron radial wavefunction for each of any number of specified electron configurations via Hartree-Fock method. The principal output consists of center-of-gravity (E_{av}) of the configuration, as well as the radial Coulomb (F^k and G^k) and spin-orbit (ζ) integrals which are necessary to calculate the energy levels. The input file required by the code when executing, is an ascii text file which contains descriptions of the electronic configurations for which the radial wavefunctions should be computed. The results of these calculations are then stored for use by the RCN2 code. The RCN program also produces a text output file, which can be used for various analyses.

The next subprogram is called ***RCN2***. It is an interface program that uses the output wavefunctions from RCN to calculate the configuration-interaction Coulomb integrals (R^k) between each pair of interacting configurations. RCN2 calculates also the electric-dipole (E1) and/or electric quadrupole (E2) radial integrals between each

pair of configurations. There are two input files required for the execution of the RCN2 code. The first is an ascii text file in which certain options can be set for the execution of the code. The second binary input file, which is produced by the RCN program, contains the actual radial wavefunctions required to calculate the radial integrals. The resulting output file prepared by RCN2 serves as input to RCG.

RCG sets up energy matrices for each possible value of the total angular momentum J. Then it diagonalizes each matrix to get eigenvalues (energy levels) and eigenvectors (multi-configuration, intermediate- coupling wavefunctions in various possible angular-momentum-coupling representations), and then computes M1 (magnetic dipole), E2, and/or E1 radiation spectra, with wavelengths, oscillator strengths, radiative transition probabilities, and radiative lifetimes. In comparison with the previous subprograms there are many files associated with the RCG code and in normal usage we can concentrate only on two of these. The first is the required ascii text file, the contents of which are data about the configurations involved in the calculation such as occupation numbers and configuration average energies, data about pairs of interacting configurations required for calculation of configuration-interaction (same parities) and for electromagnetic dipole transitions (different parities). The output file created by the RCG contains almost all relevant information about the calculation which has been performed.

The output for the RCG program is very rich, it contains:

- Details of the configuration average energies and parities for each configuration included in the calculation.
- For each possible total angular momentum resulting from the configurations, each state is labelled in terms of both the LS and jj angular-momentum-coupling schemes.
- For each configuration and for each pair of interacting configurations various integrals are listed.
- The eigenvalues and the corresponding configuration serial numbers are listed, which are followed by the eigenvector coupling matrices, corresponding to the LS and jj coupling schemes.
- The calculated spectrum with all the transition lines is listed.

Generally the first three Cowan programs (RCN/RCN2/RCG) are run in sequence with the output of each program forming an important part of the input to the next. To facilitate these codes being executed in an unbroken sequence a powerful shell script has been created.

Once considerable progress has been made in the interpretation of observed spectrum lines and in the deduction of the associated energy levels, with the aid of *ab initio* calculations, the radial integrals E_{av}, F^k, G^k, ζ and R^k are considered simply as adjustable parameters, whose values are to be determined empirically so as to give the best possible fit between the calculated eigenvalues and the observed energy levels.

For this purpose the last program of Cowan's package called ***RCE*** is used in an iterative way. The resulting least-squares-fit parameters can be used to repeat the RCG calculations with the improved energy levels and (presumably) wavefunctions. Any of the parameters can be held fixed at specified values, or groups of parameters can be forced to vary in such a way that the ratios of the values within a group remain fixed relative to each other. Parameters that are supposed to be linked together (meaning the ratios of their values held fixed), should be given equal negative values of so called "constraints" (sometimes also called "flags").

The input files required for RCE are produced when appropriate options are set in the input to the RCG program. The fitting process is carried out by an automatic iterative procedure until the parameter values no longer change from one iteration cycle to the next (by more than 0.03), or for a specified maximum number of cycles.

In RCN the internal units are Bohr units of length and Rydberg units (units of 13.6058 eV) for energy. The final line of the output for each configuration gives the quantities needed for energy-level calculations in RCG, with E_{av} in Ry and all other energy radial integrals in units of kK (1000 cm^{-1}).

Some difficulties arise for complicated transitions and rare-earth configurations involving partially filled d and f subshells, where the average spacing between energy levels may be so small as to be comparable with the standard deviation of the fit. In an attempt to improve the quality of a fit (and therefore, the accuracy of the resulting eigenvectors), a variety of "effective-operator" parameters, called α, β and γ and "illegal"-k F^k, G^k have been introduced, representing corrections to both the electrostatic and the magnetic single-configuration effects. "Illegal"-k means that these are the values of k that do not satisfy to the triangle relation discussed in the section 1.5. These effective parameters, unlike other parameters, can not be calculated *ab initio*. The resulting least-square-fit parameters can then be used to repeat the RCG calculation with the improved energy levels and wavefunctions.

Workflow of the codes The logical workflow for the Cowan codes are the following:

1. specify the atomic configurations for the calculations, an example of an input file for RCN can be seen in the top panel of figure 3.1,
2. run RCN (the result is an input file for RCN2),
3. run RCN2 (the result is an input file for RCG, see the bottom panel of figure 3.1),
4. run RCG, those first raw results are rather inaccurate, they sometimes are called *ab initio* or HFR results (X_{HFR})and can be compared with the final results. The output is an input file RCE,
5. run RCE; this step is a fitting procedure and, and as mentioned earlier, requires experimental data. If necessary this step can be retaken after checking and correcting experimental data,
6. transfer the fitted parameters resulting from previous step to RCG input file,

```
2001 0 0 2  010  4.0    5.E-08    1.E-11-2 00199 0 1.0  0.65  0.0 1.00   -6
   63    4Eu    4f6             4f6
   63    4Eu    4f5  5d         4f5  5d
   -1
```

```
    11  -12 1 12 1 12         00      7 0.000.001  1000.0000 0.00 001101-6 0 0            1  1  1  1  1
f 6  s 0  s 0  s 0  s 0  s 0  s 0  s 0  Eu    4f6          -2377079.533   0.0000
f 5  d 1  s 0  s 0  s 0  s 0  s 0  s 0  Eu    4f5  5d      -2377011.772   0.0000
Eu    4f6             65.6090  88.7325   67.7780   41.0607    0.0226 LS99999999
  -0.6050    0.2922    1.3136
Eu    4f5  5d     18  137.5000  91.2699   72.0298   45.6386    0.0226 LS99999999
  -0.6050    0.2922    1.4811    1.2900    0.0000   23.0468    0.0000 LS99999999
  16.8157    9.1132    0.0000   10.1032    0.0000    6.6038
Eu    4f6           Eu    4f5  5d         1.13062( 4F//R1// 5D)0.8384hr  31  56
                   -55555555.
                   -99999999.
   -1
```

Figure 3.1: An example of RCN (top panel) and RCG (bottom panel) input files for Eu^{3+}.

7. rerun RCG.

Steps 2 and 3 can be taken separately, however most of the cases RCN and RCN2 are run together. All the calculations are automated, except for the second to last step, the RCE run, since it is a least squares fit and can sometimes require a lot of manual work. This least squares step is very prone to a qualitative improvement. The accuracy of RCE calculations depend on the inclusion of important interacting configurations in the calculation, as well as the choice of free and constrained parameters. By comparing the fitted and predicted energies it is possible to evaluate the accuracy of the least square fitting. The accuracy of the fit is measured by means of the standard deviation:

$$s = \left[\frac{\sum (E_{th} - E_{exp})^2}{N_{\text{lev}} - N_{\text{par}}} \right]^{\frac{1}{2}}, \tag{3.1}$$

where E_{exp} are the observed energy values and the E_{th} are the computed eigenvalues, N_{lev} is the number of levels being fitted and N_{par} is the number of adjustable parameters involved in the fit [24]. It is sometimes convenient to be able to link several parameters together in such a way that the mutual ratios of their values remain constant during the iteration. Some parameters can be excluded from the fit in particular cases, i.e. these parameters will not be modified [58]. It is obvious that a low standard deviation indicates that the theoretical or computed values tend to be close to the experimental ones, while a high standard deviation indicates that the values are spread out over a wider range.

To make some comparisons between different elements and ionization stages, one often defines the scaling factor (SF) $f_X = X_{\text{fit}}/X_{\text{HFR}}$ between the fitted and the HFR value of a given parameter X.

The analysis can take from few minutes to few weeks, depending on the complexity of the configurations considered for the calculation, but they give a very reasonable accuracy, most of the cases the standard deviation is below or around 100 cm^{-1}. Another advantage of the Cowan's codes is that it can be also used to calculate transition probabilities.

Regardless of how it is crucial to follow the workflow of the codes, each user requires an individual methodology of steps and calculations specifically sketched out for a given problem. In this work the general methodology for the calculation is as follows: (a) fitting the parameters with an *ab initio* value while effective parameters are forced to be zero; (b) fixing the parameters resulting from step (a) and fitting the effective parameters; (c) using the final values of (b), fitting all the parameters together.

3.2 Results on Neodymium ion: Nd^{3+}

Neodymium is a chemical element with the symbol Nd and atomic number 60. It is the fourth member of the lanthanide series and is considered to be one of the rare-earth metals. Neodymium compounds were first commercially used as glass dyes in 1927 and remain a popular additive. The color of neodymium compounds comes from the Nd^{3+} ion and is often a reddish-purple. However, this changes with the type of lighting because of the interaction of the sharp light absorption bands of neodymium with ambient light enriched with the sharp visible emission bands of mercury, trivalent europium or terbium. Neodymium-doped glasses are used in lasers that emit infrared with wavelengths between 1047 and 1064 nanometers. These lasers have been used in extremely high-power applications, such as experiments in inertial confinement fusion. Neodymium is also used with various other substrate crystals, such as yttrium aluminium garnet in the Nd:YAG laser. In the periodic table, it appears between the lanthanides praseodymium to its left and the radioactive element promethium to its right, and above the actinide uranium (see figure 2.1).

A critical collection of lanthanides energy levels was created by Martin *et al.* [59], after that the first results for Nd^{3+} was obtained by Wyart *et al.* [60]. After it was improved by Wyart *et al.* in 2007, when the neodymium spectrum emitted by a sliding spark was photographed on the 10.7m normal incidence vacuum ultraviolet spectrographs at the National Institute of Standards and Technology and at the Paris-Meudon Observatory [53]. The work led to the determination of the entire ground configuration $4f^3$ and to a large part of the excited configurations $4f^2$ 5d, $4f^2$ 6s and $4f^2$ 6p with the support of predictions using the Cowan codes. From relatively recent works, noteworthy is the one by Arab *et al.* [55], where the authors are dealing with the core-excited configuration $5p^5$ $4f^3$5d.

In this current work the calculations have been done for two configurations of Nd^{3+}: $4f^3$ (odd parity) and $4f^25d$ (even parity). The choice of these configuration has been made keeping in mind that these two configurations are coupled by ED transition and this transition has strong character. Additionally, throughout this work, we are interested in transitions that happen between the levels of $4f^3$ configuration (see chapter 2). Moreover, the calculations with more configurations and the interpretation of Nd^{3+} and Er^{3+} spectra show that the eigenvectors are essentially composed of one configuration only and because CI mixing is very low, a one-configuration approximation can safely be applied in both parities, which is done here. The experimentally known levels that are essential for our least-square calculations are taken from the above described work of Wyart *et al.* [53]. There are 41 levels for $4f^3$ configuration and 111 for $4f^25d$

Table 3.1: Comparison between the experimental [53] and computed values for the levels of $4f^3$ configuration of Nd^{3+}, with total angular momenta from $J = 0.5$ to 7.5 and energies up to 30000 cm^{-1}, as well as at most the five leading eigenvectors with their percentages. All energy values are in cm^{-1}. The "o" superscript, indicating the odd parity, common to all terms, has been omitted.

Exp.	This work	J	Eigenvectors with non-zero percentages									
0	74	4.5	^{4}I	97.1 %	^{2}H2	2.6 %	^{2}H1	0.3 %				
1897	1961	5.5	^{4}I	99.0 %	^{2}H2	0.9 %	^{2}H1	0.1 %				
3907	3975	6.5	^{4}I	99.6 %	^{2}K	0.4 %						
5989	6075	7.5	^{4}I	98.8 %	^{2}K	1.2 %						
11698	11746	1.5	^{4}F	94.3 %	^{2}D1	4.8 %	^{2}P	0.3 %	^{2}D2	0.3 %	^{4}S	0.3 %
12748	12800	2.5	^{4}F	97.7 %	^{2}D1	2.1 %	^{2}F2	0.1 %	^{2}F1	0.1 %		
12800	13002	4.5	^{2}H2	55.7 %	^{4}F	13.4 %	^{2}G1	10.9 %	^{2}H1	7.9 %	^{2}G2	7.7 %
13720	13692	1.5	^{4}S	94.5 %	^{2}P	4.8 %	^{4}F	0.5 %	^{2}D1	0.2 %		
13792	13805	3.5	^{4}F	93.6 %	^{2}G1	3.7 %	^{2}G2	2.4 %	^{2}F2	0.1%	^{4}G	0.1 %
14995	15100	4.5	^{4}F	75.8 %	^{2}H2	19 %	^{2}H1	2.2 %	^{2}G1	1.6 %	^{2}G2	0.7 %
16162	16329	5.5	^{2}H2	80.5 %	^{2}H1	12.5 %	^{4}G	5.8 %	^{4}I	0.9 %	^{2}I	0.3 %
17707	17544	2.5	^{4}G	98.6 %	^{2}F1	0.7 %	^{2}F2	0.6 %	^{4}F	0.1 %		
17655	17711	3.5	^{4}G	41.9 %	^{2}G1	30.7 %	^{2}G2	23.1 %	^{4}F	4.3 %		
19541	19498	3.5	^{4}G	57.4 %	^{2}G1	24.3 %	^{2}G2	15.7 %	^{4}F	2.0 %	^{2}F2	0.3 %
19970	19928	4.5	^{4}G	75.8 %	^{2}G1	7.2 %	^{2}G2	6.5 %	^{2}H2	6.0 %	^{4}F	2.9 %
20005	19974	6.5	^{2}K	98.7 %	^{2}I	0.9 %	^{4}I	0.4 %				
21493	21574	4.5	^{2}G1	39.1 %	^{2}G2	26.0 %	^{4}G	21.6 %	^{4}F	7.8 %	^{2}H2	5.4 %
21701	21667	1.5	^{2}D1	45.8 %	^{2}P	43.6 %	^{4}S	3.7 %	^{4}F	3.6 %	^{4}D	1.6 %
22044	22006	7.5	^{2}K	97.7 %	^{2}L	4.1 %	^{4}I	1.2 %				
22047	21986	5.5	^{4}G	92.7 %	^{2}H1	4.1 %	^{2}H2	3.1 %				
23789	23571	0.5	^{2}P	94.1 %	^{4}D	5.9 %						
24333	24348	2.5	^{2}D1	97.5 %	^{4}F	2.1 %	^{2}D2	0.3 %	^{2}F1	0.1 %		
26761	26696	1.5	^{2}P	48.9 %	^{2}D1	44.5 %	^{2}D2	2.8 %	^{4}F	1.5 %	^{4}S	1.5 %
29010	28958	1.5	^{4}D	82.0 %	^{2}D2	15.0 %	^{2}P	1.6 %	^{2}D1	1.3 %		
29191	29121	2.5	^{4}D	79.8 %	^{2}D2	17.9 %	^{2}F2	1.1 %	^{2}F1	1.1 %	^{4}G	0.1 %
29540	29533	0.5	^{4}D	94.1 %	^{2}P	5.9 %						

configuration.

The calculations were done with the general methodology described in section 3.1. We recall here that such calculations start with the *ab initio* determination of energy parameters, later, in the next steps, these parameters are treated as adjustable parameters for least-squares fit.

The precision of calculations is measured by means of standard deviation (see equation (3.1)). For the first step, where all parameters were allowed to evolve freely, but the effective parameters were fixed to 0 the standard deviation is 475 cm^{-1}, for odd parity configuration $4f^3$ of Nd^{3+}. By including the effective parameters included in the fitting procedure, we managed to decrease the standard deviation to 130 cm^{-1}. A similar calculation was performed for even parity configuration $4f^25d$ too. For the first step the standard deviation is 228 cm^{-1}, and it is decreased to the value 75 cm^{-1} for

Table 3.2: Comparison between the experimental [53] and computed values for the first 15 levels of $4f^2$ 5d configuration of Nd^{3+}, with total angular momenta from $J = 2.5$ to 7.5, and at most the three leading eigenvectors with their percentages. All energy values are in cm^{-1}.

Exp.	This work	J	Eigenvectors with non-zero percentages					
70817	70893	4.5	^{2}H	45 %	^{4}I	46 %	^{2}H	5 %
71745	71675	5.5	^{4}K	76 %	^{2}I	11 %	^{2}I	6 %
73366	73350	4.5	^{4}I	50 %	^{2}H	32 %	^{2}H	9 %
73557	73644	5.5	^{2}H	36 %	^{4}I	43 %	^{2}H	6 %
73616	73692	2.5	^{4}G	47 %	^{4}G	22 %	^{2}F	14 %
74364	74316	3.5	^{4}H	84 %	^{2}G	7 %	^{4}G	3 %
74572	74552	5.5	^{4}I	52 %	^{2}H	15 %	^{4}K	9 %
74674	74580	6.5	^{4}K	94 %	^{2}I	3 %	^{2}I	2 %
75667	75709	3.5	^{4}G	61 %	^{4}G	24 %	^{4}H	6 %
76412	76400	4.5	^{4}H	86 %	^{4}G	6 %	^{2}G	3 %
76471	76495	6.5	^{4}I	98 %	^{2}K	1 %	^{2}I	1 %
77540	77437	7.5	^{4}K	100 %	^{2}K	1 %	^{2}I	1 %
77598	77616	2.5	^{2}F	30 %	^{4}G	23 %	^{2}F	16 %
77833	77829	3.5	^{4}H	92 %	^{2}G	3 %	^{2}G	2 %
77810	77840	4.5	^{4}G	62 %	^{4}G	24 %	^{4}H	7 %

the last cycle of fitting procedure.

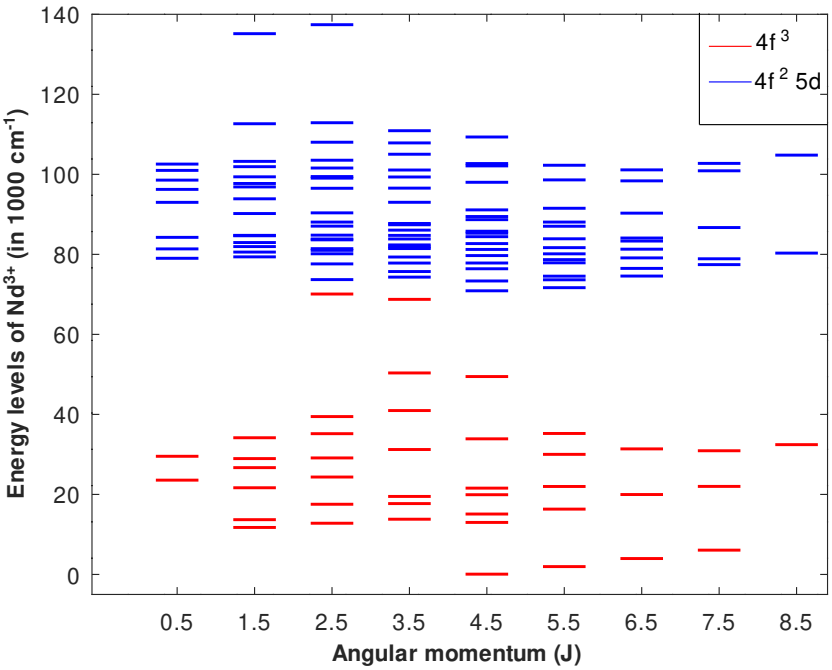

Figure 3.2: Calculated energy levels of the $4f^3$ (red) and $4f^2$ 5d (blue) configurations of Nd^{3+} as functions of the electronic angular momentum J.

Figure 3.2 shows the levels computed for both configurations, and their comparison with the data reported in [53] is shown in table 3.1 for levels of ground configuration below 30000 cm^{-1} and in table 3.2 for the first 15 levels of 4f^2 5d configuration. We provide also information about our computed eigenvectors, with at most five non-zero percentages. Our theoretical results include accurately calculated 42 levels with energy levels up to ∼70000 cm^{-1} for the ground configuration 4f^3 and 107 levels with energy levels belonging to the range ∼71000 - 137000 cm^{-1} for the first excited configuration 4f^2 5d of Nd^{3+}.

Most of levels are well described by the LS coupling, with leading components above 70 %. This is less the case for the intermediate J-values of 3.5 and 4.5, for which ^{2}H, ^{2}G, ^{4}G and ^{4}F manifolds are mixed by the spin-orbit interaction. Note that for the level at 17655 cm^{-1}, the leading component is ^{4}G with 41.9 %; but if one adds the two ^{2}G manifolds, it yields 53.8 %. This can lead to some ambiguity when labeling that level. Spin-orbit mixing is also significant between ^{2}P and ^{2}D manifolds for $J = 1.5$.

The Judd-Ofelt theory, which is described in chapter 2, requires the calculation of matrix elements:

$$\langle n'l'\|P^{(k)}\|nl\rangle = (-1)^{l'}[ll']^{1/2}\begin{pmatrix} l' & k & l \\ 0 & 0 & 0 \end{pmatrix}\int_0^\infty dr P_{n'l'}(r)r^k P_{nl}(r). \tag{3.2}$$

In our case $n'l' = 4f$ and $nl = 5d$, with $k = 1, 3, 5$. The matrix element only for $k = 1$ can be calculated by one of the subprograms of Cowan codes, RCN2, but another subprogram RCN allow to print the wavefunctions with the HFR method. In order to calculate the matrix elements for $k = 1, 3, 5$ we have written an octave code. For $k = 1$ the matrix element calculated by the octave program is $1.2877242\,a_0$, while the value calculated by RCN2 is $1.28773\,a_0$. The matrix element is -4.10141 a_0^3 and 30.49720 a_0^5 for $k = 3$ and $k = 5$, respectively.

After carrying out free-ion calculation on energy levels for Nd^{3+}, we compare our $[U^{(\lambda)}]^2$ matrix elements with those of Carnall [61] in order to check our free-ion eigenvectors. Those matrix elements are computed for transitions that will be used in our extension calculations and are present in the next subsections.

The results are shown in table 3.3, showing a very good agreement except for the transitions $^4I_{9/2} \leftrightarrow {}^4S_{3/2}$ and $^4I_{9/2} \leftrightarrow {}^4F_{7/2}$. By looking closely, we presume that the lines corresponding to those two upper levels in Table V of Ref. [62] have been interchanged. They are indeed so close in energy that their order is inverted in certain materials. In other words, their absorption peaks overlap, which makes it difficult to correctly identify them. This, for example, happens In the article by Jyothi *et al.* [63] dedicated to Nd^{3+}-doped tellurite and metaborate glasses, where those two transitions are superposed. In this case, the $[U^{(\lambda)}]^2$ matrix elements can be summed to give a single effective transition.

3.3 Results on Erbium ion: Er^{3+}

Erbium is a chemical element with the symbol Er and atomic number 68. Erbium's principal uses involve its pink-colored Er^{3+} ions, which have optical fluorescent proper-

Table 3.3: Comparison between our reduced matrix elements $[U^{(\lambda)}]^2$ for selected transitions of Nd^{3+} and those of Ref. [62].

Transition	$[U^{(2)}]^2$		$[U^{(4)}]^2$		$[U^{(6)}]^2$	
	Our	Rep.	Our	Rep.	Our	Rep.
$^4I_{9/2} \leftrightarrow {}^4F_{3/2}$	0	0	0.2297	0.2293	0.0553	0.0549
$^4I_{9/2} \leftrightarrow {}^2H_{9/2}$	0.0089	0.0092	0.0079	0.0080	0.1129	0.1154
$^4I_{9/2} \leftrightarrow {}^4F_{7/2}$ [a]	0.0009	0.0010	0.0430	0.0422	0.4238	0.4245
$^4I_{9/2} \leftrightarrow {}^4S_{3/2}$ [a]	0	0	0.0026	0.0027	0.2349	0.2352
$^4I_{9/2} \leftrightarrow {}^4F_{9/2}$	0.0009	0.0009	0.0092	0.0092	0.0421	0.0417
$^4I_{9/2} \leftrightarrow {}^4G_{5/2}$	0.8979	0.8979	0.4095	0.4093	0.0356	0.0359
$^4I_{9/2} \leftrightarrow {}^4G_{9/2}$	0.0047	0.0046	0.0603	0.0608	0.0407	0.0406
$^4I_{9/2} \leftrightarrow {}^4G_{11/2}$	0.00001	~ 0	0.0051	0.0053	0.0080	0.0080
$^4I_{9/2} \leftrightarrow {}^2P_{1/2}$	0	0	0.0350	0.0367	0	0
$^4I_{9/2} \leftrightarrow {}^4D_{1/2}$	0	0	0.2603	0.2584	0	0

[a] Probable inversion in Table V of Ref. [62]

ties particularly useful in certain laser applications. Erbium-doped glasses or crystals can be used as optical amplification media, where Er^{3+} ions are optically pumped at around 980 or 1480 nm and then radiate light at 1530 nm in stimulated emission. This process results in an unusually mechanically simple laser optical amplifier for signals transmitted by fiber optics. The 1550 nm wavelength is especially important for optical communications because standard single mode optical fibers have minimal dispersion at this particular wavelength. Moreover, a large variety of medical applications (i.e. dermatology, dentistry) utilize erbium ion's 2940 nm emission (see Er:YAG laser), which is highly absorbed in water. The triply charged ion Er^{3+} received special attention since erbium oxide has been tested as a candidate for fusion reactor blanket systems [64] and more recently for possible quantum information applications when embedded in silicon [65].

In the work of Meftah *et al.* [54] and extended by Chikh *et al.* [66], the vacuum spark spectrum of erbium is observed in the wavelength region 705–2460 Å where transitions between the low-lying configurations $4f^{11}$, $4f^{10}$ 5d, $4f^{10}$ 6s and $4f^{10}$ 6p take place. They achieved a completely revised analyses of trivalent Er, which led to determine 120 energy levels belonging to the configurations $4f^{11}$, $4f^{10}$ 5d, $4f^{10}$ 6s and $4f^{10}$ 6p.

Since we are interested in the transitions that happen between the levels of configuration $4f^{11}$ when they are coupled with the first excited one, the calculations in the present work have been done for two configurations of Er^{3+}: $4f^{11}$ (odd parity) and $4f^{10}$ 5d (even parity). The experimental levels that are necessary for our calculations are taken from the above discussed article of Meftah *et al.* [54]. There are 38 experimental levels of the configuration $4f^{11}$ and 58 of $4f^{10}$ 5d.

We followed the same general methodology for Er^{3+} as for trivalent Nd. When the effective parameters are present in the fitting procedure, we obtain standard deviation

Table 3.4: Comparison between the experimental [54] and computed values for the levels of $4f^{11}$ configuration of Er^{3+}, with total angular momenta from $J = 1.5$ to 7.5 and energies up to 30000 cm^{-1}, as well as at most five eigenvectors with non-zero percentages. All energy values are in cm^{-1}. The "o" superscript, indicating the odd parity, common to all terms, has been omitted.

Exp.	This work	J	Eigenvectors with non-zero percentages									
0	-1	7.5	^{4}I	97.0 %	^{2}K	3.0 %						
6508	6531	6.5	^{4}I	99.1 %	^{2}K	0.8 %	^{2}I	0.1 %				
10172	10167	5.5	^{4}I	82.4 %	^{2}H2	14.8 %	^{4}G	1.3 %	^{2}H1	1.1 %	^{2}I	0.4 %
12469	12429	4.5	^{4}I	53.8 %	^{2}H2	17.6 %	^{4}F	12.3 %	^{2}G1	7.7 %	^{2}G2	4.8 %
15405	15413	4.5	^{4}F	59.6 %	^{4}I	25.3 %	^{2}G1	8.7 %	^{2}G2	4.8 %	^{4}G	0.8 %
-	18755	1.5	^{4}S	67.8 %	^{2}P	18.6 %	^{2}D1	7.9 %	^{4}F	5.5 %	^{4}D	0.2 %
19332	19343	5.5	^{2}H2	48.3 %	^{4}G	34.2 %	^{4}I	15.0 %	^{2}H1	2.1 %	^{2}I	0.3 %
-	20690	3.5	^{4}F	92.3 %	^{2}G1	4.6 %	^{2}G2	2.5 %	^{2}F2	0.3 %	^{2}F1	0.2 %
-	22294	2.5	^{4}F	83.9 %	^{2}D1	13.0 %	^{2}D2	2.0 %	^{2}F2	0.5 %	^{4}D	0.2 %
-	22708	1.5	^{4}F	62.6 %	^{2}D1	20.1 %	^{4}S	16.9 %	^{2}P	0.4 %		
24736	24736	4.5	^{4}F	24.3 %	^{2}G1	19.0 %	^{2}H2	16.6 %	^{2}G2	14.9 %	^{4}I	12.4 %
26708	26739	5.5	^{4}G	61.6 %	^{2}H2	25.5 %	^{2}H1	1.5 %	^{4}I	2.4 %		
27767	27738	4.5	^{4}G	79.5 %	^{2}H2	14.5 %	^{4}I	4.7 %	^{2}H1	0.8 %	^{2}G2	0.4 %
-	27353	7.5	^{2}K	90.9 %	^{2}L	60.1 %	^{4}I	3.0 %				
-	28311	3.5	^{4}G	41.6 %	^{2}G1	26.6 %	^{2}G2	23.3 %	^{4}F	3.9 %	^{2}F2	2.2 %

equal to 37 cm^{-1} for odd configuration $4f^{11}$. For the even configuration $4f^{10}$ 5d, the standard deviation is 124 cm^{-1}. Both values are very satisfactory, since the magnitude of ion-crystal interaction in such systems of crystal doped lanthanides is in order of $\sim$ 100 cm^{-1}.

Table 3.4, where we present all the eigenvector components with non-zero percentages, shows a good agreement between experimental values and our computed values for the ground configuration $4f^{11}$ of Er^{3+}. Compared to neodymium, the density of ground-configuration levels is smaller for erbium. Table 3.4 also presents up to five eigenvector components with non-zero percentages. Although not as good as for Nd^{3+} it shows that most of the levels of Er^{3+} are well described by the LS coupling scheme, which is due to the larger spin-orbit interaction. The leading component for 8 levels out of 15 is above 70%. On the other hand, for the levels with intermediate J-values of 3.5 and 4.5 LS is less of a good coupling scheme. For the levels with calculated energies of 24736 and 28311 cm^{-1}, labeling is not trivial. For the former, the sum of ^{2}G components gives the largest contribution of 33.9 %, and so we retain the label $^2G_{9/2}$. For the latter, the sum of ^{2}G components, equal to 49.9 % exceeds the ^{4}G one: therefore we retain the label $^2G_{7/2}$ (see last column of Table 3.4). Table 3.5 shows comparison between 15 theoretical and experimental energy levels of the first excited configuration of Er^{3+}. It shows a good agreement, although, contrary to the ground configuration levels, the excited configuration levels are not very well described with LS coupling scheme.

Table 3.5: Comparison between the experimental [53] and computed values for the first 15 levels of $4f^{11}$ 5d configuration of Er^{3+}, with total angular momenta from $J = 4.5$ to 10.5, and at most the three leading eigenvectors with their percentages. All energy values are in cm^{-1}.

Exp.	This work	J	Eigenvectors with non-zero percentages					
73426	73380	7.5	^{6}H	50 %	^{6}I	28 %	^{4}I	7 %
73426	73704	8.5	^{6}I	68 %	^{6}K	16 %	^{4}K	8 %
74536	74496	6.5	^{6}G	58 %	^{6}H	23 %	^{6}I	5 %
75983	76024	9.5	^{6}K	51 %	^{4}L	22 %	^{6}L	19 %
78917	78915	6.5	^{6}I	37 %	^{6}G	26 %	^{6}H	20 %
79154	79152	8.5	^{4}K	37 %	^{6}I	23 %	^{6}K	22 %
79276	79206	10.5	^{6}L	92 %	^{4}M	6 %	^{4}M	2 %
79362	79324	7.5	^{2}K	0 %	^{6}H	32 %	^{6}I	30 %
79522	79470	9.5	^{4}L	44 %	^{6}K	40 %	^{6}L	9 %
79743	79751	5.5	^{6}G	41 %	^{6}H	36 %	^{6}I	11 %
82610	82663	8.5	^{2}L	0 %	^{6}L	38 %	^{4}K	35 %
82922	82901	6.5	^{2}I	0 %	^{6}I	22 %	^{6}K	20 %
83110	83137	5.5	^{6}I	45 %	^{6}G	29 %	^{6}K	6 %
83377	83262	7.5	^{4}I	40 %	^{6}K	30 %	^{6}L	9 %
83709	83745	4.5	^{6}H	42 %	^{6}G	23 %	^{6}I	22 %

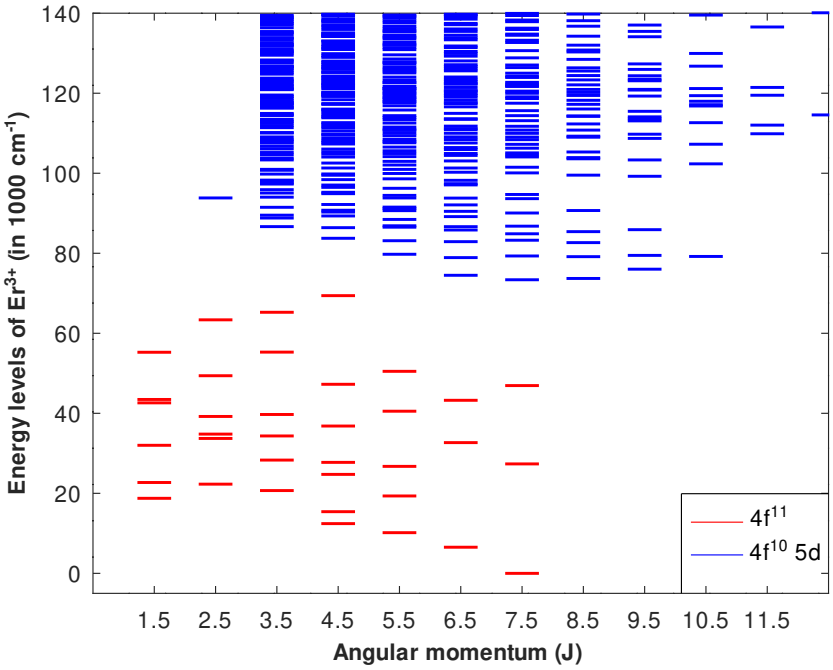

Figure 3.3: Calculated nergy levels of the $4f^{11}$ (red) and $4f^{10}5d$ (blue) configurations of Er^{3+} as functions of the electronic angular momentum J.

Overall we managed to precisely identify 39 levels with energy values up to $\sim$ 69000 cm^{-1} for the ground configuration and 692 levels in the range of $\sim$ 73000-

Table 3.6: Comparison between our reduced matrix elements $[U^{(\lambda)}]^2$ for selected transitions of Er^{3+} and those of Ref. [62].

Transition	$[U^{(2)}]^2$		$[U^{(4)}]^2$		$[U^{(6)}]^2$	
	Our	Rep.	Our	Rep.	Our	Rep.
$^4I_{15/2} \leftrightarrow {}^4I_{13/2}$	0.0195	0.0195	0.1173	0.1173	1.4304	1.4316
$^4I_{15/2} \leftrightarrow {}^4I_{11/2}$	0.0275	0.0282	0.0002	0.0003	0.3983	0.3953
$^4I_{15/2} \leftrightarrow {}^4I_{9/2}$	0	0	0.1504	0.1733	0.0053	0.0099
$^4I_{15/2} \leftrightarrow {}^4F_{9/2}$	0	0	0.5581	0.5581	0.4643	0.4643
$^4I_{15/2} \leftrightarrow {}^4S_{3/2}$	0	0	0	0	0.2191	0.2191
$^4I_{15/2} \leftrightarrow {}^2H_{11/2}$	0.6922	0.7125	0.3973	0.4125	0.0865	0.0925
$^4I_{15/2} \leftrightarrow {}^4F_{7/2}$	0	0	0.1467	0.1469	0.6272	0.6266
$^4I_{15/2} \leftrightarrow {}^4F_{5/2}$	0	0	0	0	0.2222	0.2232
$^4I_{15/2} \leftrightarrow {}^2G_{9/2}$	0	0	0.0217	0.0189	0.2215	0.2256
$^4I_{15/2} \leftrightarrow {}^4G_{11/2}$	0.9391	0.9183	0.5381	0.5262	0.1215	0.1235
$^4I_{15/2} \leftrightarrow {}^2G_{7/2}$	0	0	0.0175	0.0174	0.1158	0.1163
$^4I_{15/2} \leftrightarrow {}^4G_{9/2}$	0	0	0.2380	0.2416	0.1293	0.1235

237000 cm^{-1} for the first excited configuration of Er^{3+}. The computed levels of Er^{3+} are shown in figure 3.3. For being convenient and for the sake of simplicity, the graph is limited to 140000 cm^{-1}. The energy diagram shows in particular a large density in the excited configuration, which is due to the four vacancies in the 4f shell.

As for Nd^{3+} we have also done the calculation of matrix elements $\langle n'l'\|r^k\|nl\rangle$ for Er^{3+}, where $nl = 4f$ and $n'l' = 5d$. We obtain 0.96441 a_0, -2.37459 a_0^3 and 14.24536 a_0^5 for $k = 1$, 3 and 5, respectively, while the value calculated for this matrix element by Cowan codes is 0.9644014 a_0. We completed radial matrix elements calculations on trivalent erbium as well.

Table 3.6 shows results for $[U^{(\lambda)}]^2$ matrix elements calculated with our eigenvectors, in comparison with values reported in the article of Carnall [62]. It shows an overall good agreement, except for $[\langle {}^4I_{15/2}\|U^{(6)}\|{}^4I_{9/2}\rangle]^2$ that we find almost twice as small as Carnall.

3.4 Results on Europium ion: Eu^{3+}

Europium is a chemical element with the symbol Eu and atomic number 63. Europium is a silvery-white metal and is the most chemically reactive, least dense, and softest of the lanthanide elements. Europium was isolated in 1901 and named after the continent of Europe. Its compounds tend to exist in a trivalent oxidation state under most conditions. Europium can create a red or a blue luminescence depending on its oxidation state. Relative to most other elements, commercial applications for europium are few and rather specialized. Trivalent europium (Eu^{3+}, sometimes also named Eu IV) with

Table 3.7: Comparison between the experimental, computed and other theory [68] values for the levels of $4f^6$ configuration of Eu^{3+}, with total angular momenta from $J = 0$ to 6 and energies up to 30000 cm^{-1}, as well as first three LS-coupling eigenvectors with their percentages. All energy values are in cm^{-1}.

Exp.	This work	Other theory	J	First three eigenvectors and percentages					
0	-21	0	0	^{7}F	93.4 %	^{5}D1	3.5 %	^{5}D3	2.8 %
370	357	380	1	^{7}F	94.7 %	^{5}D1	2.8 %	^{5}D3	2.2 %
1040	1022	1040	2	^{7}F	96.3 %	^{5}D1	1.9 %	^{5}D3	1.4 %
1890	1880	1880	3	^{7}F	97.4 %	^{5}D1	1.1 %	^{5}D3	0.7 %
2860	2860	2830	4	^{7}F	97.9 %	^{5}F2	0.5 %	^{5}D1	0.4 %
3910	3912	3860	5	^{7}F	97.6 %	^{5}G1	0.8 %	^{5}G3	0.8 %
4940	4998	4970	6	^{7}F	96.4 %	^{5}G1	1.5 %	^{5}G3	1.5 %
17270	17257	17830	0	^{5}D3	45.4 %	^{5}D1	30.4 %	^{3}P6	6.7 %
19030	19015	19450	1	^{5}D3	50.6 %	^{5}D1	33.5 %	^{7}F	4.7 %
21510	21489	22140	2	^{5}D3	54.3 %	^{5}D1	36.1 %	^{7}F	2.9 %
24390	24360	25370	3	^{5}D3	55.2 %	^{5}D1	37.7 %	^{5}D2	2.0 %
	25257		6	^{5}L	88.7 %	^{3}K5	3.0 %	^{3}K1	2.2 %
	26314		2	^{5}G3	40.6 %	^{5}G1	36.0 %	^{5}G2	16.7 %
	26622		3	^{5}G3	37.8 %	^{5}G1	33.3 %	^{5}G2	16.4 %
	26814		4	^{5}G3	33.2 %	^{5}G1	28.5 %	^{5}G2	17.8 %
	26913		5	^{5}G3	30.2 %	^{5}G1	24.9 %	^{5}G2	20.2 %
	26926		6	^{5}G3	26.9 %	^{5}G2	22.7 %	^{5}G1	20.4 %
27640	27574	28960	4	^{5}D3	52.8 %	^{5}D1	37.6 %	^{5}F2	2.3 %

its partially filled f-shell attracted particular attention, since it exhibits interesting optical properties which allow its application as an activator in diverse phosphors for lightning in fluorescent light bulbs, fluorescent tubes, LEDs, and in displays, such as plasma displays, LCD displays, and the older CRTs [67].

As stated before there are no experimental studies performed for trivalent Eu. In the NIST database it is possible to find 12 levels for the ground state $4f^6$ of Eu^{3+}, but almost all the levels were determined by interpolation or extrapolation of known experimental values or by semi-empirical calculation [59]; their absolute accuracy is reflected in the number of significant figures assigned to it [52]. This is because the free-ion has not been analyzed yet. The situation is even more crucial for the excited configuration $4f^5$ 5d, since there are no level information present in the database. As in the case of Nd^{3+} and Er^{3+}, the calculations have been done for two lowest electronic configurations of Eu^{3+}: $4f^6$, of even parity, and $4f^5 5d$, of odd parity.

The standard deviation for $4f^6$ configuration is 28cm^{-1}. Table 3.7 shows a good agreement between these experimental values, our computed values and the theoretical values calculated by Freidzon and coworkers [68]. Our values are closer to the experimental ones in the ^{5}D manifold. Note that a direct comparison with the article of Ogasawara and coworkers [30] is difficult, as the authors do not give tables of energy

Table 3.8: Manifolds of quintet ($S = 2$) and septet ($S = 3$) multiplicities of $4f^6$ ground configuration of Eu^{3+}. All energy values are in cm^{-1}.

Energy	Eigenvector
3895	$\|^7F\rangle$
24561	$\sqrt{0.576}\ \|^5D3\rangle$ - $\sqrt{0.406}\ \|^5D1\rangle$ - $\sqrt{0.019}\ \|^5D2\rangle$
28212	$\|^5L\rangle$
28268	$\sqrt{0.408}\ \|^5G3\rangle$ - $\sqrt{0.328}\ \|^5G1\rangle$ - $\sqrt{0.264}\ \|^5G2\rangle$
32821	$\sqrt{0.652}\ \|^5H1\rangle$ - $\sqrt{0.348}\ \|^5H2\rangle$
35683	$\sqrt{0.970}\ \|^5I2\rangle$ - $\sqrt{0.03}\ \|^5I1\rangle$
35822	$\sqrt{0.755}\ \|^5F2\rangle$ - $\sqrt{0.245}\ \|^5F1\rangle$
39329	$\|^5K\rangle$
42446	$\sqrt{0.732}\ \|^5G2\rangle$ - $\sqrt{0.159}\ \|^5G1\rangle$ - $\sqrt{0.109}\ \|^5G3\rangle$
43892	$\sqrt{0.803}\ \|^5D3\ \rangle$ - $\sqrt{0.165}\ \|^5D1\rangle$ - $\sqrt{0.031}\ \|^5D2\rangle$
45888	$\|^5P\rangle$
47553	$\sqrt{0.652}\ \|^5H2\rangle$ - $\sqrt{0.348}\ \|^5H1\rangle$
57251	$\|^5S\rangle$
62588	$\sqrt{0.970}\ \|^5I1\rangle$ - $\sqrt{0.030}\ \|^5I2\rangle$
64164	$\sqrt{0.755}\ \|^5F1\rangle$ - $\sqrt{0.245}\ \|^5F2\rangle$
75177	$\sqrt{0.513}\ \|^5G1\rangle$ - $\sqrt{0.483}\ \|^5G3\rangle$ - $\sqrt{0.004}\ \|^5G2\rangle$
76112	$\sqrt{0.430}\ \|^5D1\rangle$ - $\sqrt{0.392}\ \|^5D3\rangle$ - $\sqrt{0.177}\ \|^5D2\rangle$

levels for Eu^{3+}. In total, the $4f^6$ configuration contains 296 levels with J values ranging from 0 to 12. Table 3.7 also illustrates that the ground-configuration levels are well described by the LS coupling scheme. Some levels are mainly characterized by a single term, like ^7F or ^5L, but others are shared between several terms with the same L and S quantum numbers, but different seniority numbers like $^5D(1,2,3)$ or $^5G(1,2,3)$, which are used to indicate that these are coming from different parent terms of $4f^5$. The small deviations from LS coupling are due to the SO interaction, for example, a small ^5D component in the ^7F levels. The terms coupled by SO are such that $\Delta L = 0, \pm 1$ and $\Delta S = 0, \pm 1$.

Finally, Table 3.8 contains the energy value and eigenvector of the manifolds with $S = 2$ and 3, calculated by setting to 0 the spin-orbit parameter ζ_f of Table 3.9. This information is necessary to build our extension theory, see Eq. (4.16). Note that the first excited manifold is a superposition of $^5D3$, $^5D1$ and $^5D2$ terms. But due to its strong importance in Eu^{3+} spectroscopic studies, it will be denoted ^5D in the rest of

Table 3.9: Scaling factors (SFs) of *ab initio* parameters (see text), values of $E_{\rm av}$ and fitted effective parameters $X_{\rm fit}$ (in $\rm cm^{-1}$) for two lowest configurations of Nd^{3+}, Er^{3+} and Eu^{3+}, as well as all the fitted parameters for Eu^{3+}. Here, for brevity, we use $F^k(fd)$ as $F^k(4f, 5d)$, ζ_f as ζ_{4f} and ζ_d as ζ_{5d}.

Param. name	$4f^w$				$4f^{w-1}5d$			
	SF(Nd^{3+})	SF(Er^{3+})	SF(Eu^{3+})	value (Eu^{3+})	SF(Nd^{3+})	SF(Er^{3+})	SF(Eu^{3+})	value (Eu^{3+})
$E_{\rm av}$	24898.0	35577.1		65609.0	88430.0	133432.5		137500.0
$F^2(ff)$	0.738	0.754	0.781	88732.0	0.759	0.756	0.758	91269.9
$F^4(ff)$	0.825	0.919	0.950	67778.0	0.909	0.988	0.949	72029.8
$F^6(ff)$	0.773	0.898	0.800	41060.7	0.870	0.798	0.834	45638.6
α	19.1	-0.2		22.6	22.6	32.4		22.6
β	-558.5	-204.7		-605.0	-605.0	-668.4		-605.0
γ	1690.5	55.8		292.2	292.2	1409.8		292.2
ζ_f	0.930	0.979	0.928	1313.6	0.947	0.995	0.971	1481.1
ζ_d					0.972	0.916	0.945	1290.0
$F^1(fd)$					1025.3	1370.6		0
$F^2(fd)$					0.726	0.776	0.751	23046.8
$F^3(fd)$					111.5	2330.4		0
$F^4(fd)$					1.128	1.124	1.126	16815.7
$G^1(fd)$					0.762	0.653	0.707	9113.2
$G^2(fd)$					2199	411.1		0
$G^3(fd)$					1.005	0.838	0.922	10103.2
$G^4(fd)$					2016.0	0		0
$G^5(fd)$					0.874	0.680	0.778	6603.8

this research work.

However, as stated before, no experimental level has been reported for the $4f^5 5d$ configuration, but the $4f^w$ configurations (with $2 \leq n \leq 12$) and the $4f^{w-1}5d$ ones (with $3 \leq n \leq 13$) possess the same energy parameters for the elements of lanthanide series. In order to overcome this obstacle we use the calculation done on Nd^{3+} and Er^{3+}. For these two ions we calculate the so-called scaling factors, which are the ratios between final and HFR value of parameters and are given in Table 3.9. Then, for Eu^{3+} we multiply the obtained scaling factors by the HFR parameters for Eu^{3+} to compute the energies of $4f^5$ 5d, which will be described later in this section.

The parameters necessary for the calculations are given in Table 3.9. Table 3.9 shows a comparison of the final SFs (for *ab initio* parameters) or the fitted values (for effective parameters), for the two lowest configurations of the above mentioned ions. It also shows the parameter values used in the Eu^{3+} spectrum calculations. In the $4f^w$ configurations, the least-square fitting calculations, performed for each element, illustrates the regularities of SFs for F^k and ζ_f parameters. Regarding effective parameters, the negative values of β are usual, while the small values of α and γ of Er^{3+} are not. The regularities are also visible between $4f^2 5d$ and $4f^{10}5d$ configurations of Nd^{3+} and Er^{3+} respectively. Therefore, we calculate our Eu^{3+} parameters by multiplying the HFR values by the average SF obtained for Nd^{3+} and Er^{3+}. The effective parameters are those obtained for Nd^{3+}, and the center-of-gravity energy of $4f^5 5d$ is calculated by assuming that the difference $E_{\rm av}(4f^{w-1}5d) - E_{\rm av}(4f^w)$ increases linearly with w.

Table 3.10: First 20 energy levels for $4f^5 5d$ configuration of Eu^{3+} with total angular momentum $J = 0$, 1 and 2, as well as first three eigenvectors with their percentages. As an example, $(^6\mathrm{H})\,^7\mathrm{H}$ is used for brevity for $4f^5(^6\mathrm{H}^o)5d\,^7\mathrm{H}^o$, where the superscript "o" indicates odd parity. All energy values are in cm^{-1}.

Energy	J	First three eigenvectors and percentages					
78744	2	$(^6\mathrm{H})\,^7\mathrm{H}$	57.6 %	$(^6\mathrm{H})\,^5\mathrm{G}$	14.1 %	$(^6\mathrm{F})\,^7\mathrm{H}$	14.0 %
79541	1	$(^6\mathrm{H})\,^5\mathrm{F}$	52.9 %	$(^6\mathrm{H})\,^7\mathrm{G}$	20.7 %	$(^6\mathrm{H})\,^7\mathrm{F}$	10.1 %
80396	2	$(^6\mathrm{H})\,^5\mathrm{F}$	41.2 %	$(^6\mathrm{H})\,^7\mathrm{F}$	23.7 %	$(^6\mathrm{H})\,^7\mathrm{G}$	12.0 %
81171	0	$(^6\mathrm{H})\,^7\mathrm{F}$	91.5 %	$(^4\mathrm{G})\,^5\mathrm{D}$	3.1 %	$(^4\mathrm{G})\,^5\mathrm{D}$	2.0 %
81493	1	$(^6\mathrm{H})\,^7\mathrm{F}$	65.0 %	$(^6\mathrm{H})\,^7\mathrm{G}$	23.1 %	$(^6\mathrm{F})\,^7\mathrm{G}$	4.3 %
82105	2	$(^6\mathrm{H})\,^7\mathrm{G}$	48.6 %	$(^6\mathrm{H})\,^7\mathrm{F}$	34.1 %	$(^6\mathrm{F})\,^7\mathrm{G}$	9.5 %
83096	1	$(^6\mathrm{H})\,^7\mathrm{G}$	32.1 %	$(^6\mathrm{H})\,^5\mathrm{F}$	26.6 %	$(^6\mathrm{H})\,^7\mathrm{F}$	17.4 %
83849	2	$(^6\mathrm{H})\,^7\mathrm{F}$	31.6 %	$(^6\mathrm{H})\,^5\mathrm{F}$	18.1 %	$(^6\mathrm{H})\,^5\mathrm{G}$	14.7 %
84398	1	$(^6\mathrm{F})\,^7\mathrm{G}$	73.0 %	$(^6\mathrm{H})\,^7\mathrm{G}$	18.5 %	$(^6\mathrm{F})\,^5\mathrm{F}$	3.9 %
84785	2	$(^6\mathrm{F})\,^7\mathrm{G}$	75.1 %	$(^6\mathrm{H})\,^7\mathrm{G}$	14.8 %	$(^6\mathrm{F})\,^5\mathrm{F}$	2.4 %
85060	2	$(^6\mathrm{F})\,^7\mathrm{H}$	47.4 %	$(^6\mathrm{H})\,^5\mathrm{G}$	18.3 %	$(^6\mathrm{H})\,^5\mathrm{F}$	10.9 %
86736	0	$(^6\mathrm{F})\,^7\mathrm{F}$	81.5 %	$(^6\mathrm{F})\,^5\mathrm{D}$	7.4 %	$(^6\mathrm{H})\,^7\mathrm{F}$	2.6 %
87056	1	$(^6\mathrm{F})\,^7\mathrm{F}$	82.2 %	$(^6\mathrm{F})\,^5\mathrm{D}$	6.7 %	$(^6\mathrm{H})\,^7\mathrm{F}$	2.4 %
87134	2	$(^6\mathrm{H})\,^5\mathrm{G}$	37.2 %	$(^6\mathrm{H})\,^7\mathrm{H}$	28.1 %	$(^6\mathrm{F})\,^7\mathrm{H}$	18.1 %
87679	2	$(^6\mathrm{F})\,^7\mathrm{F}$	80.9 %	$(^6\mathrm{F})\,^5\mathrm{D}$	5.9 %	$(^6\mathrm{P})\,^7\mathrm{F}$	2.2 %
89165	1	$(^6\mathrm{F})\,^7\mathrm{D}$	84.2 %	$(^6\mathrm{F})\,^5\mathrm{P}$	7.8 %	$(^4\mathrm{F})\,^5\mathrm{P}$	1.8 %
89220	2	$(^6\mathrm{F})\,^7\mathrm{P}$	78.1 %	$(^6\mathrm{F})\,^7\mathrm{D}$	6.0 %	$(^6\mathrm{F})\,^5\mathrm{P}$	5.0 %
90024	2	$(^6\mathrm{F})\,^7\mathrm{D}$	81.8 %	$(^6\mathrm{F})\,^7\mathrm{P}$	7.6 %	$(^6\mathrm{F})\,^5\mathrm{P}$	2.0 %
91979	0	$(^6\mathrm{F})\,^5\mathrm{D}$	61.5 %	$(^6\mathrm{F})\,^7\mathrm{F}$	7.9 %	$(^6\mathrm{P})\,^5\mathrm{D}$	5.9 %
93243	2	$(^6\mathrm{F})\,^5\mathrm{D}$	47.0 %	$(^6\mathrm{F})\,^5\mathrm{G}$	16.9 %	$(^6\mathrm{F})\,^5\mathrm{F}$	5.6 %

The $4f^5 5d$ configuration contains 1878 levels with J-values from 0 to 14, and according to our calculations, with energies from 74438 to 243060 cm^{-1}. The dominant eigenvector of the 74438-cm^{-1} level is $4f^5(^6\mathrm{H}^o)\,5d(^7\mathrm{K}^o_4)$ with 93.8 %. As examples, Table 3.10 shows the 20 lowest energy levels with $J = 0$, 1 and 2, along with their three dominant eigenvectors.

Table 3.10 shows that the levels of the $4f^5 5d$ configuration do not possess a strongly dominant eigenvector (or a group of eigenvectors) characterized by the same L and S quantum numbers. This means that, unlike the ground configuration, see Table 3.7, the LS coupling scheme is not appropriate for the excited configuration. It can be shown that the jj coupling scheme is not appropriate neither, because the spin-orbit energy of the $5d$ electron is of the same order of magnitude as the electrostatic energy between $4f$ and $5d$ electrons. The eigenvectors are therefore written in pair coupling, *i.e.* linear combination of LS-coupling states.

In a given energy level, the $\overline{L}$ and $\overline{S}$ quantum numbers, which characterize the parent term of the $4f^5$ subshell, are common to the majority of the eigenvectors. With increasing energy, the levels mainly possess $^6\mathrm{H}^o$, $^6\mathrm{F}^o$ and $^6\mathrm{P}^o$ characters; then come the

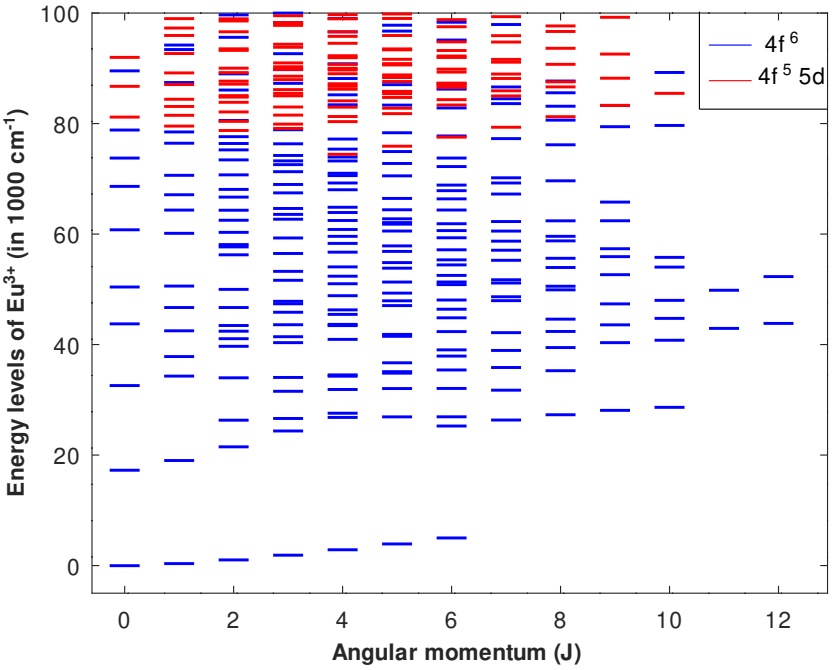

Figure 3.4: Calculated energy levels of the $4f^6$ (blue) and $4f^5 5d$ (red) configurations of Eu^{3+} as functions of the electronic angular momentum J. The plot is restricted to energy values between 0 and 100000 cm^{-1}.

quartet and doublet parent terms. Indeed the SO interaction within the $4f^5$ subshell is too small to significantly mix different $\overline{L}$ and $\overline{S}$ of the $4f^5$ subshell. By contrast, the total L and S quantum numbers of the LS states differ at most by one unity. For example, we notice the pairs ^{7}H-^{5}G ($\Delta S = 1$ and $\Delta L = 1$), ^{7}G-^{7}F ($\Delta S = 0$ and $\Delta L = 1$) and ^{5}F-^{7}F ($\Delta S = 1$ and $\Delta L = 0$) for the level at 78744, 79541 and 80396 cm^{-1} respectively. In consequence, the mixing between quintet and septet states of Eu^{3+} is mainly due to the SO interaction of the $5d$ electron. That is why we ignore the influence of the $4f$ electrons to account for the Wybourne-Downer mechanism (see Subsection 4.1.2 and Eq. (A.8)).

The resulting spectrum of Eu^{3+} is presented on Fig. 3.4, where the diagram is limited to 100000 cm^{-1}. We have done radial matrix elements calculation for Eu^{3+} too. As for Nd^{3+} and Er^{3+}, we have calculated those integrals with a the Octave code. We obtain 1.130629 a_0, -3.221348 a_0^3 and 21.727152 a_0^5 for $k = 1$, $k = 3$ and $k = 5$, respectively, while the $k = 1$ value calculated by Cowan is 1.130618 a_0. Figure 3.5 shows the wavefunctions for 4f subshell in the $4f^6$ configuration and for 5d subshell of $4f^5 5d$ configuration. We can see from figure 3.5 that 4f is located very close to the nuclei, but the 5d is a little bit further from it.

We have also calculated the reduced matrix elements of the so-called doubly reduced unit tensor operators of rank k of Eu^{3+}, $[U^{(k)}]^2$, which appear in the standard JO theory and are independent of the crystal host. This allows us to test the quality of our free-ion calculation. In this respect, Table 3.11 shows a very good agreement between our

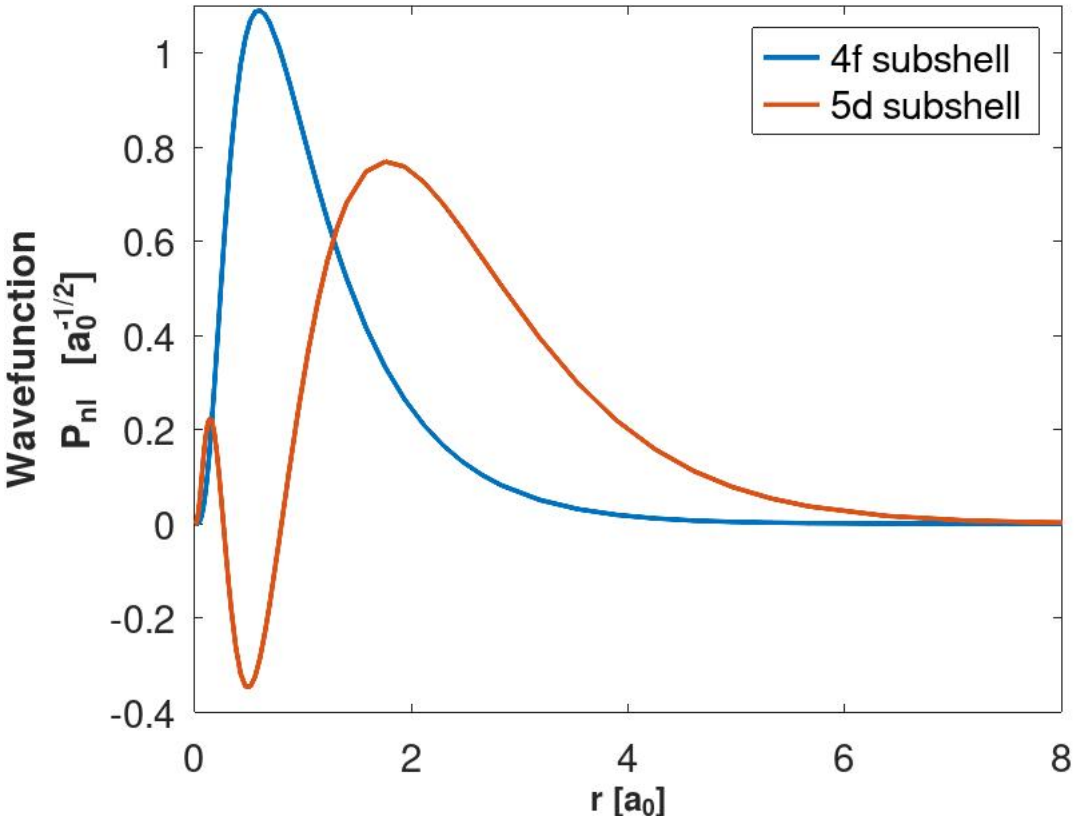

Figure 3.5: Wavefunction as a function of distance from the nucleus for the 4f subshell of $4f^6$ configuration (in blue) and for the 5d subshell of $4f^5 5d$ configuration (in red).

values and those from the seminal article of Carnall [62]. The transitions present in the table are those used in the fitting procedure with the data from Babu *et al.* [69], which will be described in the next chapter.

In conclusion, this chapter was dedicated to spectroscopic calculations. In the first section the methodology was described and the next sections was used to discuss the calculation results on three trivalent lanthanides: Eu^{3+}, Nd^{3+} and Er^{3+}. For all the elements, the standard deviation, that indicates the precision of calculated energy levels, is smaller than 100 cm^{-1}. The comparison between computed and experimental results are very good. Our calculations illustrates that the ground-configuration levels are well described by the LS coupling scheme, which is less the case for the excited configurations.

Table 3.11: Values of the reduced matrix elements of the squared unit-tensor operator $[U^{(\lambda)}]^2$ (from the present work) for the transitions of Eu^{3+} present in Ref. [69], compared with the values reported in Ref. [62] (Rep.).

Transition	$[U^{(2)}]^2$		$[U^{(4)}]^2$		$[U^{(6)}]^2$	
	Our	Rep.	Our	Rep.	Our	Rep.
$^7F_1 \leftrightarrow {}^7F_6$	0	0	0	0	0.3772	0.3773
$^7F_0 \leftrightarrow {}^7F_6$	0	0	0	0	0.1449	0.1450
$^7F_1 \leftrightarrow {}^5D_1$	0.0026	0.0026	0	0	0	0
$^7F_0 \leftrightarrow {}^5D_2$	0.0008	0.0008	0	0	0	0
$^7F_1 \leftrightarrow {}^5D_3$	0.0004	0.0004	0.0013	0.0012	0	0
$^7F_1 \leftrightarrow {}^5L_6$	0	0	0	0	0.0096	0.0090
$^7F_0 \leftrightarrow {}^5L_6$	0	0	0	0	0.0147	0.0155
$^7F_0 \leftrightarrow {}^5G_2$	0.0006	0.0006	0	0	0	0
$^7F_0 \leftrightarrow {}^5D_4$	0	0	0.0013	0.0011	0	0

Chapter 4

Extension of Judd-Ofelt theory

The Judd-Ofelt (JO) theory has been successfully applied since almost 60 years, to interpret the intensities of absorption and emission lines of crystals and glasses doped with trivalent lanthanide ions (Ln^{3+}). Despite its remarkable efficiency, this standard JO theory cannot reproduce some of the observed transitions.

An example of demanding ions for JO theory are the praseodymium ions, for which there are very often divergence between calculations and experimental observations. Moreover sometimes negative values are obtained for Ω_λ values.

	S	L	J (No $0 \leftrightarrow 0$)	Parity
Electric Dipole	$\Delta S = 0$	$\Delta L \leq 6$	$\Delta J \leq 6$ $\Delta J = 2, 4, 6$ (J or J' = 0)	opposite
Magnetic Dipole	$\Delta S = 0$	$\Delta L = 0$	$\Delta J = 0, \pm 1$	same
Electric Quadrupole	$\Delta S = 0$	$\Delta L = 0, \pm 1, \pm 2$	$\Delta J = 0, \pm 1, \pm 2$	same

Table 4.1: Selection rules in the standard Judd-Ofelt theory [29].

Europium is a very well known example to challenge the JO theory, too. In particular ${}^7F_0 \leftrightarrow {}^5D_{J_{odd}}$, ${}^7F_{J_{odd}} \leftrightarrow {}^5D_0$ and ${}^7F_0 \leftrightarrow {}^5D_0$ are forbidden transitions because of the selection rules shown in table 4.1. Although some of these transitions are of magnetic nature, in some materials they do appear as electric dipole transitions, but with low intensity. These transitions invoke the necessity for possible extension of JO theory. Many extensions of the original model have been proposed to overcome this drawback [35], including *e.g.* J-mixing [36–38], the Wybourne-Downer mechanism [39, 40], velocity-gauge expression of the electric-dipole (ED) operator [41], relativistic or configuration-interaction (CI) effects [30, 42–45], purely *ab initio* intensity calculations [46]. In this respect, Smentek and coworkers were able to reproduce experimental absorption oscillator strengths with a very high accuracy, with up to 17 adjustable parameters [47]. But in spite of all these improvements, even the most recent experimental studies use the standard version of the JO theory [48, 49].

In this chapter we present a modified version of the JO theory in which the properties of the free Ln^{3+} ions, *i.e.* energies and transition integrals, are computed using a

combination of *ab initio* and least-square fitting procedures available in Cowan's suite of codes [24, 57] described in section 3.1. This allows us to relax some of the strong assumptions of the JO theory. The line strengths appear as linear combinations of three adjustable parameters which are only functions of the crystal-field potential, giving access to the local environment around the ion. We have modeled the extension in two steps. In the first version of the extension, described in section 4.1, the spin-orbit interaction of the ion is treated using perturbation theory, both in the ground and in the first excited configurations. In section 4.2 we describe the second version of the extension, where the spin-orbit interaction is fully taken into account in the ground configuration. We include all the eigenvector components of a given level, while in the previous version only the four leading ones were included. We also account for the wavelength dependence of the host material refractive index, using the modified Sellmeier equation. We test the validity of the two models on three trivalent lanthanides: neodymium (section 4.3.2), erbium (section 4.3.3) and europium (section 4.1.3 and 4.3.1).

4.1 First extension of JO theory

The aim of the present section is to derive analytical expressions for the electric-dipole (ED) line strengths, which enable to characterize absorption and emission intensities of Ln^{3+}-doped solids. Unlike the magnetic-dipole (MD) and electric-quadrupole (EQ) transitions [28], the ED ones are activated by the presence of the host material, which relaxes the free-space selection rules. We use similar hypotheses as in the original JO model [31, 32]: the crystal-field (CF) potential slightly admixes the levels of the ground configuration [Xe]$4f^w$ and those of the first excited configuration [Xe]$4f^{w-1}5d$, where [Xe] denotes the ground configuration of xenon, dropped in the rest of the work. In the resulting perturbative expression of the ED line strength, we assume that all the levels of the excited configuration have the same energy. However, we relax some of the original hypothesis, by accounting for the energies of the ground-configuration levels, and by applying the closure relation less strictly. Unlike the standard and most common extensions of the JO model, we do not introduce effective operators, like the so-called unit-tensor operator $U^{(k)}$ [24], but rather work on the matrix elements of the CF or ED operators. To calculate the line strength, we firstly use the second-order perturbation theory (see subsection 4.1.1) and then the third-order perturbation theory (see subsection 4.1.2), for which the free-ion spin-orbit operator is within the perturbation.

The common starting point of those two calculations is the multipolar expansion of the crystal-field potential,

$$V_{\mathrm{CF}} = \sum_{kq} A_{kq} \sum_{j=1}^{N} r_j^k C_q^{(k)}(\theta_j, \phi_j) \equiv \sum_{kq} A_{kq} P_q^{(k)} \tag{4.1}$$

where k is a non-negative integer and $q = -k,\ -k+1,\ ...,\ +k$, (r_j, θ_j, ϕ_j) are the spherical coordinates of the j-th ($j = 1$ to N) electron in the referential frame centered on the nucleus of the Ln^{3+} ion, and $C_q^{(k)}$ are the Racah spherical harmonics of

rank k and component q, related to the usual spherical harmonics by $C_q^{(k)}(\theta_j, \phi_j) = \sqrt{4\pi/(2k+1)} \times Y_{kq}(\theta_j, \phi_j)$, see for example Chap. 5 of Ref. [27]. In Eq. (4.1), the quantities $P_q^{(k)}$ represent the electric multipole moment as defined in Chaps. 14 and 15 of Ref. [24]. The simplest way of calculating the CF parameters A_{kq} is to assume that they are due to distributed charges inside the host material. More elaborate models can be used, like distributed dipoles resulting in the so-called dynamical coupling [35], or the vibration of the ion center-of-mass. This would affect the physical origin of the A_{kq} coefficients, but not the validity of the forthcoming results [31].

4.1.1 Second-order correction

In the theory of light-matter interaction, the ED approximation arises at the first order of perturbation theory. Furthermore, the f-f transitions in Ln^{3+}-doped solids are only possible if the free-ion levels are perturbed by the CF potential. Therefore, using the first-order correction on the ion levels to calculate the matrix element of the ED operator gives in total a second-order correction.

We call $|\Psi_i\rangle$ the eigenvectors associated with the ion+crystal system (without electromagnetic field). In the framework of perturbation theory, we express them as $|\Psi_i\rangle = \sum_m |\Psi_i^m\rangle$, where m denotes the order of the perturbative expansion. In this subsection, we consider that the 0-th, *i.e.* unperturbed, eigenvectors $|\Psi_i^0\rangle$ are the free-ion levels. Those belonging to the ground configuration $n\ell^w$ (with $n\ell = 4f$ for Ln^{3+} ions) are written in intermediate coupling scheme [24]

$$|\Psi_i^0\rangle = \sum_{\alpha_i L_i S_i} c_{\alpha_i L_i S_i} \, |n\ell^w \, \alpha_i L_i S_i J_i M_i\rangle \tag{4.2}$$

where L_i, S_i and J_i are the quantum numbers associated with the orbital, spin and total electronic angular momentum respectively, while M_i is associated with the z-projection of the latter. The free-ion levels of energy $E_i^0 \equiv E_i$ are degenerate in M_i. Finally in Eq. (4.2), α is a generic notation containing additional information like the seniority number [24]. In the $4f^w$ configuration of Ln^{3+} ions, the energy levels are usually well described in the LS coupling scheme (see Table 3.7).

In the first excited configuration $n\ell^{w-1}n'\ell'$, with $(n\ell, n'\ell') = (4f, 5d)$ for Ln^{3+} ions, we consider free-ion levels in pure LS coupling,

$$|\Psi_t^0\rangle = |n\ell^{w-1}\overline{\alpha}\overline{LS},\, n'\ell' L' S' J' M'\rangle, \tag{4.3}$$

where the overlined quantum numbers characterize the $n\ell^{w-1}$ subshell alone. As Table 3.10 shows, the LS coupling is not appropriate for the energy levels of the excited configuration. But since, in our ED matrix element calculation, we will assume that all the levels of the excited configuration have the same energy, the choice of coupling scheme is arbitrary, and so we take the simplest one.

Now we express the ED transition amplitude D_{12} between eigenvectors $|\Psi_i^0\rangle + |\Psi_i^1\rangle$

$(i = 1, 2)$, perturbed by the CF potential up to the first order,

$$\begin{aligned} D_{12} &= \left\langle \Psi_1^1 \right| P_p^{(1)} \left| \Psi_2^0 \right\rangle + \left\langle \Psi_1^0 \right| P_p^{(1)} \left| \Psi_2^1 \right\rangle \\ &= \sum_t \left[\frac{\langle \Psi_1^0 | V_{\mathrm{CF}} | \Psi_t^0 \rangle}{E_1 - E_t} \left\langle \Psi_t^0 \right| P_p^{(1)} \left| \Psi_2^0 \right\rangle \right. \\ &\quad \left. + \left\langle \Psi_1^0 \right| P_p^{(1)} \left| \Psi_t^0 \right\rangle \frac{\langle \Psi_t^0 | V_{\mathrm{CF}} | \Psi_2^0 \rangle}{E_2 - E_t} \right], \end{aligned} \tag{4.4}$$

where the index $p = 0$ denotes π light polarization, and $p = \pm 1$ denote $\sigma^{\pm}$ polarizations. We recall that $\langle \Psi_1^0 | P_p^{(1)} | \Psi_2^0 \rangle = 0$, because in free space, there is no ED transition between levels of the same electronic configuration. In what follows, we assume that all the energies of the excited configuration are equal, $E_t \approx E_{n'\ell'}$ (see subsection 4.1.3 for the choice of $E_{n'\ell'}$). Rather than the center-of-gravity energy of the excited configuration, E_t can be regarded as the mean energy for which the coupling with both levels 1 and 2 is significant.

Equation (4.4) contains matrix elements of $P_p^{(1)}$ and V_{CF}, itself function of $P_q^{(k)}$ as Eq. (4.1) shows. Being irreducible tensor operators, the matrix elements of $P_q^{(k)}$ satisfy the Wigner-Eckart theorem [27]

$$\left\langle \Psi_i^0 \right| P_q^{(k)} \left| \Psi_t^0 \right\rangle = \frac{C^{J_i M_i}_{J' M' k q}}{\sqrt{2J_i + 1}} \left\langle \Psi_i^0 \left\| P^{(k)} \right\| \Psi_t^0 \right\rangle \tag{4.5}$$

where $C^{J_i M_i}_{J' M' k q} = \langle J' M' k q | J' k J_i M_i \rangle$ is a Clebsch-Gordan (CG) coefficient, and $\langle \Psi_i^0 \| P^{(k)} \| \Psi_t^0 \rangle$ the reduced matrix element given in Eq. (A.6), which is independent from M_i, M' and q.

By contrast, the products of the kind $\langle \Psi_i^0 | P_q^{(k)} | \Psi_t^0 \rangle \times \langle \Psi_t^0 | P_p^{(1)} | \Psi_2^0 \rangle$ are not irreducible tensors; still we overcome this problem by expanding the product of two CG coefficients given in [27], which yields

$$\begin{aligned} \left\langle \Psi_1^0 \right| P_q^{(k)} \left| \Psi_t^0 \right\rangle \left\langle \Psi_t^0 \right| P_p^{(1)} \left| \Psi_2^0 \right\rangle &= \sum_{\lambda \mu} (-1)^{J_1 + J_2 - \lambda} \sqrt{\frac{2\lambda + 1}{2J_1 + 1}} C^{\lambda \mu}_{kq1p} C^{J_1 M_1}_{J_2 M_2 \lambda \mu} \\ &\quad \times \left\{ \begin{array}{ccc} k & 1 & \lambda \\ J_2 & J_1 & J' \end{array} \right\} \left\langle \Psi_1^0 \left\| P^{(k)} \right\| \Psi_t^0 \right\rangle \left\langle \Psi_t^0 \left\| P^{(1)} \right\| \Psi_2^0 \right\rangle \end{aligned} \tag{4.6}$$

where the quantity between curly brackets is a Wigner 6-j symbol. Equation (4.6) is interesting because the only dependence on quantum numbers M_i is in the CG coefficient $C^{J_1 M_1}_{J_2 M_2 \lambda \mu}$, while M' is absent. The equation appears as a sum of irreducible tensors of rank λ and component μ coupling directly $|\Psi_1^0\rangle$ and $|\Psi_2^0\rangle$. The selection rules governing this coupling are $\Delta J = |J_2 - J_1| \leq \lambda \leq J_1 + J_2$ and $M_1 = M_2 + \mu$. Moreover, the triangle rule associated with $C^{\lambda \mu}_{kq1p}$ imposes $\lambda = k$, $k \pm 1$, $\mu = p + q$ and $-\lambda \leq \mu \leq +\lambda$.

Applying the same reasoning for the third line of Eq. (4.4), we obtain the same result as Eq. (4.6) except the permutations of the couples of indexes (k, q) and $(1, p)$.

Using the symmetry relation of CG coefficients $C^{\lambda\mu}_{1pkq} = (-1)^{1+k-\lambda} C^{\lambda\mu}_{kq1p}$, we get to the final expression for the transition amplitude

$$D_{12} = \sum_{\alpha_1 L_1 S_1} c_{\alpha_1 L_1 S_1} \sum_{\alpha_2 L_2 S_2} c_{\alpha_2 L_2 S_2} \sum_{kq} A_{kq} \sum_{\lambda\mu} (-1)^{J_1+J_2-\lambda} \sqrt{\frac{2\lambda+1}{2J_1+1}} C^{\lambda\mu}_{kq1p} C^{J_1 M_1}_{J_2 M_2 \lambda\mu} \times \sum_{J'} \left(\left\{ \begin{array}{ccc} k & 1 & \lambda \\ J_2 & J_1 & J' \end{array} \right\} \mathcal{D}^{(k1)}_{12,J'} + (-1)^{1+k-\lambda} \left\{ \begin{array}{ccc} 1 & k & \lambda \\ J_2 & J_1 & J' \end{array} \right\} \mathcal{D}^{(1k)}_{12,J'} \right), \tag{4.7}$$

where we have introduced the quantities

$$\mathcal{D}^{(k1)}_{12,J'} = \frac{1}{E_1 - E_{n'\ell'}} \times \sum_{\overline{\alpha}\overline{LS},\, L'S'J'} \left\langle n\ell^w\, \alpha_1 L_1 S_1 J_1 \left\| P^{(k)} \right\| \overline{\alpha}\overline{LS},\, L'S'J' \right\rangle \left\langle \overline{\alpha}\overline{LS},\, L'S'J' \left\| P^{(1)} \right\| n\ell^w\, \alpha_2 L_2 S_2 J_2 \right\rangle \tag{4.8}$$

$$\mathcal{D}^{(1k)}_{12,J'} = \frac{1}{E_2 - E_{n'\ell'}} \times \sum_{\overline{\alpha}\overline{LS},\, L'S'J'} \left\langle n\ell^w\, \alpha_1 L_1 S_1 J_1 \left\| P^{(1)} \right\| \overline{\alpha}\overline{LS},\, L'S'J' \right\rangle \left\langle \overline{\alpha}\overline{LS},\, L'S'J' \left\| P^{(k)} \right\| n\ell^w\, \alpha_2 L_2 S_2 J_2 \right\rangle \tag{4.9}$$

in which $|\overline{\alpha}\overline{LS},\, L'S'J'\rangle$ is a condensed representation of $|\Psi^0_t\rangle$, see Eq. (4.3). The superscripts $(k1)$ and $(1k)$ correspond to the order in which the tensor operators $P^{(k)}$ and $P^{(1)}$ are written.

For eigenvectors $|\Psi^0_{1,2}\rangle$ belonging to the ground configuration and $|\Psi^0_t\rangle$ belonging to the first excited configuration, the 3-j symbol of Eq. (A.6) imposes that the CF potential matrix elements are non-zero for $k = 1$, 3 and 5, which, according to Eq. (4.6), imposes $\lambda = 0$, 1, ..., 6. By contrast, in the standard version of the JO theory, $\lambda = k + 1 = 2$, 4 and 6. The $\lambda = 0$ contribution in Eq. (4.6) comes from the dipolar term $k = 1$ of the CF potential; it is the only non-zero contribution when $J_1 = J_2 = 0$, for instance the $^5\mathrm{D}_0 \leftrightarrow {}^7\mathrm{F}_0$ transition in Eu^{3+}. Our odd-λ contributions are responsible for the transitions like $^5\mathrm{D}_0 \leftrightarrow {}^7\mathrm{F}_{3,5}$ and $^5\mathrm{D}_3 \leftrightarrow {}^7\mathrm{F}_0$; they arise because we consider distinct energies for levels 1 and 2, $E_1 \neq E_2$, unlike the standard JO theory. But since the energy difference $|E_2 - E_1|$ is significantly smaller (although not negligible) compared to $E_{n'\ell'} - E_{1,2}$, those transitions are weak. Finally, since the operators $P^{(k)}$ do not couple different spin states, the spin-changing transitions are only due to the mixing of different spin states within the ground-configuration levels $|\Psi^0_{1,2}\rangle$, see Eq. (4.2). In other words, Eq. (4.7) does not account for the so-called Downer-Wybourne mechanism [39].

At present, we calculate the ED line strength $\mathcal{S}_{\mathrm{ED}} = \sum_{pM_1M_2} (D_{12})^2$. Expressing Eq. (4.7) twice gives many sums: in particular on p, M_1, M_2, k, q, μ and J', but also k', q', μ' and J'' (coming from the second expansion of D_{12}). Focusing on the sum

involving CG coefficients, we have

$$\sum_{pqq'\mu\mu'} C^{\lambda\mu}_{kq1p} C^{\lambda'\mu'}_{k'q'1p} \sum_{M_1 M_2} \frac{C^{J_1 M_1}_{J_2 M_2 \lambda\mu} C^{J_1 M_1}_{J_2 M_2 \lambda'\mu'}}{2J_1+1} = \sum_{pqq'\mu\mu'} C^{\lambda\mu}_{kq1p} C^{\lambda'\mu'}_{k'q'1p} \frac{\delta_{\lambda\lambda'}\delta_{\mu\mu'}}{2\lambda+1}$$
$$= \frac{\delta_{\lambda\lambda'}}{2\lambda+1} \sum_{pqq'\mu} C^{\lambda\mu}_{kq1p} C^{\lambda\mu}_{k'q'1p} = \frac{\delta_{\lambda\lambda'}\delta_{kk'}\delta_{qq'}}{2k+1}\,, \tag{4.10}$$

where the Kronecker symbols come from the orthonormalization relation of CG coefficients. Plugging Eq. (4.10) into the line strength gives

$$\begin{aligned}\mathcal{S}_{\mathrm{ED}} = & \sum_{\alpha_{1a}L_{1a}S_{1a}} c_{\alpha_{1a}L_{1a}S_{1a}} \sum_{\alpha_{2a}L_{2a}S_{2a}} c_{\alpha_{2a}L_{2a}S_{2a}} \sum_{\alpha_{1b}L_{1b}S_{1b}} c_{\alpha_{1b}L_{1b}S_{1b}} \sum_{\alpha_{2b}L_{2b}S_{2b}} c_{\alpha_{2b}L_{2b}S_{2b}} \sum_{kq} \frac{|A_{kq}|^2}{2k+1} \\ & \times \sum_{\lambda} (2\lambda+1) \sum_{J'} \left(\left\{ \begin{array}{ccc} k & 1 & \lambda \\ J_2 & J_1 & J' \end{array} \right\} \mathcal{D}^{(k1)}_{1a,2a,J'} + (-1)^{1+k-\lambda} \left\{ \begin{array}{ccc} 1 & k & \lambda \\ J_2 & J_1 & J' \end{array} \right\} \mathcal{D}^{(1k)}_{1a,2a,J'} \right) \\ & \times \sum_{J''} \left(\left\{ \begin{array}{ccc} k & 1 & \lambda \\ J_2 & J_1 & J'' \end{array} \right\} \mathcal{D}^{(k1)}_{1b,2b,J''} + (-1)^{1+k-\lambda} \left\{ \begin{array}{ccc} 1 & k & \lambda \\ J_2 & J_1 & J'' \end{array} \right\} \mathcal{D}^{(1k)}_{1b,2b,J''} \right). \end{aligned} \tag{4.11}$$

When expanded, the last two lines contain four terms: two of the kind

$$\sum_{\lambda} (2\lambda+1) \left\{ \begin{array}{ccc} k_1 & k_2 & \lambda \\ J_2 & J_1 & J' \end{array} \right\} \left\{ \begin{array}{ccc} k_1 & k_2 & \lambda \\ J_2 & J_1 & J'' \end{array} \right\} \mathcal{D}^{(k_1k_2)}_{1a,2a,J'} \mathcal{D}^{(k_1k_2)}_{1b,2b,J''} = \frac{\delta_{J'J''}}{2J'+1} \mathcal{D}^{(k_1k_2)}_{1a,2a,J'} \mathcal{D}^{(k_1k_2)}_{1b,2b,J'} \tag{4.12}$$

where the sum on λ is actually the orthonormalization relation of 6-j symbols; and two terms of the kind

$$\begin{aligned} & \sum_{\lambda} (-1)^{k_1+k_2-\lambda} (2\lambda+1) \left\{ \begin{array}{ccc} k_1 & k_2 & \lambda \\ J_2 & J_1 & J' \end{array} \right\} \left\{ \begin{array}{ccc} k_2 & k_1 & \lambda \\ J_2 & J_1 & J'' \end{array} \right\} \mathcal{D}^{(k_1k_2)}_{1a,2a,J'} \mathcal{D}^{(k_2k_1)}_{1b,2b,J''} \\ & = (-1)^{k_1+k_2+J'+J''} \left\{ \begin{array}{ccc} k_1 & J_1 & J' \\ k_2 & J_2 & J'' \end{array} \right\} \mathcal{D}^{(k_1k_2)}_{1a,2a,J'} \mathcal{D}^{(k_2k_1)}_{1b,2b,J''} \end{aligned} \tag{4.13}$$

where we use some properties of 6-j symbols (see Ref. [27], p. 305). The final expression of the line strength is

$$\begin{aligned}\mathcal{S}_{\mathrm{ED}} = & \sum_{\alpha_{1a}L_{1a}S_{1a}} c_{\alpha_{1a}L_{1a}S_{1a}} \sum_{\alpha_{2a}L_{2a}S_{2a}} c_{\alpha_{2a}L_{2a}S_{2a}} \sum_{\alpha_{1b}L_{1b}S_{1b}} c_{\alpha_{1b}L_{1b}S_{1b}} \sum_{\alpha_{2b}L_{2b}S_{2b}} c_{\alpha_{2b}L_{2b}S_{2b}} \sum_{kq} \frac{|A_{kq}|^2}{2k+1} \\ & \times \sum_{J'} \left[\frac{\mathcal{D}^{(k1)}_{1a,2a,J'} \mathcal{D}^{(k1)}_{1b,2b,J'} + \mathcal{D}^{(1k)}_{1a,2a,J'} \mathcal{D}^{(1k)}_{1b,2b,J'}}{2J'+1} + \sum_{J''} (-1)^{1+k+J'+J''} \right. \\ & \left. \times \left(\left\{ \begin{array}{ccc} k & J_1 & J' \\ 1 & J_2 & J'' \end{array} \right\} \mathcal{D}^{(k1)}_{1a,2a,J'} \mathcal{D}^{(1k)}_{1b,2b,J''} + \left\{ \begin{array}{ccc} 1 & J_1 & J' \\ k & J_2 & J'' \end{array} \right\} \mathcal{D}^{(1k)}_{1a,2a,J'} \mathcal{D}^{(k1)}_{1b,2b,J''} \right) \right]. \end{aligned} \tag{4.14}$$

Equation (4.14) looks very different from the standard JO line strength $\mathcal{S}_{\mathrm{ED}} = \sum_\lambda \Omega_\lambda \langle \Psi^0_1 \| U^{(\lambda)} \| \Psi^0_2 \rangle$, especially because it does not depend on λ, but depends on J'

and J'' (which are by contrast eliminated in the standard case). The index λ is still relevant in the ED transition amplitude D_{12}, see Eq. (4.7), because it allows for deriving the selection rules, but it disappears in the line strength, where we consider unpolarized light and ions (that is to say sums on p, M_1 and M_2). In Eq. (4.14), the influence of the CF potential are only contained in the three parameters $X_k = (2k+1)^{-1} \sum_q |A_{kq}|^2$, for $k = 1$, 3 and 5, which are q-averages of the square of A_{kq}. In what follows, they will be treated as adjustable parameters, whereas all the atomic properties have been computed using atomic-structure methods.

4.1.2 Third-order correction

In this section, we address the influence of spin-orbit (SO) mixing in the excited configuration on spin-changing f-f transitions. Contrary to the ground configuration, the LS coupling scheme is by far not appropriate to interpret the levels of the $4f^{w-1}5d$ configuration (see Table 3.10), because the electrostatic energy between $4f$ and $5d$ electrons and the SO energy of the $5d$ electron are comparable. Therefore one can expect these excited levels to play a significant role in the spin-changing transitions.

To check this hypothesis, we will investigate the effect of the SO Hamiltonian of the ion H_{SO} using perturbation theory. Namely we define a perturbation operator V containing SO and CF interactions,

$$V = H_{\mathrm{SO}} + V_{\mathrm{CF}} \,. \tag{4.15}$$

In consequence, the new unperturbed eigenvectors related to the ground configuration are called manifolds, *i.e.* atomic levels for which the SO energy is set to 0. Those manifolds $|\widetilde{\Psi}_i^0\rangle$, of energy $\widetilde{E}_i$ are degenerate in M_i as previously, but also in J_i, and they are characterized by one L_i and one S_i quantum number,

$$|\widetilde{\Psi}_i^0\rangle = \sum_{\alpha_i} \widetilde{c}_{\alpha_i} \, |n\ell^w \, \alpha_i L_i S_i J_i M_i\rangle \,. \tag{4.16}$$

Some manifolds, like the lowest ^{5}D one in Eu^{3+}, are linear combination of different terms having the same L and S but different seniority numbers, hence the sum on α in Eq. (4.16). For the excited configuration, the unperturbed eigenvectors are those given in Eq. (4.3).

The selection rules associated with H_{SO} and V_{CF} are very different. In particular, H_{SO} couples unperturbed eigenvectors of the same configuration, whereas the odd terms of V_{CF} couple configurations of opposite parities. Therefore, the influence of both SO and CF potentials appears as products of matrix elements like $\langle\widetilde{\Psi}_1^0|H_{\mathrm{SO}}|\widetilde{\Psi}_i^0\rangle\langle\widetilde{\Psi}_i^0|V_{\mathrm{CF}}|\Psi_t^0\rangle$, and we need to go to the third order of perturbation theory to calculate the transition amplitude,

$$D_{12} = \left\langle \widetilde{\Psi}_1^1 \right| P_p^{(1)} \left| \widetilde{\Psi}_2^1 \right\rangle + \left\langle \widetilde{\Psi}_1^2 \right| P_p^{(1)} \left| \widetilde{\Psi}_2^0 \right\rangle + \left\langle \widetilde{\Psi}_1^0 \right| P_p^{(1)} \left| \widetilde{\Psi}_2^2 \right\rangle \tag{4.17}$$

where the second-order correction of eigenvectors is given in Eq. (A.9).

By expanding Eq. (4.17), we get six terms corresponding to the six possible products of matrix element of H_{SO}, $P_p^{(1)}$ and $P_q^{(k)}$. Since H_{SO} couples states of the same configuration, unlike $P_p^{(1)}$ and $P_q^{(k)}$, we distinguish two kinds of terms:

- $\langle\widetilde{\Psi}_1^0|P_q^{(k)}|\Psi_t^0\rangle \times \langle\Psi_t^0|H_{\rm SO}|\Psi_u^0\rangle \times \langle\Psi_u^0|P_p^{(1)}|\widetilde{\Psi}_2^0\rangle$ and $\langle\widetilde{\Psi}_1^0|P_p^{(1)}|\Psi_t^0\rangle \times \langle\Psi_t^0|H_{\rm SO}|\Psi_u^0\rangle \times \langle\Psi_u^0|P_q^{(k)}|\widetilde{\Psi}_2^0\rangle$, for which the SO interaction mixes levels of the excited configuration, for example quintets and septets in Eu^{3+};
- $\langle\widetilde{\Psi}_1^0|H_{\rm SO}|\widetilde{\Psi}_{i_1'}^0\rangle \times \langle\widetilde{\Psi}_{i_1'}^0|P_q^{(k)}|\Psi_t^0\rangle \times \langle\Psi_t^0|P_p^{(1)}|\widetilde{\Psi}_2^0\rangle$,
$\langle\widetilde{\Psi}_1^0|H_{\rm SO}|\widetilde{\Psi}_{i_1'}^0\rangle \times \langle\widetilde{\Psi}_{i_1'}^0|P_p^{(1)}|\Psi_t^0\rangle \times \langle\Psi_t^0|P_q^{(k)}|\widetilde{\Psi}_2^0\rangle$,
$\langle\widetilde{\Psi}_1^0|P_q^{(k)}|\Psi_t^0\rangle \times \langle\Psi_t^0|P_p^{(1)}|\widetilde{\Psi}_{i_2'}^0\rangle \times \langle\widetilde{\Psi}_{i_2'}^0|H_{\rm SO}|\widetilde{\Psi}_2^0\rangle$ and
$\langle\widetilde{\Psi}_1^0|P_p^{(1)}|\Psi_t^0\rangle \times \langle\Psi_t^0|P_q^{(k)}|\widetilde{\Psi}_{i_2'}^0\rangle \times \langle\widetilde{\Psi}_{i_2'}^0|H_{\rm SO}|\widetilde{\Psi}_2^0\rangle$. In those cases, the SO interaction mixes manifolds of the ground configuration, for example in Eu^{3+}, ^{7}F with ^{5}D, ^{5}F and ^{5}G.

Because $H_{\rm SO}$ is a scalar, *i.e.* a tensor operator of rank 0, the application of the Wigner-Eckart theorem gives a CG coefficients $C_{JM00}^{J'M'} = \delta_{JJ'}\delta_{MM'}$. So, applying the Wigner-Eckart theorem to $P_q^{(k)}$ and $P_p^{(1)}$ as in Eq. (4.5), the product of three matrix elements can be expanded in a similar way to Eq (4.6). For example,

$$\begin{aligned}\left\langle\Psi_1^0\right| P_q^{(k)} \left|\Psi_t^0\right\rangle \left\langle\Psi_t^0\right| H_{\rm SO} \left|\Psi_u^0\right\rangle \left\langle\Psi_u^0\right| P_p^{(1)} \left|\Psi_2^0\right\rangle &= \sum_{\lambda\mu}(-1)^{J_1+J_2-\lambda}\sqrt{\frac{2\lambda+1}{2J_1+1}}C_{kq1p}^{\lambda\mu}C_{J_2M_2\lambda\mu}^{J_1M_1}\left\{\begin{array}{ccc} k & 1 & \lambda \\ J_2 & J_1 & J'\end{array}\right\} \\ &\times \left\langle\Psi_1^0\left\|P^{(k)}\right\|\Psi_t^0\right\rangle\left\langle\Psi_t^0\right| H_{\rm SO}\left|\Psi_u^0\right\rangle\left\langle\Psi_u^0\left\|P^{(1)}\right\|\Psi_2^0\right\rangle \qquad (4.18)\end{aligned}$$

where $|\Psi_{t,u}^0\rangle$ are two eigenvectors of the excited configuration with the same total angular momentum J'. The other products give similar results: the order of reduced matrix elements in the last line is of course the same as the order of matrix elements in the first line; if $P_p^{(1)}$ appears before $P_q^{(k)}$, the 1 and k are interchanged in the CG coefficients and 6-j symbols, like in Eq. (4.7).

Gathering the six matrix-element products, we can write the ED transition amplitude as

$$\begin{aligned}D_{12} = \sum_{\alpha_1\alpha_2}\widetilde{c}_{\alpha_1}\widetilde{c}_{\alpha_2}\sum_{kq}A_{kq}\sum_{\lambda\mu}(-1)^{J_1+J_2-\lambda}\sqrt{\frac{2\lambda+1}{2J_1+1}}C_{kq1p}^{\lambda\mu}C_{J_2M_2\lambda\mu}^{J_1M_1} \\ \times\sum_{J'}\left[\left\{\begin{array}{ccc} k & 1 & \lambda \\ J_2 & J_1 & J'\end{array}\right\}\left(\mathcal{D}_{12,J'}^{(0k1)}+\mathcal{D}_{12,J'}^{(k01)}+\mathcal{D}_{12,J'}^{(k10)}\right)\right. \\ \left.+(-1)^{1+k-\lambda}\left\{\begin{array}{ccc} 1 & k & \lambda \\ J_2 & J_1 & J'\end{array}\right\}\left(\mathcal{D}_{12,J'}^{(01k)}+\mathcal{D}_{12,J'}^{(10k)}+\mathcal{D}_{12,J'}^{(1k0)}\right)\right], \qquad (4.19)\end{aligned}$$

where the terms $\mathcal{D}_{12,J'}^{(k_1k_2k_3)}$ are built in analogy to Eqs. (4.8) and (4.9): the order of the superscripts is the one in which the matrix element of operators appear (the "0" standing for $H_{\rm SO}$). Firstly, the $\mathcal{D}_{12,J'}^{(0k_2k_3)}$ are such that

$$\begin{aligned}\mathcal{D}_{12,J'}^{(0k_2k_3)} &= \frac{1}{\Delta_{k_2k_3}}\sum_{i_1'\alpha_1'\beta_1'L_1'}\frac{\widetilde{c}_{\alpha_1'}\widetilde{c}_{\beta_1'}}{\widetilde{E}_1-\widetilde{E}_{i_1'}}\times\langle\alpha_1L_1S_1J_1\left|H_{\rm SO}\right|\alpha_1'L_1'S_2J_1\rangle \\ &\times\sum_{\overline{\alpha}\overline{LS},L_2'}\left\langle\beta_1'L_1'S_2J_1\left\|P^{(k_2)}\right\|\overline{\alpha}\overline{LS},L_2'S_2J'\right\rangle\left\langle\overline{\alpha}\overline{LS},L_2'S_2J'\left\|P^{(k_3)}\right\|\alpha_2L_2S_2J_2\right\rangle, \qquad (4.20)\end{aligned}$$

with

$$\Delta_{lm} = \begin{cases} \widetilde{E}_1 - E_{n'\ell'} & \text{for } (l,m) = (k,1) \\ \widetilde{E}_2 - E_{n'\ell'} & \text{for } (l,m) = (1,k). \end{cases} \tag{4.21}$$

In Eu^{3+} for example, for $|\widetilde{\Psi}_1^0\rangle$ in the lowest ^{5}D manifold and $|\widetilde{\Psi}_1^0\rangle$ in the ^{7}F manifold, $H_{\rm SO}$ couples $|\widetilde{\Psi}_1^0\rangle$ to the $^7L_1'$ manifolds on the ground configuration (actually there is only one: ^{7}F). The quantum numbers $(\overline{\alpha}\overline{LS}, L_2')$ characterize the septet levels ($S_2 = 3$) of the excited configuration. Similarly,

$$\begin{aligned} \mathcal{D}^{(k_1k_20)}_{12,J'} = \frac{1}{\Delta_{k_1k_2}} \sum_{\overline{\alpha}\overline{LS},L_1'} \left\langle \alpha_1 L_1 S_1 J_1 \left\| P^{(k_1)} \right\| \overline{\alpha}\overline{LS}, L_1' S_1 J' \right\rangle \times \sum_{i_2'\alpha_2'\beta_2' L_2'} \frac{\widetilde{c}_{\alpha_2'}\widetilde{c}_{\beta_2'}}{\widetilde{E}_2 - \widetilde{E}_{i_2'}} \\ \times \left\langle \overline{\alpha}\overline{LS}, L_1' S_1 J' \left\| P^{(k_2)} \right\| \alpha_2' L_2' S_1 J_2 \right\rangle \left\langle \beta_2' L_2' S_1 J_2 \left| H_{\rm SO} \right| \alpha_2 L_2 S_2 J_2 \right\rangle , \end{aligned} \tag{4.22}$$

where $\Delta_{k_1k_2}$ is given by Eq. (4.21). Here the SO Hamiltonian couples the ^{7}F manifold to the various quintet manifolds, for instance ^{5}D, ^{5}F and ^{5}G manifolds, since $L_2' - L_2 = 0, \pm 1$. Finally, the terms $\mathcal{D}^{(k_10k_3)}_{12,J'}$ correspond to the Wybourne-Downer mechanism [39] where $H_{\rm SO}$ couples the quintet and septet levels of the excited configuration. Namely,

$$\begin{aligned} \mathcal{D}^{(k_10k_3)}_{12,J'} &= \frac{1}{\Delta^2_{k_1k_3}} \sum_{\overline{\alpha}\overline{LS}} \sum_{L_1'L_2'} \left\langle \alpha_1 L_1 S_1 J_1 \left\| P^{(k_1)} \right\| \overline{\alpha}\overline{LS}, L_1' S_1 J' \right\rangle \\ &\times \left\langle \overline{\alpha}\overline{LS}, L_1' S_1 J' \right| H_{\rm SO} \left| \overline{\alpha}\overline{LS}, L_2' S_2 J' \right\rangle \left\langle \overline{\alpha}\overline{LS}, L_2' S_2 J' \left\| P^{(k_3)} \right\| \alpha_2 L_2 S_2 J_2 \right\rangle , \end{aligned} \tag{4.23}$$

where $\Delta_{k_1k_3}$ is given by Eq. (4.21).

If we assume that in Equations (4.20), (4.22) and (4.23), the spin-orbit interactions are of the same order of magnitude (see Table 3.9), the main difference between them comes from the energy denominator. The quantity Δ_{lm} is on the order of several tens of thousands of cm^{-1}, while the differences $\widetilde{E}_1 - \widetilde{E}_{i_1'}$ and $\widetilde{E}_2 - \widetilde{E}_{i_2'}$, which are the energies between different manifolds of the ground configuration, are on the order of several thousand cm^{-1}. This means that Eq. (4.23) is, roughly speaking, one order of magnitude smaller than Eqs. (4.20) and (4.22). This fact is really a precious information that brings the third order correction.

Combining Eqs. (4.14) and (4.19), we can see that the ED line strength $\mathcal{S}_{\rm ED}$ now contains 36 terms, containing products of the kind $\mathcal{D}^{(k_{1a}k_{2a}k_{3a})}_{1a,2a,J'} \times \mathcal{D}^{(k_{1b}k_{2b}k_{3b})}_{1b,2b,J''}$. For the 18 terms in which k and 1 appear in the same order in $(k_{1a}k_{2a}k_{3a})$ and $(k_{1b}k_{2b}k_{3b})$, we have the same prefactor as the second line of Eq. (4.14), that is $(2J'+1)^{-1}$. For the 18 other terms in which k and 1 appear in different orders, we have the prefactors with the 6-j symbols as in the second and third lines of Eq. (4.14). Namely, we can write the line strength as

$$\begin{aligned} \mathcal{S}_{\rm ED} = \sum_{\alpha_{1a}\alpha_{1b}} \widetilde{c}_{\alpha_{1a}}\widetilde{c}_{\alpha_{1b}} \sum_{\alpha_{2a}\alpha_{2b}} \widetilde{c}_{\alpha_{2a}}\widetilde{c}_{\alpha_{2b}} \sum_{kq} \frac{|A_{kq}|^2}{2k+1} \sum_{\kappa_a\kappa_b} \sum_{J'} \left[\frac{\widetilde{\delta}_{\kappa_a,(k1)}\widetilde{\delta}_{\kappa_b,(k1)} + \widetilde{\delta}_{\kappa_a,(1k)}\widetilde{\delta}_{\kappa_b,(1k)}}{2J'+1} \mathcal{D}^{(\kappa_a)}_{1a,2a,J'} \mathcal{D}^{(\kappa_b)}_{1b,2b,J'} \right. \\ \left. + \sum_{J''} (-1)^{1+k+J'+J''} \left(\begin{Bmatrix} k & J_1 & J' \\ 1 & J_2 & J'' \end{Bmatrix} \widetilde{\delta}_{\kappa_a,(k1)}\widetilde{\delta}_{\kappa_b,(1k)} + \begin{Bmatrix} 1 & J_1 & J' \\ k & J_2 & J'' \end{Bmatrix} \widetilde{\delta}_{\kappa_a,(1k)}\widetilde{\delta}_{\kappa_b,(k1)} \right) \mathcal{D}^{(\kappa_a)}_{1a,2a,J'} \mathcal{D}^{(\kappa_b)}_{1b,2b,J''} \right] \end{aligned} \tag{4.24}$$

where $\kappa_a = (k_{1a}k_{2a}k_{3a})$ and $\kappa_b = (k_{1b}k_{2b}k_{3b})$ designate the possible combinations of indices k, 1 and 0. The quantity $\widetilde{\delta}_{\kappa,(k1)} = 1$ if κ is a combination in which k appears firstly and 1 secondly, namely $\kappa = (k10)$, $(k01)$, $(0k1)$, and 0 otherwise. The quantity $\widetilde{\delta}_{\kappa,(1k)}$ corresponds to the inverse situation. Similarly to Eq. (4.14), the line strength (4.24) depends on the CF potential through the three parameters $X_k = (2k+1)^{-1}\sum_q |A_{kq}|^2$, which will be treated as adjustable in the next section.

4.1.3 Application to europium

Excited-configuration energy $E_{n'\ell'}$

Equations (4.14) and (4.24) show that our f-f transition line strengths require the reduced multipole moments of some free-ion transitions which only occur between levels of the ground and excited configurations. In this subsection, we focus on the electric-dipole (ED) free-ion transitions ($k = 1$), that are the most intense.

A widely used quantity for the discussion of spectral lines and transitions is the absorption oscillator strength $f_{12,\mathrm{ED}}$, which is related to the ED line strength S_{ED} (see equation (1.65)) through the expression

$$f_{12,\mathrm{ED}} = \frac{2m_e a_0^2 (E_2 - E_1)}{3\hbar^2 (2J_1 + 1)} \mathcal{S}_{\mathrm{ED}}, \tag{4.25}$$

where E_1 (E_2) and J_1 (J_2) are the lower (upper) level's energy and total angular momentum, respectively. For ED free-ion transitions, the line strength of Eq. (4.25) is the square of the reduced ED matrix element, $\mathcal{S}_{\mathrm{ED}} = |\langle \Psi_1 \| P^{(1)} \| \Psi_2 \rangle|^2$.

Figure 4.1 shows the dependence of the logarithm of the weighted oscillator strengths given by Eq. (1.66) on the energy of the excited-configuration level, for transitions involving two levels of the ground configuration. The purpose of this discussion is to determine $E_{n'\ell'}$. It shows that the energy band with strong transitions is rather narrow and lies in the range of 80000–100000 cm^{-1}, while for larger excited-level energies, the values of $\log(gf)$ for the level $^7\mathrm{F}_1$ (blue dots) decrease faster than those for $^5\mathrm{D}_1$ (red dots). Indeed, the total spin S of $4f^5 5d$ levels tends to decrease with energy (see Table 3.10), the coupling with levels of the $4f^6\,{}^7\mathrm{F}$ manifold drops faster than the coupling with levels of the quintet manifolds. Therefore, in the framework of the JO theory, the excited-configuration energy $E_{n'\ell'}$ appearing in the denominators of the line strengths, see Eqs. (4.14) and (4.24), is not the center-of-gravity energy of the excited-configuration, but rather the strong-coupling window between 80000 and 100000 cm^{-1}: in practice, we take $E_{n'\ell'} = 90000$ cm^{-1}. The free-ion ED reduced matrix elements for $k = 1$, $k = 3$ and $k = 5$ that are described in section 3.4, are required for the JO theory.

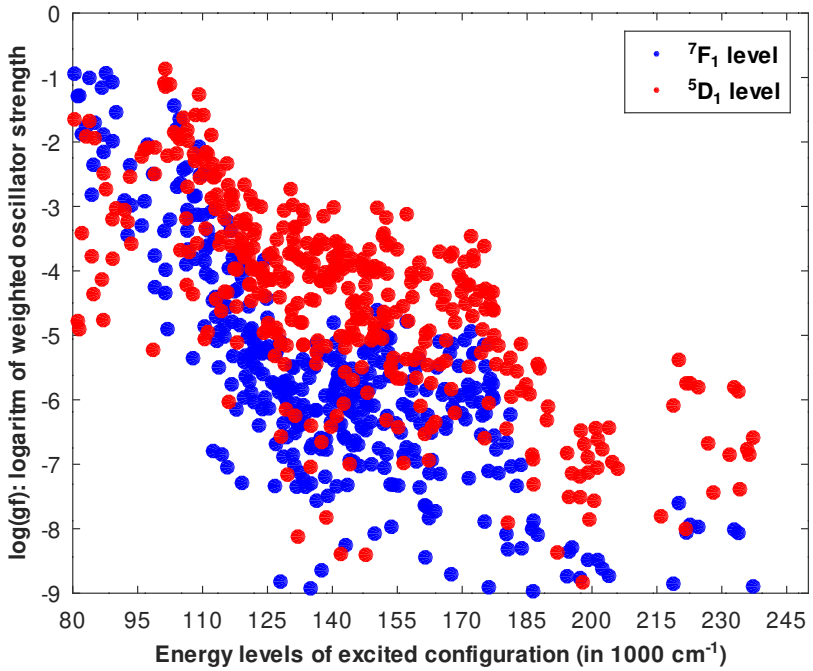

Figure 4.1: Logarithm of the weighted ED oscillator strengths, see Eq. (1.66), as functions of the energy of the excited-configuration levels, for transitions implying the $^7\mathrm{F}_1$ (blue) and $^5\mathrm{D}_1$ (red) levels of the ground configuration for Eu^{3+}.

Least-square fitting procedure

Using the expression for the ED line strength, we now seek to minimize the standard deviation between calculated and experimental line strengths

$$\sigma = \left[\frac{\sum_{i=1}^{N_{\mathrm{tr}}} \left(\mathcal{S}_{\mathrm{exp},i} - \mathcal{S}_{\mathrm{ED},i} \right)^2}{N_{\mathrm{tr}} - N_{\mathrm{par}}} \right]^{\frac{1}{2}}, \tag{4.26}$$

where N_{tr} is the number of experimental transitions included in the calculation and $N_{\mathrm{par}} = 3$ is the number of adjustable parameters. The experimental line strengths in atomic units are given as function of the measured oscillator strengths f_{exp} by

$$\mathcal{S}_{\mathrm{exp}} = \frac{3(2J_1+1)\hbar^2}{2m_e a_0^2 (E_2 - E_1)} \frac{n_r}{\chi_{\mathrm{ED}}} f_{\mathrm{exp}} \tag{4.27}$$

where n_r is the host refractive index and is dependent on wavelength and $\chi_{\mathrm{ED}} = (n_r^2 + 2)/9$ the local-field correction in the virtual-cavity model (see for example Ref. [70]). It is convenient to give the so-called relative standard deviations, which is the ratio $\sigma/\mathcal{S}_{\mathrm{max}}$ between the standard deviation and the maximum value among the experimental oscillator strengths. It is often expressed as a percentage.

After the fitting, using these optimal X_k parameters, we can predict line strengths, oscillator strengths and Einstein A coefficients, for other transitions. Of course, that procedure only involves transitions with a predominant ED character; magnetic-dipole

Table 4.2: Transition labels, experimental oscillator strengths ($\times$ 10 $^{-6}$) [69] and ratios between theoretical and experimental line strength for the standard Judd-Ofelt theory (r_0), as well as for our second-order (r_1) and third-order (r_2) corrections of our theory. The last lines present the absolute and relative standard deviations for each model (see text).

Tr. label	Exp. o.s.	r_0	r_1	r_2
$^5D_4 \leftrightarrow {}^7F_0$	0.489	1.14	0.07	0.80
$^5G_2 \leftrightarrow {}^7F_0$	0.523	0.82	0.59	0.28
$^5L_6 \leftrightarrow {}^7F_0$	3.338	0.38	0.31	0.29
$^5L_6 \leftrightarrow {}^7F_1$	1.383	0.17	0.33	0.29
$^5D_3 \leftrightarrow {}^7F_1$	0.302	0.87	0.12	1.10
$^5D_2 \leftrightarrow {}^7F_0$	0.333	1.41	1.66	0.88
$^5D_1 \leftrightarrow {}^7F_1$	0.450	0.99	1.00	1.00
$^7F_6 \leftrightarrow {}^7F_0$	1.232	1.83	1.81	1.83
$^7F_6 \leftrightarrow {}^7F_1$	1.983	0.93	0.95	0.94
σ		0.266	0.252	0.258
$\sigma/\mathcal{S}_{\max}$		8.71 %	8.24 %	8.45 %

(MD) transitions like $^5D_0 \leftrightarrow {}^7F_1$ and $^5D_1 \leftrightarrow {}^7F_0$ are therefore excluded from the fit. For them, the MD line strength $\mathcal{S}_{\mathrm{MD}}$, oscillator strengths and Einstein coefficients can be calculated from the free-ion eigenvectors.

Eu^{3+} in lithium fluoroborate

In order to validate our model with experimental data we have chosen the thorough investigation of Babu *et al.* [69], who measured absorption oscillator strengths and interpreted them with the standard JO theory. Their study deals with transitions within the ground manifold ^7F and between the ground and first excited manifold ^5D for Eu^{3+}-doped lithium fluoroborate glass. In the latter case, the transitions involve a change in spin, well known to challenge the standard JO theory. We have included 9 out of the 14 transitions measured with the so-called L6BE glass in Table 3 of Ref. [69]. We have excluded three predominant MD transitions, $^5D_0 \leftrightarrow {}^7F_1$, $^5D_1 \leftrightarrow {}^7F_0$ and $^5D_2 \leftrightarrow {}^7F_1$, as well as the $^5G_4 \leftrightarrow {}^7F_0$ and $^5D_0 \leftrightarrow {}^7F_0$ for which we observe large deviations between theory and experiment. They are probably due to the fact that the $^5D_0$ and $^5G_4$ are further from LS coupling than the other levels. In particular, the four leading components represent 88.4 and 86.9 % of the total eigenvectors respectively.

Table 4.2 shows the results of our least-square calculations with the second- and third-order theory, in comparison with the standard JO theory used in Ref. [69]. For each transition, the table contains the experimental values of the oscillator strength ($\times 10^{-6}$) [69] and the ratios r_n between the theoretical and experimental oscillator strengths, where r_0 is the ratio for the standard Judd-Ofelt theory, and the r_1 and

Table 4.3: Fitted parameters from the absorption oscillator strengths of Ref. [69]. The second column gives standard JO parameters $\Omega_{2,4,6}$; the third and fourth ones give X_k obtained with Eqs. (4.14) and (4.24), respectively.

	Std. JO	2nd-order	3rd-order
k	Ω_{k+1} (10^{-20} cm^2)	X_k (a.u.)	X_k (a.u.)
1	17.93	9.424×10^{-7}	1.441×10^{-6}
3	11.92	2.330×10^{-5}	9.916×10^{-6}
5	2.13	7.187×10^{-8}	6.406×10^{-8}

r_2 are the ratios, respectively, for second and third order corrections of theory (see subsection 4.1.1 and 4.1.2). For each model, we present the absolute σ and relative standard deviations, taken by dividing Eq. (4.26) by the largest experimental line strength $\mathcal{S}_{\max} = 3.057 \times 10^{-4}$ for the $^7\mathrm{F}_6 \leftrightarrow {}^7\mathrm{F}_1$ transition. Figure 4.2 gives a visual insight into the results of Table 4.2, with histograms of the experimental absorption oscillator strengths, and those resulting from the standard JO theory and our third-order correction, plotted as functions of the transition wavelength.

Globally, the three methods have similar performances. That shows that the SO interaction in the excited configuration has little effect, since it is included in the third-order correction and not in the second-order one. Our third-order corrections better describes transitions between ^{7}F and ^{5}D manifolds. However, it predicts the smallest oscillator strength for $^5\mathrm{G}_2 \leftrightarrow {}^7\mathrm{F}_0$, owing to the proximity between the ^{5}G3 and ^{5}H1 manifolds, which puts into question the use of SO interaction as a perturbation. On the other hand, the second-order correction fails to describe the $^5\mathrm{D}_4 \leftrightarrow {}^7\mathrm{F}_0$ transition. The three methods tend to underestimate the oscillator strengths for high-energy transitions, where the refractive index n_r is larger than 1.57.

The final fitted parameters are given in Table 4.3 for the standard JO calculation of Ref. [69] (see Set B of Table 4), as well as our second-order correction (4.14) and third-order correction (4.24). The orders of magnitude of the X_k are the same for the two corrections. The parameter X_3 are the largest, then the X_1 are roughly one order of magnitude smaller than the X_3, and the X_5 are roughly two orders of magnitude smaller than X_3. It is hard to make direct comparisons with the standard JO parameters given in Table 4 of Ref. [69] (data set B); but we see that that the Ω_6 parameter, responsible of the $^7\mathrm{F}_6 \leftrightarrow {}^7\mathrm{F}_{0,1}$ and $^5\mathrm{L}_6 \leftrightarrow {}^7\mathrm{F}_{0,1}$ transitions just like X_5 is respectively 9 and 6 times smaller than Ω_2 and Ω_4. To give more insight values of the parameter, we notice that the quantities $\sqrt{X_k} \times \langle n\ell|r^k|n'\ell'\rangle$ is the order-of-magnitude energy of the ion-field interaction: in the third-order correction, they are respectively equal to 298, 2226 and 1207 cm^{-1} for $k = 1$, 3 and 5.

Magnetic-dipole transitions

Now that we have the X_k parameters, we can calculate oscillator strengths for transitions not present in the fit. In particular, we can predict the percentage of ED and MD characters for the transitions having both characters [51,71–73], assuming that the

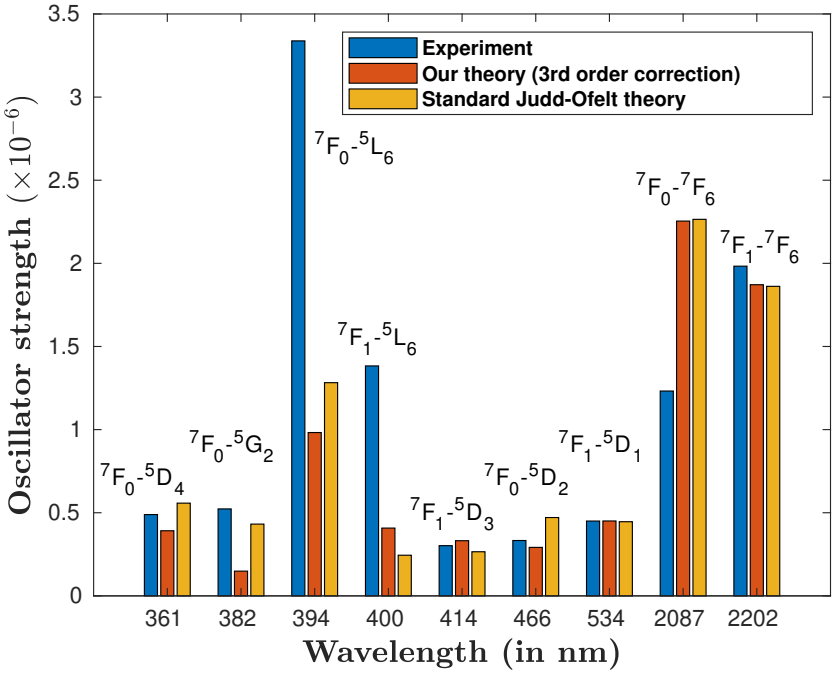

Figure 4.2: Comparison between experimental [69] and theoretical oscillator strengths of absorption, plotted as function of the transition wavelength (not at scale). The transitions are labeled with the LS-term quantum numbers of the Eu^{3+} free ion.

total oscillator strength is equal to the sum $f_{\mathrm{ED}} + f_{\mathrm{MD}}$. The ED part can be calculated by inverting Eq. (4.27) and replacing the subscripts "exp" by "ED", while the MD part reads [28]

$$f_{\mathrm{MD}} = \frac{2m_e a_0^2 (E_2 - E_1)}{3(2J_1 + 1)\hbar^2} n_r \mathcal{S}_{\mathrm{MD}} \tag{4.28}$$

where the MD line strength is given with the formula 1.68.

Table 4.4 presents experimental and theoretical absorption oscillator strengths for the transitions having in principle an ED and a MD character. The MD oscillator strengths are calculated by multiplying the free-ion one computed with Cowan's code by the host refractive index n_r, see Eq. (4.28). The table clearly shows that the $^5D_1 \leftrightarrow {}^7F_1$ transition is purely electric (at least 99.9 %), hence its inclusion in the fit. The $^5D_2 \leftrightarrow {}^7F_1$ is also mainly electric, but to a lesser extent, roughly at 95 %. The two others are mostly magnetic, but the experimental and theoretical MD oscillator strengths significantly differ from each other. Still, the ED character looks larger for the $^5D_1 \leftrightarrow {}^7F_0$ transition (4-9 %) than for the $^5D_0 \leftrightarrow {}^7F_1$ one (1-2 %).

The $^5D_0 \leftrightarrow {}^7F_0$ transition

Since the $^5D_0 \leftrightarrow {}^7F_0$ transition is forbidden by the selection rules of the standard JO model, it has attracted a lot of attention (see Ref. [34] and references therein), in order to understand its origin. Even though it is not forbidden in our model, we

Table 4.4: Experimental absorption oscillator strengths, as well as ED and MD theoretical ones, for transitions having both an ED and a MD character (numbers in brackets are the powers of 10).

Tr. label	f_{exp}	$f_{\text{th,ED}}$	$f_{\text{th,MD}}$
$^5D_1 \leftrightarrow {}^7F_0$	7.8(-8)	2.74(-9)	2.67(-8)
$^5D_0 \leftrightarrow {}^7F_1$	5.7(-8)	7.70(-10)	3.93(-8)
$^5D_1 \leftrightarrow {}^7F_1$	4.50(-7)	4.50(-7)	1.92(-11)
$^5D_2 \leftrightarrow {}^7F_1$	2.48(-7)	1.74(-7)	4.96(-9)

had to exclude it in the fit, because of a strong discrepancy between the experimental and our computed oscillator strength. With our optimal parameters X_k, we obtain an oscillator strength 1.25×10^{-7}, that is 7.8 times larger than the experimental value. In this paragraph, we investigate in closer details the possible origin of that discrepancy and how to reduce it.

Firstly, as mentioned in Subsection 4.1.2, the sums in Eqs. (4.19) and (4.24) involves quintet and septet manifolds of the ground configuration. But a closer look at the eigenvectors shows that the $^5D_0$ level contains 6.7 % of ^{3}P6 character, see Table 3.7, as well as 5.1 % of ^{3}P3, while $^7F_0$ contains 0.1 % of ^{3}P6 character. These small components are likely to contribute to the transition amplitude, and so they need to be accounted for through a complete description of the free-ion eigenvectors.

The selection rules associated with Eq. (4.19) show merely the terms with $k = 1$ of the CF potential can induce a transition of the kind $(J_1, J_2) = (0, 0)$. This result seems consistent because: (i) those terms are stronger in sites with low symmetries, and (ii) observing the $^5D_0 \leftrightarrow {}^7F_0$ transition is an indication of C_{nv}, C_n or C_s point groups at the ion site [74–76]. Although that transition is often very weak, it is unusually intense in the β-diketonate, with the Eu^{3+} ion at a site with C_3 symmetry [77]. Unusually high intensities for the $^5D_0 \leftrightarrow {}^7F_0$ transition are also observed for Eu^{3+} in fluorapatite, hydroxyapatite, oxysulfates, α-cordierite, mullite, etc.

Chen *et al.* listed some anomalous Eu^{3+} containing systems, in which very strong ratios of $\frac{I_{00}}{I_{01}}$ are found, where I_{00} is the intensity of $^5D_0 \leftrightarrow {}^7F_0$ and I_{01} is the intensity of $^5D_0 \leftrightarrow {}^7F_1$ [78]. Several interesting features can be noted from their list: (i) anomalous CF spectra are often found in those systems in which there are oxygen-compensating sites; and (ii) all the systems with a ratio larger than 20 have C_s symmetry. The most probable explanation for this is that Eu ions, which occupy the C_s position, are surrounded by oxygen atoms from other host groups, and the CF is deformed by O [79]. This could mean that the presence of oxygen atoms in the host material tends to induce a rather strong $^5D_0 \leftrightarrow {}^7F_0$ transition. This is the case in the crystals studied in many articles: for example, the composition of lithium borate of Ref. [69] is L6BE $= 39.5Li_2CO_3 + 59.5\ H_3BO_3 + 1Eu_2O_3$.

Another frequently invoked mechanism to explain the $^5D_0 \leftrightarrow {}^7F_0$ transition is J-mixing [36–38], especially between levels of the lowest manifold ^{7}F. However, because this mixing is limited to 10 %, it cannot explain the strongest 0-0 transitions listed

in Ref. [78]. Charge-transfer states are also likely to play a role in the 0-0 transition, especially in hosts with oxygen-compensating sites around by which the CF tends to be strongly deformed [79]. However, those two mechanisms are not present in our model.

We recall that, in our extension model the $^7\mathrm{F}_0 \leftrightarrow {}^5\mathrm{D}_0$ transition is allowed. With Babu's data [69], the ratio between the theoretical and experimental OSs is equal to 20 in the third-order correction and 7.8 in the second-order one.

Radiative lifetime of the $^5\mathrm{D}_0$ level

In addition to absorption oscillator strengths, our model also makes it possible to calculate the ED Einstein coefficient for the spontaneous emission from level 2 to 1,

$$A_{\mathrm{ED}} = \frac{e^2 a_0^2 (E_2 - E_1)^3}{3\pi\varepsilon_0 \hbar^4 c^3 (2J_2 + 1)} n_r \chi_{\mathrm{ED}} \mathcal{S}_{\mathrm{ED}}, \tag{4.29}$$

where c is the speed of light and $\mathcal{S}_{\mathrm{ED}}$ is given by Eq. (4.24). We can also compute the MD Einstein coefficients A_{MD}, by multiplying the free-ion value calculated with Cowan by n_r^3; namely

$$A_{\mathrm{MD}} = \frac{e^2 a_0^2 (E_2 - E_1)^3}{3\pi\varepsilon_0 \hbar^4 c^3 (2J_2 + 1)} n_r^3 \mathcal{S}_{\mathrm{MD}} \tag{4.30}$$

where $\mathcal{S}_{\mathrm{MD}}$ is given by Eq. (1.68).

From them, we can deduce the radiative lifetime τ of a given level. In particular for the $^5\mathrm{D}_0$ level, it reads

$$\tau(^5\mathrm{D}_0) = \left(\sum_{J=0}^{6} A_{\mathrm{ED}}(^5\mathrm{D}_0, {}^7\mathrm{F}_J) + A_{\mathrm{MD}}(^5\mathrm{D}_0, {}^7\mathrm{F}_1) \right)^{-1}. \tag{4.31}$$

Transitions $^5D_0 \leftrightarrow {}^7F_J$, where $J = 1$ to 6, are not included in our fit, and so are considered as additional transitions, for which our program calculated line strengths and Einstein coefficients. For the transition $^5D_0 \leftrightarrow {}^7F_1$, the total Einstein coefficient is the sum of the electric and the magnetic parts, calculated using Cowan code. The latter is found to be $A_{\mathrm{MD}}(^5\mathrm{D}_0, {}^7\mathrm{F}_1) = 53.44\ \mathrm{s}^{-1}$. The sum of Einstein coefficients for all other transitions, including the electric part of transition $^5D_0 \leftrightarrow {}^7F_1$, is 500.529 s^{-1}. That sum includes the transition $^5D_0 \leftrightarrow {}^7F_0$, whose Einstein coefficient (4.29) is calculated using the line strength deduced from the experimental oscillator strength following Eq. (4.27). This yields the very small value of 0.029 s^{-1}. The resulting radiative lifetime is $\tau(^5\mathrm{D}_0) = 1805\ \mu\mathrm{s}$, which is close to the experimental value of 1920 μs reported in Ref. [69]. In principle, the relaxation limiting the lifetime is due to radiative as well as nonradiative processes; however the latter are expected to be unlikely for the $^5\mathrm{D}_0$ level [80], due to the large gap between the $^5\mathrm{D}_0$ and $^7\mathrm{F}_6$ levels, see Table 3.7.

Although this version of the extension works good for Eu^{3+} and the oscillator strengths are well described, the extension can be improved by incorporating all the eigenvector components and account for the wavelength dependence of the refractive index. The second version of extension will be described in the next section.

4.2 Second extension of JO theory

Transition amplitude and line strength

In the previous version of extension, we present two different calculations: (i) where the spin-orbit (SO) interaction within the $4f^{w-1}5d$ configuration is not included, and (ii) where it is included. In the first version, described in section 4.1, the ED transition amplitude D_{12} is calculated with the second-order perturbation theory in which the perturbation operator is $V_{\rm CF}$. The unperturbed states are the free-ion levels of the lowest configuration $4f^w$. Therefore the $4f^w$ SO interaction is fully accounted for, as it is part of the unperturbed Hamiltonian. In the second version, the perturbation operator is $V_{\rm CF} + H_{\rm SO}$, and in order to catch the effect of both terms, D_{12} is calculated with the third-order perturbation theory. Because $H_{\rm SO}$ is accounted for in a perturbative way both in the ground and the excited configurations, the unperturbed states are the free-ion manifolds, *i.e.* levels without SO interaction. In other words, all the J levels inside a given manifold, like ${}^7F_J$ in Eu^{3+}, are degenerate.

In the present version, we merge the two previous versions as follows. As before we consider as unperturbed states the free-ion levels of the ground configuration written in pair coupling, as in the first version of the extension:

$$|\Psi_i^0\rangle = \sum_{\alpha_i L_i S_i} c_{\alpha_i L_i S_i} \, |n\ell^w \, \alpha_i L_i S_i J_i M_i\rangle \ , \tag{4.32}$$

where $i = 1, 2$ describes the lower and upper levels, and L_i, S_i, J_i, M_i respectively denote the orbital, spin, total angular momenta and their z-projections. The indices α_i, standing for the seniority numbers, are sometimes necessary to distinguish manifolds with the same L_i and S_i (for example ${}^5D1$, ${}^5D2$ and ${}^5D3$ in Eu^{3+}). The $c_{\alpha_i L_i S_i}$ coefficients are the eigenvector components of the ionic Hamiltonian in LS coupling scheme. Because for Ln^{3+} ion in the lowest configuration, there is most often one dominant LS component (with $|c_{\alpha_i L_i S_i}|^2 > 0.7$), the free-ion levels are labeled with that component. In the present work, we take all the components into account, whereas in the first version we only took the four leading ones (due to practical reasons).

The transition amplitude D_{12} is now the sum of the second-order contribution describing the bare influence of the CF, and a third-order contribution describing the influence of the CF and excited-configuration SO interaction (the so-called Downer-Wybourne mechanism). The expression of D_{12} becomes

$$\begin{aligned} D_{12} = \sum_t \Bigg[& \frac{\langle\Psi_1^0|V_{\rm CF}|\Psi_t^0\rangle\langle\Psi_t^0|P_p^{(1)}|\Psi_2^0\rangle}{E_1 - E_t} \\ & + \frac{\langle\Psi_1^0|P_p^{(1)}|\Psi_t^0\rangle\langle\Psi_t^0|V_{\rm CF}|\Psi_2^0\rangle}{E_2 - E_t} \\ & + \sum_u \Bigg\{ \frac{\langle\Psi_1^0|V_{\rm CF}|\Psi_t^0\rangle\langle\Psi_t^0|H_{\rm SO}|\Psi_u^0\rangle\langle\Psi_u^0|P_p^{(1)}|\Psi_2^0\rangle}{(E_1 - E_t)^2} \\ & + \frac{\langle\Psi_1^0|P_p^{(1)}|\Psi_t^0\rangle\langle\Psi_t^0|H_{\rm SO}|\Psi_u^0\rangle\langle\Psi_u^0|V_{\rm CF}|\Psi_2^0\rangle}{(E_2 - E_u)^2} \Bigg\} \Bigg] \ , \end{aligned} \tag{4.33}$$

where $|\Psi^0_{t,u}\rangle = |n\ell^{w-1}\overline{\alpha}\overline{LS},\, n'\ell' L'_{1,2} S'_{1,2} J' M'\rangle$ are unperturbed LS states of the excited configuration: namely $n\ell = 4\mathrm{f}$ and $n'\ell' = 5\mathrm{d}$.

Performing the same angular-momentum properties as in the first version, we obtain for the transition amplitude

$$D_{12} = \sum_{\alpha_1 L_1 S_1} c_{\alpha_1 L_1 S_1} \sum_{\alpha_2 L_2 S_2} c_{\alpha_2 L_2 S_2} \sum_{kq} A_{kq} \sum_{\lambda\mu} (-1)^{J_1+J_2-\lambda} \sqrt{\frac{2\lambda+1}{2J_1+1}} C^{\lambda\mu}_{kq1p} C^{J_1 M_1}_{J_2 M_2 \lambda\mu} \times \sum_{J'} \left[\left\{ \begin{array}{ccc} k & 1 & \lambda \\ J_2 & J_1 & J' \end{array} \right\} \left(\mathcal{D}^{(k1)}_{12,J'} + \mathcal{D}^{(k01)}_{12,J'} \right) + (-1)^{1+k-\lambda} \left\{ \begin{array}{ccc} 1 & k & \lambda \\ J_2 & J_1 & J' \end{array} \right\} \left(\mathcal{D}^{(1k)}_{12,J'} + \mathcal{D}^{(10k)}_{12,J'} \right) \right], \tag{4.34}$$

where $C^{c\gamma}_{a\alpha b\beta}$ is a Clebsch-Gordan coefficient and the quantity between curly brackets is a Wigner 6-j symbol. For the line strength $\mathcal{S}_{\mathrm{ED}} = \sum_{M_1 M_{2p}} (D_{12})^2$, one has

$$\mathcal{S}_{\mathrm{ED}} = \sum_{\alpha_{1a} L_{1a} S_{1a}} c_{\alpha_{1a} L_{1a} S_{1a}} \sum_{\alpha_{2a} L_{2a} S_{2a}} c_{\alpha_{2a} L_{2a} S_{2a}} \sum_{\alpha_{1b} L_{1b} S_{1b}} c_{\alpha_{1b} L_{1b} S_{1b}} \sum_{\alpha_{2b} L_{2b} S_{2b}} c_{\alpha_{2b} L_{2b} S_{2b}} \sum_{kq} \frac{|A_{kq}|^2}{2k+1} \times \sum_{J'} \left[\frac{1}{2J'+1} \left(\widetilde{\mathcal{D}}^{(k1)}_{1a,2a,J'} \widetilde{\mathcal{D}}^{(k1)}_{1b,2b,J'} + \widetilde{\mathcal{D}}^{(1k)}_{1a,2a,J'} \widetilde{\mathcal{D}}^{(1k)}_{1b,2b,J'} \right) + \sum_{J''} (-1)^{1+k+J'+J''} \times \left(\left\{ \begin{array}{ccc} k & J_1 & J' \\ 1 & J_2 & J'' \end{array} \right\} \widetilde{\mathcal{D}}^{(k1)}_{1a,2a,J'} \widetilde{\mathcal{D}}^{(1k)}_{1b,2b,J''} + \left\{ \begin{array}{ccc} 1 & J_1 & J' \\ k & J_2 & J'' \end{array} \right\} \widetilde{\mathcal{D}}^{(1k)}_{1a,2a,J'} \widetilde{\mathcal{D}}^{(k1)}_{1b,2b,J''} \right) \right]. \tag{4.35}$$

where $\widetilde{\mathcal{D}}^{(k_1 k_2)}_{12,J'} = \mathcal{D}^{(k_1 k_2)}_{12,J'} + \mathcal{D}^{(k_1 0 k_2)}_{12,J'}$, and $\mathcal{D}^{(k_1 k_2)}_{12,J'}$ and $\mathcal{D}^{(k_1 0 k_2)}_{12,J'}$ are given in Eqs. (8), (9) and (23) of the first version.

Due to angular-momentum selection rules, these equations impose some conditions on the indices:

- $|\ell - \ell'| \leq k \leq \ell + \ell'$ and $\ell + \ell' + k$ even, which gives $k = 1$, 3 and 5, since $\ell = 3$ and $\ell' = 2$.
- $k - 1 \leq \lambda \leq k + 1$, which gives $\lambda = 0$ to 6. In the standard JO theory, one has $\lambda = k + 1$.
- $|J_1 - J_2| \leq \lambda \leq J_1 + J_2$, which gives $0 \leq |J_1 - J_2| \leq 6$.
- $0 \leq |L_1 - L_2| \leq 7$.
- $|S_1 - S_2| = 0$ or 1.

Regarding the last rule, the second-order correction, given by the two first lines of Eq. (4.33), imposes $|S_1 - S_2| = 0$. Therefore spin changing comes from the fact the free-ion $4\mathrm{f}^w$ levels have different spin components S_i, even though one is by far dominant. The two last lines of Eq. (4.33) may in contrast given $S_1 - S_2 = \pm 1$ due to the SO interaction within the $4\mathrm{f}^{w-1}5\mathrm{d}$ configuration.

Wavelength dependence of refractive index

The refractive index of a material depends on the optical frequency or wavelength; this dependence is called chromatic dispersion. Typical refractive index values for glasses and crystals in the visible spectral region are in the range from 1.4 to 2.8, and typically the refractive index increases for shorter wavelengths (normal dispersion). The wavelength-dependent refractive index of a transparent optical material can often be described analytically with Cauchy's equation, which contains several empirically obtained parameters. The most general form of Cauchy's equation is

$$n_r(\lambda) = A + \frac{B}{\lambda^2} + \frac{C}{\lambda^4} + \cdots , \tag{4.36}$$

where n_r is the refractive index, λ is the wavelength, A, B, C, etc. are coefficients that can be determined for a material by fitting the equation to measured refractive indices at known wavelengths.

The Sellmeier equation is a later development of Cauchy's work that handles anomalously dispersive regions, and more accurately models a material refractive index across the ultraviolet, visible, and infrared spectrum. In its original and the most general form, the Sellmeier equation is given by

$$n_r^2(\lambda) = n_0^2 + \sum_{i=1}^{m} \frac{A_i \lambda^2}{\lambda^2 - B_i}, \tag{4.37}$$

where n_0 is the refractive index in vacuum, λ is the wavelength, and A_i and B_i are experimentally determined Sellmeier coefficients. The literature contains a great variety of modified equations which are also often called Sellmeier formulas. A somehow general form, used in many papers dealing with the study of the intensities of Ln^{3+} ions in various crystals, is as follows:

$$n_r^2(\lambda) = n_0^2 + \sum_{i=1}^{m} \frac{A_i \lambda^2}{\lambda^2 - B_i} - \sum_{j=1}^{p} \frac{C_j}{\lambda^2} \tag{4.38}$$

However, in the experimental studies with which we deal here, the authors use the simple formula

$$n_r^2(\lambda) = n_0^2 + \frac{A\lambda^2}{\lambda^2 - B}. \tag{4.39}$$

obtained by setting $m = 1$ and $p = 0$.

4.3 JO extension application on trivalent lanthanides

The goal of this section is to check the effectiveness of the second version of the extension model. For that purpose we have chosen two sets of experimental data of oscillator strengths (OS) for each ion: Eu^{3+}, Nd^{3+} and Er^{3+}. We start the discussions from Eu^{3+} in order to make the transition from first extension results, discussed in subsection 4.1.3, to results of the second extension smooth. The calculations and results for europium is discussed in subsection 4.3.1. Subsections 4.3.2 and 4.3.3 are dedicated to discussion on application results for Nd^{3+} and Er^{3+}, respectively.

Table 4.5: Values of Judd-Ofelt parameters (in 10^{-20} cm^2) and $|A_{kq}|^2$ (in a.u.) for Eu^{3+} from the present work (Our), compared to values reported in the literature (Rep.). The experimental oscillator strengths and Judd-Ofelt parameters from Babu *et al.* [69] are from set B (with thermal corrections). Judd-Ofelt parameters are calculated with the transition set from Kedziorski *et al.* [47].

	X_1 (10^{-4} a.u.)	Ω_2 (10^{-20} cm^2)		X_3 (10^{-5} a.u.)	Ω_4 (10^{-20} cm^2)		X_5 (10^{-8} a.u.)	Ω_6 (10^{-20} cm^2)	
		Our	Rep.		Our	Rep.		Our	Rep.
Eu^{3+} in Li fluoroborate [69]	1.816	18.73	17.96	1.898	12.58	11.92	6.882	2.253	2.13
Eu^{3+} in acetate [47]	0.7887	6.991	-	0.1317	8.326	-	0.1008	4.940	-

4.3.1 Application to europium

In addition to the free-ion ED reduced matrix element ($k = 1$), our model requires those for $k = 3$ (octupole) and $k = 5$, which depend on the radial transition integral $\langle 4f|r^k|5d\rangle$, the calculations of which are recalled in section 3.4. We bring back those values for the convenience: we obtain $1.130629\,a_0$, $-3.221348\,a_0^3$ and $21.727152\,a_0^5$ for $k = 1$, $k = 3$ and $k = 5$, respectively, while the $k = 1$ value calculated by Cowan is $1.130618\,a_0$.

Eu^{3+} in lithium fluoroborate

Now we will benchmark our model with two sets of experimental data. The first one comes from the thorough investigation of Babu *et al.* [69] which was used to test the first extension of JO theory in subsection 4.1.3. In the article they measure absorption oscillator strengths and interpret them with standard JO theory. As for the calculation with the first version of the extension model, here as well, we focus on the oscillator strengths given in their Table 3. Since we want to check the effect of the inclusion of the wavelength dependence of the refractive index we need Sellmeier coefficients for the L6BE glasses that are discussed by Babu *et al.*. We have found those coefficients of the host refractive index from Adamiv *et al.* [81], where optical properties of borate glasses have been measured.

Similarly to the calculations done in the first version, here we apply the first extension and the standard JO theory to 9 transitions out of 14. For standard JO calculation we find a relative standard deviation (4.26) of 8.52 %. With our model (4.35), we find the standard deviation to be 8.19 % by assuming a wavelength-independent refractive index. When we apply the Sellmeier equation (4.39), standard deviation drops to 8.03 %. Therefore our model has slightly better performance, especially when we include the dispersion in the host material.

We have also performed calculations for the JO parameters by investigating the effect of dispersion on them. When including the wavelength-dependence, all of them decrease: Ω_2 from 25.79×10^{-20}cm^2 to 18.73×10^{-20} cm^2, Ω_4 from 17.88×10^{-20} cm^2 to 12.58×10^{-20} cm^2 and, finally, Ω_6 from 3.015×10^{-20} cm^2 to 2.253×10^{-20} cm^2, making the comparison with values reported in Babu *et al.* [69] better. The results are

summarised in table 4.5. This table also presents the optimal fitted parameters X_k of our extension in atomic units, that is to say $(E_h/a_0^k)^2$ with E_h the Hartree energy. Performing a direct comparison between them and the Ω_λ parameters is a bit tricky, because they do not represent the same quantity, but it is detectable that they follow similar trends, namely $\Omega_2 > \Omega_4 > \Omega_6$ and $X_1 > X_3 > X_5$.

At present, we investigate the agreement between theory and experiment for each transition included in the fit. From the data set of [69] we have excluded the three transitions that have a significant MD character, namely $^7F_1$-$^5D_0$, $^7F_0$-$^5D_1$ and $^7F_1$-$^5D_2$, but also $^7F_0$-$^5D_0$ (see subsections 4.1.3 and 4.3.1), and $^7F_0$-$^5G_4$ for which we obtain a large discrepancy. For the 9 remaining transitions, the upper panel of figure 4.3 presents, as functions of the wavelength but not at scale, histograms of the experimental and various calculated oscillator strengths, obtained with the standard JO model, our third-order correction of the first version, and the current (second) version.

Our present model show equal or better performance than the standard JO model, except for the $^7F_0$-$^5G_2$ transition. The same trend is observed between the present model and the one of the first version, except for $^7F_0$-$^5D_2$ transition, see also Table 4.6. Remarkably, the three models give significantly smaller oscillator strengths than the experimental ones, for the transitions involving the $^5L_6$ level. This could come from an inaccuracy in the free-ion eigenvector of this level, underlying the three models. However, such an overestimation of the OS is not visible on the bottom panel of figure 4.3 with another data set. Another possible explanation is that those transitions overlap with ones involving another excited level close in energy.

Eu^{3+} in acetate

As a second data set we use absorption transitions from Kedziorski *et al.* [47], where the authors present OSs for Eu^{3+} in acetate crystal. We only consider resolved transitions between individual free-ion levels: namely we exclude those labeled $^7F_0$-$^5G_{4,5,6}$ and $^7F_0$-$^5H_{4,5,6}$. We also exclude the $^7F_1$-$^5D_2$ due to its strong MD character, as well as the $^7F_0$-$^5D_0$ one due to strong discrepancy. Unlike for the borate glass, we could not find Sellmeier coefficients in the literature for acetate crystal, and the calculations were carried out under the assumption that the refractive index is constant and equal to 1.570.

Table 4.5 presents the optimal fitting parameters X_k and Ω_λ. Comparison with literature values of standard JO parameters was not possible because in the article of Kedziorski *et al.* [47] these quantities are not discussed.

The calculations were carried out with 12 transitions included from Kedziorski *et al.* [47]. The relative standard given by the JO model is 6.49 %, for the present model it is 4.92 %, while the standard deviation from the first version is 6.21 %.

Most of the discussion in the article of Kedziorski *et al.* is based on the article of Bukietynska *et al.* [83], where the transition $^7F_0 \leftrightarrow {}^5I_6$ is mentioned to have superimposed absorption bands with transition $^7F_0 \leftrightarrow {}^5H_6$. In order to avoid the possible confusion in identification of the peaks we exclude this transition from our fitting procedure. Transition $^7F_0 \leftrightarrow {}^5I_4$ is also excluded because our model overestimates the oscillator strength for this transition in comparison with the one mentioned in the

Table 4.6: Transition labels and ratios between theoretical and experimental oscillator strength for the third-order correction of the first version (noted as "Version I") and for the second version of the model (noted as "Present") for Eu^{3+}, when the experimental data are taken from [69] (second and third columns), and [47] (two last columns). The last line presents the relative standard deviations for each model.

Transition Label	Eu^{3+} in Li fluoroborate (Babu [69])		Eu^{3+} in acetate (Kedziorski [47])	
	Version I	Present	Version I	Present
$^7F_0 \leftrightarrow {}^7F_4$			0.82	1.36
$^7F_0 \leftrightarrow {}^7F_2$			0.16	1.06
$^7F_0 \leftrightarrow {}^5D_4$	0.80	1.10	0.88	1.35
$^7F_1 \leftrightarrow {}^5D_4$			0.98	0.70
$^7F_0 \leftrightarrow {}^5G_2$	0.28	1.25	0.83	2.16
$^7F_0 \leftrightarrow {}^5L_6$	0.29	0.58	0.99	1.00
$^7F_1 \leftrightarrow {}^5L_6$	0.29	0.31		
$^7F_0 \leftrightarrow {}^5D_3$			2.96	1.74
$^7F_1 \leftrightarrow {}^5D_3$	1.10	0.94	1.18	0.98
$^7F_0 \leftrightarrow {}^5D_2$	0.88	1.53	0.75	0.98
$^7F_2 \leftrightarrow {}^5D_2$			1.11	0.83
$^7F_1 \leftrightarrow {}^5D_1$	1.00	0.95	0.82	0.87
$^7F_0 \leftrightarrow {}^5D_2$			0.26	1.44
$^7F_0 \leftrightarrow {}^7F_6$	1.83	1.84		
$^7F_1 \leftrightarrow {}^7F_6$	0.94	0.94		
$\sigma/\mathcal{S}_{\max}$	8.45 %	8.03 %	6.21 %	4.92 %

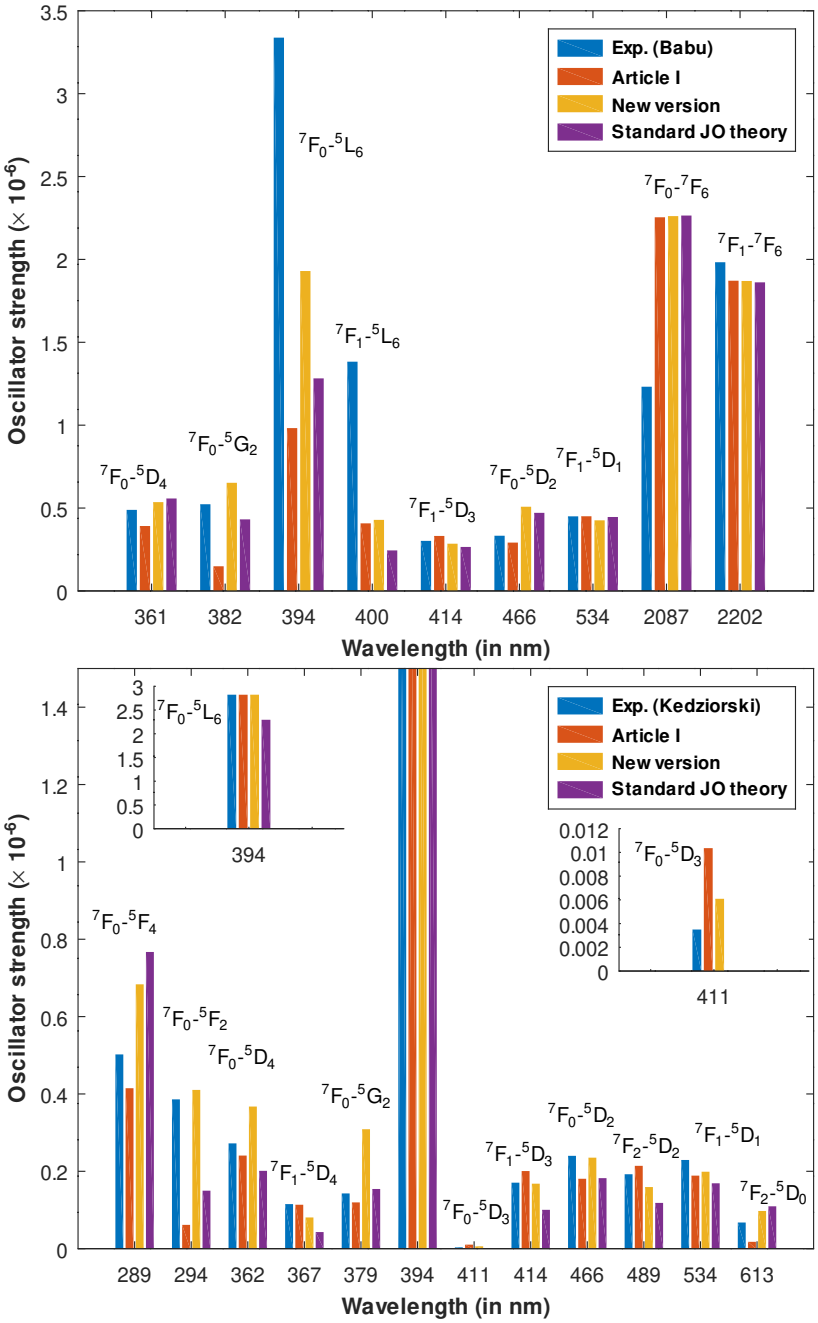

Figure 4.3: Comparison between experimental (top panel: [69], bottom panel: [47]) and theoretical (3rd order correction of the first version (article I is article [82]) and new versions) oscillator strengths of absorption, plotted as function of the transition wavelength (not at scale). The transitions are labeled with the LS-term quantum numbers of the Eu^{3+} free ion.

article.

A comparison between experimental and the OSs calculated with the standard JO model, the one resulting from version I and the one of the present version are shown

in the bottom panel of figure 4.3. The two insets are dedicated to the $^7F_0 \leftrightarrow {}^5L_6$ and the $^7F_0 \leftrightarrow {}^5D_3$ transitions which are not well visible on the main plot. In accordance with the relative standard deviations, our models systematically give better OSs than the standard JO one, except for the $^7F_0 \leftrightarrow {}^5G_2$ transition. Note that the JO model cannot describe the $^7F_0 \leftrightarrow {}^5D_3$ transition [29, 34], and that the present model gives a closer OS than the model of version I. For some transitions our present extension works better, while for others, the one of version I has better results, as shows Table 4.6. Note that in contrary to the calculations done with the first data set, the current calculations give better results for for the transition involving the $^5L_6$ level.

0-0 transition

As mentioned before the $^5D_0 \leftrightarrow {}^7F_0$ transition is strictly forbidden according to the standard Judd–Ofelt theory. The occurrence of this transition is a well-known example of the breakdown of the selection rules of the Judd–Ofelt theory, because this transition is forbidden by the selection rule of the theory.

There have been many attempts for a possible explanations of this transition; including the J-mixing or to mixing of low-lying charge-transfer states into the wavefunctions of the $4f^6$ configuration.

In our models of extension I and of the present model, the $^7F_0 \leftrightarrow {}^5D_0$ transition is allowed. With Babu's data [69] in extension I, the ratio between the theoretical and experimental OSs is equal to 20 in the third-order correction and 7.8 in the second-order correction (see subsection 4.1.3). With the present model, it goes down to 4.4 with or without the host dispersion (the theoretical OS is respectively 6.995×10^{-8} and 7.00×10^{-8}). This improved prediction is certainly due to the inclusion of all eigenvector components in both levels, especially the ^{3}P6 one, as mentioned in article [82]. Still, it is important to mention that, with the data set of Ref. [47], the ratio is very large, namely equal to 20.9 (the calculated OS is 3.13×10^{-8}).

4.3.2 Application to neodymium

Our ability to derive rather simple formulas for the OSs relies in particular on the approximation that all the levels of the first-excited configuration, namely $E_{t,u}$ in Eq. (4.4), are equal. In order to estimate the best possible value, we search for the range in which the ED coupling involving various levels of the ground configuration is strong. In figure 4.4, we plot the weighted free-ion absorption OSs in log scale, that is the OS multiplied by the degeneracy factor $2J_1 + 1$ of the lower level. That quantity is indeed proportional to the ED line strength and so to $(\langle 4f|r|5d\rangle)^2$. For $^4I_{9/2}$, the OS shows strong values between 70000 and 80000 cm^{-1}, and then it strongly drops. For the two other levels, no such trend is visible. But because the measured transitions in solids most often involve ^4I_J levels, we select 75000 cm^{-1} for the energy of excited configuration levels.

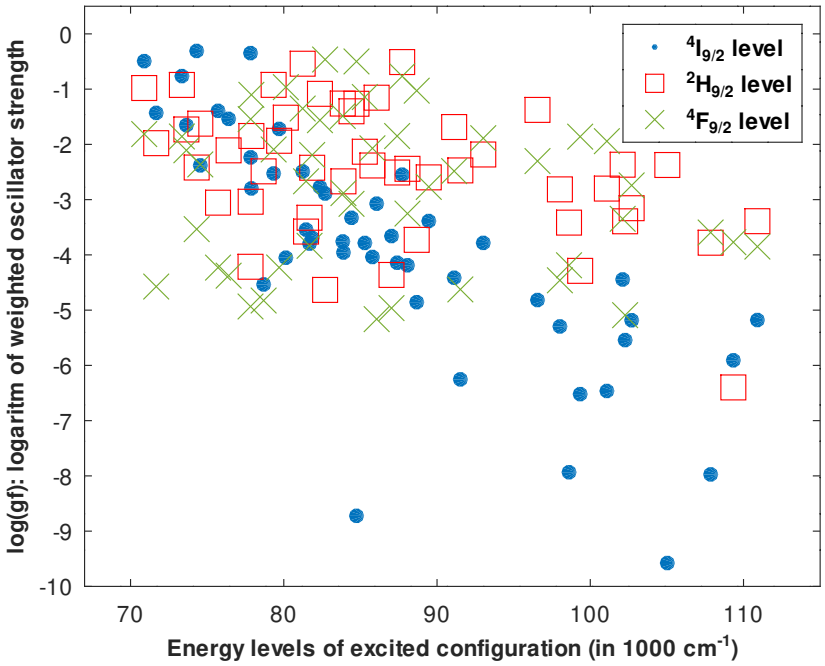

Figure 4.4: Logarithm of the weighted ED oscillator strengths, as functions of the energy of the excited-configuration levels, for transitions implying the $^4I_{9/2}$ (blue dots), $^2H_{9/2}$ (red squares) and $^4F_{9/2}$ (green cross) levels of the ground configuration of Nd^{3+}.

Nd^{3+} in $SrGdGa_3O_7$

For the purpose of testing the validity of the extension model we have chosen two experimental data set for Nd^{3+}. The first set of experimental oscillator strengths is taken from Zhang *et al.* [84], where the authors describe the growth of Nd:$SrGdGa_3O_7$ (Nd:SGGM) laser crystal by Czochralski method [85] and thermal properties, absorption and emission spectra were measured. In that work, the host refractive index is also measured at different wavelengths and fitted, using Sellmeier's equation (4.38) with $m = p = 1$, which will help in our further discussions since we intend to include the Sellmeier coefficients too. In the article of Zhang *et al.* nine absorption transitions were measured in σ and π polarizations, and the OSs were averaged with factors 2/3 and 1/3 to obtain unpolarized spectra. In our analysis we use the Tables IV and V of Ref. [84], we take as upper levels those written in the table rows where the OSs are written. In other words, we assume no overlapping transitions.

As for Eu^{3+} we calculate the JO parameters for Nd^{3+} as well. The results are shown in table 4.7. Note that, although, our theoretical value of standard JO parameter Ω_6 is different from the one reported by Zhang *et al.*, the general tendency of $\Omega_4 < \Omega_6$ reported in many other articles [86–91], is conserved.

When 9 transitions are included, the relative standard deviation is 23.78 % for the present model and 26.61 % for the standard JO one. Our model is slightly better, but the relative standard deviation remains large. This is certainly because there are several overlapping transitions that our code do not account for. In Ref [84], the authors obtain a relative standard deviation of 5.4 %. Those deviations are also visible

Table 4.7: Values of Judd-Ofelt parameters (in 10^{-20} cm^2) and X_k (in a.u.), calculated by us (Our), compared with values reported by Zhang *et al.* [84] and Chanthima *et al.* [86] (Rep.) for Nd^{3+}.

	X_1 (10^{-6} a.u.)	Ω_2 (10^{-20} cm^2)		X_3 (10^{-6} a.u.)	Ω_4 (10^{-20} cm^2)		X_5 (10^{-8} a.u.)	Ω_6 (10^{-20} cm^2)	
		Our	Rep.		Our	Rep.		Our	Rep.
Nd^{3+}:$SrGdGa_3O_7$ [84]	2.069	1.304	1.883	1.972	5.265	4.441	3.784	7.586	2.956
Nd^{3+}:CaO-BaO-P_2O_5 [86]	5.035	1.547	1.09	1.859	2.850	1.97	1.702	2.388	3.37

on the JO parameters, as shows Table 4.7.

Detailed comparisons between experimental and calculated OSs are presented in the top panel of figure 4.5 and the left column of Table 4.8. The figure gives a visual insight with histograms of the experimental OSs, and those resulting from our standard JO model and our present extension. The performances of the two models are similar. Table 4.8 shows the ratios between experimental OSs and calculated ones with the present model. The agreement is very good for the intense $^4I_{9/2} \leftrightarrow {}^4G_{5/2}$ transition, which according to Ref. [84] is isolated. This transition is usually referred as hypersensitive transition (HST) since it strongly depends on the ion-ligand bond environment and have influence on the magnitude of JO parameters. On the contrary, the transition $^4I_{9/2} \leftrightarrow {}^4D_{1/2}$ has a significantly larger experimental OS, certainly due to superimposition with transition peaks with upper states like $^4D_{3/2}$, $^4D_{5/2}$ and $^2I_{11/2}$ as described in the articles of Florez *et al.* [88], Singh *et al.* [92], in Ma *et al.* [89], or in Sardar *et al.* [93]. We see the same phenomenon with the transition $^4I_{9/2} \leftrightarrow {}^2H_{9/2}$: in many articles [88, 92–95], this transition is reported to be superimposed with a transition with upper state of $^4F_{5/2}$. Very often it is rather challenging to separate the properties of superimposed absorption bands. This can explain the difference between theoretical oscillator strengths (calculated with the standard and extended versions of the theory) and the experimental values.

Nd^{3+} in CaO-BaO-P_2O_5

We did similar calculations with another set of absorption transitions, reported in Chanthima *et al.*, where the authors do luminescence study and Judd-Ofelt analysis of CaO-BaO-P_2O_5 glasses doped with Nd^{3+} ions. For this glass we had difficulties to find the Sellmeier parameters, consequently the refractive index is assumed to be constant and equal to 1.556. When 11 transitions are included in the calculations, the relative standard deviation for standard JO calculation is 8.86 %. The resulting JO parameters are shown in table 4.8, with a comparison with values reported in the article. The relative standard deviation with the present model is 8.16 %, a little better than the JO one, and much better than the one obtained with the data of Zhang *et al.*.

The results of calculations for this data set are summarized in the bottom panel of figure 4.5 and in the right part of Table 4.7. They confirm that the overall agreement is better than for the data set of Zhang and coworkers [84], probably because there

Table 4.8: Transition labels and ratios between theoretical and experimental oscillator strength for Nd^{3+}, when the experimental data for the calculation is taken from [84] (left part) and [86] (right part). The last line presents the relative standard deviations for each calculation.

Transition Label	Nd^{3+}:$SrGdGa_3O_7$ Zhang [84]	Nd^{3+}:CaO-BaO-P_2O_5 Chanthima [86]
$^4I_{9/2} \leftrightarrow {}^4F_{3/2}$	3.18	1.13
$^4I_{9/2} \leftrightarrow {}^2H_{9/2}$	0.37	
$^4I_{9/2} \leftrightarrow {}^4F_{5/2}$		1.10
$^4I_{9/2} \leftrightarrow {}^4S_{3/2}$	1.49	
$^4I_{9/2} \leftrightarrow {}^4F_{7/2}$		0.95
$^4I_{9/2} \leftrightarrow {}^4F_{9/2}$	2.13	0.98
$^4I_{9/2} \leftrightarrow {}^2H_{11/2}$		0.59
$^4I_{9/2} \leftrightarrow {}^4G_{5/2}$	1.00	1.00
$^4I_{9/2} \leftrightarrow {}^4G_{7/2}$		0.81
$^4I_{9/2} \leftrightarrow {}^4G_{9/2}$	0.57	0.50
$^4I_{9/2} \leftrightarrow {}^2G_{9/2}$		0.21
$^4I_{9/2} \leftrightarrow {}^4G_{11/2}$	0.30	0.11
$^4I_{9/2} \leftrightarrow {}^2P_{1/2}$	1.55	1.21
$^4I_{9/2} \leftrightarrow {}^4D_{1/2}$	0.80	
$\sigma/\mathcal{S}_{\max}$	23.78 %	8.16 %

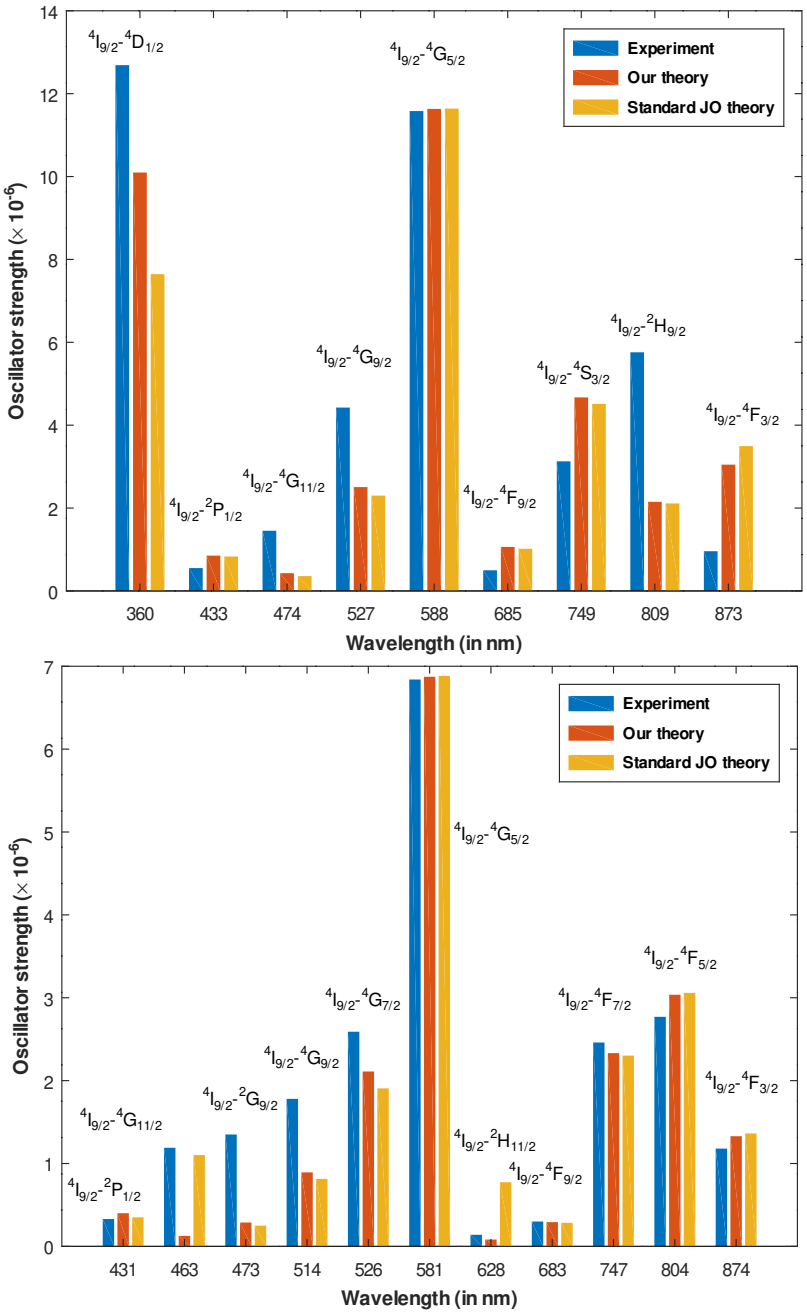

Figure 4.5: Comparison between experimental (top panel: [84], bottom panel: [86]) and theoretical oscillator strengths of absorption, plotted as function of the transition wavelength (not at scale). The transitions are labeled with the LS-term quantum numbers of the Nd^{3+} free ion.

are less overlapping transitions. Still, the OSs of the $^4I_{9/2} \leftrightarrow {}^2G_{9/2}$ and $^4I_{9/2} \leftrightarrow {}^4G_{11/2}$ transitions are strongly underestimated by our model (as in Table 2 of Ref. [86]), which may be due to the overlap with the upper level transitions at 22044 and 20005 cm^{-1}, respectively.

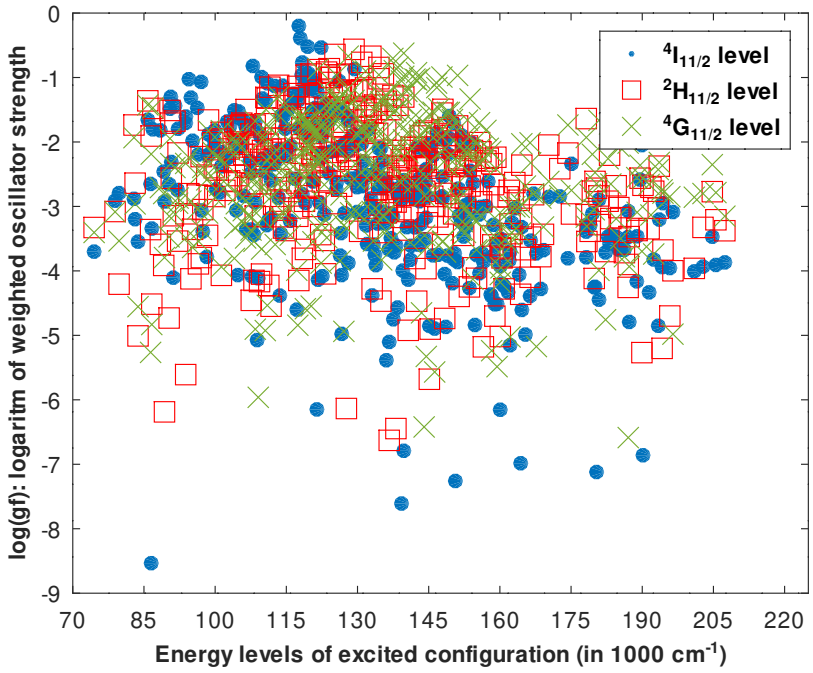

Figure 4.6: Logarithm of the free-ion weighted ED oscillator strengths, as functions of the energy of the excited-configuration levels, for transitions implying the $^4\mathrm{I}_{11/2}$ (blue dots), $^2\mathrm{H}_{11/2}$ (red squares) and $^4\mathrm{G}_{11/2}$ (green cross) levels of the ground configuration of Er^{3+}.

4.3.3 Application to erbium

In this section we perform extension calculations on Er^{3+}. The free-ion calculations are described in detail in section 3.3.

We have also calculated the matrix elements $\langle n'l'|r^k|nl\rangle$ for Er^{3+}, where $nl = 4f$ and $n'l' = 5d$. We obtain 0.96441 a_0, -2.37459 a_0^3 and 14.24536 a_0^5 for $k = 1$, 3 and 5, respectively, while the value calculated for this matrix element by Cowan codes is 0.9644014. Based on $\langle 4\mathrm{f}|r|5\mathrm{d}\rangle$, we plot on Figure 4.6 the logarithm of the weighted free-ion oscillator strengths as functions of the excited-configuration level energy, for transitions involving three $J = 11/2$ levels of the ground configuration. It shows that the energy band with strong transitions, in other words, the strong-coupling window for Er^{3+} is between 115000 and 160000 cm^{-1}. Therefore, as the excited-configuration energy $E_{t,u}$ in Eq. (4.4), we do not take the center-of-gravity energy of the excited-configuration, but a value of 145000 cm^{-1}.

Er^{3+} in $\mathrm{Lu_3Ga_5O_{12}}$

To investigate the viability of our extension theory for Er^{3+}. As a first set of OSs, we take the article by Liu *et al.* [96], where the authors report growth, refractive index dispersion, optical absorption and Judd-Ofelt spectroscopic properties of Er^{3+}-doped lutetium gallium garnet ($\mathrm{Lu_3Ga_5O_{12}}$) single-crystal. A fit of their measured refractive index with Eq. (4.39) gives $n_0 = 1$, $A = 2.72452$ and $B = 0.0172907$ $\mu\mathrm{m}^2$. Following

Table 4.9: Transition labels and ratios between theoretical and experimental line strength for Er^{3+}, when the experimental data for the calculation is taken from [96] and [97]. The last line presents the relative standard deviations for each calculation.

Transition Label	Er^{3+}:$Lu_3Ga_5O_{12}$ Liu [96]	Er^{3+}:$SrGdGa_3O_7$ Piao [97]
$^4I_{15/2} \leftrightarrow {}^4I_{13/2}$	0.87	0.88
$^4I_{15/2} \leftrightarrow {}^4I_{11/2}$	0.90	1.52
$^4I_{15/2} \leftrightarrow {}^4I_{9/2}$		0.93
$^4I_{15/2} \leftrightarrow {}^4F_{9/2}$	0.80	0.97
$^4I_{15/2} \leftrightarrow {}^4S_{3/2}$	1.33	1.14
$^4I_{15/2} \leftrightarrow {}^2H_{11/2}$	0.85	0.84
$^4I_{15/2} \leftrightarrow {}^4F_{7/2}$	2.83	1.53
$^4I_{15/2} \leftrightarrow {}^4F_{5/2}$		1.29
$^4I_{15/2} \leftrightarrow {}^2G_{9/2}$	2.34	1.67
$^4I_{15/2} \leftrightarrow {}^4G_{11/2}$	1.10	1.09
$^4I_{15/2} \leftrightarrow {}^2G_{7/2}$	3.07	
$^4I_{15/2} \leftrightarrow {}^4G_{9/2}$		0.93
$\sigma/\mathcal{S}_{\max}$	13.36 %	7.48 %

the discussion of Table 3.4, we cautiously examine the transition labels of the article.

The first challenge in this kind of calculations is to identify the lower and upper levels of a given experimental transition based on the free-ion calculations. For the transition labeled $^4I_{15/2} \leftrightarrow {}^2H_{9/2}$, Liu *et al.* report a wavelength of 410 nm, which corresponds to the energy level close to 245000 cm^{-1}. In our free-ion calculations (see Table 3.4) the dominant eigenvector component of this level is 24.3 % ^4F, but its largest LS term is ^2G.

We exclude from the fit the overlapping transitions $^4I_{15/2} \leftrightarrow {}^4F_{5/2,3/2}$, as well as the transition $^4I_{15/2} \leftrightarrow {}^4I_{9/2}$ because we obtain a very small ratio of $\sim 10^{-2}$ between calculated and experimental OSs.

The relative standard deviation with the JO model is 11.49 %; the one with our model is 13.36 %. The better performance of the standard JO model is visible for each transition of the left panel of Figure 4.7. Regarding the fitted parameters, we obtain negative values of X_3 and Ω_4, which is abnormal since all parameters should be positive. The Ω_4 value of Liu *et al.* [96], although positive, is small compared to the other Ω_λ. Their Ω_2 and Ω_6 strongly differ from ours.

Er^{3+} in $SrGdGa_3O_7$

The second set of experimental OSs, that we use to check the reliability of the extension model, is taken from the article of Piao *et al.*, where the authors describe optical and Judd-Ofelt spectroscopic study of Er^{3+}-doped strontium gadolinium gallium garnet single-crystal [97]. For this second set of absorption data we did the calculations

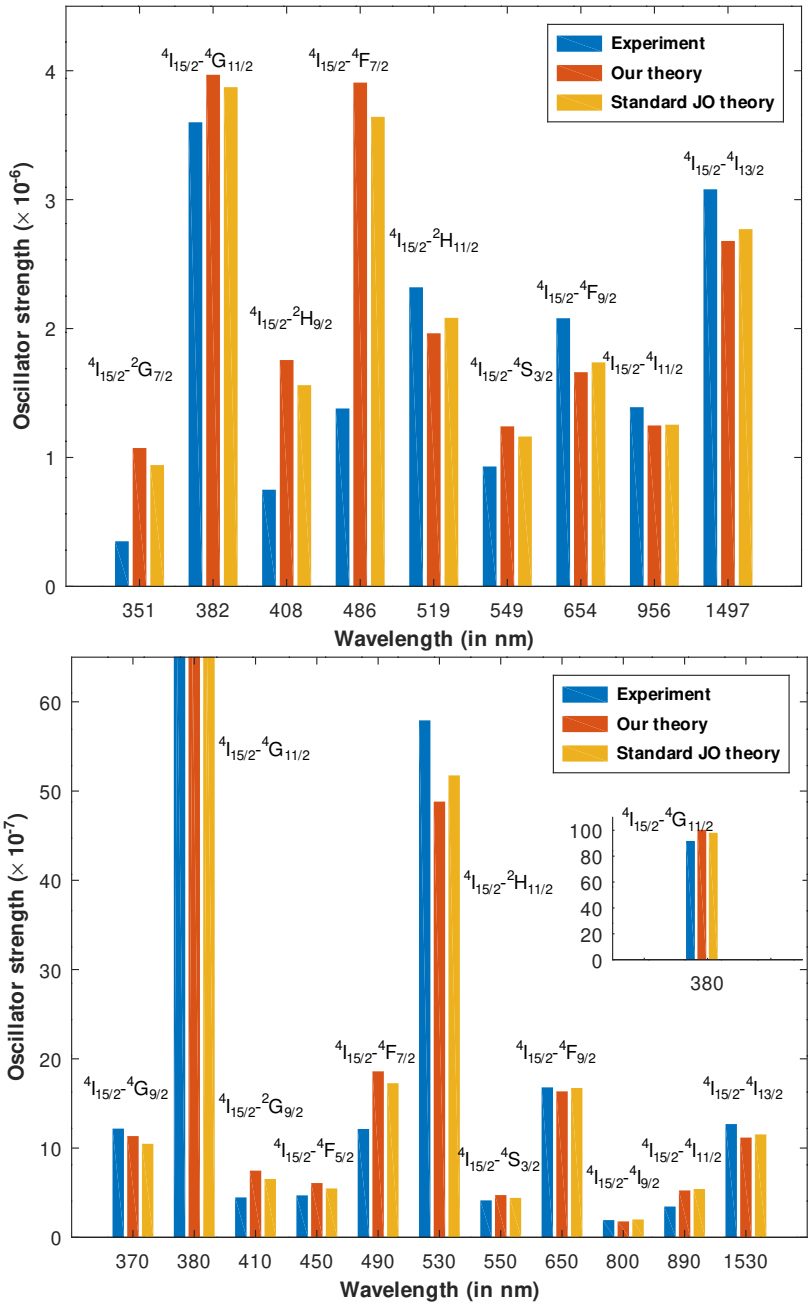

Figure 4.7: Comparison between experimental (top panel: [96], bottom panel: [97]) and theoretical oscillator strengths of absorption, plotted as function of the transition wavelength (not at scale). The transitions are labeled with the LS-term quantum numbers of the Er^{3+} free ion.

once, assuming the refractive index is constant and equal to 1.81014 for all wavelength values, since it was impossible to find values for Sellmeier coefficients for the crystal investigated in the article of Piao *et al.* [97].

The level identification for this data set was a bit delicate. This is especially the case for transitions $^4I_{15/2} \leftrightarrow {}^2H_{9/2}$ and $^4I_{15/2} \leftrightarrow {}^2G_{9/2}$ as identified in the article of

Table 4.10: Values of Judd-Ofelt parameters (in 10^{-20} cm^2) for Er^{3+}, compared with values reported in Liu *et al.* [96] and Piao *et al.* [97].

	X_1 (10^{-5} a.u.)	Ω_2 (10^{-20} cm^2)		X_3 (10^{-6} a.u.)	Ω_4 (10^{-20} cm^2)		X_5 (10^{-7} a.u.)	Ω_6 (10^{-20} cm^2)	
		Our	Rep.		Our	Rep.		Our	Rep.
Er^{3+}:$Lu_3Ga_5O_{12}$ [96]	17.11	2.095	0.89 ± 0.16	-13.82	-0.5706	0.16 ± 0.10	10.71	4.296	1.85 ± 0.25
Er^{3+}:$SrGdGa_3O_7$ [97]	19.17	2.792	2.46	11.97	0.8883	1.24	2.387	0.9541	0.51

Piao *et al.* However our free-ion calculations show that the first one should rather be identified as $^4I_{15/2} \leftrightarrow {}^2G_{9/2}$, and the second as $^4I_{15/2} \leftrightarrow {}^4G_{9/2}$. This is confirmed by the fact that the peak of the first transition is at 410 nm, which corresponds to the energy level value of 24300 cm^{-1}, having a first term of ^{4}F with 24.3% and two terms of ^{2}G with 19.0% and 14.9% percentages, making the term ^{2}G a dominant one with a percentage of 33.9%. The identification is possible because this level has ^{2}H term with a 16.6% (see table 3.4).

We have a tricky situation for the second absorption band as well, which in the article of Piao *et al.* is indicated to be at 370 nm, corresponding to the energy level of ∼27000 cm^{-1}. Our free-ion calculations show that the first and dominant LS term for this level is 79.5% ^{4}G, but it has a ^{2}G term with 0.4%, which makes the identification somehow possible (see table 3.4). It our calculations, however, we will use the labeling corresponding to our free-ion calculation results.

When 11 transitions were included the standard deviation with the JO model is 5.63 %, with our model it is 7.48 %. Table 4.10 shows results for JO parameters Ω_λ, in comparison with values reported in Piao *et al.* [97] as well as the fitting parameters X_k, which are all positive, and follow the trend $X_5 < X_3 < X_1$. Table 4.9 and figure 4.7 show, unlike the previous data set, a good match between the OSs of the $^4I_{15/2} \leftrightarrow {}^4I_{9/2}$ transition.

In this chapter, two versions of the Judd-Ofelt theory extension are presented, and then tested on lanthanide ions: first one on Eu^{3+} and version two on Eu^{3+}, Nd^{3+} and Er^{3+}. The version one not only shows good results on Eu^{3+}, but it also gives a simple physical insight into a transition that was forbidden by standard version of Judd-Ofelt theory. The extension theory is then improved by adding more eigenvector components and incorporating the wavelength dependence of the refractive index of the host material. Compared to version I, the spin-orbit interaction within the first excited configuration $4f^{w-1}5d$ is described in a perturbative way, whereas it is exactly taken into account in the ground configuration $4f^w$. This new model shows better results in the case of Eu^{3+}: not only it allows for interpreting more transitions that the standard Judd-Ofelt model, but it also reproduces more accurately the other oscillator strengths. For the two other ions, in one data set, we obtain comparable performances. But for one data set of Nd^{3+} [84], we observe large discrepancies that we expect to come from overlapping transitions involving close excited levels. To solve this problem, we will add in our code the possibility to treat such situations. In one data set of Er^{3+} [96], we observe some negative fitting parameters, whereas they are supposed

to be positive. That abnormal situation is all the more difficult to interpret that the Ω_4 parameter published in Ref. [96], though positive, is small compared to other parameters. As a prospect, we plan to treat transitions with polarized light or between individual ion-crystal sublevels. This will be possible in our model, because the only fitted parameters are the crystal-field ones. This can open the possibility to model the spectroscopic properties of Ln^{3+}-doped nanometer-scale host materials [51]. The latest version of the code with necessary input files are published on GitLab [98].

Part III

Neutral Lanthanides

Chapter 5

Experimental and theoretical study of a metastable level of erbium

Up to now, I have dealt with trivalent lanthanide ions in solids. In the next two chapters, I will focus on neutral lanthanide atoms in the context of ultracold gases. An ultracold atom is an atom with temperature near absolute zero. Typical temperatures of an ultracold gas is under $1\mu K$. In order to reach such temperatures, a combination of special techniques has to be used. As electromagnetic fields are used to probe the structure of internal states and the extension of such techniques are developed for spectroscopy to allow control the internal degrees of freedom coherently, the laser cooling and trapping techniques are used to do the same for external degrees of freedom of the atom [99]. Ultracold atoms are typically made by first trapping and pre-cooling via laser cooling in a magneto-optical trap. Further cooling is performed using evaporative cooling in a magnetic or optical trap. The first magneto-optical trap (MOT) was created by Raab *et al.* in 1987 [100], then, in 1997 the Nobel Prize was awarded to Steven Chu, Claude Cohen-Tannoudji and William D. Phillips for development of methods to cool and trap atoms with laser light. Four years after, in 2001, Eric A. Cornell, Wolfgang Ketterle and Carl E. Wieman got the Nobel Prize for the achievement of Bose-Einstein condensate in dilute gases of alkali atoms.

In order to have a greater control of ultracold atoms the interactions have to be considered strongly. The interaction type is dependent on the atomic species that are used. For example the alkali and alkaline-earth atoms interact via contact interactions [11, 101–104]. Lanthanides open up new opportunities for interactions, because of their large ground-state magnetic dipole moments [13]. This large magnetic moment leads to relatively strong dipole–dipole interactions. Lanthanides have multiple valence electrons and this gives a possibility of a rich excitation spectrum. Moreover, many lanthanides exhibit fine structure splitting even in their ground state. They are interesting candidates also because they have both bosonic and fermionic isotopes. f-d orbital transitions are of great interest, since they couple the ground level with opposite-parity excited ones. So far, laser cooling has been demonstrated for elements belonging to the right part of the lanthanide row, namely erbium [15, 16, 105, 106], dysprosium [17, 18, 107, 108], holmium [19], thulium [20, 21] and europium [22], as well as in erbium–dysprosium mixtures [23].

In high precision measurements and when controlling and manipulating atoms on a quantum level ultranarrow transitions are immensely important tools, the reason is their small spectral linewidth, which allows the high-resolution detection of energy shifts on very fine scales. Noteworthy examples are clock transitions in alkaline-earth-like atoms [109, 110]. In addition, these narrow transitions allow the optical manipulation and coherent control of ultracold atoms. It allowed the creation of ultracold molecules via Raman state transfer [111–113], the preparation of the atoms in different nuclear spin configurations [114], and the creation of spin-orbit coupled quantum gases [115–117]. Moreover, with the coherent excitation the realization of quantum computation and quantum simulations becomes possible, e.g., with neutral atoms loaded into optical lattices [118, 119].

As said before, lanthanides are multi-valence electron atoms and have a special electron configuration, in which the $6s$ shell is filled, while the lower-lying $4f$ and $5d$ subshells are open (see chapter 2). This characteristic leads to a large variety of transitions in these elements, whose with linewidths ranging from tens of μHz to tens of MHz. In addition to that they possess a magnetic moment in their ground state, which allows the combination of a narrow transition with a large magnetic moment. This chapter is dedicated to erbium. It is a lanthanide, a rare-earth element, originally found in the gadolinite mine in Ytterby, Sweden, which is the source of the element's name. A silvery-white solid metal when artificially isolated, natural erbium is always found in chemical combination with other elements. The electronic configurations of Er in its ground state reads as [Xe]$4f^{12}6s^2$, accounting for a xenon core, an open inner f shell with a two-electron vacancy, and a closed s shell. The corresponding total angular momentum is J=6, given by the sum of the orbital (L=5) and the spin (S=1) quantum number.

For the specific case of erbium, there is a prediction of a narrow inner-shell transition, which has a change in the total angular moment of $\Delta J = +1$ and a change in the total spin of $\Delta S = 1$. The transition involves the excitation of a $4f$ ground-state electron to a $5d$ state. Experimental observation of the narrow transition and theoretical study of that state is the main objective of the collaborative work done with the Austrian group of Francesca Ferlaino. The experimental findings were compared with our semi-empirical model. The first section of this chapter includes discussions on laser cooling and trapping of lanthanides atoms. Then I recall the experimental observations by the group in Innsbruck, Austria and the theoretical study of energy levels, extraction of the state lifetime. The chapter includes also calculation done to find the atomic polarizability, revealing few magic-wavelength conditions.

5.1 Laser cooling and trapping of lanthanide atoms

Lanthanides are open-shell atoms, which means that they have a rich internal structure with many $\Delta J = \pm 1$ transitions for laser cooling. The electrons in the f shell have a high orbital angular momentum $L = 3$. This partial occupancy can lead to ground state configurations with large total angular momentum [13]. There are many consequences of the large angular momentum of the ground state, such as the large magnetic

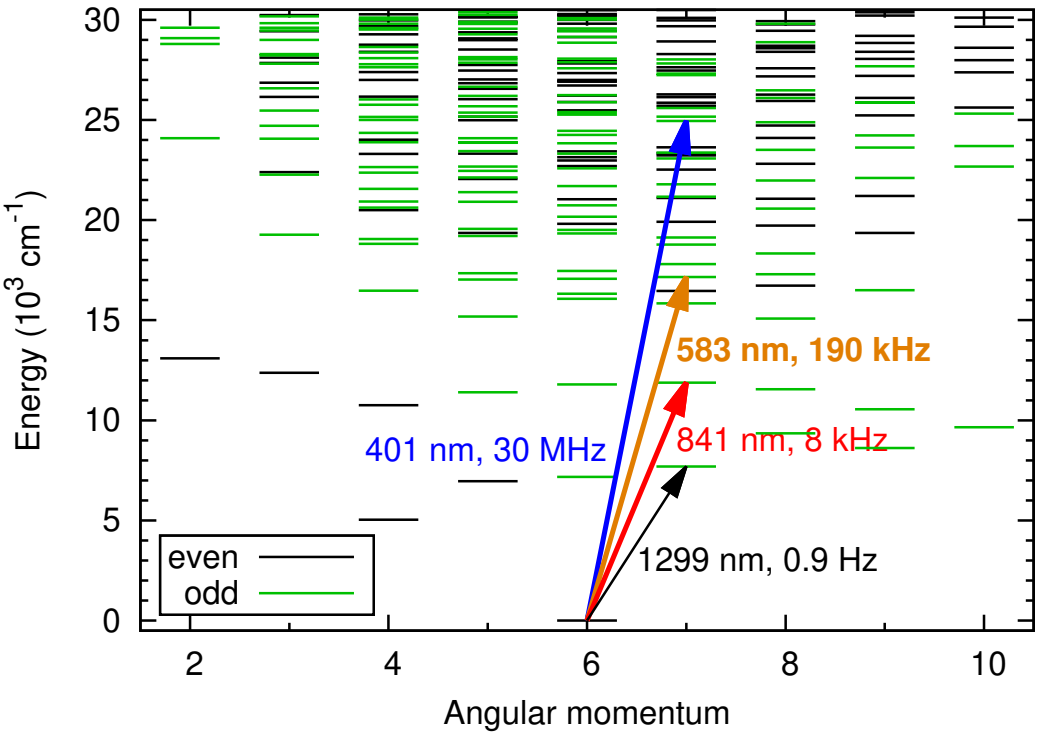

Figure 5.1: Energy levels of erbium, showing 3 possible laser cooling transitions. Adapted from [120].

moment, as well as the large number of accessible levels, and the resulting consequences for interparticle scattering. In order to analyze the laser cooling possibilities for a given atom, we need to analyze the energy spectrum and then the transition rates (or the Einstein coefficients). Moreover, associated lifetime and the natural linewidth determines many important quantities. Another important step in cooling is to take care of the optical leaks via spontaneous decay to other metastable levels instead of to the ground state. This decay can interfere with laser cooling, because it permits atoms to escape continued absorption and reemission process. This will lead to loss of atoms and will be unfavourable for the laser cooling. Possible optical leaks can be identified by discussing the selection rules for spontaneous emission and considering energy levels below the upper level of the transition in question.

Figure 5.1 shows energy levels of Er and three possible transitions for laser cooling. It is worth noting that this scheme is also valid for Dy, Ho, Tm. The ground state with a term $^3H_6$ is at $4f^{12}\ 6s^2$ configuration, which has an even parity and its total angular momentum is $J = 6$. It is preferential to consider transitions to odd parity excited states that have $J = 7$ angular momentum, since $J = 6$ is the largest angular momentum that the ground configuration can have and we are interested in transitions with $\Delta J = 1$ to avoid possible leakages. All the lower-lying states are accessible to common lasers. The $4f^{11}(4I^o_{15/2})5d_{3/2}6s^2\ (\frac{15}{2}, \frac{3}{2})^o_7$ level at 11887.503 cm^{-1} can be reached with a laser operating at 841nm. The $4f^{12}\ (^3H_6)$ 6s 6p $(^3P^o_1)\ (6,1)^o_7$ level at 17157.307

cm^{-1} can be reached with a laser operating at 583nm and, finally, the $4f^{12}$ $(^3H_6)$ 6s 6p $(^1P_1^o)$ $(6,1)_7^o$ level at 24943.272 cm^{-1} can be reached with a laser operating at 401nm. Generally speaking, while considering laser cooling, one has to start with a broader transition (the blue one in the case of Er), which is used to slow down hot atoms, then move to a narrower one (the yellow one), which is very common for reaching smaller temperatures. This is the usual way for other elements as well, but rarely the even narrower red one can be used too (see figure 5.1). Bellow the 841nm state there is an even-parity level, but it involves a forbidden J value. There are also some odd-parity levels, to which leakages are possible but they have forbidden J value or are separated by a small energy. For the 583nm level the leaks are possible, since the selection rule $\Delta J = 0, \pm 1$ are satisfied, but since these levels are very close and the Einstein coefficient will be extremely small these leakages are not happening. This is the case for 401nm level too. But as for the 583nm level, the available levels are either very close to each other or, very high in energy. Bellow the 1299nm state there are two even-parity levels with J values of 4 and 5, which forbids the electric dipole radiation.

In the current study we concentrate on the 1299nm opportunity, and for this we have performed spectroscopic calculations, that will allow us to perform lifetime and linewidth measurements. Those calculations are described in the next section. In the case of anisotropic trapping given ultracold atoms confined in a dipole trap are submitted to a potential with a depth, that is proportional to the real part of their dynamic dipole polarizability. Its imaginary part is associated with photon scattering rate. The response of non-spherically-symmetric atoms such as erbium to an electromagnetic field depends on its polarization and on the magnetic sublevel M_J. In the general case of an elliptically polarized light with unit vector of polarization e, the trapping potential is the following:

$$U_{M_J}^{ell}(\mathbf{r};\theta_p;\theta_k;\mathcal{A};\omega) = -\frac{1}{2\varepsilon_0 c} I(\mathbf{r}) \Bigg\{ Re[\alpha_{scal}(\omega)] + \mathcal{A} cos\theta_k \frac{M_J}{2J} Re[\alpha_{vect}(\omega)] + \frac{3M_J^2 - J(J+1)}{J(2J-1)} \times \frac{3cos^2\theta_p - 1}{2} Re[\alpha_{tens}(\omega)] \Bigg\}, \tag{5.1}$$

were ω and $I(\mathbf{r})$ are the angular frequency and intensity of the electromagnetic wave, ε_0 denotes the vacuum permittivity and c is the speed of light. θ_p is the angle between the light polarization and the z axis, while θ_k is the angle with the wave vector $\mathbf{k}$ and $\mathcal{A}$ is the ellipticity parameter. In equation (5.1) α_{scal}, α_{vect} and α_{tens} are, respectively, the scalar, vector and tensor dynamic dipole polarizabilities, given by:

$$\begin{aligned} Re[\alpha_{scal}(\omega)] &= \frac{1}{3(2J+1)} \sum_{\beta' J'} \frac{(E_{\beta' J'} - E_{\beta J}) |\langle \beta' J' \| P^{(1)} \| \beta J \rangle|^2}{(E_{\beta' J'} - E_{\beta J})^2 - \hbar^2 \omega^2} \\ Re[\alpha_{vect}(\omega)] &= 2 \sum_{\beta' J'} X_{JJ'}^{(1)} \frac{\hbar\omega |\langle \beta' J' \| P^{(1)} \| \beta J \rangle|^2}{(E_{\beta' J'} - E_{\beta J})^2 - \hbar^2 \omega^2} \\ Re[\alpha_{tens}(\omega)] &= -4 \sum_{\beta' J'} X_{JJ'}^{(2)} \frac{(E_{\beta' J'} - E_{\beta J}) |\langle \beta' J' \| P^{(1)} \| \beta J \rangle|^2}{(E_{\beta' J'} - E_{\beta J})^2 - \hbar^2 \omega^2}, \end{aligned} \tag{5.2}$$

where $X^{(k)}_{JJ'}$ are angular factors given by:

$$X^{(1)}_{JJ'} = (-1)^{(J+J')}\sqrt{\frac{6J}{(J+1)(2J+1)}}\left\{\begin{array}{ccc} 1 & 1 & 1 \\ J & J & J' \end{array}\right\}$$
$$X^{(1)}_{JJ'} = (-1)^{(J+J')}\sqrt{\frac{5J(2J-1)}{6(J+1)(2J+1)(2J+3)}}\left\{\begin{array}{ccc} 1 & 1 & 2 \\ J & J & J' \end{array}\right\} \quad (5.3)$$

It is shown that polarizability is very sensitive to configuration-interaction coefficients [121], hence the necessity to calculate the former as precisely as possible.

5.2 Description of calculations

The goal of our theoretical calculations is to improve configuration interaction parameters and transition dipole moments in comparison with [122] and [123]. In the previous studies, the 4f-5d integrals could not be considered as free parameters, because the fit did not converge. It was constrained to the 6s-6p integral. The idea of improving the energy fit, with more free CI parameters, can give possibilities for an improvement of the eigenvector precision. Since for possible laser cooling techniques we need to have a good data on energy levels and then Einstein coefficients, eigenvector precision is crucial. Einstein coefficients necessary for discussion of laser cooling will be fitted using FitAik package [124].

I have done the spectroscopic calculations of energy levels. The calculations done on neutral erbium are based on the semi-empirical method provided by the COWAN suite of codes [58] and the methodology is described in section 3.1. To recall briefly: ab initio radial wavefunctions are computed with the relativistic Hartree-Fock (HFR) method for all the subshells of the considered configurations. Then energy parameters are calculated using those wave functions and these parameters, being the building blocks of the atomic Hamiltonian, these parameters are adjusted in the next step so that calculated eigenvalues are in a good agreement with the experimental ones. This last step is a least squares fitting, where we use the experimental levels of the NIST database as experimentally known levels. In the NIST database the main source is Martin *et al.* [59]. With the help of wave functions it is possible to calculate the mono-electronic transition integral, that have the following form $\langle n\ell|r|n'\ell'\rangle = \int P_{n\ell}(r) r P_{n'\ell'}(r) dr$ and are pivotal in calculations of A_{ik} Einstein coefficients for spontaneous emission.

To calculate the polarizability of this excited state, a ground state data set is also required. During the calculations the even electronic configurations are separated into three groups: $4f^{12}\ 6s^2 + 4f^{12}\ 5d\ 6s + 4f^{11}\ 6s^2\ 6p$, $4f^{12}\ 6s^2 + 4f^{11}\ 5d\ 6s\ 6p$ and $4f^{12}\ 6s^2 + 4f^{12}\ 6s\ 7s + 4f^{12}\ 6s\ 6d + 4f^{12}\ 6p^2$. Each group is associated with a different least-square fitting calculation with experimental levels belonging to the corresponding configurations. The calculation is carried out using the Kramida version of the COWAN codes [57].

Compared to Refs. [122, 123], the odd-parity level calculations have been improved by adding some high-lying experimental energy levels that were previously excluded

from the fitting procedure, as well as incorporating a larger number of free configuration-interaction (CI) parameters into the fitting procedure. The following configurations are included in the calculation: $4f^{11}$ 5d $6s^2$, $4f^{11}$ $5d^2$ 6s, $4f^{12}$ 6s 6p, $4f^{12}$ 5d 6p and $4f^{13}$ 6s. The latter is included for technical purpose, but does not play a physical role. The fitting procedure is performed using a total of 30 free groups of parameters and 219 levels. The calculation results on level values can be found in table 5.1, where we present few energy levels smaller than 30000 cm^{-1} for $4f^{11}$ 5d $6s^2$, $4f^{11}$ $5d^2$ 6s, $4f^{12}$ 6s 6p, and $4f^{13}$ 6s configurations of neutral erbium and their comparison with NIST database values [52]. Table also contains theoretical Lande-g factors compared with experimental ones (if possible) and the dominant terms with their percentages. In the table we use the following abbreviations: $4f^{12}$ $6s^2$ = A-6s2, $4f^{11}$ 5d $6s^2$ = B-ds2, $4f^{11}$ $5d^2$ 6s = B-ds2 and $4f^{12}$ 6s 6p = A-s6p.

Table 5.1: Comparison between the experimental and computed values for some levels of neutral Er. The levels are chosen such that the table includes energy levels from each configuration. All energy levels are in cm^{-1}.

Conf.	J	Energy		Landé g		Dom. term	
		Theory	Exp.	Theory	Exp.		
A-6s2	4	5034	5035	1.141	1.147	^{3}F	63%
A-6s2	4	10755	10751	0.944	0.936	^{3}H	62%
A-6s2	3	12378	12378	1.084	1.065	^{3}F	100%
A-6s2	2	13099	13098	0.740	0.750	^{3}F	80%
B-ds2	6	7190	7177	1.305	1.302	^{5}G	77%
B-ds2	9	8610	8621	1.137	1.150	^{3}L	46%
B-ds2	10	9652	9656	1.197	1.194	^{5}L	95%
B-ds2	7	11880	11888	1.150	1.153	^{3}I	48%
B-ds2	5	15228	15185	1.172	1.160	^{3}G	54%
A-s6p	6	16337	16321	1.239	1.220	^{5}G	52%
A-s6p	7	17135	17157	1.189	1.195	^{5}I	40%
A-s6p	8	18325	18335	1.250	1.250	^{5}I	98%
B-ds2	4	19014	19048	1.014	1.010	^{3}G	28%
A-s6p	6	19349	19327	1.175	1.180	^{5}H	31%
B-d2s	6	20200	20166	1.475	1.485	^{7}F	78%
B-ds2	7	21168	21168	1.061	1.065	^{3}K	33%
B-d2s	8	21935	21979	1.294	1.295	^{7}H	35%
A-s6p	3	22277	22269	1.065	1.065	^{3}G	16%
B-d2s	6	22556	22450	1.375	1.360	^{7}F	36%
B-d2s	11	23455	23473	1.216	1.215	^{7}M	49%
A-s6p	6	23842	23831	1.247	1.250	^{5}G	56%
A-s6p	5	24061	24083	1.123	1.128	^{3}G	45%

Table 5.1 Continued

Conf.	J	Energy		Landé g		Dom. term	
		Theory	Exp.	Theory	Exp.		
B-ds2	3	24689	24713	0.974	0.970	^{3}G	48%
B-d2s	11	24759	24754	1.241	1.235	^{7}L	64%
A-s6p	7	24968	24943	1.146	1.160	^{3}I	57%
B-ds2	5	25195	25163	1.010	1.010	^{3}I	25%
B-d2s	10	25311	25319	1.194	1.190	^{7}L	29%
A-s6p	7	25591	25598	1.166	1.155	^{3}I	39%
B-ds2	4	25800	25754	0.981	0.955	^{3}H	24%
B-d2s	8	26035	26093	1.334	-	^{7}H	58%
A-s6p	5	26240	26199	1.069	1.045	^{5}H	49%
B-ds2	3	26606	26585	1.346	1.360	^{5}D	31%
B-d2s	7	27367	27307	1.245	1.225	^{7}H	27%
A-s6p	4	27791	27777	1.039	1.020	^{5}I	15%
B-d2s	4	27946	28083	1.060	1.075	^{7}F	9%
B-ds2	7	28119	28018	1.072	1.080	^{3}K	23%
B-ds2	3	28271	28290	1.155	1.140	^{5}F	25%
A-s6p	2	28848	28790	0.625	0.630	^{5}G	34%
B-d2s	6	29054	29153	1.198	1.175	^{7}H	13%
B-ds2	2	29099	29080	0.812	0.830	^{5}G	42%
A-s6p	2	29060	29595	1.171	1.170	^{5}G	34%
B-d2s	6	29655	29561	1.115	1.175	^{3}I	8%
B-d2s	8	29727	29805	1.132	-	^{5}I	11%
A-s6p	4	29861	29974	1.090	-	^{5}H	19%
A-s6p	1	29927	29940	0.260	0.270	^{5}F	63%

The standard deviation between experimental and calculated energies is equal to 53 cm^{-1}, which is satisfactory for a semi-empirical calculation. Tables 5.2 and 5.3 show non configuration-interaction (non CI) parameters, constraints and the scaling factors of these parameters ($f_X = X_{\text{fit}}/X_{\text{HFR}}$) for odd parity configurations of neutral Erbium. The $4f^{13}$ 6s configuration is not included here because we do not have experimental levels for the $4f^{13}$ 6s configuration. The flags for energy parameters are set according to the article [122], the configuration-interaction (CI) parameter flags are set to be free progressively by groups (depending on the nature of the interactions). Table 5.4 shows configuration-interaction (CI) parameters, constraints and the scaling factors of these parameters.

Then, the $\langle nl|r|n'l'\rangle$ transition integrals were adjusted, especially the transitions involving levels of ground state configurations [Xe]$4f^{12}$ $6s^2$. For this purpose the A_{ik}

Table 5.2: Parameters, constraints (const.), fitted parameters and their scaling factors ($f_X = P_{fit} \ / \ P_{HFR}$) for $4f^{11}$ 5d $6s^2$ and $4f^{11}$ $5d^2$ 6s configurations of neutral Er. All parameters are in cm^{-1}.

Parameter P	Constr.	P_{fit}	f_X	P_{fit}	f_X
		$4f^{11}$ 5d $6s^2$		$4f^{11}$ $5d^2$ 6s	
E_{av}		46412		65531.6	
F^2(4f 4f)	r_1	98177.6	0.761	98004.7	0.761
F^4(4f 4f)	r_2	69264	0.856	69134	0.856
F^6(4f 4f)	r_3	50068	0.861	49972.2	0.861
α	r_4	20		20	
β	fix	-650		-650	
γ	fix	2000		2000	
F^2(5d 5d)				21668.3	0.663
F^4(5d 5d)				17208.2	0.831
ζ_{4f}	r_5	2389.8	0.984	2387.8	0.984
ζ_{5d}	r_6	788.2	0.831	652.6	0.831
F^1(4f 5d)	r_7	741.7		741.7	
F^2(4f 5d)	r_8	15711.7	0.775	13597.8	0.775
F^4(4f 5d)	r_9	10558.2	1.149	8970.9	1.149
G^1(4f 5d)	r_{10}	5054.1	0.580	4325.8	0.580
G^2(4f 5d)	r_{11}	1717.4		1717.4	
G^3(4f 5d)	r_{12}	6400.3	0.928	5422.6	0.928
G^4(4f 5d)	r_{13}	1630.6		1630.6	
G^5(4f 5d)	r_{14}	3809.7	0.732	3216.7	0.732
G^3(4f 6s)	r_{15}			1254.3	0.844
G^2(5d 6s)	r_{17}			11696.8	0.609

coefficients of Ref. [125] are used as experimentally known values. The goal is to minimize the standard deviation on Einstein coefficients, but the fact that the latter is highly sensitive to $\langle 4f|r|5d\rangle$ makes the finding of such an integral difficult, especially since it was not possible to set free that integral. In order to overcome that issue a scaling factor with respect to the HFR integral equal to $f_{4f,5d} = 0.95$ was chosen based on calculation done on Dy [126] and Ho [121]. After the fitting procedure, $\langle 6s|r|6p\rangle$ is found to be $f_{6s,6p} = 0.768$. The polarizability of the excited level also depends on $\langle 5d|r|6p\rangle$, for which we took a scaling factor of 0.8.

With this optimized set of energies and transition integrals, we have calculated the polarizabilities of the ground and excited states using the sum-over-state formula coming from second-order perturbation theory. From our theory we obtain a wavenumber of $\nu_{th} = 7729.3$ cm^{-1}, a factor of $g_J = 1.2622$, and an excited-state lifetime of $\tau_{th} =$ 602 ms. For ν_{th} and g_J we find satisfactory agreement with the values reported from the experiment. Note that, by included least-square fitted energy parameters in the theoretical calculations, we obtain better agreement with the experimental data. Our theoretically obtained result of 602 ms for the lifetime is about a factor of 3 longer compared to the experimentally measured value. This discrepancy comes from the fact

that the underlying transition dipole moment involves small components in the eigenvector associated with the excited level. Those small components are more difficult to optimize, as they are less affected by the least-square fitting procedure on energies.

The results on calculated polarizability α (in a.u.) is shown in figure 5.4 in a broad wavelength range from 350 nm to 1500 nm. The polarizability spectrum becomes very dense at lower wavelengths. A very important ingredient for the coherent control of two two-level system is the atomic polarizability of each state, as well as the ratio between the polarizability of each state.

The bottom panel of figure 5.4 shows interesting regions of wavelengths where the polarizabilities of the excited and ground state cross, which means that atoms in both states will experience the same optical trapping potential. These specific values of the wavelength produce so called *magic* conditions.

Table 5.3: Parameters, constraints (Constr.), fitted parameters and their scaling factors ($f_X = P_{fit}$ / P_{HFR}) for $4f^{12}$ 6s 6p and $4f^{12}$ 5d 6p configurations of neutral Er. All parameters are in cm^{-1}.

Parameter P	Constr.	P_{fit}	f_X	P_{fit}	f_X
		$4f^{12}$ 6s 6p		$4f^{12}$ 5d 6p	
E_{av}		36278.6		60020.5	
F^2(4f 4f)	r_1	92716.3	0.761	92496.8	0.761
F^4(4f 4f)	r_2	65123.3	0.856	64956.1	0.856
F^6(4f 4f)	r_3	46996.3	0.861	46876.2	0.861
α	r_4	20		20	
β	fix	-650		-650	
γ	fix	2000		2000	
ζ_{4f}	r_5	2250.3	0.984	2250.3	0.985
ζ_{5d}	r_6			454.7	0.831
ζ_{6p}	r_{18}	1513	1.461	1119.6	1.461
F^1(4f 5d)	r_7			741.7	
F^2(4f 5d)	r_8			11092.6	0.775
F^4(4f 5d)	r_9			7222.8	1.149
F^1(4f 6p)	fix	100		150	
F^2(4f 6p)	r_{19}	3776.9	1.156	3006.1	1.151
F^2(6p 5d)	fix			11470.1	0.794
G^1(4f 5d)	fix			3897.8	0.585
G^2(4f 5d)	fix			1091.6	
G^3(4f 5d)	fix			4397.4	0.895
G^4(4f 5d)	fix			1028.3	
G^5(4f 5d)	fix			2761.2	0.761
G^3(4f 6s)	r_{15}	1405.1	0.843		
G^2(4f 6p)	r_{19}	864.4	1.155	656.3	1.155
G^4(4f 6p)	r_{19}	751.9	1.156	568.2	1.157
G^1(6s 6p)		12209.7	0.522		
G^1(6p 5d)	fix			7880	0.600
G^3(6p 5d)	fix			5052	0.600

Table 5.4: Configuration-interaction parameters, constraints (Constr.), fitted parameters and their scaling factors ($F_s = P_{fit} \ / \ P_{HFR}$) even configurations of neutral Er. All parameters are in cm^{-1}.

Parameter P	Constr.	P_{fit}	F_s
		$4f^{11}$ 5d $6s^2$ - $4f^{11}$ $5d^2$ 6s	
R^2 (4f 6s, 4f 5d)	r_{21}	-799.8	0.852
R^3 (4f 6s, 4f 5d)	r_{21}	1128.5	1.465
R^2 (5d 6s, 5d 5d)	r_{17}	-13663.3	0.621
		$4f^{11}$ 5d $6s^2$ - $4f^{12}$ 6s 6p	
R^1 (5d 6s, 4f 6p)	r_{20}	-3173.6	0.461
R^3 (5d 6s, 6p 4f)	r_{20}	-679.9	0.461
		$4f^{11}$ $5d^2$ 6s - $4f^{12}$ 6s 6p	
R^1 (5d 5d, 4f 6p)	r_{22}	2405.6	0.647
R^3 (5d 5d, 4f 6p)	r_{22}	643.7	0.647
		$4f^{11}$ $5d^2$ 6s - $4f^{12}$ 5d 6p	
R^1 (5d 6s, 4f 6p)	r_{22}	-2536.8	0.427
R^3 (5d 6s, 4f 6p)	r_{22}	-564.5	0.427
		$4f^{12}$ 6s 6p - $4f^{12}$ 5d 6p	
R^2 (4f 6s, 4f 5d)	r_{23}	-5359.9	
R^3 (4f 6s, 5d 4f)	r_{23}	2758.3	
R^2 (6s 6p, 5d 6p)	r_{22}	-6833.7	
R^1 (6s 6p, 6p 5d)	r_{22}	-7463.2	

5.3 Experimental measurements and comparison with theoretical results

The experimental part of the joint project was implemented by the Erbium group of Francesca Ferlaino from the University of Innsbruck, Austria [127]. They reported on the observation and coherent excitation of atoms on the narrow inner-shell orbital transition, connecting the erbium ground state [Xe]$4f^{12}$ ($^3H_6$)$6s^2$ to the excited state [Xe]$4f^{11}$ $(^4I_{15/2})^0 5d(^2D_{3/2})6s^2(15/2, 3/2)^0_7$.

The experimentalists of Innsbruck group observe the transition at 1299 nm for the bosonic isotopes ^{164}Er, ^{166}Er, ^{168}Er, and ^{170}Er and for the fermionic isotope ^{167}Er. The search for this narrow inner-shell transition is done by performing measurements on trapped quantum degenerate erbium gas. An erbium Bose-Einstein condensate (BEC) is created when atoms are loaded into an optical dipole trap operating at 1064 nm after being laser cooled in a magneto optical trap. The BEC is then created by evaporative cooling down to quantum degeneracy. The BEC typically contains $N = 2 \times 10^4$ atoms. To ensure that the atomic cloud remains spin-polarized in the lowest Zeeman level, a homogeneous magnetic field is applied. The light for driving the narrow inner-shell

transition is generated from an external-cavity diode laser (ECDL) operating at 1299 nm.

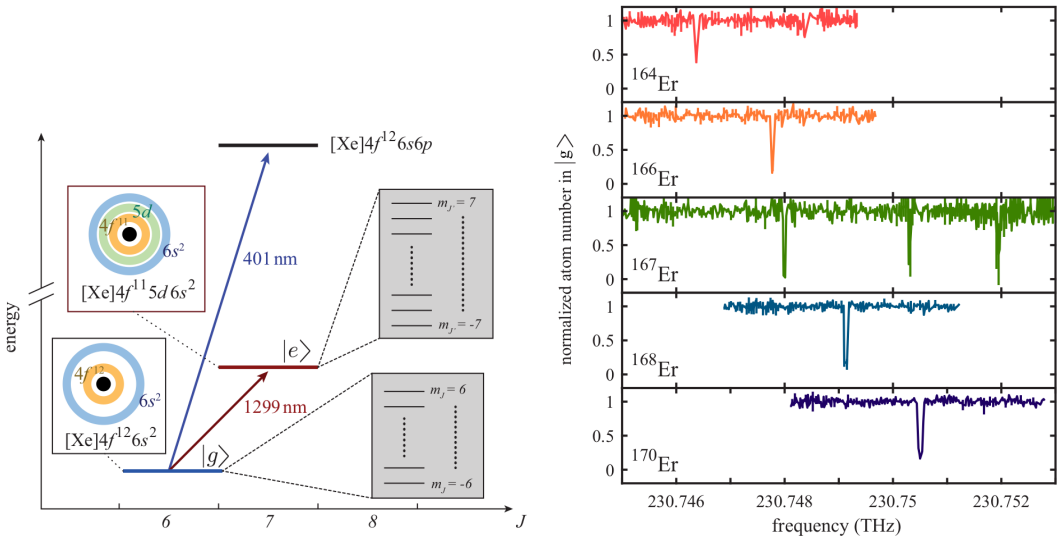

Figure 5.2: *Left panel*: Schematic level scheme illustrating the inner-shell orbital transition at 1299 nm, and the transition at 401 nm used for absorption imaging. The horizontal lines indicate the energy levels for ground (blue, even parity), excited (red, odd parity), and the state at 401 nm (black, odd parity). The grey boxes are Zeeman manifolds. Energies are not presented on scale. *Right panel*: Coarse spectroscopy results for the four bosonic isotopes and one fermionic one.

After 1299nm spectroscopy light was shine on the sample and after an irradiation time of 100 ms, the atoms are released from the trap for 30 ms. The number of ground state atoms are recorded by performing absorption imaging with resonant light at 401 nm (see the left panel of figure 5.2). The tabulated frequency is $\nu_{\mathrm{NIST}} = 230.738$ THz ($= 7696.956\ \mathrm{cm}^{-1}$), and each repetition of the measurements have a 40 MHz step size. The results are shown in the right panel of figure 5.2. As expected, all the bosonic isotopes (^{164}Er, ^{166}Er, ^{168}Er, and ^{170}Er) have one absorption line, since their nuclear spin is 0, on the other hand, the fermionic isotope ^{167}Er shows three resonances corresponding to three transitions, since it possesses a hyperfine structure ($I = \frac{7}{2}$ and the resonances are attributed to $F' = 21/2$, $19/2$ and $17/2$.

The next step is the high resolution spectroscopy measurements with a much higher spectral resolution and lower laser intensity, allowing also to resolve the magnetic Zeeman sublevels. After sample preparation, all trapping lights are switched off, and the prepared sample is irradiated with a 1299 nm spectroscopy pulse of 1 ms, corresponding to a Fourier limited linewidth of 800 Hz. The light contains contributions from all light polarizations, such that the 1299-nm beam can induce σ^+ , σ^-, and π transitions. Using a wavemeter the absolute wavenumber is determined to be $\nu = 7696.955(2) cm^{-1}$. From our theory we obtain a wavenumber of 7729.3 cm^{-1}. The relatively long wavelength of the transition is advantageous for studies of collective scattering from ordered atomic samples. This transition allows the coherent control of magnetic Zeeman levels for dipolar bosonic atoms.

An important quantity to describe the atomic interaction with an external magnetic field, or the interaction between different atoms via their magnetic dipoles and to benchmark atomic spectrum calculations is the Lande g_j factor, which is extracted with the following formula:

$$g_j = \frac{(\nu^{\sigma+} - \nu^{\pi})h}{\mu_b B}, \tag{5.4}$$

where B is the applied magnetic field, μ_b is the Bohr magneton and h is the Planck constant. Experimentally measured g_j value of the excited state is $g_j = 1.2599(5)$, while in the NIST database it is 1.266. On the other hand, we calculated the Landé g factor to be 1.2622, while the experimental group measured it as 1.2599(5). This agreement is very satisfactory and is consistent with the NIST database value.

In addition to g_j factor, the high resolution spectroscopy allows the experimentalists to extract the isotope shift with high precision. It is the shift in various forms of spectroscopy that occurs when one isotope is replaced by another. Generally they are caused by the field shift (that arise from the change of the nuclear size) and the mass shift (caused by the change of the mass). In the case of erbium, involved $4f \leftrightarrow 5d$ transition, both contributions are large. The discussion of possible isotope shifts can provide an exceptional insight into intranuclear interactions. Erbium is an interesting potential candidate, because it has four isotopes with zero nuclear spin and a large number of different narrow transitions. Table 5.5 gives the results on isotope shifts,

Isotope pair	$\nu_0 - \nu_0^{168}$ (MHz)
164 - 168	–2732.290(3)
166 - 168	–1371.710(3)
170 - 168	1414.920(5)

Table 5.5: Isotope shifts for three bosonic isotopes in dependence of the ^{168}Er isotope.

where the error bars denote the statistical error, mainly given by uncertainties of B, but it can not be compared to theory.

Another important opportunity arises with narrow line transitions and plays a fundamental role, e.g., in quantum information and communication protocols, is the possibility to coherently control the atomic state. The coherent control allows to transfer atoms from ground state to excited state with an efficiency higher than 97%. This high efficiency opens the possibility to measure the lifetime of atoms in excited state. The mean lifetime of the excited state is experimentally measured to be $\tau = 178(19)$ ms. Theoretically we have obtained an excited-state lifetime of $\tau_{th} = 602$ ms. The disagreement comes from the fact that there are small components in the eigenvector originating from the excited level in the underlying transition dipole moment.

The experimentalists carried out trap frequency measurements to determine the atomic polarizability of the excited state relative to the ground state with the trapping light at 532.2 nm. They were able to get close to a magic-wavelength condition, where the ground and excited states feature the same polarizability. Finally, with already optimized set of energies and transition integrals, we have calculated the polarizabilities

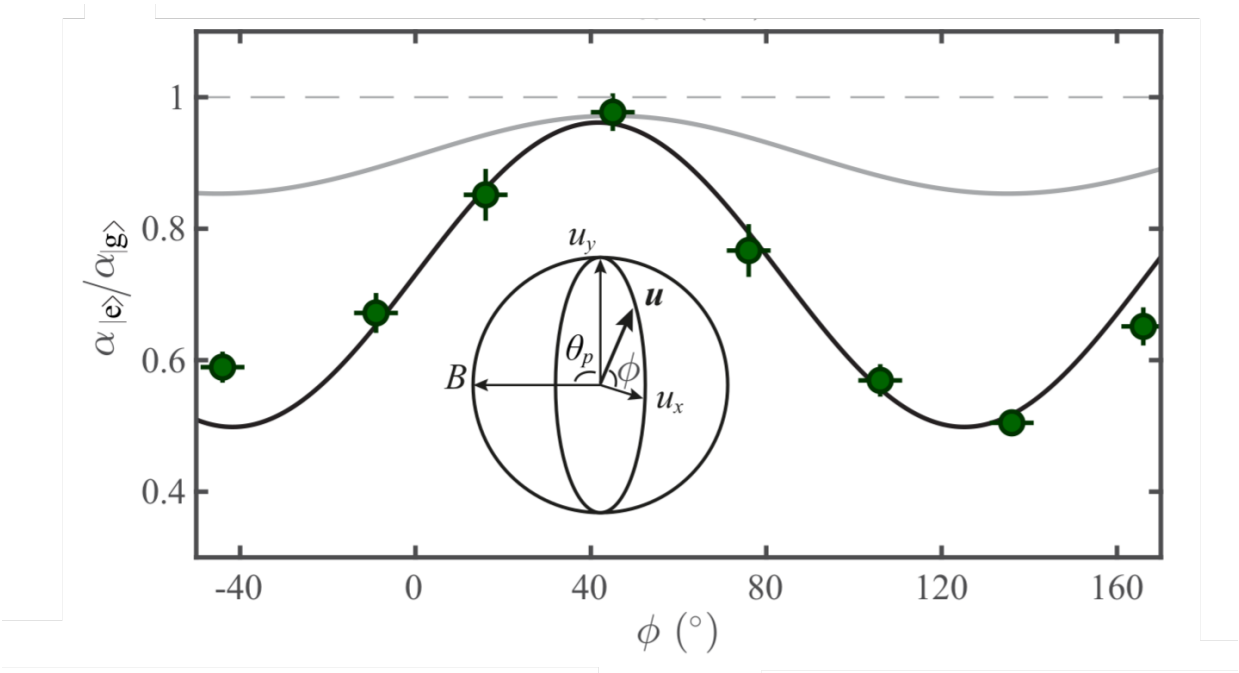

Figure 5.3: Polarizability ratio $\alpha_{|e\rangle}$ / $\alpha_{|g\rangle}$ for different polarizations of the trapping light defined by the angle ϕ between u and the optical axis of the λ / 4 waveplate. The black solid line is a guide to the eye based on a sinusoidal fit to the experimental data and the grey solid represents theoretical results obtained from the sum-over-states method. The inset illustrates the experimental configuration for the shown data.

of the ground and excited states using the sum-over-state formula coming from second-order perturbation theory. In our calculations, we were able to confirm the magic trapping condition at 532 nm, and we have also predicted several alternative options for magic wavelengths.

Another interesting exploration is the impact of the vectorial polarizability on the ratio α_e/α_g for a commonly used trapping wavelength of 532.2 nm. In order to study the impact of the vectorial polarizability, α_e/α_g is measured for different polarization of the light at 532.2 nm. In each measurement the orientation of the polarization vector u with respect to B is $\theta = 90°$, while the angle ϕ defining the polarization vector of the laser field is varied. A periodic behaviour of α_e/α_g is observed and at angle $\phi = 45°$, the ratio is 0.98(3). Theoretical value for $(\alpha_e/\alpha_g)_{th}$ is 0.97, moreover theory predicts crossings at 528.9 nm and 532.5 nm, which are interesting options to explore with tunable laser systems.

Figure 5.3 summarizes the results. A periodic behaviour of $\alpha_{|e\rangle}$ / $\alpha_{|g\rangle}$ as a function of ϕ is observed. It reaches its maximum for σ^- polarized light ($\phi = 45°$). The figure also has theoretical calculation results, which qualitatively reproduces the experimental values, although with a smaller amplitude, which might indicate a shift of the close by transition as well as an underestimation of the transition strength.

The summary of results and comparison is shown on table 5.6.

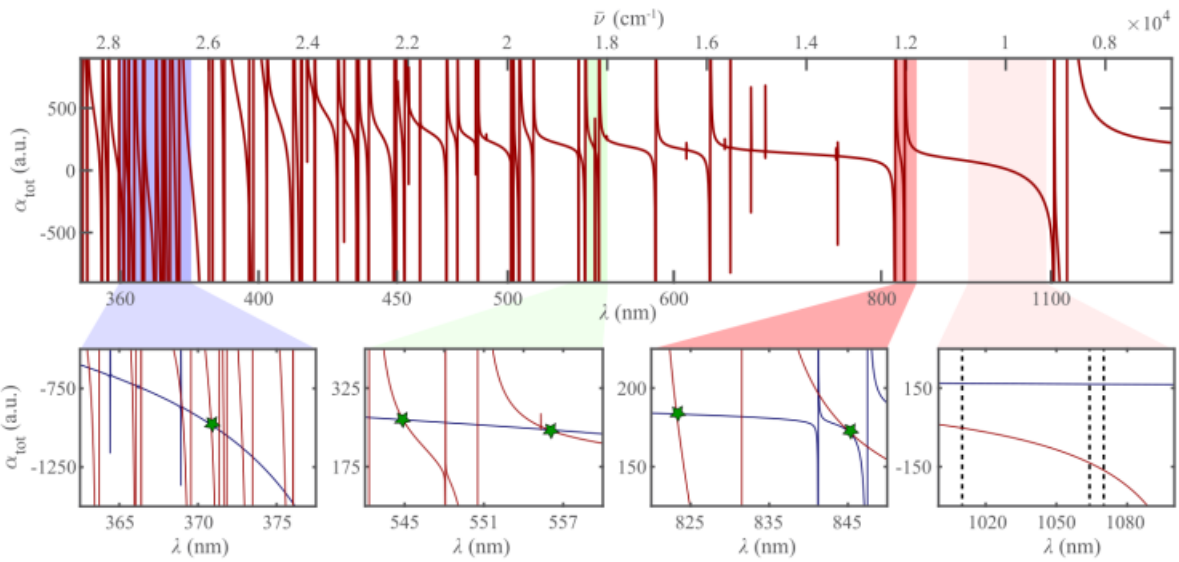

Figure 5.4: *Top panel*: Theoretically calculated polarizability for the excited state as a function of the wavelength. *Bottom panel*: Zoom-in into different wavelength regions to show polarizability of ground (blue) and excited (red) states. The green stars are possible magic wavelengths.

	Experiment	Theory
Landé g	1.2599(5)	1.2622
Absolute wavenumber	7696.955(2) cm^{-1}	7729.3 cm^{-1}
Lifetime of $\|e\rangle$	178(19) ms	602 ms
$\alpha_{\|e\rangle}/\alpha_{\|g\rangle}$	0.98(3)	0.97

Table 5.6: Comparison between experimental and theoretical results on Er.

In conclusion, we have done spectroscopic calculations to improve the CI parameters and transition dipole moments. The odd-parity levels have been improved by adding some high-lying experimental energy levels that were previously excluded from the fitting procedure. With the optimized set of energies we have calculated the polarizabilities of the ground and excited states using the sum-over-state formula. We have calculated the wavenumber and the excited-state lifetime. Both were compared with experimental results. The comparison between experimental and calculated wavenumber is great, but there is a disagreement when discussing the excited-level lifetime. We have calculated the Lande g factor and the results are very satisfactory in comparison not only with the experimental one but also with the value reported in NIST database. Several magic wavelength conditions were proposed. The results can still be improved. Some limitations, such as inability to calculate the isotopic shifts, are coming from the semi empirical COWAN codes. Another possibility is to use GRASP (General Relativistic Atomic Structure Package), which is a fully relativistic computational method for producing atomic data [128]. Although the precision of energy

levels calculated by GRASP are not as good as in the case of COWAN, but less accuracy is accepted if resulting eigenvector components and Einstein coefficients have better precision. Moreover, the software allows to calculate isotope shift, which can be interesting for comparison with their experimental counterparts.

Chapter 6

Prospect for laser-cooling of neutral neodymium

In the field of ultracold atomic and molecular matter dipolar gases have become very attractive since they can be controlled by external electric field or magnetic fields. The production and study of highly correlated quantum matter, which is critical for quantum information or for modeling many-body or condensed matter physics [9–11], is enabled thanks to dipolar gases through long-range and anisotropic interactions between particles. Among the different families of systems, open-shell atoms have a permanent magnetic dipole moment that is determined by their total electronic angular momentum. Laser cooling and trapping of lanthanides has opened the possibility to carry out new experiments with ultracold dipolar gases, for example for quantum simulation of solid state physics. All this special characteristics open the question of identifying new suitable species for laser cooling within lanthanides, especially in the left part series. Among them, we notice that, cerium (Ce, $Z = 58$) has the ground configuration $4f\,5d\,6s^2$, which makes this element *a priori* not convenient for such experiments. On the other hand, when we go to the middle of the series, we have radioactive promethium (Pm, $Z = 61$), after which the spectrum of the elements becomes more and more dense, starting with samarium (Sm, $Z = 62$), making these elements not favourable for possible laser cooling studies. Therefore, neodymium (Nd, $Z = 60$) and praseodymium (Pr, $Z = 59$) represent the most promising energy spectrum for the formation of a dipolar gas. Their lowest configurations are very close in energy, namely $4f^w\ 6s^2$, $4f^w\,5d\,6s$, $4f^{w-1}\,5d\,6s^2$ and $4f^{w-1}\,5d^2\,6s$, where $w = 3$ for Pr and $w = 4$ for Nd. Meanwhile, the lowest levels of $4f^w\,5d\,6s$ and $4f^{w-1}\,5d^2\,6s$ configurations are mainly characterized by a spin $S = w/2 + 1$, which makes the decay by spontaneous emission toward levels of $4f^w\,6s^2$ and $4f^{w-1}\,5d\,6s^2$ rather unlikely and denoting that laser-cooling transitions may be chosen among the latter configurations. The $4f^w\,5d\,6s$ and $4f^{w-1}\,5d^2\,6s$ configurations also have levels that are very close in energy, and that can be significantly mixed to induce an electric dipole moment in addition to the magnetic one. The idea and the goal is to find in Nd levels with larger lifetime than the levels in Dy, mentioned in [129]. Moreover Nd represents the great advantage of having bosonic and fermionic stable isotopes, while Pr has only one bosonic stable isotope.

In order to find possible laser-cooling transitions for neutral Nd, it is essential to

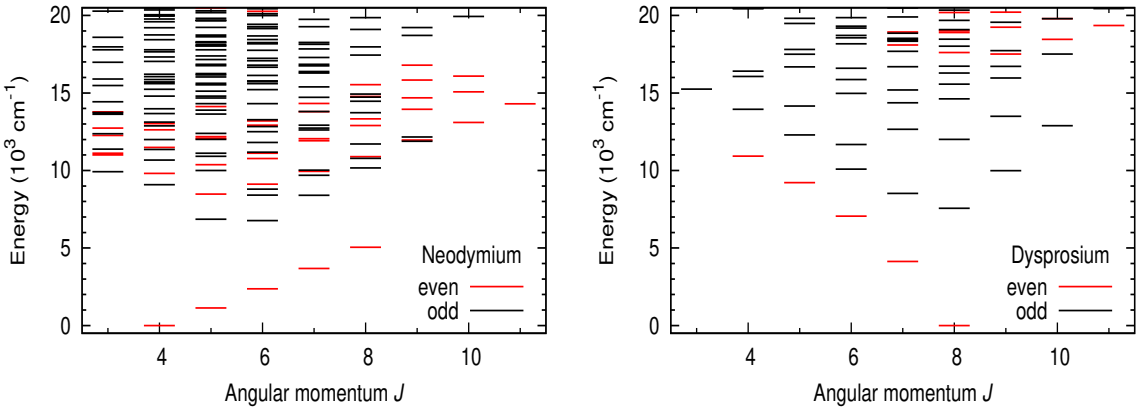

Figure 6.1: Energy diagrams as functions of the electronic angular momentum J and sorted by electronic parity are shown for neodymium (Nd, left panel) and dysprosium (Dy, right panel) for comparison.

carefully model the spectrum, *i.e.* energies and transition dipole moments (TDMs). In this work, as a first step, we carefully study the Nd energy levels. Particular attention is paid to accurately describing configuration-interaction (CI) mixing, to which TDMs are very sensitive, especially those that lead to weak transitions, which play an important role in this design. Since Nd belongs to the left part of the lanthanide row, it presents a high density of levels in the range 8000-15000 cm^{-1} in contrast with Dy (see figure 6.1). To calculate energies, we use the combination of *ab initio* and least-square fitting techniques implemented in the Cowan codes [24, 57] (see section 3.1). We include the three lowest configurations of each parity which allows us to interpret more than 200 energy levels given in the NIST ASD database [52]. The main technical difficulty of this work comes from the least-squares fitting of close energy levels, because we need to determine to which experimental counterparts each computed level should converge.

6.1 Description of calculations

The calculations were performed with three configurations in each parity, namely:

- $4f^4\,6s^2$, $4f^4\,5d\,6s$, $4f^3\,5d\,6s\,6p$ for the even parity;
- $4f^4\,6s\,6p$, $4f^3\,5d\,6s^2$, $4f^3\,5d^2\,6s$ for the odd parity.

The choice was made keeping in mind that the other even configurations are very high. Moreover, we have tried to add the configuration $4f^4\,5d\,6p$, but could not find a convergence. For both parities, we use values from the NIST database as reference energy levels [52]. The primary source of data on neutral Nd levels in the NIST database is Martin *et al.* [59].

Since it belongs to the left part of the lanthanide row of the Periodic Table of the Elements, Nd possesses a dense spectrum, which makes it difficult to identify the levels.

In order to overcome this issue, we have divided the calculation into steps. As a first step, for even parity, the configurations $4f^4\,6s^2$ and $4f^4\,5d\,6s$ were considered together, and the calculations for the configuration $4f^3\,5d\,6s\,6p$ were carried out separately. For the first group when we have included 42 experimental levels and the fitting is done with 11 groups of parameters, the standard deviation is 91 cm^{-1}. For the configuration $4f^3\,5d\,6s\,6p$ the calculations were done with 10 groups of parameters. When 14 interpreted experimental levels are included the standard deviation is 101 cm^{-1}.

Table 6.1: Differences between NIST database and theoretical results for energies, Landé-g factors and dominant *LS* terms with the percentage of the theoretical one. Case 1: when the configurations are the same, but there are differences in terms. All energy levels are in cm^{-1}.

		Energy		Landé g		Dominant term		
Configuration	J	Theory	Exp.	Theory	Exp.	Theory		Exp.
B-d6sp	7	24187	24218	1.095	0.870	58%	^{7}K	^{5}M
B-d2s	4	15457	15600	0.704	0.630	15%	^{5}I	^{7}G
A-6sp	4	20273	20361	0.957	0.735	27%	^{5}H	^{5}I
A-6sp	5	20271	20301	1.169	0.775	35%	^{7}G	^{5}K
A-6sp	5	21015	21005	1.176	0.960	28%	^{7}F	^{5}I
B-d2s	6	15522	15598	0.958	1.210	31%	^{7}K	^{7}H
B-d2s	6	18535	18679	1.008	1.080	17%	^{3}K	^{7}I
B-ds2	6	20112	20119	1.039	1.015	21%	^{5}H	^{3}K
B-d2s	7	16633	16747	1.059	1.265	21%	^{7}K	^{7}H

After the calculation, the optimal values of the energy parameters were determined. The final parameter values of the first step serve as initial values of the second step. In the next step, these two groups were combined together, and the optimal parameters of the individual calculations were taken as an initial set for the combined calculation. In this step 54 interpreted experimental levels are included for three even parity configurations and the fitting is done with 12 groups of free parameters. The standard deviation for this combined calculation is 89 cm^{-1}. The latter results are discussed in more details in section 6.2.

We followed a similar method for odd parity configurations. We have treated separately the configurations $4f^3\,5d\,6s^2$ and $4f^3\,5d^2\,6s$ on one hand, and $4f^4\,6s\,6p$ on the other hand. For the first group of odd parity configurations the calculation is done with 11 parameter groups and 79 experimental levels are included. After the final calculation the standard deviation is 94 cm^{-1}. For configuration $4f^4\,6s\,6p$ we have 19 experimental levels included and 10 parameter groups. For this configuration standard deviation is 160 cm^{-1}. When these two separate analyzes have been completed, we treated these three configurations together. The final least square fitting is done with 15 parameter groups and there are 96 levels included. Standard deviation in this case is 111 cm^{-1}.

Table 6.2: Differences between NIST database and theoretical results for energies, Landé-g factors and dominant LS terms, with the percentage of the theoretical one. Case 2: when there is a good match in energy levels, but the configurations are different. All energy levels are in cm^{-1}.

J	Energy		Configuration		Landé g		Dominant term		
	Theory	Exp.	Theory	Exp.	Theory	Exp.	Theory		Exp.
4	14716	14802	B-d2s	A-6sp	0.443	0.825	80%	^{7}K	^{5}H
4	15898	15863	B-ds2	A-6sp	1.059	1.020	62%	^{3}G	^{7}H
4	16293	16210	B-d2s	B-ds2	0.771	1.055	66%	^{7}I	^{3}G
4	18701	18741	B-d2s	B-ds2	0.926	0.930	8%	^{5}I	^{5}H
5	15049	14797	B-ds2	B-d2s	1.084	0.760	37%	^{3}H	^{5}K
5	15215	15114	B-d2s	B-ds2	0.872	1.110	27%	^{7}K	^{3}H
7	22752	22761	B-d2s	A-6sp	1.098	1.035	14%	^{3}K	^{5}K
8	24148	24121	B-d2s	A-6sp	1.089	1.135	12%	^{5}L	^{5}K
9	20594	20523	B-d2s	A-6sp	1.082	1.230	42%	^{5}M	^{7}I

Again, the latter results are discussed in more details in section 6.2.

Table 6.3: Differences between NIST database and theoretical results for energies, Landé-g factors and dominant LS terms, with the percentage of the theoretical one. Case 3: when the configurations are different, but among the other components of the level eigenvectors, there is one whose configuration or term makes identification possible (see the last three columns). All energy levels are in cm^{-1}.

J	Energy		Configuration		Landé g		Dominant term			Other component		
	Theory	Exp.	Theory	Exp.	Theory	Exp.	Theory		Exp.			
3	15886	15899	A-6sp	B-d2s	0.737	0.600	48%	^{7}H	^{5}H	B-d2s	18%	^{7}I
3	20600	20595	B-d2s	B-ds2	1.037	0.910	11%	^{5}H	^{3}G	B-ds2	9%	^{5}P
5	19912	19816	B-d2s	B-ds2	1.016	1.110	8%	^{7}H	^{5}H	B-ds2	7%	^{3}H
6	14270	14308	B-d2s	B-ds2	1.041	1.106	30%	^{7}I	^{5}H	B-ds2	16%	^{5}H
6	20690	20673	B-d2s	B-ds2	1.099	1.185	16%	^{5}I	^{5}H	B-ds2	7%	^{3}I
6	21548	21543	B-d2s	A-6sp	1.109	0.900	7%	^{5}H	^{5}K	A-6sp	6%	^{5}I
7	19192	19271	A-6sp	B-d2s	1.249	1.260	48%	^{7}H	^{7}G	B-d2s	11%	^{7}I
9	25649	25519	B-d2s	A-6sp	1.205	1.220	17%	^{5}K	^{5}K	A-6sp	16%	^{5}K

In what follows we will use the following abbreviations for even parity configurations: $4f^4\,6s^2$ = A-6s2, $4f^4\,5d\,6s$ = A-ds and $4f^3\,5d\,6s\,6p$ = B-d6sp and for odd parity configurations: $4f^4\,6s\,6p$ = A-6sp, $4f^3\,5d\,6s^2$ = B-ds2 and $4f^3\,5d^2\,6s$ = B-d2s.

6.2 NIST interpreted levels

In the NIST database, some of the Nd levels are well interpreted: detailed information are given, such as Landé g-factors, dominant configurations, terms, etc. To distinguish these levels from other levels present in the NIST database, we refer to them as "NIST interpreted" levels. This subsection is devoted to the calculation when only the interpreted experimental levels are included in the fitting process.

As stated before the dense spectrum of neutral neodymium makes it difficult to identify the levels. This is especially true for levels of $J = 4$, 5 and 6. For most levels, the matching between theory and the NIST database is quite good. However, we noticed differences which can be divided into three groups:

Case 1: when the configurations are the same, but there are differences in the leading terms (see table 6.1).

Case 2: when there is a good match in energy levels, but the configurations are different (see table 6.2).

Case 3: when the configurations are different, but in the second or third component of the level eigenvector, the configuration and/or the term is the same as in the experimental leading term, which makes the identification possible (see table 6.3).

We can see that except the first level of table 6.1, those three tables only contain levels of odd parity, mostly with intermediate angular momenta $J = 4$ to 6, for which the energy spectrum is the densest. Their leading term have a low percentage (mostly below 50 %), which means that the leading term coming out of calculations can be sensitive to the radial parameters. The corresponding optimal radial parameters and their SFs are given in the appendix, section B.

6.3 Newly interpreted levels

After successfully performing the calculation for six Nd configurations with NIST-interpreted levels and finding the optimal parameters for each configuration, we proceeded to include in the fit levels that are present in the database but are not interpreted. We were able to identify 25 levels for even-parity configurations and over 200 levels for odd-parity configurations (see figure 6.2). The newly identified levels of even parity are shown and compared with NIST values in table 6.4. In the case of odd parity configurations for each J value we show 10 newly interpreted levels and their comparison with NIST database in table 6.5. Tables for each J values containing the whole list of newly identified levels and their comparison with the data reported in NIST, can be found in Appendix B.

The inclusion of these new interpreted levels produced the following results: for even parity, with 83 levels included and 12 parameter groups, the standard deviation is 90 cm^{-1}, and for even parity, with 298 levels included and 15 parameter groups, the standard deviation drops to 74 cm^{-1}.

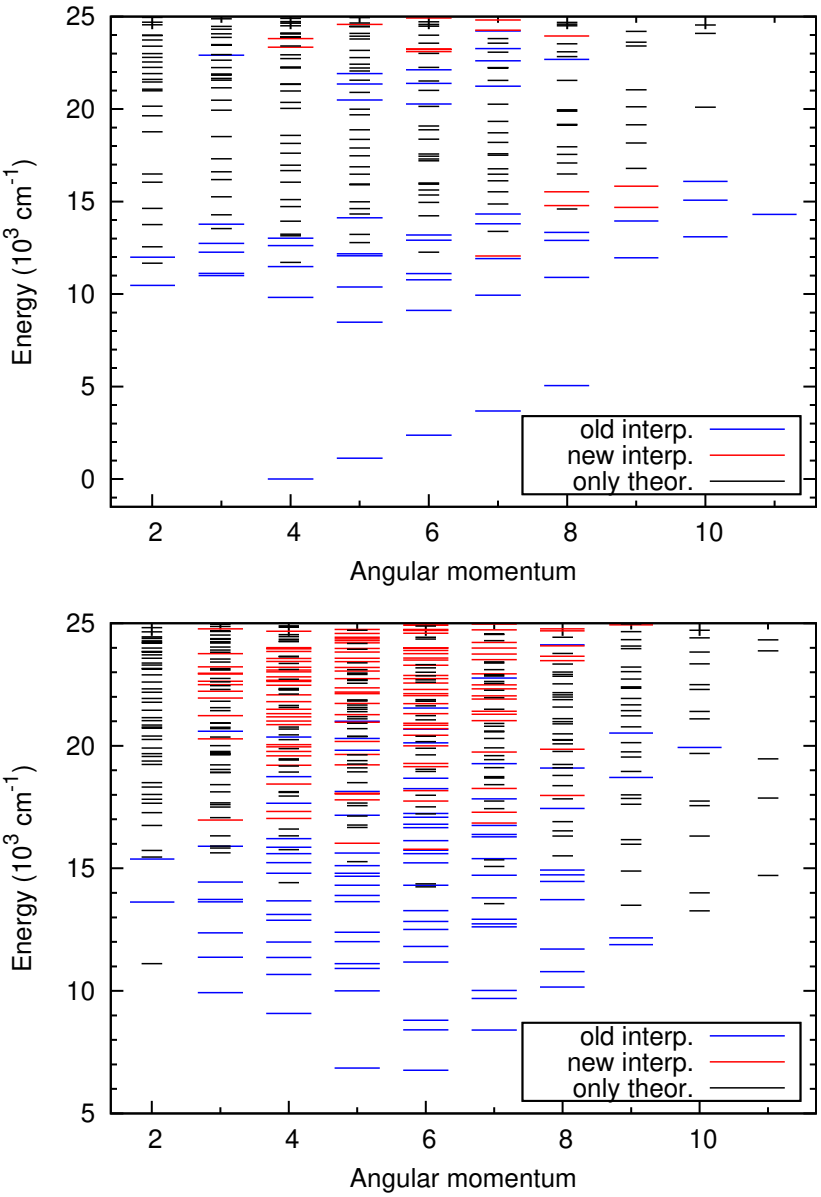

Figure 6.2: Experimental (*blue*), newly interpreted (*red*) and newly predicted (only theoretical) (*black, short*) energy levels of even parity (top) and odd parity (bottom) configurations of neutral Nd as functions of the electronic angular momentum J. Plots are limited to energy values of 25000 cm^{-1}.

Figure 6.2 shows the energies of even and odd configurations as functions of the angular momentum J. Note that unlike figure 6.1, figure 6.2 has one panel for each parity. The blue lines show the experimental energy of interpreted levels present in the NIST database, red lines correspond to the experimental energies of levels that are present in the database but have not been interpreted in detail. Finally, black short lines correspond to newly predicted levels, indicating that their energies are purely theoretical. We see that the latter are numerous and that they are located among experimental

levels. In the even parity, there are no experimental levels between approximately 16000 and 20000 cm^{-1}, corresponding respectively to the highest interpreted levels of the $4f^4\,5d\,6s$ configuration and the lowest ones of the $4f^3\,5d\,6s\,6p$ configuration. In the odd parity, the density of levels is even larger. For extreme values of J, the predicted levels are significantly more present than experimental ones. This trend is not visible for intermediate values $J = 4$–7 where more experimental levels were observed spectroscopically.

When identifying the levels and trying to find corresponding counter-experimental levels to the theoretical ones calculated by us for the least-square fit, we noticed some differences in the Landé g-factors for some levels. Figure 6.3 shows that for most levels, the difference in Landé g-factors is limited to the region [-0.1:0.1]. However, there are levels for which the absolute value of the difference exceeds 0.4. There are three such levels: the Landé g-factor of level $J = 3$ of configuration A-6s2, with an energy value of 11129 cm^{-1}, differs from its counter-experimental level by 1.237. The $J = 5$ level of the A-ds configuration with an energy value of 21899 cm^{-1} has a Landé g-factor that differs from the experimental one by 0.790. And, finally, the Landé g-factor of the level $J = 6$ of the A-ds configuration with an energy value of 11134 cm^{-1} diverges from the experimental one by -0.451.

Table 6.5: Identification and comparison with NIST database values for 10 levels of odd parity configurations for each J value. All energy levels are in cm^{-1}.

Conf.	J	Energy		Landé g		Dom. term	
		Theory	Exp.	Theory	Exp.		
B-d2s	3	16924	16974	0.685	0.520	^{7}H	49%
B-d2s	3	20303	20282	0.302	0.895	^{7}I	77%
B-ds2	3	21139	21228	1.259	1.032	^{5}D	26%
B-d2s	3	21890	21952	0.974	1.070	^{7}G	33%
B-d2s	3	22208	22229	0.817	0.705	^{5}H	36%
B-d2s	3	22504	22491	0.766	0.830	^{5}H	24%
B-d2s	3	22649	22631	0.790	1.130	^{7}H	18%
B-d2s	3	22888	22930	1.012	0.765	^{3}G	7%
B-d2s	3	23034	22956	0.997	0.990	^{5}G	14%
B-ds2	3	23280	23218	0.956	1.060	^{3}G	15%
B-d2s	4	17073	17032	1.231	1.020	^{7}F	26%
B-d2s	4	17206	17320	0.983	0.865	^{7}H	33%
B-ds2	4	18518	18436	0.954	1.075	^{3}H	21%
B-ds2	4	19232	19209	0.888	0.990	^{5}G	12%
A-6sp	4	19569	19590	1.124	0.785	^{7}G	33%
B-d2s	4	19770	19770	0.873	0.920	^{5}I	15%
A-6sp	4	19952	19957	0.798	0.910	^{5}I	23%

Table 6.5 Continued

Conf.	J	Energy		Landé g		Dom. term	
		Theory	Exp.	Theory	Exp.		
B-ds2	4	19984	20047	0.917	0.900	^{3}G	12%
B-d2s	4	20960	20860	0.886	1.080	^{7}I	35%
A-6sp	4	20995	21009	1.611	1.280	^{7}D	89%
A-6sp	5	15963	16028	1.000	0.915	^{7}I	75%
B-ds2	5	17826	17791	0.907	1.005	^{3}I	20%
B-d2s	5	17985	18030	0.990	0.970	^{5}K	13%
B-d2s	5	18060	18068	1.142	0.920	^{7}H	21%
B-ds2	5	19180	19226	0.944	0.944	^{5}H	31%
A-6sp	5	19722	19648	0.931	1.070	^{5}K	12%
A-6sp	5	20186	20177	1.229	0.960	^{7}G	54%
B-d2s	5	20982	20963	0.994	0.990	^{5}I	20%
B-ds2	5	21337	21272	1.054	1.040	^{1}H	9%
B-d2s	5	21746	21727	1.063	1.000	^{5}F	9%
B-d2s	6	15923	15780	0.924	0.945	^{5}K	17%
B-d2s	6	17832	17749	1.133	1.090	^{7}I	24%
A-6sp	6	18184	18172	1.236	1.080	^{7}H	61%
B-d2s	6	19108	19152	1.074	0.930	^{5}I	8%
B-d2s	6	19225	19281	1.081	1.055	^{7}H	24%
B-d2s	6	19974	19995	1.321	0.920	^{7}F	30%
B-d2s	6	20518	20432	1.101	1.040	^{5}K	13%
B-d2s	6	20784	20703	0.881	1.035	^{5}L	17%
B-ds2	6	20873	20839	1.062	0.940	^{3}I	15%
B-d2s	6	20994	20918	0.948	0.840	^{5}L	10%
B-d2s	7	16839	16845	1.071	1.120	^{5}K	22%
B-d2s	7	17312	17290	1.188	1.070	^{7}H	29%
B-d2s	7	18121	18257	0.852	0.955	^{5}M	42%
B-d2s	7	19682	19746	1.279	1.090	^{7}G	21%
B-ds2	7	21090	21026	1.160	1.235	^{5}H	39%
B-d2s	7	21306	21286	1.035	1.050	^{5}K	22%
B-d2s	7	21365	21412	1.064	1.067	^{5}K	12%
A-6sp	7	21910	21909	1.086	0.970	^{5}K	14%
A-6sp	7	22055	22042	1.376	1.020	^{7}G	79%
B-d2s	7	22334	22320	1.133	1.128	^{5}I	15%
B-d2s	8	18080	17973	1.141	1.200	^{7}K	38%
A-6sp	8	19921	19862	1.162	1.290	^{7}H	14%
A-6sp	8	23542	23474	1.135	1.123	^{5}K	19%
B-d2s	8	23665	23653	1.206	1.128	^{7}I	27%

Table 6.5 Continued

Conf.	J	Energy		Landé g		Dom. term	
		Theory	Exp.	Theory	Exp.		
A-6sp	8	23972	24078	1.167	1.070	^{5}K	14%
B-d2s	8	24651	24688	1.183	1.155	^{7}I	17%
B-d2s	8	24756	24773	1.180	1.145	^{5}I	21%
B-d2s	8	25191	25191	1.191	1.195	^{5}I	16%
B-d2s	8	25212	25281	1.174	1.115	^{5}I	15%
B-d2s	8	25477	25383	1.157	1.140	^{5}I	17%
B-d2s	9	24933	24935	1.098	1.150	^{3}M	20%
B-d2s	9	25224	25142	1.102	1.120	^{3}M	17%
B-d2s	9	26424	26511	1.121	1.165	^{3}L	28%
B-d2s	9	27862	27842	1.121	1.160	^{3}L	24%
B-ds2	9	28734	28781	1.105	1.215	^{3}L	72%
B-d2s	9	28983	29061	1.220	1.015	^{5}K	25%

When the optimal set of parameters and the best (smallest) standard deviation are found, it is interesting to calculate the scaling factors (SF) for all parameters and groups of parameters that participated in the calculations, including CI ones. Table 6.6 shows the optimal parameters (X_{fit}) for even parity configurations, as well as their constraints and scaling factors (f_X) if the parameter had an initial HFR value. Table 6.7 presents the same information for odd parity configurations, and table 6.8 for the CI parameters of even and odd parity configuration pairs.

Table 6.6–6.8 also presents the constraints defining groups of fitting parameters: the parameters having the same r_n value belong to the same group. Because our fit was made in several steps, in which the constraints have not been the same, the parameters with the same r_n coefficients do not necessarily have the same scaling factors. Among the latter, we note especially large values for G^k parameters of the $4f^4\,6s\,6p$ configuration and small values for CI parameters for even configuration pairs implying $4f^3\,5d\,6s\,6p$. We can compare our fitted parameters to Ref. [130] which is dedicated to even-parity configurations $4f^4\,6s^2$ + $4f^4\,5d\,6s$. The agreement between theoretical and experimental levels is very good, but we note surprisingly small values of $F^k(4f\,4f)$ parameters of the $4f^4\,5d\,6s$ configuration. All the results are shown in the article [131].

6.4 Possible laser-cooling transitions

The natural next step after the energy level calculations is to calculate the A_{ik} coefficients with the FitAik package [124]. Transitions necessary for magneto-optical trap

Table 6.4: Newly interpreted levels and their comparison with NIST database values for even parity of neutral Nd. All energy levels are in cm^{-1}.

Conf.	J	Energy		Landé g		Dom. term	
		Theory	Exp.	Theory	Exp.		
B-d6sp	4	23329	23347	0.744	0.740	^{7}I	62%
A-ds	4	23840	23808	1.391	0.610	^{5}D	39%
A-ds	5	24555	24578	0.926	0.870	^{7}I	22%
A-6s2	6	23113	23109	1.028	0.895	^{3}I	69%
A-ds	6	23093	23222	1.002	0.965	^{5}K	14%
A-ds	6	23331	23242	1.373	1.115	^{7}F	60%
A-ds	6	24950	24927	1.062	0.955	^{5}K	15%
B-d6sp	6	25166	25207	1.023	0.905	^{7}I	42%
B-d6sp	6	25733	25746	0.905	0.860	^{5}L	10%
A-ds	7	24396	24260	1.063	1.010	^{5}L	14%
A-ds	7	24773	24821	1.233	1.060	^{5}H	36%
B-d6sp	7	25037	25005	0.906	0.905	^{3}L	30%
A-ds	7	25406	25384	1.086	0.971	^{5}K	18%
B-d6sp	7	26444	26516	1.043	1.085	^{7}I	12%
A-ds	7	26871	26898	1.184	1.040	^{5}I	16%
A-ds	7	27038	27000	1.148	1.055	^{7}I	17%
B-d6sp	8	23919	23953	1.080	1.053	^{7}L	64%
A-ds	8	25177	25190	1.096	1.110	^{5}K	25%
B-d6sp	8	25572	25529	1.184	0.990	^{7}K	62%
A-ds	8	26472	26425	1.013	1.135	^{1}L	22%
A-ds	8	27451	27324	1.109	1.040	^{5}I	25%
A-ds	8	27660	27815	0.951	1.015	^{5}N	18%
B-d6sp	8	27997	27922	1.158	1.125	^{7}K	38%
A-ds	9	26928	26987	1.077	1.140	^{1}M	24%
A-ds	9	27418	27266	1.036	1.040	^{1}M	23%

of type I should have a $\Delta J \to J+1$ change in angular momentum. Although this is the most common technique, it is not the only one. Transitions $\Delta J \to J-1$ are less usual but with this type we can avoid leakages, so sometimes those are considered too. Towards the goal of proposing new laser-cooling transitions for neodymium, the next step after doing precise spectroscopic calculations, is to model the transition dipole moments (TDMs). A good and promising starting point can be transitions involving the ground level $4f^4\ 6s^2\ ^5I_4$. The low levels of the $4f^3\ 5d\ 6s^2$ are interesting, because they have the same electronic spin $S = 2$ as the ground level. Although it is not the common MOT type, but transitions with upper levels of electronic angular momentum

Table 6.6: Parameter names, constraints, fitted values and scaling factors ($f_X = X_{\rm fit}/P_{\rm HFR}$) for even configurations of neutral Nd. All parameters are in cm^{-1}.

Param. X	Cons.	$X_{\rm fit}$	f_X	Param. X	Cons.	$X_{\rm fit}$	f_X	Cons.	$X_{\rm fit}$	f_X
	A-6s2				A-ds			B-d6sp		
$E_{\rm av}$		29612		$E_{\rm av}$		43472			61355	
F^2(4f 4f)	r_1	67945	0.740	F^2(4f 4f)	fix	68255	0.750	fix	86247	0.853
F^4(4f 4f)	r_2	38310	0.670	F^4(4f 4f)	fix	42450	0.750	fix	37856	0.597
F^6(4f 4f)	r_3	28534	0.696	F^6(4f 4f)	fix	30437	0.750	fix	35027	0.769
α	fix	37		α	fix	37		r_{51}	97	
β	fix	-963		β	fix	-963		fix	-655	
γ	fix	478		γ	fix	478		fix	1691	
ζ_{4f}	r_4	770	0.912	ζ_{4f}	r_4	765	0.912	r_4	975	1.032
				ζ_{5d}	r_4	353	0.912	r_4	736	1.032
				ζ_{6p}				r_4	868	1.032
				F^1(4f 5d)				r_9	1854	
				F^2(4f 5d)	r_1	12316	0.740	r_1	27733	1.171
				F^3(4f 5d)				r_9	1854	
				F^4(4f 5d)	r_2	5307	0.670	r_2	31253	2.71
				F^1(4f 6p)				r_5	613	
				F^2(4f 6p)				r_1	4730	1.171
				F^1(5d 6p)				r_5	613	
				F^2(5d 6p)				r_5	16009	1.171
				G^1(4f 5d)	r_5	5393	0.584	r_6	13100	1.147
				G^2(4f 5d)	r_9	207				
				G^3(4f 5d)	r_5	3868	0.584	r_6	10316	1.147
				G^4(4f 5d)	r_9	1562				
				G^5(4f 5d)	r_5	2832	0.584	r_6	7794	1.147
				G^3(4f 6s)	r_5	947	0.584	r_6	2111	1.147
				G^2(4f 6p)				r_7	1073	1.175
				G^4(4f 6p)				r_7	682	0.842
				G^2(5d 6s)	r_5	9719	0.584	r_7	17957	1.176
				G^1(5d 6p)				r_6	9118	1.147
				G^3(5d 6p)				r_6	6613	1.147
				G^1(6s 6p)				r_6	26970	1.147

$J' = 3$ are preferential, since they can not decay towards other levels of the ground manifold ^5I. $\Delta L = 1, \Delta S = 0$ selection rules and parity change is satisfied for the level 4f^3 5d 6s^2 ($^5H^o_3$) at 9927 cm^{-1}. The corresponding transition wavelength is around 1007 nm. The upper $J' = 3$ level of configuration 4f^3 5d 6s^2 at 11375 cm^{-1} is very interesting. It has a dominant term of 59 % $^5G^o_3$, i.e. $L' = 4$ and $S' = 2$, and second term of 23% $^3G^o_3$, i.e. $L' = 4$ and $S' = 1$. The remaining 18 % is not known on NIST database [52], but it may strongly influence the transition probability. Our calculations show that the third term is 9 % $^5H^o_3$, which means $L' = 5$ and $S' = 2$.

Beside the ground level, it is very interesting also to consider laser-cooling of the

Table 6.7: Parameter names, constraints, fitted values and scaling factors ($f_X = X_{\rm fit}/P_{\rm HFR}$) for odd configurations of neutral Nd. All parameters are in cm^{-1}.

Param. X	Cons.	$X_{\rm fit}$	f_X	Param. X	Cons.	$X_{\rm fit}$	f_X	Cons.	$X_{\rm fit}$	f_X
	A-6sp				B-ds2			B-d2s		
E_{av}		52188		E_{av}		32792			40755	
F^2(4f 4f)	r_1	72210	0.785	F^2(4f 4f)	r_1	70314	0.696	r_1	69931	0.696
F^4(4f 4f)	r_1	45150	0.789	F^4(4f 4f)	r_1	36982	0.584	r_1	36765	0.584
F^6(4f 4f)	r_1	32379	0.789	F^6(4f 4f)	r_1	21619	0.475	r_1	21489	0.475
α	r_{58}	237		α	r_8	73		r_8	73	
β	r_{58}	-159		β	r_8	-667		r_8	-667	
γ	r_{58}	411		γ	r_8	1744		r_8	1744	
				F^2(5d 5d)				r_5	19957	0.600
				F^4(5d 5d)				r_5	10733	0.501
				α				r_8	71	
				β				r_8	-650	
ζ_{4f}	r_4	828	0.980	ζ_{4f}	r_4	881	0.932	r_4	877	0.932
ζ_{6p}	r_4	699	0.980	ζ_{5d}	r_4	523	0.767	r_4	443	0.767
F^1(4f 6p)	r_3	1742		F^2(4f 5d)	r_2	13678	0.598	r_2	12185	0.598
F^2(4f 6p)	r_3	2355	0.593	F^4(4f 5d)	r_2	5523	0.499	r_2	4846	0.499
G^3(4f 6s)	r_6	6463	3.384	G^1(4f 5d)	r_6	6267	0.570	r_6	5583	0.570
G^2(4f 6p)	r_7	4754	5.185	G^3(4f 5d)	r_6	4921	0.570	r_6	4323	0.570
G^3(4f 6p)	r_7	3842		G^5(4f 5d)	r_6	3714	0.570	r_6	3248	0.570
G^4(4f 6p)	r_7	2702	3.357	G^3(4f 6s)				r_7	866	0.566
G^1(6s 6p)	r_7	17539	0.783	G^2(5d 6s)				r_7	8719	0.566

metastable highest $^5I_8$ level of the ground manifold, which has an energy value of 5048.6 cm^{-1}. This can open up a possibility of a more usual cooling scheme with an upper level $J' = J + 1 = 9$, without any leakage toward levels of the 4f^4 6s^2 ^5I manifold. A promising candidate is the level 4f^3 5d 6s^2 ($^5K^o_9$) which is not tabulated in NIST database but according to our calculations is at 13491 cm^{-1}. For cooling in the $^5I_8$ level, it will be required to calculate the radiative lifetime of this metastable level and populate that level using, for example, two Stimulated Raman Adiabatic Passage (STIRAP) steps from the ground level $^5I_4$. Table 6.9 shows 10 possible laser cooling transitions involving the ground level 4f^4 6s^2 $^5I_4$ and three transitions involving the level 4f^4 6s^2 $^5I_8$.

In this chapter, we have given a theoretical interpretation of the spectrum of neutral neodymium, which is an essential component for new experiments with ultracold dipolar gases. We did the calculations for three even configurations: 4f^4 6s^2, 4f^4 5d 6s, 4f^3 5d 6s 6p, and three odd configurations: 4f^4 6s 6p, 4f^3 5d 6s^2 and 4f^3 5d^2 6s. For this purpose we used Cowan's suite of codes. We were able to interpret more than 200 levels for odd parity configurations and 25 levels for even parity configurations, for which there were no detailed information in the NIST ASD database. In the course

Table 6.8: Fitted configuration interaction (CI) parameters, their scaling factors (f_X = $X_{\rm fit}$ / $X_{\rm HFR}$) and constraints for even and odd configurations of neutral Nd. All parameters are in cm^{-1}.

Parameter X	$X_{\rm fit}$	f_X	Parameter X	$X_{\rm fit}$	f_X
	A-6s2 –A-ds			**A-6sp –B-ds2**	
R^2 (4f 6s, 4f 5d)	-1074	0.441	R^1 (4f 6p, 5d 6s)	-4065	0.475
R^3 (4f 6s, 4f 5d)	231	0.441	R^3 (4f 6p, 5d 6s)	-866	0.475
	A-6s2 –B-d6sp			**A-6sp –B-d2s**	
R^1 (4f 6s, 5d 6p)	-1517	0.163	R^1 (4f 6p, 5d 5d)	1464	0.347
R^3 (4f 6s, 5d 6p)	-260	0.163	R^3 (4f 6p, 5d 5d)	440	0.347
	A-ds –B-d6sp			**B-ds2 –B-d2s**	
R^2 (4f 4f, 4f 6p)	-531	0.163	R^2 (4f 6s, 4f 5d)	-628	0.487
R^4 (4f 4f, 4f 6p)	-348	0.163	R^3 (4f 6s, 4f 5d)	607	0.487
R^1 (4f 5d, 5d 6p)	1047	0.163	R^2 (5d 6s, 5d 5d)	-9305	0.487
R^3 (4f 5d, 5d 6p)	354	0.163			
R^2 (4f 5d, 5d 6p)	27	0.163			
R^4 (4f 5d, 5d 6p)	58	0.164			

Table 6.9: Lower and upper states, wavelengths, Einstein coefficients and widths for some possible laser cooling transitions for neutral Nd organized by increasing order of upper level energy. It is based on experimental studies of Stockett *et al.* [132].

Upper level			Lower level			Wavelength	A_{ik}	Width
Energy (cm^{-1})	Parity	J	Energy (cm^{-1})	Parity	J	(nm)	(10^6 s^{-1})	(MHz)
17787.0	odd	3	0	even	4	562	13.1	0.525
17976.9	odd	3	0	even	4	556	3.3	2.085
21572.6	odd	3	0	even	4	463	88.0	14.006
23487.0	odd	3	0	even	4	425	10.7	1.703
24935.0	odd	9	5048.6	even	8	503	12.8	2.037
25141.5	odd	9	5048.6	even	8	498	18.5	2.944
25518.7	odd	9	5048.6	even	8	488	108	17.188

of calculations, we noticed discrepancies with the NIST database values, for example, in Landé g-factors. After comparison we showed that for all levels except for three,

the absolute value of the difference between the theoretical and experimental Landé g values does not exceed 0.4. The logical continuation and perspective of this work for the future will be the calculation of the transition dipole moments (TDMs) and Einstein coefficients, which are necessary to characterize the efficiency of laser cooling and trapping of atoms. The test with the data set from [133] was not very conclusive, because we had difficulties to identify the strongest transitions involving the ground level. Therefore, it is logical to use experimental A_{ik} coefficients to give a first answer about laser-cooling transitions. For better accuracy, we plan to fit the Einstein coefficients using the FitAik package [124], for which we will use the optimal set of parameters that we have determined in this study. We plan to test the limits of FitAik package on Nd and as an alternative use Pr, since it has simpler configuration than Nd.

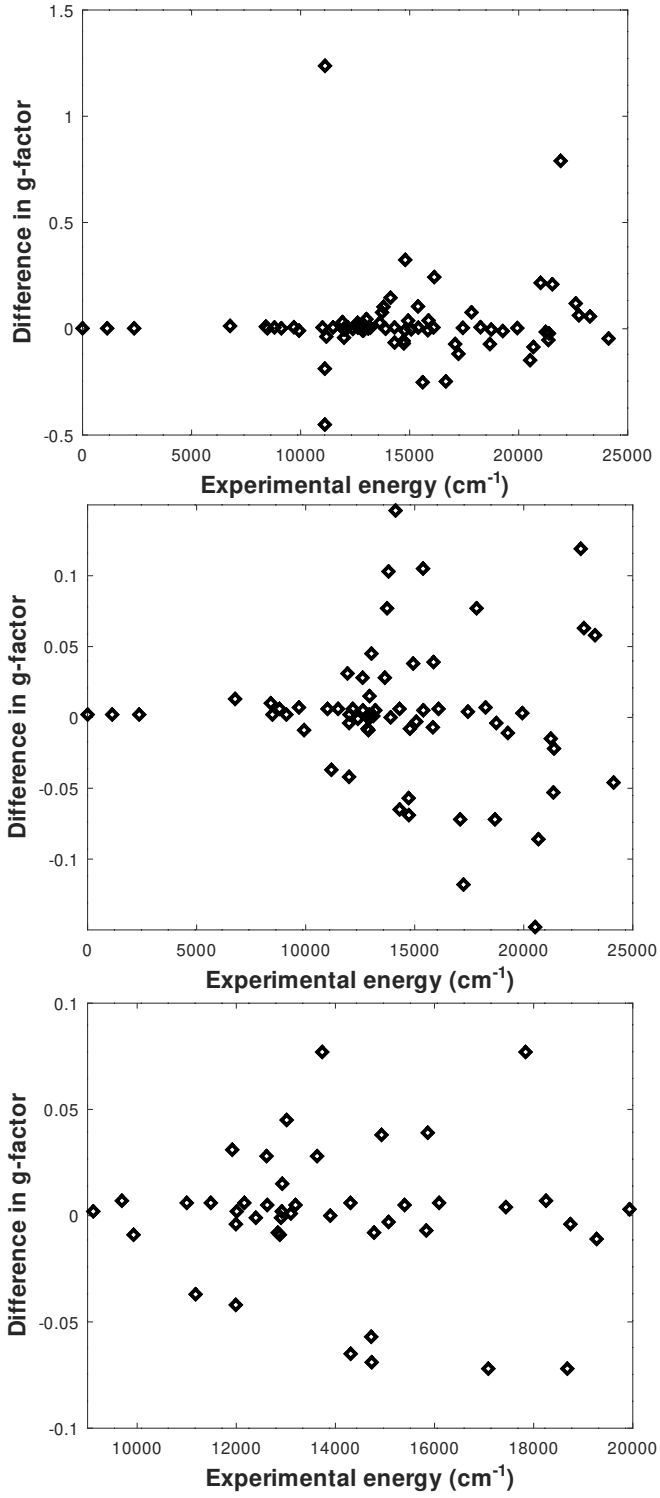

Figure 6.3: Differences between calculated and experimental Landé g-factors for energy levels for neutral Nd with an experimentally known g-factors. The second and the third pictures are enlarged versions to show the differences in detail. The largest difference at 11129 cm^{-1} (first panel) is out of the y-scale on the last panel. Energy levels are in cm^{-1}.

Conclusion

The work carried out during the preparation of this thesis is designated to improve the spectroscopic knowledge of lanthanides and unravel their spectral fingerprints. All the theoretical background necessary for the work is presented in chapter 1, which begins with description of characteristics of spectra atoms and ions, as well as summary on angular momentum. One-electron and two-electron atoms are introduced in this chapter and the idea is generalized to reach the N-electron atom, which is more complex and is the main concern of the work. The chapter has information for coupled angular momentum states and different coupling schemes and is concluded with description of state notations and transition properties as well as $3n - j$ symbols, which are very crucial in the calculations.

The work that has been done for the thesis had two global directions. First one was dedicated to trivalent lanthanides and their transition intensities when they are hosted in solids. Chapter 2 was dedicated to describe generally the lanthanides as elements, covering their properties and their significance in various applications. The chapter includes also explanations on ion-solid systems, mainly focusing on trivalent lanthanides as ions hosted in a crystal field. The last section of the chapter was devoted to description of Judd-Ofelt theory, which described the intensities of trivalent ions when they are in a crystal field. It covered information about the standard version of the JO theory and challenges coming into play when we consider solids doped with Eu^{3+}, Pr^{3+}, Sm^{3+}, etc. The theory is based on free-ion calculations, which I have done with the methodology described in section 3.1. It includes description of the suits of codes used for spectroscopic calculations of trivalent lanthanides and the general working mechanism I have been incorporated. I have done calculations of energy levels of the ground and the first excited configuration of Eu^{3+}, Nd^{3+} and Er^{3+}. The comparison with the experimental results is very good.

During the thesis an extension of the Judd-Ofelt model was developed, enabling to calculate intensities of absorption and emission transitions for Ln^{3+}-doped solids. It is described in chapter 4. In our model, the properties of the Ln^{3+} impurity are fixed parameters calculated with free-ion spectroscopy, while the crystal-field ones are adjusted by least-square fitting. In particular, the line strengths, oscillator strengths and Einstein coefficients are functions of three least-square fitted crystal-field parameters. All the free-ion spectroscopic calculations for this extension were carried out by the semi empirical method: *ab initio* + least square fit. For this purpose, we used Cowan codes, while the actual extension codes are written in FORTRAN. The extension is realized in two steps, in the first model, described in section 4.1, the spin-orbit interac-

tion within the first excited configuration $4f^{w-1}5d$ is described in a perturbative way, whereas it is exactly taken into account in the ground configuration $4f^w$. Section 4.2 is devoted to the second version of the extension, where all the eigenvector components of the free-ion levels are included, while in the previous version only four leading ones are taken into account. The wavelength dependence of the refractive index of the host material is also accounted for by means of the Sellmeier equation, while in the first version the refractive index was assumed to be constant. The first version of the extension is tested only on Eu^{3+}, while the second version is also applied on Nd^{3+} and Er^{3+}. For each ion we have performed a calculation of the $[U^{(k)}]^2$ matrix elements and compared them with the values reported in the articles of Carnall [61, 62]. As a way to validate our model we also calculating the Ω_λ parameters of standard JO theory and compared them with the values reported in the articles where the experimental transition for our fitting calculations were taken from. Both calculations are in a good agreement with reported data. By doing the standard JO calculations twice (with and without the inclusion of the wavelength dependence of the refractive index) we have noticed that when the Sellmeier coefficients are included and so the dispersion is accounted for, our results of Ω_λ are closer to the ones reported in other articles.

We have tested the validity of the extension on two experimental absorption data set for each ion. We have noticed that all the changes made to the extension model has also improved the results. It's worth mentioning that although for second data sets it was impossible to find the Sellmeier coefficients to include the wavelength dependence of the refractive index, the results of the extension are satisfactory.

Generally speaking, our extended model works as good as the standard version, but while for some transitions the oscillator strengths resulting from standard JO calculations are closer to the experimental values, for others the extended version gives better results. In comparison with the version described in article [82], the updated version of the extension works better. This result was demonstrated for the case of Eu^{3+} for two sets of experimental oscillator strengths. However we notice that for the absorption transitions that were measured in σ and π polarizations the resulting OS are diverging more from experimental values than for unpolarized spectra. As a perspective and a possible improvement of the extension of JO theory we plan to include the polarization. This will give the possibility to include the experimentally measured OS as they are and not average them with factors of 2/3 and 1/3 to obtain the unpolarized spectra. We expect this improvement to give more precise and satisfactory results for the calculations. Finally, separating the dopant and crystal-field parameters can open the possibility to interpret transitions between individual crystal-field levels, which can be especially relevant for nanometer-scale host materials.

The second global direction of the thesis was the spectroscopic calculation on neutral lanthanides. I have worked with neutral Er (chapter 5) and Nd (chapter 6). Compared to the calculations performed earlier, for the odd-parity erbium configurations, we have added some high-lying experimental energy levels that were previously excluded from the fitting procedure. We also incorporated a larger number of free configuration-interaction (CI) parameters into the fitting procedure. The experimental group in Innsbruck observed the narrow inner-shell orbital transition at 1299 nm. They characterize the transition by measuring the Landé g factor and the atomic po-

larizability at 532.2 nm, which was compared with our semi-empirical model. We have good agreement with the experimental data for calculating the Landé g factor and the wavenumber for our level of interest. But our theoretical result for the excited-state lifetime is 3 times higher than the experimental result. This comes from the fact that the underlying transition dipole moment involves small components in the eigenvector associated with the excited level.

We have given a theoretical interpretation of the spectrum of neutral neodymium, which is an essential component for new experiments with ultracold dipolar gases. We did the calculations for three even configurations: $4f^4\,6s^2$, $4f^4\,5d\,6s$, $4f^3\,5d\,6s\,6p$, and three odd configurations: $4f^4\,6s\,6p$, $4f^3\,5d\,6s^2$ and $4f^3\,5d^2\,6s$. For this purpose we used Cowan's suite of codes.

Although Nd is a difficult element for such calculations, due to its very dense spectrum, we have been able to carry out the calculations by introducing a method in which we divide the calculation of each parity into two parts. The challenging part of this calculation was the least squares fit, because we needed to find experimental analogs for each theoretical level to which they should converge. We were able to interpret more than 200 levels for odd parity configurations and 25 levels for even parity configurations, for which there were no detailed information in the NIST ASD database. In the course of calculations, we noticed discrepancies with the NIST database values, for example, in Landé g-factors. After comparison we showed that for all levels except for three, the absolute value of the difference between the theoretical and experimental Landé g values does not exceed 0.4.

The logical continuation and perspective of this work for the future will be the calculation of the transition dipole moments (TDMs) and Einstein coefficients, which are necessary to characterize the efficiency of laser cooling and trapping of atoms. For better accuracy, we plan to fit the Einstein coefficients using the FitAik package [124], for which we will use the optimal set of parameters that we have determined in this study.

In the thesis we have done spectroscopic calculation for two neutral lanthanides: Er and Nd, and three trivalent ones: Eu^{3+}, Nd^{3+} and Er^{3+}. Precise spectroscopic data of neutrals is necessary for ultracold experiments. On the other hand, trivalent cations are attractive because of their wide scientific and industrial purposes. All the calculations have been done with the semi-empirical model implemented in Cowan codes. The results are in a good agreement with experimental ones. For neutral lanthanides possible laser cooling and trapping conditions has been discussed. For trivalent ones, an extension of Judd-Ofelt theory, describing the transitions within the ground configuration of discussed ions, has been introduced. The new model has been tested on Eu^{3+}, Nd^{3+} and Er^{3+} and not only gives very satisfactory results, but also allows the description of transitions that were forbidden before by the standard version.

Appendix A

Appendix: Theoretical background

Antisymmetrization of a wavefunction

We can do the antisymmetrization for either the coupled or uncoupled function. We start with an uncoupled one:

$$|n_1 l_1 m_{l_1} m_{s_1} n_2 l_2 m_{l_2} m_{s_2}\rangle_A = N[n_1 l_1 m_{l_1} m_{s_1} n_2 l_2 m_{l_2} m_{s_2}\rangle - |n_2 l_2 m_{l_2} m_{s_2} n_1 l_1 m_{l_1} m_{s_1}\rangle], \tag{A.1}$$

where $N = \frac{1}{\sqrt{2(1+\delta_{m_1 m_2}\delta_{l_1 l_2})}}$ called normalisation factor. $P_{12}|n_1 l_1 m_{l_1} m_{s_1} n_2 l_2 m_{l_2} m_{s_2}\rangle = -|n_2 l_2 m_{l_2} m_{s_2} n_1 l_1 m_{l_1} m_{s_1}\rangle$ called permutation operator. Equation (A.1) comes from the action of the permutation operator P_{12} between the two electrons. The action of this operator on coupled wavefunction is:

$$\begin{aligned} P_{12}|n_1 l_1 n_2 l_2 LSJM\rangle = \sum_{M_L M_S} C^{JM}_{LM_L SM_S} \sum_{m_{l_1} m_{s_1}} \sum_{m_{l_2} m_{s_2}} C^{LM_L}_{l_1 m_{l_1} l_2 m_{l_2}} \\ \times C^{SM_S}_{s_2 m_{s_2} s_1 m_{s_1}} |n_2 l_2 m_{l_2} m_{s_2} n_1 l_1 m_{l_1} m_{s_1}\rangle. \end{aligned} \tag{A.2}$$

Now, we want to make a change of the indices in the coefficients, in order to have similarity with the permutation operator. So,

$$C^{LM_L}_{l_1 m_{l_1} l_2 m_{l_2}} = (-1)^{l_1+l_2-L} C^{LM_L}_{l_2 m_{l_2} l_1 m_{l_1}}, \tag{A.3}$$

and

$$C^{SM_S}_{s_1 m_{s_1} s_2 m_{s_2}} = (-1)^{s_1+s_2-S} C^{SM_S}_{s_2 m_{s_2} s_1 m_{s_1}}. \tag{A.4}$$

So, the action of the permutation operator will be:

$$\begin{aligned} P_{12}|n_1 l_1 n_2 l_2 LSJM\rangle &= (-1)^{l_1+l_2-L+s_1+s_2-S} \sum_{M_L M_S} C^{JM}_{LM_L SM_S} \sum_{m_{l_1} m_{l_2}} C^{LM_L}_{l_2 m_{l_2} l_1 m_{l_1}} \\ &\times \sum_{m_{s_1} m_{s_2}} C^{SM_S}_{s_2 m_{s_2} s_1 m_{s_1}} |n_2 l_2 m_{l_2} m_{s_2} n_1 l_1 m_{l_1} m_{s_1}\rangle \\ &= (-1)^{l_1+l_2-L+s_1+s_2-S} |n_2 l_2 n_1 l_1 LSJM\rangle. \end{aligned} \tag{A.5}$$

If we have equivalent electrons $s_1 = s_2$ and $l_1 = l_2$, so $s_1 + s_2 = 1$ and $l_1 + l_2 = 2l$ is always even. But because of the antisymmetrization principle the coefficient

$(-1)^{l_1+l_2-L+s_1+s_2-S} = (-1)^{1-L-S}$ must be -1. This fact imposes that $L+S$ must be even.

Useful relations

In the appendix, the LS-coupling basis functions of the ground and excited configurations are respectively written $|\alpha LSJ\rangle$ and $|\overline{\alpha}\overline{LS},\, L'S'J'\rangle$. The reduced matrix element of the electric-multipole operator $P_q^{(k)}$ are given by [24]

$$\begin{aligned}\left\langle \overline{\alpha}\overline{LS},\, L'S'J' \left\| P^{(k)} \right\| \alpha LSJ \right\rangle &= (-1)^{S+J+\overline{L}+k} \\ &\times \sqrt{w\,(2J+1)\,(2J'+1)\,(2L+1)\,(2L'+1)\,(2\ell+1)\,(2\ell'+1)} \\ &\times (n\ell^{w-1}\,\overline{\alpha}\overline{LS}|\}n\ell^w\,\alpha LS) \left\{ \begin{array}{ccc} L & S & J \\ J' & k & L' \end{array} \right\} \left\{ \begin{array}{ccc} \ell & \overline{L} & L \\ L' & k & \ell' \end{array} \right\} \\ &\times \left(\begin{array}{ccc} \ell' & k & \ell \\ 0 & 0 & 0 \end{array} \right) \langle n'\ell'|\, r^k\, |n\ell\rangle\,, \end{aligned} \tag{A.6}$$

where $(n\ell^{w-1}\,\overline{\alpha}\overline{LS}|\}n\ell^w\,\alpha LS)$ is a coefficient of fractional parentage introduced by Racah [26]. The matrix element of the spin-orbit operator within the ground configuration is

$$\begin{aligned}&\langle \alpha_1 L_1 S_1 J_1|\, H_{\rm SO}\, |\alpha_2 L_2 S_2 J_2\rangle \\ &= \delta_{J_1 J_2}\,(-1)^{L_2+S_1+J_1}\; w\zeta_{n\ell}\,\sqrt{\ell\,(\ell+1)\,(2\ell+1)\,s\,(s+1)\,(2s+1)\,(2L_1+1)\,(2L_2+1)} \\ &\times \sqrt{(2S_1+1)\,(2S_2+1)} \sum_{\overline{\alpha}\overline{LS}} (-1)^{\ell+s+\overline{L}+\overline{S}+L_1+S_1} \left\{ \begin{array}{ccc} \ell & \ell & 1 \\ L_1 & L_2 & \overline{L} \end{array} \right\} \left\{ \begin{array}{ccc} s & s & 1 \\ S_1 & S_2 & \overline{S} \end{array} \right\} \\ &\times (n\ell^{w-1}\,\overline{\alpha}\overline{LS}|\}n\ell^w\,\alpha_1 L_1 S_1) \times (n\ell^{w-1}\,\overline{\alpha}\overline{LS}|\}n\ell^w\,\alpha_2 L_2 S_2) \end{aligned} \tag{A.7}$$

In the excited configuration, we assume that the off-diagonal matrix elements are only due to the outermost $n'\ell' = 5d$ electron,

$$\begin{aligned}&\left\langle \overline{\alpha}\overline{LS},\, L'_1 S'_1 J'_1 \right|\, H_{\rm SO}\, \left|\overline{\alpha}\overline{LS},\, L'_2 S'_2 J'_2\right\rangle \\ &= \delta_{J'_1 J'_2}\,(-1)^{\ell'+s+\overline{L}+\overline{S}+L'_1+L'_2+2S'_1+J'_1}\; \zeta_{n'\ell'}\,\sqrt{\ell'\,(\ell'+1)\,(2\ell'+1)\,s\,(s+1)\,(2s+1)} \\ &\times \sqrt{(2L'_1+1)\,(2L'_2+1)\,(2S'_1+1)\,(2S'_2+1)} \left\{ \begin{array}{ccc} L'_1 & S'_1 & J'_1 \\ S'_2 & L'_2 & 1 \end{array} \right\} \left\{ \begin{array}{ccc} \ell' & \ell' & 1 \\ L'_1 & L'_2 & \overline{L} \end{array} \right\} \left\{ \begin{array}{ccc} s & s & 1 \\ S'_1 & S'_2 & \overline{S} \end{array} \right\} \end{aligned} \tag{A.8}$$

The second-order correction on the eigenvector $|\Psi_i^2\rangle$ is

$$\left|\Psi_i^2\right\rangle = \sum_{t,u\neq i} \left|\Psi_t^0\right\rangle \frac{V_{tu}V_{ui}}{\Delta_{it}\Delta_{iu}} - \sum_{t\neq i} \left|\Psi_t^0\right\rangle \frac{V_{ti}V_{ii}}{\Delta_{it}^2} - \frac{1}{2}\left|\Psi_i^0\right\rangle \sum_{t\neq i} \frac{V_{it}V_{ti}}{\Delta_{it}^2} \tag{A.9}$$

where $V_{it} = \langle\Psi_i^0|V|\Psi_t^0\rangle$ and $\Delta_{it} = E_i - E_t$.

Appendix B

Appendix: Neutral neodymium

Fitted energy parameters

In this section, we present tables with fitted parameter values (X_{fit}) for configurations of Nd after the last calculation and their scaling factors (f_X) (if the parameter had an initial HFR value), when only NIST interpreted levels are included in the fitting process (see Section 6.2 of the main text).

Table B.1: Parameters, constraints, fitted parameters and their scaling factors (f_X = X_{fit} / X_{HFR}) for even configurations of neutral Nd. All parameters are in cm^{-1}.

Param. X	Cons.	X_{fit}	f_X	Param. X	Cons.	X_{fit}	f_X	Cons.	X_{fit}	f_X
	A-6s2				A-ds			B-d6sp		
E_{av}		29054		E_{av}		43510			61333	
F^2(4f 4f)	r_1	67029	0.730	F^2(4f 4f)	fixed	68255	0.750	fixed	86247	0.853
F^4(4f 4f)	r_2	36840	0.645	F^4(4f 4f)	fixed	42450	0.750	fixed	37856	0.597
F^6(4f 4f)	r_3	25772	0.629	F^6(4f 4f)	fixed	30437	0.750	fixed	35027	0.769
α	fixed	37		α	fixed	37		r_{51}	96	
β	fixed	963		β	fixed	963		fixed	655	
γ	fixed	478		γ	fixed	478		fixed	1691	
ζ_{4f}	r_4	775	0.917	ζ_{4f}	r_4	770	0.918	r_4	981	1.039
				ζ_{5d}	r_4	356	0.918	r_4	741	1.038
				ζ_{6p}				r_4	873	1.038
				F^1(4f 5d)				r_9	2111	
				F^2(4f 5d)	r_1	12150	0.730	r_1	27359	1.155
				F^3(4f 5d)				r_9	2111	
				F^4(4f 5d)	r_2	5104	0.645	r_2	30055	2.610
				F^1(4f 6p)				r_5	619	
				F^2(4f 6p)				r_1	4667	1.115

Table B.1 Continued

Param. X	Cons.	X_{fit}	f_X	Param. X	Cons.	X_{fit}	f_X	Cons.	X_{fit}	f_X
	A-6s2				A-ds			B-d6sp		
				F^1(5d 6p)				r_5	619	
				F^2(5d 6p)				r_5	15793	1.115
				G^1(4f 5d)	r_5	5443	0.589	r_6	12950	1.134
				G^2(4f 5d)	r_9	235				
				G^3(4f 5d)	r_5	3904	0.586	r_6	10198	1.134
				G^4(4f 5d)	r_9	1779				
				G^5(4f 5d)	r_5	2858	0.589	r_6	7705	1.134
				G^3(4f 6s)	r_5	956	0.589	r_6	2087	1.134
				G^2(4f 6p)				r_7	1138	1.247
				G^4(4f 6p)				r_7	723	0.893
				G^2(5d 6s)	r_5	9809	0.589	r_7	19047	1.247
				G^1(5d 6p)				r_6	6537	1.134
				G^3(5d 6p)				r_6	6613	1.134
				G^1(6s 6p)				r_6	26659	1.134

Table B.2: Parameters, constraints, fitted parameters and their scaling factors ($f_X = X_{\text{fit}} / X_{\text{HFR}}$) for odd configurations of neutral Nd. All parameters are in cm^{-1}.

Param. X	Cons.	X_{fit}	f_X	Param. X	Cons.	X_{fit}	f_X	Cons.	X_{fit}	f_X
	A-6sp				B-ds2			B-d2s		
E_{av}		52415		E_{av}		32902			40943	
F^2(4f 4f)	r_1	72969	0.793	F^2(4f 4f)	r_1	71053	0.703	r_1	70665	0.703
F^4(4f 4f)	r_1	45624	0.797	F^4(4f 4f)	r_1	37370	0.590	r_1	37151	0.589
F^6(4f 4f)	r_1	32719	0.797	F^6(4f 4f)	r_1	21846	0.479	r_1	21714	0.479
α	r_{58}	255		α	r_8	78		r_8	78	
β	r_{58}	-171		β	r_8	-717		r_8	-717	
γ	r_{58}	441		γ	r_8	1875		r_8	1875	
				F^2(5d 5d)				r_5	20344	0.612
				F^4(5d 5d)				r_5	10941	0.511
				α				r_8	76	
				β				r_8	-698	
ζ_{4f}	r_4	832	0.985	ζ_{4f}	r_4	885	0.937	r_4	881	0.937

Table B.2 Continued

Param. X	Cons.	$X_{\rm fit}$	f_X	Param. X	Cons.	$X_{\rm fit}$	f_X	Cons.	$X_{\rm fit}$	f_X
	A-6sp				B-ds2			B-d2s		
ζ_{6p}	r_4	702	0.985	ζ_{5d}	r_4	524	0.771	r_4	445	0.771
F^1(4f 6p)	r_3	1726		F^2(4f 5d)	r_2	13821	0.604	r_2	12313	0.604
F^2(4f 6p)	r_3	2333	0.588	F^4(4f 5d)	r_2	5580	0.505	r_2	4897	0.505
G^3(4f 6s)	r_6	6406	3.354	G^1(4f 5d)	r_6	6212	0.565	r_6	5534	0.565
G^2(4f 6p)	r_7	4762	5.194	G^3(4f 5d)	r_6	4878	0.565	r_6	4285	0.565
G^3(4f 6p)	r_7	3848		G^5(4f 5d)	r_6	3682	0.565	r_6	3219	0.565
G^4(4f 6p)	r_7	2706	3.363	G^3(4f 6s)				r_7	867	0.567
G^1(6s 6p)	r_7	17566	0.784	G^2(5d 6s)				r_7	8733	0.567

Table B.3: Fitted configuration interaction (CI) parameters, their scaling factors (f_X = $X_{\rm fit}$ / $X_{\rm HFR}$) and constraints for even and odd configurations of neutral Nd. All parameters are in $\rm cm^{-1}$.

Parameter X	$X_{\rm fit}$	f_X	Parameter X	$X_{\rm fit}$	f_X
	A-6s2 –A-ds			**A-6sp –B-ds2**	
R^2 (4f 6s, 4f 5d)	-1033	0.425	R^1 (4f 6p, 5d 6s)	-4049	0.473
R^3 (4f 6s, 4f 5d)	222	0.425	R^3 (4f 6p, 5d 6s)	-863	0.474
	A-6s2 –B-d6sp			**A-6sp –B-d2s**	
R^1 (4f 6s, 5d 6p)	-1496	0.161	R^1 (4f 6p, 5d 5d)	1476	0.351
R^3 (4f 6s, 5d 6p)	-257	0.161	R^3 (4f 6p, 5d 5d)	443	0.351
	A-ds –B-d6sp			**B-ds2 –B-d2s**	
R^2 (4f 4f, 4f 6p)	-524	0.161	R^2 (4f 6s, 4f 5d)	-595	0.461
R^4 (4f 4f, 4f 6p)	-343	0.161	R^3 (4f 6s, 4f 5d)	575	0.461
R^1 (4f 5d, 5d 6p)	1033	0.161	R^2 (5d 6s, 5d 5d)	-8813	0.461
R^3 (4f 5d, 5d 6p)	349	0.161			
R^2 (4f 5d, 5d 6p)	26	0.161			
R^4 (4f 5d, 5d 6p)	57	0.161			

Identified levels

Here we present detailed tables for newly interpreted levels for even and odd parity configurations of neutral Nd. In what follows we use the abbreviations: conf.=configuration, exp.=experimental data taken from the NIST database and dom. term=dominant eigenvalue term with its percentage.

Table B.4: Identification and comparison with NIST database values for $J = 3$ levels of odd parity configurations. All energy levels are in cm^{-1}.

Conf.	Energy		Landé g		Dom. term	
	Theory	Exp.	Theory	Exp.		
B-d2s	16924	16974	0.685	0.520	^{7}H	49%
B-d2s	20303	20282	0.302	0.895	^{7}I	77%
B-ds2	21139	21228	1.259	1.032	^{5}D	26%
B-d2s	21890	21952	0.974	1.070	^{7}G	33%
B-d2s	22208	22229	0.817	0.705	^{5}H	36%
B-d2s	22504	22491	0.766	0.830	^{5}H	24%
B-d2s	22649	22631	0.790	1.130	^{7}H	18%
B-d2s	22888	22930	1.012	0.765	^{3}G	7%
B-d2s	23034	22956	0.997	0.990	^{5}G	14%
B-ds2	23280	23218	0.956	1.060	^{3}G	15%
B-ds2	23687	23762	1.108	1.190	^{1}F	15%
B-d2s	24804	24775	1.180	1.352	^{5}G	8%
B-d2s	25061	25164	1.088	1.050	^{5}G	16%
A-6sp	25331	25282	1.209	1.360	^{5}D	10%
A-6sp	25535	25500	0.904	0.825	^{7}H	44%
B-d2s	25669	25642	1.117	0.900	^{3}F	8%
B-d2s	25754	25788	1.166	0.900	^{7}G	26%
B-d2s	25996	26061	1.134	1.360	^{7}G	12%
B-d2s	26170	26096	0.759	0.980	^{7}I	24%
B-d2s	26219	26163	1.057	1.180	^{7}S	4%
B-ds2	26283	26346	1.065	1.025	^{3}D	4%
B-d2s	26359	26395	0.880	1.060	^{7}I	13%
A-6sp	26425	26463	1.133	0.865	^{7}G	49%

Table B.5: Identification and comparison with NIST database values for $J = 4$ levels of odd parity configurations. All energy levels are in cm^{-1}.

Conf.	Energy		Landé g		Dom. term	
	Theory	Exp.	Theory	Exp.		
B-d2s	17073	17032	1.231	1.020	^{7}F	26%
B-d2s	17206	17320	0.983	0.865	^{7}H	33%
B-ds2	18518	18436	0.954	1.075	^{3}H	21%
B-ds2	19232	19209	0.888	0.990	^{5}G	12%
A-6sp	19569	19590	1.124	0.785	^{7}G	33%
B-d2s	19770	19770	0.873	0.920	^{5}I	15%
A-6sp	19952	19957	0.798	0.910	^{5}I	23%
B-ds2	19984	20047	0.917	0.900	^{3}G	12%
B-d2s	20960	20860	0.886	1.080	^{7}I	35%
A-6sp	20995	21009	1.611	1.280	^{7}D	89%
B-d2s	21125	21185	0.827	0.920	^{5}I	10%
B-d2s	21297	21314	0.916	0.985	^{5}G	16%
B-d2s	21448	21488	0.909	0.910	^{5}I	12%
B-ds2	22038	22077	1.046	1.035	^{3}F	10%
B-ds2	22392	22471	1.099	0.995	^{3}F	12%
B-d2s	22584	22623	1.003	1.135	^{3}H	15%
B-d2s	22651	22678	1.033	0.885	^{7}G	9%
B-ds2	22867	22815	0.846	0.975	^{5}I	23%
B-ds2	22953	23016	0.794	0.810	^{5}I	28%
B-d2s	23026	23089	0.941	1.250	^{7}H	27%
B-d2s	23284	23204	1.170	1.200	^{7}P	11%
B-d2s	23444	23439	0.998	0.885	^{7}H	18%
B-d2s	23527	23563	1.067	0.940	^{5}H	7%
B-d2s	23877	23846	0.989	1.175	^{5}I	7%
B-ds2	23962	23953	0.899	0.830	^{3}G	12%
B-d2s	24070	24001	1.237	1.110	^{7}D	16%
B-ds2	24747	24674	1.070	1.060	^{3}G	11%
B-d2s	25352	25448	1.148	1.175	^{7}D	10%
B-ds2	25494	25476	0.881	0.915	^{5}H	23%
B-ds2	25621	25621	1.085	1.175	^{5}H	17%
B-d2s	25674	25641	1.041	1.120	^{5}F	7%
B-ds2	25798	25791	1.138	0.920	^{5}G	18%
B-d2s	26182	26232	1.083	1.025	^{5}F	5%
B-d2s	26642	26662	1.120	1.000	^{5}D	5%
B-d2s	26734	26684	1.172	1.130	^{5}D	8%
B-d2s	26770	26770	1.052	1.200	^{3}G	7%

Table B.5 Continued

Conf.	Energy		Landé g		Dom. term	
	Theory	Exp.	Theory	Exp.		
B-ds2	26995	27144	1.137	0.965	^{5}G	14%
B-d2s	27261	27230	0.972	1.125	^{7}I	10%
B-d2s	27478	27490	1.109	1.085	^{3}H	10%
A-6sp	27678	27717	1.038	0.890	^{3}G	8%
B-d2s	27801	27780	1.059	1.030	^{3}G	4%
B-d2s	27924	27860	1.208	1.125	^{5}D	9%
B-d2s	28004	27990	1.166	0.930	^{5}F	7%

Table B.6: Identification and comparison with NIST database values for $J = 5$ levels of odd parity configurations. All energy levels are in cm^{-1}.

Conf.	Energy		Landé g		Dom. term	
	Theory	Exp.	Theory	Exp.		
A-6sp	15963	16028	1.000	0.915	^{7}I	75%
B-ds2	17826	17791	0.907	1.005	^{3}I	20%
B-d2s	17985	18030	0.990	0.970	^{5}K	13%
B-d2s	18060	18068	1.142	0.920	^{7}H	21%
B-ds2	19180	19226	0.944	0.944	^{5}H	31%
A-6sp	19722	19648	0.931	1.070	^{5}K	12%
A-6sp	20186	20177	1.229	0.960	^{7}G	54%
B-d2s	20982	20963	0.994	0.990	^{5}I	20%
B-ds2	21337	21272	1.054	1.040	^{1}H	9%
B-d2s	21746	21727	1.063	1.000	^{5}F	9%
B-d2s	22069	22129	1.052	1.060	^{5}H	7%
B-ds2	22108	22192	0.943	1.090	^{3}I	12%
B-d2s	22415	22367	1.211	1.085	^{7}G	9%
B-d2s	22828	22737	1.062	1.070	^{3}H	13%
B-ds2	22987	23050	1.025	1.060	^{3}G	11%
B-d2s	23262	23198	1.053	1.085	^{7}H	18%
B-d2s	23459	23434	1.047	0.965	^{7}H	15%
B-d2s	23598	23573	1.083	1.080	^{5}H	11%
B-d2s	23830	23830	1.152	1.165	^{5}H	6%

Table B.6 Continued

Conf.	Energy		Landé g		Dom. term	
	Theory	Exp.	Theory	Exp.		
B-ds2	24063	23968	1.017	0.980	^{5}I	12%
B-d2s	24266	24292	1.037	1.060	^{5}H	10%
A-6sp	24333	24364	0.984	1.090	^{3}I	19%
B-d2s	24443	24428	0.981	1.190	^{3}I	20%
B-d2s	24638	24586	1.107	1.110	^{7}D	8%
B-d2s	24743	24746	1.245	1.185	^{7}F	17%
A-6sp	25036	25075	1.035	1.020	^{3}H	15%
B-d2s	25257	25227	0.832	0.995	^{5}K	17%
B-d2s	25914	25924	1.227	1.050	^{7}D	12%
A-6sp	26071	26029	1.304	1.035	^{5}F	20%
B-d2s	26332	26345	1.178	1.100	^{3}H	6%
B-d2s	26495	26484	1.144	1.035	^{5}G	12%
B-d2s	26516	26503	1.231	1.180	^{7}K	7%
B-d2s	26580	26595	1.079	1.015	^{3}G	4%
B-d2s	27447	27474	1.116	1.080	^{3}G	7%
B-ds2	27509	27524	1.058	0.970	^{3}I	15%
B-d2s	27853	27841	1.175	0.990	^{7}F	17%
B-d2s	28032	28000	1.105	0.915	^{7}I	6%
B-d2s	28146	28179	1.053	0.965	^{3}I	5%
B-d2s	28262	28280	1.095	1.070	^{7}I	7%
B-d2s	28556	28567	1.132	1.090	^{3}G	14%
A-6sp	28576	28531	1.394	1.115	^{7}F	56%
B-d2s	28689	28662	1.136	0.960	^{3}I	5%
B-d2s	28785	28723	1.060	0.895	^{5}H	4%
B-d2s	28865	28844	1.201	1.100	^{7}D	7%
A-6sp	28893	28863	1.077	0.945	^{5}I	13%

Table B.7: Identification and comparison with NIST database values for $J = 6$ levels of odd parity configurations. All energy levels are in cm^{-1}.

Conf.	Energy		Landé g		Dom. term	
	Theory	Exp.	Theory	Exp.		

Table B.7 Continued

Conf.	Energy		Landé g		Dom. term	
	Theory	Exp.	Theory	Exp.		
B-d2s	15923	15780	0.924	0.945	^{5}K	17%
B-d2s	17832	17749	1.133	1.090	^{7}I	24%
A-6sp	18184	18172	1.236	1.080	^{7}H	61%
B-d2s	19108	19152	1.074	0.930	^{5}I	8%
B-d2s	19225	19281	1.081	1.055	^{7}H	24%
B-d2s	19974	19995	1.321	0.920	^{7}F	30%
B-d2s	20518	20432	1.101	1.040	^{5}K	13%
B-d2s	20784	20703	0.881	1.035	^{5}L	17%
B-ds2	20873	20839	1.062	0.940	^{3}I	15%
B-d2s	20994	20918	0.948	0.840	^{5}L	10%
A-6sp	21261	21314	1.080	1.060	^{5}K	12%
B-d2s	21695	21718	1.066	0.960	^{5}K	10%
B-d2s	22028	22050	1.069	1.040	^{3}I	9%
B-d2s	22222	22124	1.037	1.170	^{7}I	15%
B-d2s	22308	22303	1.053	1.080	^{7}I	40%
B-ds2	22539	22560	1.050	1.135	^{3}H	10%
B-d2s	22759	22739	1.000	0.985	^{5}L	10%
B-d2s	22883	22871	0.934	1.164	^{3}K	12%
B-d2s	23254	23284	1.131	1.040	^{3}I	11%
B-d2s	23508	23496	1.039	0.930	^{1}I	9%
B-d2s	23649	23578	1.089	0.985	^{5}H	7%
B-ds2	23718	23756	1.105	1.075	^{3}H	10%
B-d2s	23884	23889	1.185	1.030	^{7}H	26%
B-d2s	23990	23986	1.065	1.100	^{5}I	13%
B-d2s	24085	23996	1.176	1.045	^{7}H	7%
A-6sp	24558	24590	1.007	1.010	^{3}K	24%
B-d2s	24689	24702	1.058	1.135	^{7}H	13%
A-6sp	24750	24751	0.974	0.925	^{3}K	34%
A-6sp	24946	24922	1.088	1.080	^{3}K	7%
B-d2s	25033	24984	1.170	1.210	^{3}H	19%
B-d2s	25111	25115	1.196	1.225	^{5}G	17%
B-d2s	25139	25196	1.023	1.120	^{3}K	7%
B-d2s	25313	25301	1.162	1.210	^{5}G	9%
B-d2s	25526	25478	1.084	1.085	^{5}I	16%
B-ds2	25581	25609	1.064	0.895	^{5}I	57%
B-d2s	25695	25662	1.043	1.190	^{5}K	10%
B-d2s	25802	25751	1.258	1.200	^{7}F	20%

Table B.7 Continued

Conf.	Energy		Landé g		Dom. term	
	Theory	Exp.	Theory	Exp.		
B-d2s	26535	26511	1.090	1.040	^{3}K	5%
B-d2s	26727	26696	1.129	1.040	^{5}H	11%
A-6sp	26805	26816	1.174	1.215	^{5}G	6%
A-6sp	26882	26908	1.240	1.125	^{5}G	31%

Table B.8: Identification and comparison with NIST database values for $J = 7$ levels of odd parity configurations. All energy levels are in cm^{-1}.

Conf.	Energy		Landé g		Dom. term	
	Theory	Exp.	Theory	Exp.		
B-d2s	16839	16845	1.071	1.120	^{5}K	22%
B-d2s	17312	17290	1.188	1.070	^{7}H	29%
B-d2s	18121	18257	0.852	0.955	^{5}M	42%
B-d2s	19682	19746	1.279	1.090	^{7}G	21%
B-ds2	21090	21026	1.160	1.235	^{5}H	39%
B-d2s	21306	21286	1.035	1.050	^{5}K	22%
B-d2s	21365	21412	1.064	1.067	^{5}K	12%
A-6sp	21910	21909	1.086	0.970	^{5}K	14%
A-6sp	22055	22042	1.376	1.020	^{7}G	79%
B-d2s	22334	22320	1.133	1.128	^{5}I	15%
A-6sp	22513	22483	1.053	1.120	^{5}K	23%
B-d2s	23084	22939	1.059	1.065	^{7}I	12%
A-6sp	23518	23518	1.147	1.052	^{5}I	16%
B-d2s	23779	23745	1.097	1.040	^{5}L	13%
B-d2s	24072	23991	1.072	1.225	^{5}K	10%
A-6sp	24177	24213	1.255	1.060	^{5}H	36%
B-d2s	24676	24730	1.216	1.150	^{5}H	19%
B-d2s	24825	24968	1.120	1.145	^{5}H	8%
B-d2s	25079	25064	1.136	1.100	^{3}I	21%
B-d2s	25164	25198	1.222	1.120	^{5}H	17%
B-d2s	25485	25504	1.140	1.115	^{5}I	7%
B-d2s	25569	25596	1.234	1.095	^{7}G	17%

Table B.8 Continued

Conf.	Energy		Landé g		Dom. term	
	Theory	Exp.	Theory	Exp.		
B-ds2	25919	25849	0.951	1.085	^{3}L	57%
B-d2s	25954	25886	1.068	0.965	^{1}K	11%
B-ds2	26162	26155	1.116	0.950	^{5}I	11%
A-6sp	26270	26327	1.124	1.250	^{3}K	14%
B-d2s	26424	26395	1.118	1.080	^{3}I	8%
B-d2s	26509	26635	1.060	1.125	^{3}L	13%

Table B.9: Identification and comparison with NIST database values for $J = 8$ levels of odd parity configurations. All energy levels are in cm^{-1}.

Conf.	Energy		Landé g		Dom. term	
	Theory	Exp.	Theory	Exp.		
B-d2s	18080	17973	1.141	1.200	^{7}K	38%
A-6sp	19921	19862	1.162	1.290	^{7}H	14%
A-6sp	23542	23474	1.135	1.123	^{5}K	19%
B-d2s	23665	23653	1.206	1.128	^{7}I	27%
A-6sp	23972	24078	1.167	1.070	^{5}K	14%
B-d2s	24651	24688	1.183	1.155	^{7}I	17%
B-d2s	24756	24773	1.180	1.145	^{5}I	21%
B-d2s	25191	25191	1.191	1.195	^{5}I	16%
B-d2s	25212	25281	1.174	1.115	^{5}I	15%
B-d2s	25477	25383	1.157	1.140	^{5}I	17%
B-d2s	25538	25514	1.100	1.140	^{3}L	12%
B-d2s	26738	26783	1.087	1.118	^{3}L	15%
B-ds2	26996	27044	1.026	1.015	^{3}L	53%
B-d2s	27168	27131	1.196	1.170	^{5}I	13%

Table B.10: Identification and comparison with NIST database values for $J = 9$ levels of odd parity configurations. All energy levels are in cm^{-1}.

Conf.	Energy		Landé g		Dom. term	
	Theory	Exp.	Theory	Exp.		
B-d2s	24933	24935	1.098	1.150	^{3}M	20%
B-d2s	25224	25142	1.102	1.120	^{3}M	17%
B-d2s	26424	26511	1.121	1.165	^{3}L	28%
B-d2s	27862	27842	1.121	1.160	^{3}L	24%
B-ds2	28734	28781	1.105	1.215	^{3}L	72%
B-d2s	28983	29061	1.220	1.015	^{5}K	25%

Bibliography

[1] L.A. Seneca, J. Clarke, and A. Geikie. *Physical Science in the Time of Nero: Being a Translation of the Quaestiones Naturales of Seneca*. Landmarks of science. Macmillan and Company, Limited, 1910.

[2] J.C.D. Brand. *Lines of Light: The Sources of Dispersive Spectroscopy, 1800-1930*. Gordon & Breach Publ., 1995.

[3] Max Planck. Ueber das Gesetz der Energieverteilung im Normalspectrum. *Annalen der Physik*, 309(3):553–563, January 1901.

[4] A. Einstein. Über einen die Erzeugung und Verwandlung des Lichtes betreffenden heuristischen Gesichtspunkt. *Annalen der Physik*, 322(6):132–148, January 1905.

[5] Niels Bohr. On the Constitution of Atoms and Molecules. Pt.II. *Philosophical Magazine*, 26:476–502, December 1913.

[6] Erkki Soini and I Hemmilä. Fluoroimmunoassay: present status and key problems. *Clinical chemistry*, 25(3):353–361, 1979.

[7] Nanae Domoto, Masaomi Tanaka, Daiji Kato, Kyohei Kawaguchi, Kenta Hotokezaka, and Shinya Wanajo. Lanthanide features in near-infrared spectra of kilonovae. *The Astrophysical Journal*, 939(1):8, 2022.

[8] Ian McGill. Rare earth elements. *Ullmann's Encyclopedia of Industrial Chemistry*, 2000.

[9] Immanuel Bloch, Jean Dalibard, and Sylvain Nascimbene. Quantum simulations with ultracold quantum gases. *Nature Physics*, 8(4):267–276, 2012.

[10] Mikhail A Baranov. Theoretical progress in many-body physics with ultracold dipolar gases. *Physics Reports*, 464(3):71–111, 2008.

[11] Immanuel Bloch, Jean Dalibard, and Wilhelm Zwerger. Many-body physics with ultracold gases. *Reviews of modern physics*, 80(3):885, 2008.

[12] Axel Griesmaier, Jörg Werner, Sven Hensler, Jürgen Stuhler, and Tilman Pfau. Bose-einstein condensation of chromium. *Physical Review Letters*, 94(16):160401, 2005.

[13] Matthew A Norcia and Francesca Ferlaino. Developments in atomic control using ultracold magnetic lanthanides. *Nature Physics*, 17(12):1349–1357, 2021.

[14] Lauriane Chomaz, Igor Ferrier-Barbut, Francesca Ferlaino, Bruno Laburthe-Tolra, Benjamin L Lev, and Tilman Pfau. Dipolar physics: A review of experiments with magnetic quantum gases. *arXiv preprint arXiv:2201.02672*, 2022.

[15] A Frisch, K Aikawa, M Mark, A Rietzler, J Schindler, Erik Zupanič, R Grimm, and F Ferlaino. Narrow-line magneto-optical trap for erbium. *Physical Review A*, 85(5):051401, 2012.

[16] Bojeong Seo, Peng Chen, Ziting Chen, Weijun Yuan, Mingchen Huang, Shengwang Du, and Gyu-Boong Jo. Efficient production of a narrow-line erbium magneto-optical trap with two-stage slowing. *Physical Review A*, 102(1):013319, 2020.

[17] Mingwu Lu, Seo Ho Youn, and Benjamin L Lev. Trapping ultracold dysprosium: a highly magnetic gas for dipolar physics. *Physical review letters*, 104(6):063001, 2010.

[18] William Lunden, Li Du, Michael Cantara, Pierre Barral, Alan O Jamison, and Wolfgang Ketterle. Enhancing the capture velocity of a dy magneto-optical trap with two-stage slowing. *Physical Review A*, 101(6):063403, 2020.

[19] Jinlu Miao, James Hostetter, Georgios Stratis, and Mark Saffman. Magneto-optical trapping of holmium atoms. *Physical Review A*, 89(4):041401, 2014.

[20] D Sukachev, A Sokolov, K Chebakov, A Akimov, S Kanorsky, N Kolachevsky, and V Sorokin. Magneto-optical trap for thulium atoms. *Physical Review A*, 82(1):011405, 2010.

[21] GA Vishnyakova, ES Kalganova, DD Sukachev, SA Fedorov, AV Sokolov, AV Akimov, NN Kolachevsky, and VN Sorokin. Two-stage laser cooling and optical trapping of thulium atoms. *Laser Physics*, 24(7):074018, 2014.

[22] Ryotaro Inoue, Yuki Miyazawa, and Mikio Kozuma. Magneto-optical trapping of optically pumped metastable europium. *Physical Review A*, 97(6):061607, 2018.

[23] P Ilzhöfer, G Durastante, A Patscheider, A Trautmann, MJ Mark, and F Ferlaino. Two-species five-beam magneto-optical trap for erbium and dysprosium. *Physical Review A*, 97(2):023633, 2018.

[24] Robert D. Cowan. *The theory of atomic structure and spectra*. Number 3. Univ of California Press, 1981.

[25] G. Breit. ¡i¿the theory of atomic spectra¡/i¿. by e. u. condon and g. h. shortley. cambridge university press, pp. 431, 1935. *Science*, 83(2142):57–59, 1936.

[26] Giulio Racah. Theory of complex spectra. III. *Phys. Rev.*, 63(9-10):367, 1943.

[27] D.A. Varshalovich, A.N. Moskalev, and V.K. Khersonskii. *Quantum theory of angular momentum*. World Scientific, 1988.

[28] Christopher M Dodson and Rashid Zia. Magnetic dipole and electric quadrupole transitions in the trivalent lanthanide series: Calculated emission rates and oscillator strengths. *Phys. Rev. B*, 86(12):125102, 2012.

[29] Brian M Walsh. Judd-Ofelt theory: principles and practices. In *Advances in spectroscopy for lasers and sensing*, pages 403–433. Springer, 2006.

[30] K Ogasawara, S Watanabe, H Toyoshima, T Ishii, MG Brik, H Ikeno, and I Tanaka. Optical spectra of trivalent lanthanides in $LiYF_4$ crystal. *Journal of Solid State Chemistry*, 178(2):412–418, 2005.

[31] Brian R Judd. Optical absorption intensities of rare-earth ions. *Physical review*, 127(3):750, 1962.

[32] GS Ofelt. Intensities of crystal spectra of rare-earth ions. *The journal of chemical physics*, 37(3):511–520, 1962.

[33] Peter A Tanner. Some misconceptions concerning the electronic spectra of tripositive europium and cerium. *Chem. Soc. Rev.*, 42(12):5090–5101, 2013.

[34] Koen Binnemans. Interpretation of europium (III) spectra. *Coordination Chemistry Reviews*, 295:1–45, 2015.

[35] Lidia Smentek. Theoretical description of the spectroscopic properties of rare earth ions in crystals. *Phys. Rep.*, 297(4):155–237, 1998.

[36] Masanori Tanaka, Goro Nishimura, and Takashi Kushida. Contribution of J mixing to the $^5D_0$-$^7F_0$ transition of Eu^{3+} ions in several host matrices. *Phys. Rev. B*, 49(24):16917, 1994.

[37] Takashi Kushida and Masanori Tanaka. Transition mechanisms and spectral shapes of the $^5D_0$-$^7F_0$ line of Eu^{3+} and Sm^{2+} in solids. *Phys. Rev. B*, 65(19):195118, 2002.

[38] Takashi Kushida, Atusi Kurita, and Masanori Tanaka. Spectral shape of the 5d0–7f0 line of Eu^{3+} and Sm^{2+} in glass. *J. Lumin.*, 102:301–306, 2003.

[39] M.C. Downer, G.W. Burdick, and D.K. Sardar. A new contribution to spin-forbidden rare earth optical transition intensities: Gd^{3+} and Eu^{3+}. *J. Chem. Phys.*, 89(4):1787–1797, 1988.

[40] GW Burdick, MC Downer, and DK Sardar. A new contribution to spin-forbidden rare earth optical transition intensities: Analysis of all trivalent lanthanides. *J. Chem. Phys.*, 91(3):1511–1520, 1989.

[41] Lidia Smentek and B Andes Hess. Theoretical description of $0 \leftrightarrow 0$ and $0 \leftrightarrow 1$ transitions in the Eu^{3+} ion in hosts with C_{2v} symmetry. *Mol. Phys.*, 92(5):835–846, 1997.

[42] Lidia Smentek and Brian G Wybourne. Relativistic f↔f transitions in crystal fields. *J. Phys. B*, 33(18):3647, 2000.

[43] Lidia Smentek and Brian G Wybourne. Relativistic f↔f transitions in crystal fields: Ii. beyond the single-configuration approximation. *J. Phys. B*, 34(4):625, 2001.

[44] Brian G Wybourne and Lidia Smentek. Relativistic effects in lanthanides and actinides. *Journal of Alloys and Compounds*, 341(1-2):71–75, 2002.

[45] Elena B Dunina, Alexey A Kornienko, and Liudmila A Fomicheva. Modified theory of f-f transition intensities and crystal field for systems with anomalously strong configuration interaction. *Cent. Eur. J. Phys.*, 6(3):407–414, 2008.

[46] Jun Wen, Michael F Reid, Lixin Ning, Jie Zhang, Yongfan Zhang, Chang-Kui Duan, and Min Yin. *Ab-initio* calculations of Judd–Ofelt intensity parameters for transitions between crystal-field levels. *J. Lumin.*, 152:54–57, 2014.

[47] A Kędziorski and Lidia Smentek. Extended parametrization scheme of f-spectra. *J. Lumin.*, 127(2):552–560, 2007.

[48] Aleksandar Ćirić, Stevan Stojadinović, Milica Sekulić, and Miroslav D Dramićanin. JOES: An application software for Judd-Ofelt analysis from Eu^{3+} emission spectra. *J. Lumin.*, 205:351–356, 2019.

[49] Aleksandar Ćirić, Stevan Stojadinović, and Miroslav D Dramićanin. An extension of the Judd-Ofelt theory to the field of lanthanide thermometry. *J. Lumin.*, 216:116749, 2019.

[50] Markus P Hehlen, Mikhail G Brik, and Karl W Krämer. 50th anniversary of the judd–ofelt theory: An experimentalist's view of the formalism and its application. *J. Lumin.*, 136:221–239, 2013.

[51] Reinaldo Chacon, Aymeric Leray, Jeongmo Kim, Khalid Lahlil, Sanro Mathew, Alexandre Bouhelier, Jong-Wook Kim, Thierry Gacoin, and Gérard Colas Des Francs. Measuring the magnetic dipole transition of single nanorods by spectroscopy and Fourier microscopy. *Phys. Rev. Applied*, 14(5):054010, 2020.

[52] A. Kramida, Yu. Ralchenko, J. Reader, and and NIST ASD Team. NIST Atomic Spectra Database (ver. 5.7.1), [Online]. Available: `https://physics.nist.gov/asd` [2020, April 10]. National Institute of Standards and Technology, Gaithersburg, MD., 2019.

[53] Jean-François Wyart, Ali Meftah, Wan-Ü Lydia Tchang-Brillet, Norbert Champion, Omar Lamrous, Nissan Spector, and Jack Sugar. Analysis of the free ion Nd^{3+} spectrum (Nd IV). *J. Phys. B*, 40(19):3957, 2007.

[54] A Meftah, S Ait Mammar, JF Wyart, W-Ü L Tchang-Brillet, N Champion, C Blaess, D Deghiche, and O Lamrous. Analysis of the free ion spectrum of Er^{3+} (Er IV). *J. Phys. B*, 49(16):165002, 2016.

[55] Kamel Arab, Djamel Deghiche, Ali Meftah, Jean-François Wyart, Wan-Ü Lydia Tchang-Brillet, Norbert Champion, Christophe Blaess, and Omar Lamrous. Observation and interpretation of the $5p^5 4f^3 5d$ core-excited configuration in triply ionized neodymium Nd^{3+} (Nd IV). *J. Quant. Spec. Radiat. Transf.*, 229:145–156, 2019.

[56] C. McGuinness. Los alamos version of the cowan codes for linux, 2009.

[57] Alexander Kramida. Cowan code: 50 years of growing impact on atomic physics. *Atoms*, 7(3):64, 2019.

[58] Robert D. Cowan. Program RCE MOD20, least-squares fitting of atomic energy levels, 1968.

[59] William Clyde Martin, Romuald Zalubas, and Lucy Hagan. Atomic energy levels-the rare-earth elements. Technical report, NATIONAL STANDARD REFERENCE DATA SYSTEM, 1978.

[60] Jean-François Wyart, Ali Meftah, Annik Bachelier, Jocelyne Sinzelle, Wan-Ü Lydia Tchang-Brillet, Norbert Champion, Nissan Spector, and Jack Sugar. Energy levels of 4f3 in the nd3+ free ion from emission spectra. *Journal of Physics B: Atomic, Molecular and Optical Physics*, 39(5):L77, 2006.

[61] WT Carnall, GL Goodman, K Rajnak, and RS Rana. A systematic analysis of the spectra of the lanthanides doped into single crystal LaF_3. *The Journal of Chemical Physics*, 90(7):3443–3457, 1989.

[62] WT Carnall, PR Fields, and K Rajnak. Electronic energy levels of the trivalent lanthanide aquo ions. iv. eu3+. *The Journal of Chemical Physics*, 49(10):4450–4455, 1968.

[63] L Jyothi, V Venkatramu, P Babu, CK Jayasankar, M Bettinelli, G Mariotto, and A Speghini. Composition and concentration dependence of spectroscopic properties of nd3+-doped tellurite and metaborate glasses. *Optical Materials*, 33(6):928–936, 2011.

[64] D Levchuk, S Levchuk, H Maier, H Bolt, and A Suzuki. Erbium oxide as a new promising tritium permeation barrier. *Journal of Nuclear Materials*, 367:1033–1037, 2007.

[65] Chunming Yin, Milos Rancic, Gabriele G de Boo, Nikolas Stavrias, Jeffrey C McCallum, Matthew J Sellars, and Sven Rogge. Optical addressing of an individual erbium ion in silicon. *Nature*, 497(7447):91–94, 2013.

[66] A Chikh, D Deghiche, A Meftah, W-Ü L Tchang-Brillet, J-F Wyart, C Balança, N Champion, and C Blaess. Extended analysis of the free ion spectrum of Er^{3+} (Er IV). *J. Quant. Spectrosc. Rad. Transf.*, 272:107796, 2021.

[67] S. Shionoya, W.M. Yen, and H. Yamamoto. *Phosphor Handbook*. CRC Press laser and optical science and technology series. CRC Press, 2018.

[68] Alexandra Ya Freidzon, Ilia A Kurbatov, and Vitaliy I Vovna. Ab initio calculation of energy levels of trivalent lanthanide ions. *Physical Chemistry Chemical Physics*, 20(21):14564–14577, 2018.

[69] P Babu and CK Jayasankar. Optical spectroscopy of Eu^{3+} ions in lithium borate and lithium fluoroborate glasses. *Physica B: Condensed Matter*, 279(4):262–281, 2000.

[70] Antoine Aubret, MAGJ Orrit, and Florian Kulzer. Understanding local-field correction factors in the framework of the Onsager-Bottcher model. *Chem. Phys. Chem.*, 20(3):345–355, 2018.

[71] Simon Freed and SI Weissman. Multiple nature of elementary sources of radiation—wide-angle interference. *Phys. Rev.*, 60(6):440, 1941.

[72] RE Kunz and W Lukosz. Changes in fluorescence lifetimes induced by variable optical environments. *Phys. Rev. B*, 21(10):4814, 1980.

[73] Tim H Taminiau, Sinan Karaveli, Niek F Van Hulst, and Rashid Zia. Quantifying the magnetic nature of light emission. *Nat. Comm.*, 3(1):1–6, 2012.

[74] WC Nieuwpoort and G Blasse. Linear crystal-field terms and the 5do-7fo transition of the eu3+ ion. *Solid State Communications*, 4(5):227–229, 1966.

[75] Koen Binnemans and Christiane Görller-Walrand. Application of the Eu^{3+} ion for site symmetry determination. *J. Rare Earths*, 14(3):173–180, 1996.

[76] Koen Binnemans, Karel Van Herck, and Christiane Görller-Walrand. Influence of dipicolinate ligands on the spectroscopic properties of europium (III) in solution. *Chem. Phys. Lett.*, 266(3-4):297–302, 1997.

[77] Andrew F Kirby and FS Richardson. Detailed analysis of the optical absorption and emission spectra of Eu^{3+} in the trigonal (C3) Eu (DBM) 3. H2O system. *The Journal of Physical Chemistry*, 87(14):2544–2556, 1983.

[78] XY Chen and GK Liu. The standard and anomalous crystal-field spectra of eu3+. *Journal of Solid State Chemistry*, 178(2):419–428, 2005.

[79] M Karbowiak and S Hubert. Site-selective emission spectra of Eu^{3+}:$Ca_5(PO_4)_3F$. *J. Alloys Compounds*, 302(1-2):87–93, 2000.

[80] Freddy T Rabouw, P Tim Prins, and David J Norris. Europium-doped $NaYF_4$ nanocrystals as probes for the electric and magnetic local density of optical states throughout the visible spectral range. *Nano letters*, 16(11):7254–7260, 2016.

[81] VT Adamiv, Ya V Burak, RV Gamernyk, GM Romanyuk, and IM Teslyuk. Optical properties, electronic polarizability and optical basicity of lithium borate glasses. *Physics and Chemistry of Glasses-European Journal of Glass Science and Technology Part B*, 52(4):152–156, 2011.

[82] Gohar Hovhannesyan, Vincent Boudon, and Maxence Lepers. Transition intensities of trivalent lanthanide ions in solids: Extending the judd-ofelt theory. *Journal of Luminescence*, 241:118456, 2022.

[83] Krystyna Bukietyńska and Anna Mondry. f–f transition intensities of europium (iii) acetate complexes in a single crystal and in solution. *Journal of alloys and compounds*, 323:150–154, 2001.

[84] YY Zhang, HJ Zhang, HH Yu, JY Wang, WL Gao, M Xu, SQ Sun, MH Jiang, and RI Boughton. Synthesis, growth, and characterization of nd-doped srgdga 3 o 7 crystal. *Journal of Applied Physics*, 108(6):063534, 2010.

[85] N Usami. Types of silicon–germanium (sige) bulk crystal growth methods and their applications. In *Silicon–Germanium (SiGe) Nanostructures*, pages 72–82. Elsevier, 2011.

[86] N dkk Chanthima, J Kaewkhao, Y Tariwong, N Sangwaranatee, and NW Sangwaranatee. Luminescence study and judd-ofelt analysis of cao-bao-p2o5 glasses doped with nd3+ ions. *Materials Today: Proceedings*, 4(5):6091–6098, 2017.

[87] JH Choi, Alfred Margaryan, Ashot Margaryan, and FG Shi. Judd–ofelt analysis of spectroscopic properties of nd3+-doped novel fluorophosphate glass. *Journal of luminescence*, 114(3-4):167–177, 2005.

[88] A Florez, JF Martinez, M Florez, and P Porcher. Optical transition probabilities and compositional dependence of judd–ofelt parameters of nd3+ ions in fluoroindate glasses. *Journal of non-crystalline solids*, 284(1-3):261–267, 2001.

[89] Chaoyang Ma, Jiangfeng Zhu, Zhongqi Hu, Zicheng Wen, Jiaqi Long, Xuanyi Yuan, and Yongge Cao. Spectroscopic properties and continuous wave laser performances at 1064 nm of nd3+: Luag transparent ceramic. *IEEE Photonics Journal*, 9(2):1–14, 2017.

[90] Tássia Souza Gonçalves, JFM dos Santos, LF Sciuti, Tomaz Catunda, and Andrea Simone Stucchi de Camargo. Thermo-optical spectroscopic investigation of new nd3+-doped fluoro-aluminophosphate glasses. *Journal of Alloys and Compounds*, 732:887–893, 2018.

[91] Juniastel Rajagukguk, Rappel Situmorang, Mitra Djamal, R Rajaramakrishna, J Kaewkhao, Pham Hong Minh, et al. Structural, spectroscopic and optical gain of nd3+ doped fluorophosphate glasses for solid state laser application. *Journal of Luminescence*, 216:116738, 2019.

[92] Gurvinderjit Singh, VS Tiwari, and PK Gupta. Spectroscopic analysis on the basis judd–ofelt theory of nd3+ in (y0. 985nd0. 015) 2o3: A transparent laser-host ceramic. *Materials Research Bulletin*, 60:838–842, 2014.

[93] Dhiraj K Sardar, John B Gruber, Bahram Zandi, J Andrew Hutchinson, and C Ward Trussell. Judd–ofelt analysis of the $er^{3+}(4f^{11})$ absorption intensities in phosphate glass: Er 3+, yb 3+. *Journal of applied physics*, 93(4):2041–2046, 2003.

[94] RT Karunakaran, K Marimuthu, S Arumugam, S Surendra Babu, SF Leon-Luis, and CK Jayasankar. Structural, optical absorption and luminescence properties of nd3+ ions in nao-naf borate glasses. *Optical materials*, 32(9):1035–1041, 2010.

[95] Qingguo Wang, Liangbi Su, Hongjun Li, Lihe Zheng, Xin Guo, Dapeng Jiang, Hengyu Zhao, Jun Xu, Witold Ryba-Romanowski, Piotr Solarz, et al. Optical spectra and excited state relaxation dynamics of nd3+ in caf2 single crystal. *Journal of alloys and compounds*, 509(36):8880–8884, 2011.

[96] Mei-Hong Liu, Yan-Xue Shao, Rui-Qi Piao, De-Long Zhang, and Yan Wang. Sellmeier dispersion and spectroscopic properties of er3+-doped lutetium gallium garnet single crystal. *Results in Physics*, 30:104876, 2021.

[97] Rui-Qi Piao, Yan Wang, Zi-Bo Zhang, Chao-Yang Zhang, Xiao-Fei Yang, and De-Long Zhang. Optical and judd-ofelt spectroscopic study of er3+-doped strontium gadolinium gallium garnet single-crystal. *Journal of the American Ceramic Society*, 102(3):873–878, 2019.

[98] The jo_so code at `https://gitlab.com/labicb/joso`, 2023.

[99] The cold atom predoc school at `https://coldatoms2021.sciencesconf.org/`, 2021.

[100] Eric L Raab, Mara Prentiss, Alex Cable, Steven Chu, and David E Pritchard. Trapping of neutral sodium atoms with radiation pressure. *Physical review letters*, 59(23):2631, 1987.

[101] Cheng Chin, Rudolf Grimm, Paul Julienne, and Eite Tiesinga. Feshbach resonances in ultracold gases. *Reviews of Modern Physics*, 82(2):1225, 2010.

[102] Wenhui Li, Paul J Tanner, and Thomas F Gallagher. Dipole-dipole excitation and ionization in an ultracold gas of rydberg atoms. *Physical review letters*, 94(17):173001, 2005.

[103] Jean-Michel Raimond, Michel Brune, and Serge Haroche. Manipulating quantum entanglement with atoms and photons in a cavity. *Reviews of Modern Physics*, 73(3):565, 2001.

[104] H Jeff Kimble. Strong interactions of single atoms and photons in cavity qed. *Physica Scripta*, 1998(T76):127, 1998.

[105] HY Ban, Marcus Jacka, James L Hanssen, Joseph Reader, and Jabez J McClelland. Laser cooling transitions in atomic erbium. *Optics Express*, 13(8):3185–3195, 2005.

[106] Andrew J Berglund, James L Hanssen, and Jabez J McClelland. Narrow-line magneto-optical cooling and trapping of strongly magnetic atoms. *Physical review letters*, 100(11):113002, 2008.

[107] Mingwu Lu, Seo Ho Youn, and Benjamin L Lev. Spectroscopy of a narrow-line laser-cooling transition in atomic dysprosium. *Physical Review A*, 83(1):012510, 2011.

[108] Davide Dreon, Leonid A Sidorenkov, Chayma Bouazza, Wilfried Maineult, Jean Dalibard, and Sylvain Nascimbene. Optical cooling and trapping of highly magnetic atoms: the benefits of a spontaneous spin polarization. *Journal of Physics B: Atomic, Molecular and Optical Physics*, 50(6):065005, 2017.

[109] Andrew D Ludlow, Martin M Boyd, Jun Ye, Ekkehard Peik, and Piet O Schmidt. Optical atomic clocks. *Reviews of Modern Physics*, 87(2):637, 2015.

[110] Florian Schäfer, Takeshi Fukuhara, Seiji Sugawa, Yosuke Takasu, and Yoshiro Takahashi. Tools for quantum simulation with ultracold atoms in optical lattices. *Nature Reviews Physics*, 2(8):411–425, 2020.

[111] K Winkler, F Lang, G Thalhammer, P vd Straten, R Grimm, and J Hecker Denschlag. Coherent optical transfer of feshbach molecules to a lower vibrational state. *Physical review letters*, 98(4):043201, 2007.

[112] K-K Ni, S Ospelkaus, MHG De Miranda, A Pe'Er, B Neyenhuis, JJ Zirbel, S Kotochigova, PS Julienne, DS Jin, and Jun Ye. A high phase-space-density gas of polar molecules. *science*, 322(5899):231–235, 2008.

[113] G Reinaudi, CB Osborn, M McDonald, S Kotochigova, and T Zelevinsky. Optical production of stable ultracold sr 2 88 molecules. *Physical review letters*, 109(11):115303, 2012.

[114] Francesco Scazza, Christian Hofrichter, Moritz Höfer, PC De Groot, Immanuel Bloch, and Simon Fölling. Observation of two-orbital spin-exchange interactions with ultracold su (n)-symmetric fermions. *Nature Physics*, 10(10):779–784, 2014.

[115] M Zahid Hasan and Charles L Kane. Colloquium: topological insulators. *Reviews of modern physics*, 82(4):3045, 2010.

[116] LF Livi, Giacomo Cappellini, Marcel Diem, Lorenzo Franchi, C Clivati, M Frittelli, F Levi, D Calonico, Jacopo Catani, Massimo Inguscio, et al. Synthetic dimensions and spin-orbit coupling with an optical clock transition. *Physical review letters*, 117(22):220401, 2016.

[117] S Kolkowitz, SL Bromley, T Bothwell, ML Wall, GE Marti, AP Koller, X Zhang, AM Rey, and J Ye. Spin–orbit-coupled fermions in an optical lattice clock. *Nature*, 542(7639):66–70, 2017.

[118] Andrew J Daley, Martin M Boyd, Jun Ye, and Peter Zoller. Quantum computing with alkaline-earth-metal atoms. *Physical review letters*, 101(17):170504, 2008.

[119] André Heinz, Annie Jihyun Park, Neven Šantić, Jan Trautmann, SG Porsev, MS Safronova, Immanuel Bloch, and Sebastian Blatt. State-dependent optical lattices for the strontium optical qubit. *Physical Review Letters*, 124(20):203201, 2020.

[120] Gregory A Phelps, Anne Hébert, Aaron Krahn, Susannah Dickerson, Furkan Öztürk, Sepehr Ebadi, Lin Su, and Markus Greiner. Sub-second production of a quantum degenerate gas. *arXiv preprint arXiv:2007.10807*, 2020.

[121] Hui Li, Jean-François Wyart, Olivier Dulieu, and Maxence Lepers. Anisotropic optical trapping as a manifestation of the complex electronic structure of ultracold lanthanide atoms: The example of holmium. *Physical Review A*, 95(6):062508, 2017.

[122] Maxence Lepers, J-F Wyart, and Olivier Dulieu. Anisotropic optical trapping of ultracold erbium atoms. *Physical Review A*, 89(2):022505, 2014.

[123] Jan Hendrik Becher, Simon Baier, Kiyotaka Aikawa, Maxence Lepers, J-F Wyart, Olivier Dulieu, and Francesca Ferlaino. Anisotropic polarizability of erbium atoms. *Physical Review A*, 97(1):012509, 2018.

[124] Maxence Lepers, Olivier Dulieu, and Jean-François Wyart. Fitaik: a package to calculate least-square fitted atomic transitions probabilities. application to the er+ lanthanide ion. *arXiv preprint arXiv:2207.14001*, 2022.

[125] JE Lawler, JF Wyart, and EA Den Hartog. Atomic transition probabilities of er i. *Journal of Physics B: Atomic, Molecular and Optical Physics*, 43(23):235001, 2010.

[126] Hui Li, Jean-Francois Wyart, Olivier Dulieu, Sylvain Nascimbene, and Maxence Lepers. Optical trapping of ultracold dysprosium atoms: transition probabilities, dynamic dipole polarizabilities and van der waals c6 coefficients. *Journal of Physics B: Atomic, Molecular and Optical Physics*, 50(1):014005, 2016.

[127] Alexander Patscheider, Bing Yang, Gabriele Natale, Daniel Petter, Lauriane Chomaz, Manfred J Mark, Gohar Hovhannesyan, Maxence Lepers, and Francesca

Ferlaino. Observation of a narrow inner-shell orbital transition in atomic erbium at 1299 nm. *Physical Review Research*, 3(3):033256, 2021.

[128] C Froese Fischer, Gediminas Gaigalas, Per Jönsson, and Jacek Bieroń. Grasp2018—a fortran 95 version of the general relativistic atomic structure package. *Computer Physics Communications*, 237:184–187, 2019.

[129] Maxence Lepers, Hui Li, Jean-François Wyart, Goulven Quéméner, and Olivier Dulieu. Ultracold rare-earth magnetic atoms with an electric dipole moment. *Phys. Rev. Lett.*, 121(6):063201, 2018.

[130] P Aufmuth, A Bernard, and E-G Kopp. New levels and calculations in the Nd I spectrum. *Z. Phys. D*, 23(1):15–18, 1992.

[131] Gohar Hovhannesyan and Maxence Lepers. Improving the spectroscopic knowledge of neutral neodymium. *Physica Scripta*, 2022.

[132] MH Stockett, MP Wood, EA Den Hartog, and JE Lawler. Atomic transition probabilities of nd i. *Journal of Physics B: Atomic, Molecular and Optical Physics*, 44(23):235003, 2011.

[133] EA Den Hartog, AJ Fittante, and JE Lawler. Radiative lifetimes of neutral neodymium. *Journal of Physics B: Atomic, Molecular and Optical Physics*, 44(22):225001, 2011.